RICE UNIVERSITY

Investigating the Synthesis, Structure, and Catalytic Properties of Versatile Au-Based Nanocatalysts

By

Lori A. Pretzer

A THESIS SUBMITTED
IN PARTIAL FULFILLMENT OF THE
REQUIREMENTS FOR THE DEGREE

Doctor of Philosophy

APPROVED, THESIS COMMITTEE

Michael S. Wong, Professor, Chair
Chemical and Biomolecular Engineering,
Civil and Environmental Engineering,
Chemistry

Angel A. Marti, Assistant Professor
Chemistry, Bioengineering

Jason H. Hafner, Associate Professor
Physics and Astronomy, Chemistry

HOUSTON, TEXAS
April 2013

ABSTRACT

Investigating the Synthesis, Structure, and Catalytic Properties of Versatile Au-Based Nanocatalysts

By

Lori A. Pretzer

Transition metal nanomaterials are used to catalyze many chemical reactions, including those key to environmental, medicinal, and petrochemical fields. Improving their catalytic properties and lifetime would have significant economic and environmental rewards. Potentially expedient options to make such advancements are to alter the shape, size, or composition of transition metal nanocatalysts.

This work investigates the relationships between structure and catalytic properties of synthesized Au, Pd-on-Au, and Au-enzyme model transition metal nanocatalysts. Au and Pd-on-Au nanomaterials were studied due to their wide-spread application and structure-dependent electronic and geometric properties. The goal of this thesis is to contribute design procedures and synthesis methods that enable the preparation of more efficient transition metal nanocatalysts.

The influence of the size and composition of Pd-on-Au nanoparticles (NPs) was systematically investigated and each was found to affect the catalyst's surface structure and catalytic properties. The catalytic hydrodechlorination of trichloroethene and reduction of 4-nitrophenol by Pd-on-Au nanoparticles were investigated as these reactions are useful for environmental and pharmaceutical synthesis applications, respectively. Structural characterization revealed that the dispersion and oxidation state of surface Pd atoms are controlled by the Au particle size and concentration of Pd. These

structural changes are correlated with observed Pd-on-Au NP activities for both probe reactions, providing new insight into the structure-activity relationships of bimetallic nanocatalysts.

Using the structure-dependent electronic properties of Au NPs, a new type of light-triggered biocatalyst was prepared and used to remotely control a model biochemical reaction. This biocatalyst consists of a model thermophilic glucokinase enzyme covalently attached to the surface of Au nanorods. The rod-like shape of the Au nanoparticles made the thermophilic-enzyme complexes responsive to near infrared electromagnetic radiation, which is absorbed minimally by biological tissues. When enzyme-Au nanorod complexes are illuminated with a near-infrared laser, thermal energy is generated which activates the thermophilic enzyme. Enzyme-Au nanorod complexes encapsulated in calcium alginate are reusable and stable for several days, making them viable for industrial applications.

Lastly, highly versatile Au nanoparticles with diameters of ~3-12 nm were prepared using carbon monoxide (CO) to reduce a Au salt precursor onto preformed catalytic Au particles. Compared to other reducing agents used to generate metallic NPs, CO can be used at room temperature and its oxidized form does not interfere with the colloidal stability of NPs suspended in water. Controlled synthesis of different sized particles was verified through detailed ultraviolet-visible spectroscopy, small angle X-ray scattering, and transmission electron microscopy measurements. This synthesis method should be extendable to other monometallic and multimetallic compositions and shapes, and can be improved by using preformed particles with a narrower size distribution.

Acknowledgements

First, I would like to thank the Lord for the opportunity He gave me to study at Rice University, forge new friendships and networks, and learn more about His world. The intricacies of nanotechnology and catalysis continue to astound me and remind me just how great my God is. While in Houston, I have had the privilege of attending College Park Baptist Church. I particularly thank the Melton and the Miller families for their continual hospitality and unending support. During my time at Rice, I have met amazingly talented individuals, who I am sure I will never forget. I am convinced that such networks and friendships are a blessing from God that are not to be taken for granted.

I would like to acknowledge my advisor, Professor Michael S. Wong, for the time and energy he invested to ensure my development as a successful independent researcher. His critiques and insight have inspired me on several occasions. I appreciate the many collaborations he organized that were vital for several of my projects. The group presentations that he facilitated significantly enhanced my critical thinking and presentation skills. Collectively, these and the related technical skills that I have acquired under his tutelage will undoubtedly last a lifetime.

I am deeply indebted to my numerous co-authors, whose diligent work greatly contributed to the success of my projects. I thank Dr. Jeffrey T. Miller and his team of post-docs at Argonne National Laboratory. Dr. Miller's enthusiasm for EXAFS analysis and deep understanding of the technique made discussions with him an educational delight. I would particularly like to acknowledge Dr. Neng Guo and Dr. Tianpin Wu, who stayed awake many nights helping me collect EXAFS data. I am also grateful to Dr. Ilke

Arslan at Pacific Northwest National Laboratory, who successfully imaged my Pd-on-Au nanoparticles.

I am thankful for the opportunity I had to mentor two undergraduate co-authors, Hyun Song and Sean Kim. I sincerely hope that you learned as much from me as I learned from you. I wish you both the best as you continue your education and professional development.

Additionally, I would like to acknowledge my co-author, Mr. Quang Nguyen, who significantly contributed to my first paper published during my graduate studies. Quang, your humor, encouragement, and positive attitude greatly helped me when I began my doctorate studies. I am so thankful and honored to have worked with you during your time at Rice.

I thank my co-first author on the Au-enzyme project, Dr. Matthew Blankschien, for his patience and perseverance on a project that was typically down-right frustrating. Thanks to you, Matt, I realized that I really like Buffalo Wild Wings. “Wing Tuesdays” were so much fun. Working with you also allowed me to interact with other researchers in the Gonzalez lab (Jake, Maria, Angela, and James), whom I have enjoyed laughing with on so many occasions. Even though we had such a difficult project, we made it through!

I would like to acknowledge my fellow colleagues that have worked with me in the Catalysis and Nanomaterials Laboratory: Sravani Gullapalli, Nikolaos Soultanidis, Hitesh Bagaria, Jerimiah Forsythe, Quang Nguyen, Gautam Kini, Juan Velasquez, Yu-lun Fang, Sukit Leekumjorn, Zachary Schaefer, Shyam Benegal, Huifeng Qian, Kimberly

Heck, Zhun Zhao, Varun Gangoli, Li Chen, Yinhong Chen, and Hassan Alasiri. Thank you for your help and advice. I wish you the best for your future endeavors.

To Juan, Jerimie, Nikos, Sravani, Hitesh, Shyla, and Gautam, thank you for all of the many coffee breaks, meals, and late-night research discussions these last few years. There is truly nothing like a cup of coffee and deep research conversations. These breaks were very motivational for me. Juan, Sravani, and Jerimie, thank you so much for making coffee in the office and for your willingness to listen and help me solve difficult research problems. I am pretty sure that I drove you all crazy on more than one occasion, so thank you for your patient tolerance. Gautam, thank you for your patience, encouragement, and time helping me with my research and training me on the TEM. Thanks to your in-depth knowledge of Houston cuisine, I have tried more new foods these last five years than any other time in my life.

To Hitesh and Shyla, thank you so much for your continual support, advice, and encouragement. Shyla, your spunk and self-confidence inspire me. Your charisma and humor have made me realize that laughter is a true medication for the heart. Thank you for your willingness to listen and help even late at night. Hitesh, I am so incredibly grateful for the opportunity that I was given to work with you at Rice. Your wise advice, patience, and excellent teaching significantly influenced me. I will never forget your kind and encouraging words before my second year qualifying exam. They meant so much and helped me make it through. Both you and Shyla are an inspiration to me, and I am so thankful for the opportunity I have had to meet and get to know both of you.

To my dear friends, Sravani, Nikos, and Melissa Miller, you all have been my Houston stabilizing agents that I am sure God put in my life to prevent me from crashing

on so many occasions. Melissa, you have endured so much. Thanks for taking the time to go shopping with Sravani and I. Those were such wonderfully fun times! Thank you also for the late-night discussions and coffees that we shared. Your quiet support and encouragement these last five years have meant more than you will ever know. Thank you for keeping me accountable and on track. I also appreciate the opportunity you gave me to meet and spend time with your wonderful family. Please know that they and you are so incredibly special to me.

To my dear friends, Sravani Gullapalli and Nikolaos Soultanidis, you all are truly in a class all your own. In my estimation, our crazy friendship is best explained as a synergistic effect of our diverse personalities and backgrounds. I have so many treasured memories of countless car rides, coffee breaks, and running on the Rice track that just make me smile and want to laugh. You all were my pressure-release valve on so many occasions. I am 100% sure that I drove you nearly out of your minds more than once. I am so thankful though that you are my friends anyways. Thank you for pushing me when I thought I could not go any further. There were so many times that you all served as catalysts, lowering my energy barrier for a given task, so that it became possible on a realistic time-scale. I wish I could accurately describe how much your continual support and encouragement mean to me. I pray that I can be as good a friend to you as you have been to me. Thank you for being such a blessing.

I would like to acknowledge my undergraduate advisor, Dr. Joel Boyd, for inspiring me to pursue a doctorate in chemistry at Rice University. I am truly grateful for his guidance, passion for chemistry, and dedication to equipping his students for success. I also thank Kerri Boyd for her continued friendship over many years. Kerri, thank you

for your encouragement and support despite being many miles away. Thank you for taking the time to help me learn how to run. Running is one of the best stress-relievers that I have yet to find. Thank you for keeping me on track in so many ways. I am certain that I can never adequately repay you for all you have done, despite my best efforts.

Last but far from least, I would like to acknowledge my dear family. You all have always been there through thick and thin, loving me even when I do not deserve it. To my sister, Anna, and brothers, Nilen-Lee and Nathan, I am so proud of each of you and love you so much. I will never forget all of the wonderful times that we enjoyed together growing up. Please know that I will always endeavor to be there for you; and Anna, you will always be my favorite sister. To my mother, Marcia, and father, Nilen, thank you for the many sacrifices that you both made to ensure all your children received a quality education. Thank you for always being there for all of us and encouraging us when things were tough. I love both of you and thank you for inspiring me academically and spiritually.

To my sister, Anna, my brothers, Nilen-Lee and Nathan, and my parents, Marcia and Nilen Pretzer, I dedicate this thesis.

Dedicated to My Family.

Anna, Nilen-Lee, Nathan, Marcia, and Nilen Pretzer

Lori A. Pretzer

April 2013

Table of Contents

Table of Figures

Table of Tables

Chapter 1
Background and Research Motivation

1.1 Introduction to Transition Metal Nanocatalysis.

Transition metal (T-metal) catalysts are catalysts comprised of elements from periodic table groups 3-12 that are able to catalyze a myriad of chemical processes, particularly those applied in petrochemical, medicinal, and environmental fields.[1-3] A catalyst is a moiety that increases the rate of a thermodynamically favorable chemical reaction without being consumed by the reaction.[4] Only kinetic factors of the chemical reaction, such as its rate, nature of the transition state, and activation energy can be affected by the catalyst.[4] A catalyst's performance is generally evaluated based on: (1) activity, which is the reaction rate per catalytic metal site, and (2) selectivity, or the molar ratio of desired product to total products formed.[5]

Many modern commercialized reactions are catalyzed by heterogeneous transition metal catalysts, such as Ag, Pd, Pt, Cu, Rh, and Ni.[6] Such heterogeneously-catalyzed reactions occur at the interface between the solid catalyst phase and the liquid or gaseous reaction phase.[1,4] A significant advantage of using heterogeneous catalysts is that they can be easily reused and separated from the product stream. Since metal-based catalysts are expensive and potentially toxic to humans and other organisms, improving their efficiency (*i.e.*, activity, product selectivity, and lifetime) is highly desirable.

1.1.1 Motivation for Nano-sized Transition Metal Catalysts.

Nanoparticulate T-metal catalysts are a class of heterogeneous catalysts having at least one dimension between 1 and 100 nm.[7] Sometimes referred to as semi-heterogeneous catalysts due to their small size,[8] these catalysts can be supported on materials such as carbon, metal oxides, and polymeric resins to simplify catalyst recycling and removal

from the reaction phase. Such transition metal nanomaterials have structure-dependent electronic, chemical, and geometric properties that can improve their catalytic activity and selectivity, making them more efficient than larger-sized bulk metals. The ability to tune the catalytic properties of transition metal nanomaterials by controlling their size, shape, or composition is a potentially expedient way to increase catalyst versatility and efficiency.[7,9] The following sections briefly introduce these structural characteristics and explore how each influences the catalytic properties of transition metal nanocatalysts.

1.1.2 Catalytic Effects of Nanocatalyst Size and Shape.

The activity of Pt,[10,11] Pd,[12,13] Au,[14,15] Rh,[16,17] Ir,[18] and many other transition metal nanocatalysts[19,20] has been shown to differ with particle size.[20-23] As the particle size decreases, a greater fraction of catalyst atoms will be on the surface thereby increasing the probability of interaction with adsorbate molecules.[24] Concomitantly, such size reduction can significantly affect adsorbate-catalyst interactions by altering the catalyst's geometric and electronic properties.[6,25,26]

Changes to the electronic configuration of the transition metal catalyst that become evident at particle diameters $\leq$ 10 nm are referred to as quantum size effects.[6,27] Since the size of the particle is on the same order as the de-Broglie wavelength of the valence electrons, the particle's electronic behavior follows quantum mechanical rules, such that the electrons can be described as "particles in a box".[25,27] Therefore unlike the bulk metal, the electron wavefunctions of the nanoparticles (NPs) are more confined and discrete energy levels can be formed (Fig 1.1).[24,27]

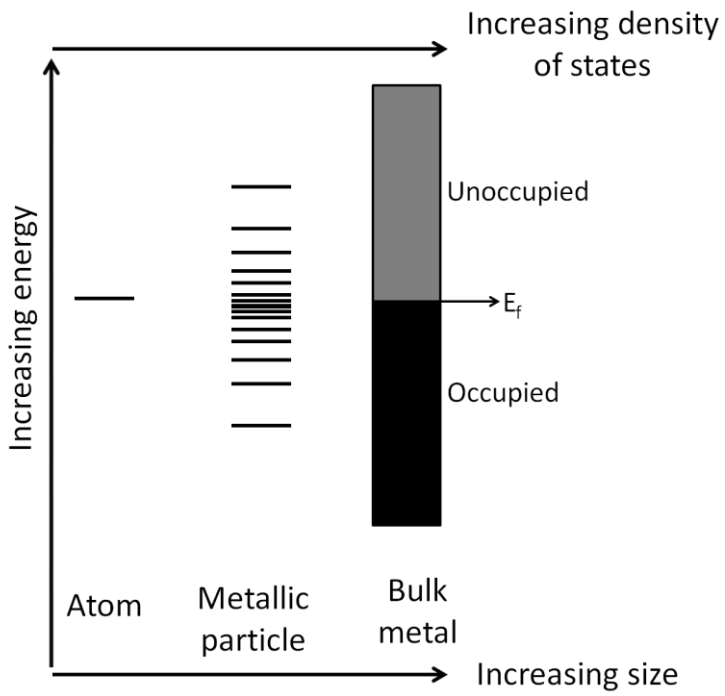

Figure 1.1 Visual representation of the changes in electronic configuration as the number of metal atoms increases. E_f denotes the Fermi level of the metal. (Adapted from Refs. 25, 28)

Changes to the valence d-band of transition metal catalysts are particularly important because they can directly affect the strength of the adsorbate-metal bond.[29,30] As the size of the nanoparticle decreases the d-band narrows such that the center, or average energy of the band, moves closer to the Fermi level of the bulk metal and the density of states (DOS) decreases.[6,25,26,31] In general, as the d-band center moves closer to the Fermi level, the strength of the metal-adsorbate bond increases.[29] Stronger adsorbate-metal interactions do not necessarily increase the rate at which the catalyzed reaction occurs.[5] If reaction molecules (*i.e.,* reactant, intermediate, or product) bind strongly to metal surface atoms (heat of adsorption ~100-800 kJ/mol), the catalyst surface may become saturated with adsorbates resulting in decreased catalytic activity.[5,32] Alternatively, weak van der Waals interactions between adsorbates and metal surface

atoms (heat of adsorption <80 kJ/mol) can result in reaction molecule surface coverages too low to sustain the reaction.[5] Ideal metal-adsorbate interactions perturb the reactant(s) toward the transition state, such that an adsorbed product is formed that can readily desorb from the catalyst's surface. Hence, the manner in which size-dependent shifts of a transition metal catalyst's d-band center affect its catalytic activity will vary depending on the desired chemical reaction.

Within the size range that the electronic structure of a transition metal nanoparticle changes, the particle's geometry can concomitantly be altered and affect how adsorbates interact with the catalyst surface.[33-35] As the particle diameter is decreased below 5 nm, the relative number of edge and corner surface atoms increases.[35] Low-coordinated atoms (coordination number ≤6), such as those on the particle edge and corner, can have unique catalytic properties due to a shift in their d-band center toward the catalyst's Fermi level.[1,36] The coordination number of corner, edge, and face surface atoms and the distance between these atoms varies with the particle's shape; hence, different shaped particles can exhibit unique catalytic activity.[4,37,38] Recently, El-Sayed and colleagues demonstrated that the geometry of Pt nanoparticles (NPs) can influence their ability to catalyze electron transfer reactions between $Fe(CN)_6^{3-}$ and $S_2O_3^{2-}$ ions.[39,40] Bratlie *et al.* alternatively found that Pt cubic and Pt cuboctahedral particles exhibit similar catalytic activity for the hydrogenation of benzene, but cubic NPs have a higher selectivity to cyclohexane.[37] Similar geometric effects have also been noted for Pd[41,42] and Rh[43-45] NP catalysts. Due to the morphology-dependent geometric and electronic properties of transition metal nanocatalysts, control of particle size and shape can significantly improve their activity and selectivity.

1.1.3 Bimetallic Nanocatalysts: Catalytic Effects of Composition.

In the early 1900s, the discovery that the addition of Pd to Pt could improve catalytic activity for ammonia oxidation gave rise to the development and study of bimetallic transition metal catalysts.[30] Many bimetallic catalysts, particularly Pt and Pd-based catalysts with Ir, Re, Ge, Sn, Au, Cu, or Pb, are currently used to catalyze a variety of chemical reactions, including oxidation, hydrogenation, and reforming reactions.[30,46] Such catalysts usually exhibit high catalytic activity, selectivity, and deactivation resistance, exceeding that of their monometallic analogues.[4]

In general, two types of bimetallics can be synthesized: those in which both metallic components are catalytically active and those in which one component is predominantly active while the other is relatively inert. The relatively inert metal can either enhance the activity of the original transition metal catalyst or act as a diluent. In turn, it is possible that the catalytic properties of the more inert transition metal can be enhanced due to interaction between the two metals.[4]

The unique catalytic properties of bimetallic catalysts are generally ascribed to geometric and electronic effects caused by interaction between the two metals.[47] The geometric effect describes how the interaction between two metals affects adsorption of reaction molecules by changing the coordination number and bond length between a given metal's atoms.[48] Reactions, such as alkane hydrogenolysis, that require a particular arrangement of neighboring catalyst atoms are strongly influenced by the geometric effect.[30] Chen *et al.* recently demonstrated that deposition of Pd atoms onto Au (100) and (111) surfaces changed the catalytic activity of the Pd-Au surface for the acetoxylation of ethylene to vinyl acetate.[49] Since the distance between Pd atoms on the Au (100) surface

was closer to the optimized distance for bond formation between adsorbed acetic acid and ethylene, the catalytic activity of the Pd-Au (100) surface was significantly higher than the Pd-Au (111) surface.[49] Changing the bond length between atoms of a given metal can also alter the metal's d-band center, which can potentially affect the overall catalytic properties of a bimetallic nanomaterial.[50]

The electronic effect describes how the heterometallic bonding interactions between two metals changes their electronic structures and affects adsorption of reaction molecules.[51] Adding a second metal to a transition metal can change both metal's d-band density of states, which results in shifting of the d-band center and change in band width.[30,52] While early theories, such as the rigid band model, attributed these effects to charge transfer between the two metals, several studies have revealed that such *inter*metallic transfer is small (≤ 2%) and instead *intra*metallic d-band charge transfer (hybridization) predominantly occurs.[30,53] For Ni, Pt, and Pd this *intra*metallic d-band charge transfer is such that the d-band filling does not change but instead the metal's d-band width and center shift.[29,51] The manner in which the d-band of a given metal changes upon interaction with a second metal varies with the native electronic properties of the two metals and the extent to which they are mixed.[54] Changes to the d-band due to heterometallic bonding interactions and altered bond-lengths between metal atoms can explain the reason that bimetallic catalysts resist poisoning by molecules such as carbon monoxide that readily deactivate pure catalysts.[55]

The ability to tune the catalytic properties of transition metal nanomaterials by controlling their structure makes them truly versatile and potentially highly efficient catalysts. A variety of techniques have therefore been developed to synthesize transition

metal nanomaterials. An introduction to common methods used to prepare monometallic and bimetallic transition metal nanocatalysts is provided in the following sections.

1.2 Introduction to Transition Metal Nanocatalyst Synthesis.

Monometallic T-metal nanocatalysts can be synthesized using physical methods (top-down approach) in which the bulk metal is subdivided to form smaller nanoparticles or chemical methods (bottom-up approach) in which ionic metal precursors are chemically reduced or organometallic compounds are controllably decomposed.[56,57] Chemical methods are typically used to synthesize transition metal nanocatalysts because these methods are versatile, inexpensive, technologically simple to implement, and often provide better control of particle morphology and size distribution than physical methods.[7,56,57] Chemical methods can be used to prepare transition metal nanoparticles that are dispersed in the solid, liquid, or gaseous state; however, liquid state methods are more widely applied since they offer better control of particle morphology and can be conducted in a relatively simple synthesis apparatus.[9,58] For this reason, only liquid chemical synthesis methods will be discussed in further detail below.

1.2.1 Synthesis of Monometallic Transition Metal Nanocatalyst Sols.

The colloid formed when metal nanoparticles are suspended in a liquid is referred to as a metal particle sol. Five general methods used to chemically synthesize transition metal nanocatalyst sols are: (1) chemical reduction of metal salts, (2) thermal, photochemical, or sonochemical decomposition and/or reduction methods, (3) electrochemical synthesis, (4) controlled decomposition of metastable organometallic compounds, and (5) metal vapor synthesis.[9,46,56,58,59] Chemical reduction of metal salts occurs by reducing a dissolved liquid-phase metal salt with a chemical reducing agent such as hydrogen,

carbon monoxide, citrate, formaldehyde, hydrazine, or sodium borohydride, typically in the presence of an added stabilizing agent.[9,57,59] Thermal, photochemical, or sonochemical methods use heat, ultra-violet or gamma radiation, or ultrasound waves, respectively, to decompose or reduce metallic precursors into zero-valent metal nanoparticles.[57,59] Alternatively, electrochemical synthesis is performed by oxidizing metal from a bulk metal anode, reducing the resulting cations to zerovalent metal atoms at the cathode, and forming metal nanoparticles by controllably aggregating the zerovalent metal atoms.[57] Decomposition of low-valent organometallic complexes due to heat, light, or ultrasound can also result in the formation of transition metal nanoparticles.[57,59] Transition metal nanoparticle sols of relatively volatile metals (*i.e.,* Au, Pd, Cu, Ni, Pt, Pr, Yb, Er) can lastly be synthesized by evaporating the metal at reduced pressures, co-condensing with an organic solvent at low temperatures (~ -196°C), and warming the frozen metal/organic mixture, which causes small particles to form and grow.[59,60]

For chemical t-metal sol synthesis methods, the particle size distribution can be controlled if nucleation, or the formation of ultrasmall particles consisting of a few atoms, and particle growth are sequential and separated from one another in time.[61-63] The final shape of the nanoparticle depends on the crystallinity of seed particles, which are larger than nuclei but smaller than the final particle, and relative growth rates of the seed's different crystal facets.[64] Stabilizing agents such as polymers, surfactants, dendrimers, ionic compounds (halides, carboxylates, or polyoxoanions), phosphines, thiols, or amines must be used to prevent colloidal nanoparticle aggregation to the bulk.[57,59,65] Such particle aggregation occurs at short interparticle distances due to

attractive van der Waals forces but is prevented by a stabilizing agent that induces a repulsive force greater than the van der Waals forces. This repulsive force can be generated due to: (1) charge stabilization, in which stabilizing agents form an electrical double-layer around particles that results in Coulombic repulsion between particles and/or (2) steric stabilization, which occurs when macromolecular stabilizing agents of two particles are confined in an interparticle space and cause a decrease in entropy (increase in free energy) and osmotic repulsion between the two particles.[59]

Of the liquid-state chemical synthesis methods used to synthesize t-metal nanomaterials, the chemical reduction of metal salts is most widely used due to its simplicity, high versatility and reproducibility, and the ability to readily control particle morphology and size distribution.[57,59] In general, chemical reduction of metal salts can occur through a homogeneous or heterogeneous nucleation pathway. For homogeneous nucleation routes, nanoparticles (NPs) are nucleated and grown in one reaction vessel at a specific temperature, reactant and stabilizing agent concentration, and synthesis time.[27] For heterogeneous nucleation (also called seeded-growth) routes, monodisperse NPs (relative size distribution (rsd) < 15%) are produced by carefully reducing the metal salt onto smaller, monodisperse seed NPs.[66,67] Control of particle shape and size for both the homogeneous and heterogeneous pathways is done by selecting suitable reactants, such as the metal precursor, reducing agent, and stabilizing agents, and reaction conditions, including relative concentrations of the aforementioned reactants, temperature, and time.[9,57-59] For the heterogeneous pathway, particle size and shape is highly dependent upon the crystal structure and size of the seed NPs as well as the relative growth rates of the seed's different crystal faces.[64] The size distribution of particles synthesized via the

heterogeneous pathway is also limited by the size distribution of the preformed sol. Post-synthesis approaches to narrow a particle size distribution include centrifugation,[68,69] electrophoresis,[70,71] etching,[72,73] chromatography,[74,75] and "digestive ripening," in which NPs with a broad size are refluxed in a solvent.[76,77]

1.2.2 Synthesis of Bimetallic Transition Metal Nanocatalyst Sols.

Since chemical reduction of metal salts provides better control of particle size, shape, and composition, only this method of bimetallic nanocatalyst sol synthesis will be discussed. There are several review articles concerning bimetallic nanocatalyst synthesis, which include discussions of alternative chemical reduction methods.[46,47,56,58,78] In general, there are two metal salt reduction methods that can be used to synthesize bimetallic transition metal nanocatalyst sols; namely, co-reduction and successive reduction.[56] For co-reduction techniques, both metal salts are reduced simultaneously while for successive reduction methods the metal salt of one metal is reduced onto the surface of preformed, suspended particles of the other metal.[46] Akin to monometallic metal sol synthesis, it is important to separate bimetallic particle nucleation and growth in time so that variations in particle composition and morphology are minimized. The two metals comprising the NP can be arranged in core-shell, three-shell, cluster segregated, or mixed patterns, as seen in Figure 1.2, depending upon their relative bonding strengths, extent of charge transfer, atomic size, bulk surface energy, bonding strength to surface ligands, and specific electronic/magnetic properties.[79]

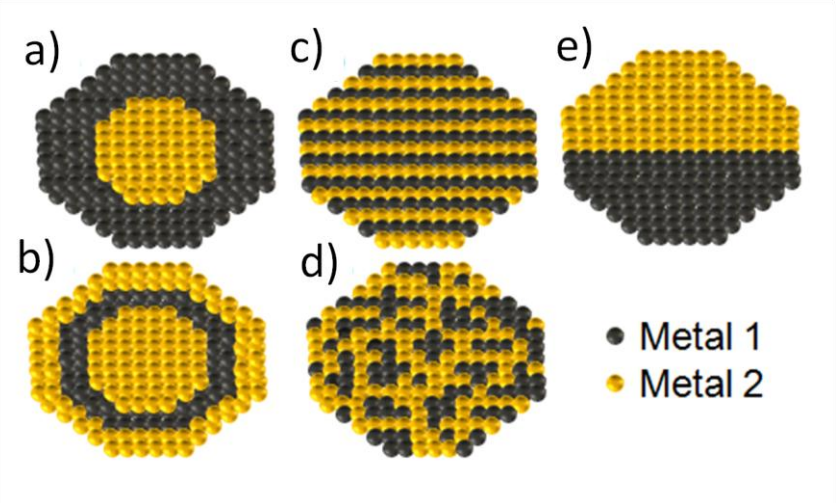

Figure 1.2 (a) Core-shell, (b) three shell, (c) mixed (organized), (d) mixed (random), and (e) cluster segregated patterns of metals in bimetallic particles.

Core-shell NPs are particularly interesting given the ability to systematically tune the catalytic activity of the shell metal by altering the shape and thickness of the shell and/or the size of the core.[80-83] Furthermore, such core-shell particles often exhibit higher catalytic activity[84,85] and selectivity[86] than that of their mixed counterparts.

For co-reduction methods, separation of particle nucleation and growth in time can be achieved by using a correct combination of reducing and stabilizing agents as well as suitable reaction conditions, such as temperature, time of synthesis, and atmosphere (*i.e.*, oxidizing *vs.* reducing).[46,58] By using two metals with different reduction potentials, the metal with the higher reduction potential can be reduced first, forming a particle core upon which the second metal can subsequently deposit at a later stage in the co-reduction reaction. The stability of the resulting core-shell particle depends on the surface energies, chemical nature, and relative bond strengths of the two metals. For example, if Pd and Ag are co-reduced, the Pd will reduce first due to its higher reduction potential such that $Pd_{core}Ag_{shell}$ NPs are formed. If the NPs are synthesized in the presence of ammonia, $Pd_{shell}Ag_{core}$ NPs will form as the Pd migrates to the particle surface due to the formation

of stable Pd-NH_3 bonds.[46]

During successive reduction synthesis methods, a second metal is selectively reduced onto a preformed particle of the first metal. Such bimetallic synthesis occurs only if heterogeneous nucleation is thermodynamically favored over homogeneous nucleation.[46] If the reaction system can offer enough energy to overcome the homogeneous nucleation energy barrier, nucleation of the second metal will occur resulting in the formation of two monometallic nanoparticle populations in the same sol. Hence reaction parameters, such as the temperature and reducing agent, must be appropriately selected so that the thermodynamic requirements for heterogeneous nucleation are maintained.[58]

For successive reduction methods, the final structure of the bimetallic particle depends on the size and shape of the preformed particle sol and the relative growth rates of the different crystal facets as well as the surface energies, chemical nature (*i.e.*, electronegativity), and relative bond strengths of the two metals.[46,58,64] Hence, it is possible to make alloyed (mixed) bimetallic nanoparticles using a successive reduction method although core-shell and heterostructures are more common.[58] The minimum size distribution of the final bimetallic particle sol is limited by the size distribution of the preformed seed particle sol. The size and shape of the preformed particles can significantly influence the nucleation and growth of the second metal. Generally, sites with the lowest coordination number and highest degree of curvature on the seed particle surface have high activity and therefore act as heterogeneous nucleation sites.[58]

1.3 Research Motivation and Thesis Outline.

Transition metal nanomaterials are widely used to catalyze a myriad of chemical reactions key to environmental, medicinal, and petrochemical fields. Therefore, improving their catalytic activity and lifetime would have significant economic and environmental rewards. Potentially expedient options to improve catalytic activity and lifetime are to alter the shape, size, or composition of transition metal nanomaterials. The development of simplified, less-toxic methods to prepare highly versatile and efficient nanocatalysts would be helpful to bring such efforts to full fruition.

Prediction of the ideal catalyst morphology for a given chemical reaction is limited by the complexity of the relationship between the activity and structure of a given transition metal nanocatalyst. Experimental studies are often conducted to probe the effect of a transition metal nanomaterial's size, shape, or composition on its catalytic properties and can provide insight for future catalyst design. Controlling the size, shape and composition of such catalysts independently from one another requires highly-controlled synthesis procedures. Therefore, interpretation of experimental studies is often complicated because more than one structural parameter has been affected during synthesis, particularly in the case of bimetallic catalysts.

This thesis explores the relationships between structure and catalytic properties of synthesized Au, Pd-on-Au, and Au-enzyme model transition metal nanocatalysts. Au and Pd-on-Au nanomaterials were selected for these studies due to their wide-spread application and structure-dependent electronic and geometric properties. The influence of the size and composition of Pd-on-Au nanocatalysts was systematically investigated and each was found to affect the catalyst's surface structure and catalytic properties. Using

the electronic properties of Au nanoparticles, a new type of light-triggered biocatalyst was prepared and used to remotely control a model biochemical reaction. Lastly, highly versatile Au nanoparticles with diameters of ~3-12 nm were prepared using a new seeded-growth synthesis method based on the ability of preformed Au seed particles to catalyze carbon monoxide oxidation. The results of these collective works contribute design procedures and synthesis methods that enable the preparation of more efficient future transition metal nanocatalysts. The following amplifies each of these key studies.

In Chapters 2 and 3, it will be shown that the dispersion and oxidation state of surface Pd atoms of Pd-on-Au NPs influence the particles' ability to catalyze two model reactions, specifically the aqueous hydrodechlorination (HDC) of trichloroethene (TCE) and reduction of 4-nitrophenol (4-NL) (Fig. 1.3). Catalytic TCE HDC was investigated since this reaction could be used to remove TCE and similar organochloride groundwater contaminants from the environment. The catalytic reduction of 4-nitrophenol was studied because it is a model nitroaromatic reduction reaction and such reactions are highly commercialized and widely applied.

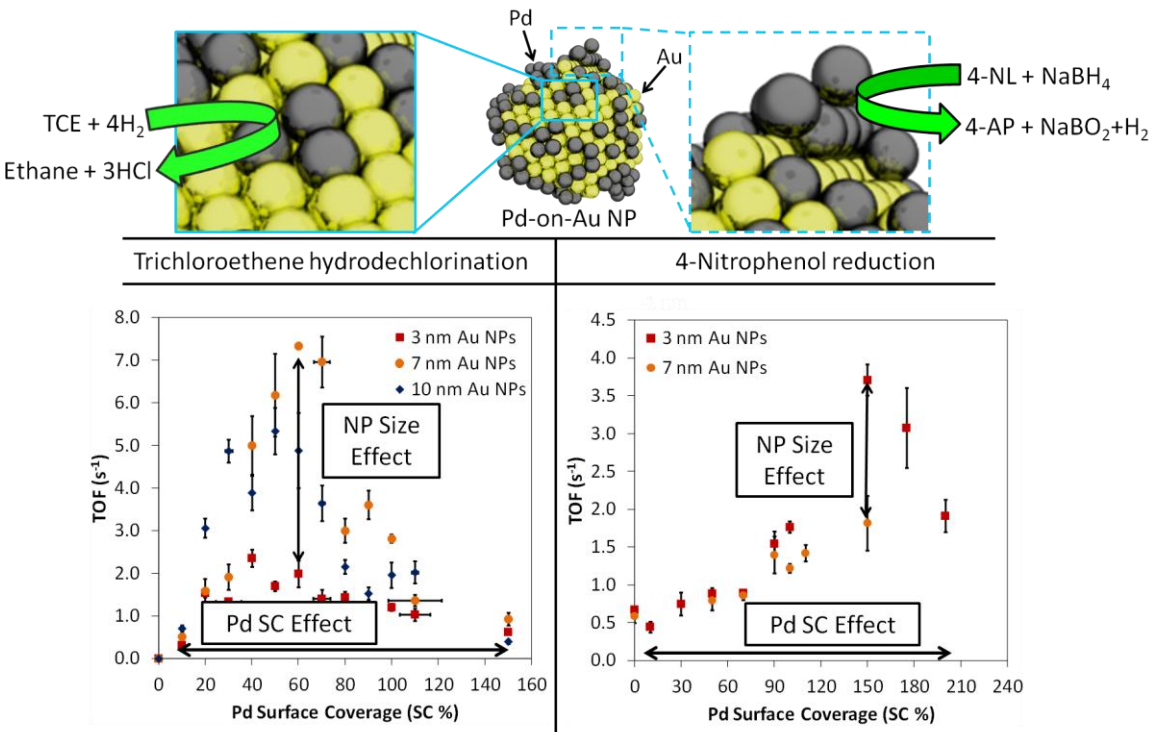

Figure 1.3 Schematic of overall Pd-on-Au nanoparticle (NP) and highly active sites for trichloroethene (TCE) hydrodechlorination and 4-nitrophenol (4-NL) reduction. Catalytic activity (quantified as turnover frequency (TOF)) of different sized particles for trichloroethene (TCE) hydrodechlorination and 4-nitrophenol (4-NL) as a function of Pd surface coverage (Pd SC) is compared. Effects of NP size and the Pd SC are noted. Vertical error bars represent the standard deviation of at least three replicate experiments. Horizontal error bars are based on inductively-coupled plasma optical emission spectroscopy (ICP-OES) measurements. 4-AP represents 4-aminophenol.

In-depth extended X-ray absorption fine structure spectroscopy (EXAFS) and aberration-corrected scanning transmission electron microscopy (STEM) structural analyses, revealed that the dispersion and oxidation state of Pd surface atoms is controlled by the Pd-on-Au NP size and Pd surface coverage. EXAFS and STEM experiments were performed in collaboration with researchers at Argonne and Pacific Northwest National Laboratories, respectively. The Pd dispersion and oxidation state changed with the Pd surface coverage, but the Au NP size affected the Pd SC at which metallic Pd monomers, metallic two-dimensional (2-D) and partially oxidized 3-D Pd ensembles were formed. This evidence of Au particle size affecting the nature of Pd

surface species of Pd-on-Au NPs illustrates a new approach to control and modify metal active sites of bimetallic NP catalysts. The study concerning the hydrodechlorination of trichloroethene and aforementioned EXAFS and STEM characterization of Pd-on-Au NPs is published in the *Journal of Catalysis*.[87]

In Chapter 4, it is shown that thermophilic enzyme-gold nanorod complexes can be fabricated and used as light-triggered biocatalysts to remotely control a biochemical reaction at traditional bulk reaction temperatures (~50 °C). Plasmonic nanoparticles, such as Au nanorods, have surface-localized collective electronic oscillations (surface plasmons) that can convert optical energy to thermal energy with high efficiency upon resonant optical illumination.[88-90] The rod-like shape of the Au nanoparticles is important, causing their longitudinal surface plasmons to resonate with near-infrared electromagnetic radiation (λ~690−900 nm)[91] that is absorbed minimally by biological tissues.[92] The use of such plasmonic nanoparticles to noninvasively trigger biochemical pathways has been largely unexplored, but could significantly improve how biochemical pathways are controlled for *in vitro* and, quite possibly, *in vivo* use.

This study shows that the thermal energy generated upon optical excitation of Au NR surface plasmons can be used to activate thermophilic enzymes covalently attached to the NR surface. The model thermophilic enzyme used in this study was *Aeropyrum pernix* glucokinase, a key enzyme for the decomposition of glucose *via* the glycolysis pathway. The enzyme's rate of reaction was increased by ~60% when the thermophilic enzyme-gold nanorod complexes were exposed to a laser beam of λ~800 nm (Fig 1.6).

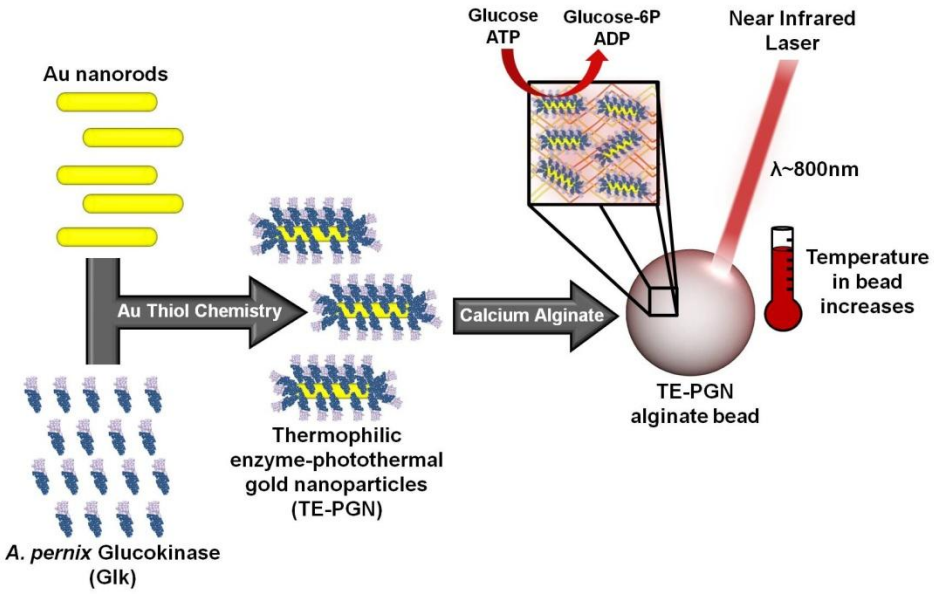

Figure 1.4 Schematic of the synthesis of thermophilic enzyme-photothermal gold nanoparticles (TE-PGNs), encapsulation in calcium alginate, and light-trigerred biocatalysis of glucose to glucose-6-phosphate (glucose-6P) by TE-PGN alginate beads. ATP and ADP represent adenosine triphosphate and adenosine diphosphate, respectively.[93]

The observed increase in enzyme activity corresponded to a local temperature increase within a calcium alginate encapsulate of ~20 °C when compared to the bulk medium maintained at standard, nonthermophilic temperatures. The encapsulated nanocomplexes were reusable and stable for several days, making them potentially useful in industrial applications. This study is published in *ACS Nano* and a U.S. patent application (No. 61 734 566) has been filed.[93]

In Chapter 5, CO reduction of gold(III) hydroxide-chloride ions ($[AuCl_{4-x}(OH)_x]^-$) onto preformed Au NPs is introduced as a new method to synthesize aqueous-phase Au NP sols with diameters between 3 nm and 12 nm. Controlled synthesis of different sized particle sols is verified through detailed ultraviolet-visible spectroscopy, small angle X-ray scattering, and transmission electron microscopy measurements (Fig 1.5).

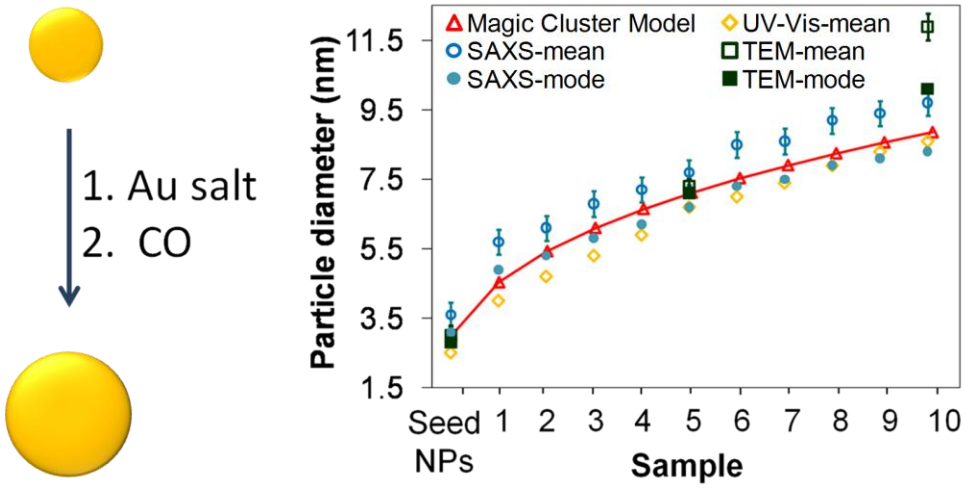

Figure 1.5 Heterogeneous nucleation (seeded-growth) of Au NPs by CO reduction of gold(III) hydroxide-chloride species onto preformed Au seed NPs. Ten samples with increasing concentration of gold(III) hydroxide-chloride species were prepared and the corresponding Au particle sizes after CO reduction were probed by ultraviolet-visible spectroscopy (UV-Vis), small angle X-ray scattering (SAXS), and transmission electron microscopy (TEM). Error bars for TEM and SAXS measurements denote the relative standard deviation. Error bars for UV-Vis measurements are not visible.[94]

A detailed reaction mechanism for the growth process is presented, in which the high-pH hydrolysis of chloroauric acid and stoichiometry among the reactants were considered. Compared to other reducing agents used to generate metallic NPs, CO can be used at room temperature and its oxidized form does not interfere with the colloidal stability of the NPs. This seeded method of growing NPs should be extendable to other monometallic and multimetallic compositions and shapes, and can be improved by using seed particles with a narrower size distribution. This study is published in the *Journal of Physical Chemistry C*.[94]

In Chapter 6, a summary of the aforementioned studies concerning model Au and Pd-on-Au nanocatalysts and suggestions for further investigations are provided. Further characterization of Pd-on-Au nanoparticles under the reaction conditions for TCE HDC and 4-NL reduction could provide further insight into the structure-activity correlations

presented. X-ray absorption near edge spectroscopy (XANES) of the Pd and Au L_{III} adsorption edges of Pd-on-Au NPs could probe the electronic effects of the NP's size and composition. Metal carbide catalysts are presented as an emerging alternative to traditional bimetallic catalysts. Such metal carbide catalysts can exhibit catalytic properties similar to Pd and Pt and would be an interesting alternative to Pd-on-Au NPs. Lastly, the application and design of thermophilic enzyme-gold nanoparticles for enzymatic biohydrogen production is discussed.

1.4 References.

(1) Zaera, F. *Prog. Surf. Sci.* **2001**, *69*, 1.

(2) Sinfelt, J. H. *Surf. Sci.* **2002**, *500*, 923.

(3) Farrauto, R. J.; Heck, R. M. *Catal. Today* **2000**, *55*, 179.

(4) Augustine, R. L. *Heterogeneous Catalysis for the Synthetic Chemist*; Marcel Dekker, 1996.

(5) Thomas, J. M.; Thomas, W. J. *Principles and Practice of Heterogeneous Catalysis*; Wiley, 1997.

(6) Moshfegh, A. Z. *J. Phys. D-Appl. Phys.* **2009**, *42*, 233001.

(7) Sau, T. K.; Rogach, A. L. *Adv. Mater.* **2010**, *22*, 1781.

(8) Astruc, D.; Lu, F.; Aranzaes, J. R. *Angew. Chem. Int. Ed.* **2005**, *44*, 7852.

(9) Semagina, N.; Kiwi-Minsker, L. *Catal. Rev.-Sci. Eng.* **2009**, *51*, 147.

(10) Bergamaski, K.; Pinheiro, A. L. N.; Teixeira-Neto, E.; Nart, F. C. *J. Phys. Chem. B* **2006**, *110*, 19271.

(11) Rhee, C. K.; Kim, B. J.; Ham, C.; Kim, Y. J.; Song, K.; Kwon, K. *Langmuir* **2009**, *25*, 7140.

(12) Zhou, W. P.; Lewera, A.; Larsen, R.; Masel, R. I.; Bagus, P. S.; Wieckowski, A. *J. Phys. Chem. B* **2006**, *110*, 13393.

(13) Le Bars, J.; Specht, U.; Bradley, J. S.; Blackmond, D. G. *Langmuir* **1999**, *15*, 7621.

(14) Valden, M.; Lai, X.; Goodman, D. W. *Science* **1998**, *281*, 1647.

(15) Panigrahi, S.; Basu, S.; Praharaj, S.; Pande, S.; Jana, S.; Pal, A.; Ghosh, S. K.; Pal, T. *J. Phys. Chem. C* **2007**, *111*, 4596.

(16) Hoxha, F.; van Vegten, N.; Urakawa, A.; Krurneich, F.; Mallat, T.; Baiker, A. *J. Catal.* **2009**, *261*, 224.

(17) Ojeda, M.; Rojas, S.; Boutonnet, M.; Perez-Alonso, F. J.; Garcia-Garcia, F. J.; Fierro, J. L. G. *Appl. Catal., A* **2004**, *274*, 33.

(18) Xu, Z.; Xiao, F. S.; Purnell, S. K.; Alexeev, O.; Kawi, S.; Deutsch, S. E.; Gates, B. C. *Nature* **1994**, *372*, 346.

(19) Che, M. The Influence of Particle Size on the Catalytic Properties of Supported Metals. In *Advances in Catalysis*; Eley, D. D., Pines, H., Weisz, P. B., Eds.; Academic Press Inc.: San Diego, 1989; Vol. 36; pp 55.

(20) Halperin, W. P. *Rev. Mod. Phys.* **1986**, *58*, 533.

(21) Louis, C. Gold Nanoparticles: Recent Advances in CO Oxidation. In *Nanoparticles and Catalysis*; Astruc, D., Ed.; Wiley-VCH Verlag GmbH & Co. KGaA: Weinheim, 2008; pp 485.

(22) Cleveland, C. L.; Landman, U.; Schaaff, T. G.; Shafigullin, M. N.; Stephens, P. W.; Whetten, R. L. *Phys. Rev. Lett.* **1997**, *79*, 1873.

(23) Perenboom, J.; Wyder, P.; Meier, F. *Phys. Rep.* **1981**, *78*, 173.

(24) Rao, C. N. R.; Kulkarni, G. U.; Thomas, P. J.; Edwards, P. P. *Chem. Eur. J.* **2002**, *8*, 29.

(25) Roduner, E. *Chem. Soc. Rev.* **2006**, *35*, 583.

(26) Zhang, G.-R.; Zhao, D.; Feng, Y.-Y.; Zhang, B.; Su, D. S.; Liu, G.; Xu, B.-Q. *ACS Nano* **2012**, *6*, 2226.

(27) Daniel, M.-C.; Astruc, D. *Chem. Rev.* **2004**, *104*, 293.

(28) Kamat, P. V. *J. Phys. Chem. B* **2002**, *106*, 7729.

(29) Chen, J. G.; Menning, C. A.; Zellner, M. B. *Surf. Sci. Rep.* **2008**, *63*, 201.

(30) Coq, B.; Figueras, F. *J. Mol. Catal., A* **2001**, *173*, 117.

(31) van Bokhoven, J. A.; Miller, J. T. *J. Phys. Chem. C* **2007**, *111*, 9245.

(32) Webb, P. A.; Orr, C.; Micromeritics Instrument, C. *Analytical Methods in Fine Particle Technology*; Micromeritics Instrument Corporation, 1997.

(33) Goodman, D. W. *Surf. Sci.* **1982**, *123*, L679.

(34) Silvestre-Albero, J.; Rupprechter, G.; Freund, H. J. *J. Catal.* **2005**, *235*, 52.

(35) Shiju, N. R.; Guliants, V. V. *Appl. Catal., A* **2009**, *356*, 1.

(36) Marx, S.; Baiker, A. *J. Phys. Chem. C* **2009**, *113*, 6191.

(37) Bratlie, K. M.; Lee, H.; Komvopoulos, K.; Yang, P. D.; Somorjai, G. A. *Nano Lett.* **2007**, *7*, 3097.

(38) Somorjai, G. A.; Blakely, D. W. *Nature* **1975**, *258*, 580.

(39) Narayanan, R.; El-Sayed, M. A. *Nano Lett.* **2004**, *4*, 1343.

(40) Narayanan, R.; El-Sayed, M. A. *J. Phys. Chem. B* **2005**, *109*, 12663.

(41) Telkar, M. M.; Rode, C. V.; Chaudhari, R. V.; Joshi, S. S.; Nalawade, A. M. *Appl. Catal., A* **2004**, *273*, 11.

(42) Berhault, G.; Bisson, L.; Thomazeau, C.; Verdon, C.; Uzio, D. *Appl. Catal., A* **2007**, *327*, 32.

(43) Park, K. H.; Jang, K.; Kim, H. J.; Son, S. U. *Angew. Chem. Int. Ed.* **2007**, *46*, 1152.

(44) Kundu, S.; Wang, K.; Liang, H. *J. Phys. Chem. C* **2009**, *113*, 18570.

(45) Renzas, J. R.; Zhang, Y. W.; Huang, W. Y.; Somorjai, G. A. *Catal. Lett.* **2009**, *132*, 317.

(46) Sankar, M.; Dimitratos, N.; Miedziak, P. J.; Wells, P. P.; Kiely, C. J.; Hutchings, G. J. *Chem. Soc. Rev.* **2012**, *41*, 8099.

(47) Tao, F.; Zhang, S.; Luan, N.; Zhang, X. *Chem. Soc. Rev.* **2012**, *41*, 7980.

(48) Yu, W.; Porosoff, M. D.; Chen, J. G. *Chem. Rev.* **2012**, *112*, 5780.

(49) Chen, M. S.; Kumar, D.; Yi, C. W.; Goodman, D. W. *Science* **2005**, *310*, 291.

(50) Mavrikakis, M.; Hammer, B.; Norskov, J. K. *Phys. Rev. Lett.* **1998**, *81*, 2819.

(51) Kitchin, J. R.; Norskov, J. K.; Barteau, M. A.; Chen, J. G. *Phys. Rev. Lett.* **2004**, *93*.

(52) Guczi, L. *Catal. Today* **2005**, *101*, 53.

(53) Nahm, T. U.; Jung, R.; Kim, J. U.; Park, W. G.; Oh, S. J.; Park, J. H.; Allen, J. W.; Chung, S. M. *Phys. Rev. B* **1998**, *58*, 9817.

(54) Hammer, B.; Norskov, J. K. Theoretical Surface Science and Catalysis—Calculations and Concepts. In *Impact of Surface Science on Catalysis*; Gates, B. C., Knozinger, H., Eds.; Acad. Press, 2000; Vol. 45; pp 71.

(55) Babu, P. K.; Kim, H. S.; Oldfield, E.; Wieckowski, A. *J. Phys. Chem. B* **2003**, *107*, 7595.

(56) Toshima, N.; Yonezawa, T. *New J. Chem.* **1998**, *22*, 1179.

(57) Bonnemann, H.; Richards, R. M. *Eur. J. Inorg. Chem.* **2001**, 2455.

(58) Wang, D.; Li, Y. *Adv. Mater.* **2011**, *23*, 1044.

(59) Roucoux, A.; Schulz, J.; Patin, H. *Chem. Rev.* **2002**, *102*, 3757.

(60) Lin, S. T.; Franklin, M. T.; Klabunde, K. J. *Langmuir* **1986**, *2*, 259.

(61) Skrabalak, S. E.; Xia, Y. A. *ACS Nano* **2009**, *3*, 10.

(62) Watzky, M. A.; Finke, R. G. *J. Am. Chem. Soc.* **1997**, *1198*, 10382.

(63) Yu, H.; Gibbons, P. C.; Kelton, K. F.; Buhro, W. E. *J. Am. Chem. Soc.* **2001**, *123*, 9198.

(64) Xia, Y.; Xiong, Y. J.; Lim, B.; Skrabalak, S. E. *Angew. Chem. Int. Ed.* **2009**, *48*, 60.

(65) Scott, R. W. J.; Wilson, O. M.; Crooks, R. M. *J. Phys. Chem. B* **2005**, *109*, 692.

(66) Park, J.; Joo, J.; Kwon, S. G.; Jang, Y.; Hyeon, T. *Angew. Chem. Int. Ed.* **2007**, *46*, 4630.

(67) Wilcoxon, J. P.; Provencio, P. P. *J. Am. Chem. Soc.* **2004**, *126*, 6402.

(68) Lee, J. S.; Stoeva, S. I.; Mirkin, C. A. *J. Am. Chem. Soc.* **2006**, *128*, 8899.

(69) Svedberg, T.; Nichols, J. B. *J. Am. Chem. Soc.* **1923**, *45*, 2910.

(70) Peterson, R. R.; Cliffel, D. E. *Anal. Chem.* **2005**, *77*, 4348.

(71) Schaaff, T. G.; Knight, G.; Shafigullin, M. N.; Borkman, R. F.; Whetten, R. L. *J. Phys. Chem. B* **1998**, *102*, 10643.

(72) Schaaff, T. G.; Whetten, R. L. *J. Phys. Chem. B* **1999**, *103*, 9394.

(73) Wilcoxon, J. P.; Provencio, P. *J. Phys. Chem. B* **2003**, *107*, 12949.

(74) Jimenez, V. L.; Georganopoulou, D. G.; White, R. J.; Harper, A. S.; Mills, A. J.; Lee, D. I.; Murray, R. W. *Langmuir* **2004**, *20*, 6864.

(75) Tsunoyama, H.; Negishi, Y.; Tsukuda, T. *J. Am. Chem. Soc.* **2006**, *128*, 6036.

(76) Stoeva, S.; Klabunde, K. J.; Sorensen, C. M.; Dragieva, I. *J. Am. Chem. Soc.* **2002**, *124*, 2305.

(77) Prasad, B. L. V.; Stoeva, S. I.; Sorensen, C. M.; Klabunde, K. J. *Langmuir* **2002**, *18*, 7515.

(78) Munoz-Flores, B. M.; Kharisov, B. I.; Jimenez-Perez, V. M.; Martinez, P. E.; Lopez, S. T. *Ind. Eng. Chem. Res.* **2011**, *50*, 7705.

(79) Ferrando, R.; Jellinek, J.; Johnston, R. L. *Chem. Rev.* **2008**, *108*, 845.

(80) Habas, S. E.; Lee, H.; Radmilovic, V.; Somorjai, G. A.; Yang, P. *Nat. Mater.* **2007**, *6*, 692.

(81) Scott, R. W. J.; Wilson, O. M.; Oh, S. K.; Kenik, E. A.; Crooks, R. M. *J. Am. Chem. Soc.* **2004**, *126*, 15583.

(82) Alayoglu, S.; Eichhorn, B. *J. Am. Chem. Soc.* **2008**, *130*, 17479.

(83) Alayoglu, S.; Zavalij, P.; Eichhorn, B.; Wang, Q.; Frenkel, A. I.; Chupas, P. *ACS Nano* **2009**, *3*, 3127.

(84) Pachon, L. D.; Thathagar, M. B.; Hartl, F.; Rothenberg, G. *Phys. Chem. Chem. Phys.* **2006**, *8*, 151.

(85) Bazin, D.; Guillaume, D.; Pichon, C.; Uzio, D.; Lopez, S. *Oil Gas. Sci. Technol. Rev. IFP* **2005**, *60*, 801.

(86) Zhou, S. H.; Varughese, B.; Eichhorn, B.; Jackson, G.; McIlwrath, K. *Angew. Chem. Int. Ed.* **2005**, *44*, 4539.

(87) Pretzer, L. A.; Song, H. J.; Fang, Y.-L.; Zhao, Z.; Guo, N.; Wu, T.; Arslan, I.; Miller, J. T.; Wong, M. S. *J. Catal.* **2013**, *298*, 206.

(88) Govorov, A. O.; Richardson, H. H. *Nano Today* **2007**, *2*, 30.

(89) Mayer, K. M.; Hafner, J. H. *Chem. Rev.* **2011**, *111*, 3828.

(90) Guerrero-Martinez, A.; Grzelczak, M.; Liz-Marzan, L. M. *ACS Nano* **2012**, *6*, 3655.

(91) Alkilany, A. M.; Thompson, L. B.; Boulos, S. P.; Sisco, P. N.; Murphy, C. J. *Adv. Drug Deliv. Rev.* **2012**, *64*, 190.

(92) Weissleder, R. *Nat. Biotechnol.* **2001**, *19*, 316.

(93) Blankschien, M. D.; Pretzer, L. A.; Huschka, R.; Halas, N. J.; Gonzalez, R.; Wong, M. S. *ACS Nano* **2012**, *7*, 654.

(94) Pretzer, L. A.; Nguyen, Q. X.; Wong, M. S. *J. Phys. Chem. C* **2010**, *114*, 21226.

Chapter 2

Hydrodechlorination Catalysis of Pd-on-Au Nanoparticles Varies With Particle Size

2.1 Introduction.

PdAu catalysts have been studied as a model material for a myriad of chemical reactions, such as those useful in biomass conversion,[1,2] chemical production,[3-5] air pollution control,[6] fuel cells,[7,8] and more recently, water pollution control.[9,10] Catalytic enhancement when Pd and Au metals are combined is generally attributed to (1) an electronic effect, in which interaction between the Pd and Au results in a change of valence electron density of states, (2) a geometric effect, in which specific atomic arrangements of metal atoms act as the active site, or (3) a bifunctional effect, in which Pd and Au atoms catalyze different steps in a reaction.[3,11,12] A deeper understanding of the source(s) of improved catalysis can be gained through better control of the PdAu nanostructure, as has been recently done with a catalytic material designed for water decontamination.[11]

Trichloroethene (TCE), a common degreasing agent, is one of the most common groundwater contaminants in the United States, being found at 852 of the 1,416 sites included on the U.S. Environmental Protection Agency (EPA) National Priorities List.[13-15] TCE concentrations at these sites exceed the EPA-mandated maximum contaminant level (MCL) of 5 ppb (0.005 mg/L).[16] In the 2006 report, *Assessing the Human Health Risks of Trichloroethylene*, the U.S. National Research Council concluded that TCE is a carcinogenic, neurological, and reproductive toxin.[15] Once introduced into the groundwater system via chemical spills or leaks, TCE is difficult to remove completely as it is progressively solubilized as a contaminant plume (concentration at 25 °C = 1,100

ppm).[17] Conventional pump-and-treat methods to remove TCE, such as granular activated carbon adsorption, and air-stripping merely displace TCE into a different phase.[18-20]

The catalytic hydrodechlorination (HDC) of TCE in water to ethane (Eqn. 2.1) is an attractive treatment alternative.

$$ClHC{=}CCl_2 + 4H_2 \rightarrow CH_3CH_3 + 3HCl \qquad (2.1)$$

Palladium (Pd) and other Group VIIIB metals are excellent hydrodehalogenation catalysts.[21] Field studies in the United States and Germany have already demonstrated that Pd nanoparticles supported on either alumina or zeolite materials can catalytically hydrodechlorinate TCE dissolved in groundwater.[22-24] Unfortunately, the use of such monometallic Pd materials is site-specific, because common groundwater ions, particularly sulfide and chloride, cause catalytic deactivation.[25-27]

Our group has shown that ~20 nm Pd-on-Au bimetallic nanoparticles ("Pd-on-Au NPs") catalyze TCE HDC nearly two orders of magnitude faster than pure Pd NPs and that they show enhanced deactivation resistance to chloride and sulfide ions.[10,28,29] We reduced the size of the Pd-on-Au NPs by using 4 nm Au NPs and found that catalytic activity varied with a volcano-shape dependence on Pd surface coverage (SC).[9] With Au NPs inactive for the reaction, TCE HDC activity (quantified as initial turnover frequencies) of the Pd-on-Au NPs increased with Pd SC up to ~70% on a per-Pd-atom basis, which we hypothesized was due to formation of 2-dimensional (2-D) Pd atom ensembles. The term "2-D Pd ensembles" refers to a contiguous group of Pd atoms (at least 2 atoms) on the particle surface arranged in two directions with no vertical stacking. Maximum activity was around a Pd SC of 70%, before decreasing at higher Pd SC's due

to a lesser amount of 2-D ensembles and a greater amount of 3-dimensional (3-D) Pd ensembles.

The 4 nm Au NPs with a 60% Pd SC were confirmed to have a Au-rich core and Pd-rich shell through extended X-ray absorption fine-structure spectroscopy (EXAFS).[11] Sulfide poisoning experiments gave indirect evidence for the existence of 2-D and 3-D Pd ensembles,[29] which was consistent with experimental observations of 2-D and 3-D Pd ensembles forming on Au surfaces under ultrahigh vacuum conditions at room temperature.[5,30,31] A recent report by Andersin and Honkala showed that 2-D Pd surface ensembles with 2, 3, 4, and 7 Pd atoms can be the active sites for Pd-on-Au NPs, based on TCE and H_2 adsorption energies calculated using density functional theory (DFT).[32] They proposed that larger ensembles were more active than smaller ones, in order for TCE and H_2 adsorption to occur simultaneously. They did not find that TCE formed bonds to mixed sites of Pd and Au atoms, unlike the case of PdCu mixed sites.[33,34]

Unlike the Pd SC effect, the Au particle size effect on Pd-on-Au NP TCE HDC catalysis is not known. Some published reports suggest that Au NP size differences can cause the Pd metal in Pd-coated Au NPs to assume different surface structures,[35] which presumably would result in different catalytic behavior. Pd atoms prefer to bind to (111) facets of Au NPs, according to DFT and Monte Carlo calculations.[36,37] From a geometric effect perspective, larger Au NPs can have more Au (111) surface atoms than smaller Au NPs percentage-wise, and should therefore contain a greater percentage of Pd surface atoms bound to Au(111) atoms after Pd deposition. From an electronic effect perspective, a quantum size effect, or change in the Au valence electron density of states, could affect how Pd atoms deposit on the Au NP surface as the particle size decreases below 5 nm.

Such an electronic effect could also influence how reactants and products of TCE HDC adsorb and desorb, respectively, from the bimetallic NP surface.[38,39]

We recently studied TCE HDC catalysis using Au NPs that were either 20 nm or 4 nm but were unable to determine if there was a definitive size effect.[10] In this work, we studied the effect of different Au NP sizes (3, 7, and 10 nm) on the TCE HDC catalysis of Pd-on-Au NPs. We analyzed the kinetics of each of the three series of NP samples, verifying that all three exhibited volcano-like HDC activity dependence on Pd SC. Our EXAFS analysis indicated the presence of 2-D Pd ensembles in the most active samples, namely those with Pd SC's of 50-70%. We collected visual evidence of these Pd ensembles on Au NPs for the first time using aberration-corrected scanning transmission electron microscopy (STEM), in 7 nm Pd-on-Au NPs with Pd SC's above and below 100%.

2.2 Experimental Methods.

2.2.1 Materials.

Gold (III) chloride trihydrate ($HAuCl_4 \cdot 3H_2O$, 99%), palladium(II) chloride ($PdCl_2$; >99.99%), octane (>99%), Pd/Al_2O_3 (1 wt% Pd), potassium carbonate (>99.5%), tannic acid (>99.5%), TCE (>99.5%), hydrochloric acid (12 M) were purchased from Sigma-Aldrich. Sodium citrate dihydrate (>99.5%) and nitric acid (16 M) were obtained from Fischer Scientific. Amorphous carbon powder (Vulcan XC-72 and Monarch 700) was purchased from Cabot. Ultra-high purity hydrogen gas was obtained from Matheson Tri-gas. Deionized water from a Barnstead NANOpure Diamond purifier (resistivity > 18 MΩ/cm) was used for all experiments. All chemicals were used as-received unless otherwise noted.

2.2.2 Au Nanoparticle Synthesis.

Tannic acid/citrate Au NPs (diameter (d) = 3, 7, and 10 nm) were synthesized using the Slot-Geuze method,[40] which we modified to prepare the ~4 nm Au NPs of our earlier work.[9] A 0.32 mM chloroauric acid ($HAuCl_4$) solution was prepared by diluting 200 µL of a 127 mM solution (~5 g $HAuCl_4 \cdot 3H_2O$ in 95 mL H_2O) with 79.8 mL of water. For 3 nm Au NPs, a second solution containing 4 mL of a 1 wt% trisodium citrate dihydrate solution, 5 mL of a 1 wt% tannic acid solution, 5 mL of a 25 mM potassium carbonate solution (~0.070 g K_2CO_3 in 20 mL H_2O) , and 6 mL of water was prepared. The 0.32 mM $HAuCl_4$ solution was stirred while both solutions were heated to 60 ºC. At this temperature, the second solution was added to the 0.32 mM $HAuCl_4$ which was vigorously stirred. Upon addition, the solution changed color immediately from pale yellow to reddish brown and was left to boil for ~2 min. The resulting sol was cooled to room temperature (~23 °C) and water was added so that the final sol volume = 100 mL. Greater than 95% of the $HAuCl_4$ was reduced, according to ICP-OES elemental analysis (data not shown) and which is in agreement with previous ICP-OES elemental analysis of ~4 nm Au NPs and Pd-on-Au NPs.[41]

Larger Au NPs with d = 7 and 10 nm were similarly prepared but no potassium carbonate was used, and the concentration of tannic acid in the second solution was changed. For ~7 nm Au NPs, the second solution was prepared using 0.5 mL of a 1 wt% tannic acid solution, 4 mL of a 1 wt% trisodium citrate dihydrate solution, and 15.5 mL of water. 10 nm Au NPs were made using a second solution containing 0.1 mL of a 1 wt% tannic acid solution, 4 mL of a 1 wt% trisodium citrate dihydrate solution, and 15.9 mL of water.

2.2.3 Pd-on-Au Nanoparticle Synthesis.

Respective volumes of a 2.5 mM H_2PdCl_4 solution (66, 25, and 18 µL) were added to the 3, 7, and 10 nm Au NP sols. Vigorous bubbling of hydrogen gas in the fluid for ~1 min was sufficient to completely reduce the Pd^{2+} onto the NP surface, to form 3, 7, and 10 nm Pd-on-Au NPs with a calculated 50 SC%. The notation "50 SC%" indicates a Pd surface coverage (SC) of 50%. Additional 3 nm, 7 nm, and 10 nm Pd-on-Au NPs with surface coverages between 10 and 150 SC% (in increments of 10%) were synthesized by changing the volume of 2.5 mM H_2PdCl_4 added to the 3, 7, and 10 nm Au NP sols (Tables A1-A3).

The volume of H_2PdCl_4 solution needed was calculated using the magic cluster model.[9,42,43] By considering a Au NP to be a central Au atom surrounded by closed shells of Au atoms, the 3, 7, and 10 nm Au NPs were geometrically modeled as 3.0, 7.3, and 10.0 nm magic clusters, respectively, with 5, 13, and 18 Au shells (Table A4). Since Pd and Au have nearly identical atomic sizes, Pd atoms at <100 SC% were treated as atoms residing in the 6^{th}, 14^{th}, or 19^{th} shell of the respective Au magic clusters. The condition of >100 SC% indicated a sufficient amount of Pd atoms to form a complete 6^{th}, 14^{th}, or 19^{th} shell and to form a partial 7^{th}, 15^{th}, or 20^{th} shell, respectively. A 3 nm Au NP with 150 SC%, for example, meant that Pd atoms formed a complete 6^{th} shell and 50% of the 7^{th} shell. The concentrations of 3 nm, 7 nm, and 10 nm Au NPs were calculated (using the magic cluster model) to be 2.7×10^{14}, 1.9×10^{13}, and 7.2×10^{12} NP/mL, respectively, assuming 100% $HAuCl_4$ reduction and monodisperse NPs. Pd-on-Au NPs were synthesized one day prior to use to ensure stability of the sol. All sols were stored in air at room temperature (~23 °C).

2.2.4 Catalytic Testing.

Catalytic testing was conducted using batch reactors.[9,41] A screw-cap amber bottle (250 mL, Alltech) containing deionized water and a magnetic stir bar was sealed with Teflon tape and a PTFE-silicone septum. The initial water volume was varied such that the final liquid volume was ~173 mL after addition of the catalyst. The sealed bottle was purged with hydrogen gas for 15 min to displace dissolved oxygen and fill the headspace with H_2 (~1 atm). TCE (7 µL; final concentration ~59 ppm) and octane (~1 µL; internal standard) were injected into the purged bottles. All reactors were equilibrated prior to catalyst injection by stirring (rate ~600 rpm) for at least 3 hr at room temperature (~23 °C). After reaching equilibrium, an aliquot of a Pd-on-Au NP sol was injected at time t=0 such that the total concentration of Pd in the batch reactor was ~0.04 ppm Pd (~4.0×10^{-7} M Pd). The reaction was monitored by sampling the reactor headspace (aliquot volume ~ 100 µL) using a gas-tight syringe. All headspace samples were analyzed using a Varian 3800 gas chromatograph (GC) equipped with an Agilent GasPro capillary column (length = 30 mm; inner diameter = 0.32 mm) and a Saturn 2000 mass spectrometer (MS) detector. The sampling conditions were the same as our previous studies except for the use of a MS detector, which had a lower detection limit than the flame ionization detector previously used.[9]

Reaction rate constants were determined from the pseudo-first order rate law of the TCE HDC reaction, as reported previously:[9,41]

$$-dC_{TCE}/dt = k_{meas}C_{TCE} \qquad (2.2)$$

where k_{meas} is the measured pseudo-first-order rate constant and C_{TCE} is the TCE concentration in the reactor. Based on total Pd atoms (unless indicated otherwise), initial

turnover frequency (TOF) values were calculated after accounting for the gas-liquid transfer effect, which we previously studied,[41] as shown in Equations 2.3 and 2.4:

$$1/k_{corr} = 1/k_{meas} - 1/k_{gl}a_{gl} \qquad (2.3)$$

$$TOF = (C_{liq,0}/[Pd])\times(k_{corr}) \qquad (2.4)$$

where k_{corr} is the corrected, measured first-order rate constant, $C_{liq,0}$ is the initial molar concentration of TCE in the liquid, [Pd] is the molar concentration of Pd in the batch reactor (~4.0×10^{-7} M for all Pd-on-Au NPs), k_{gl} is the gas-liquid mass transfer coefficient, and a_{gl} is the gas-liquid interfacial area. The gas-liquid mass transfer resistance ($1/k_{gl}a_{gl}$ = 5.11 min) was previously determined for our batch reactor system operating with a stirring rate of 600 rpm.[41] The pH of the reaction medium decreased during the course of reaction, but this drop did not influence the Pd-on-Au NP TCE HDC activity as verified by performing several controlled runs using water buffered at pH ~7.0. The reaction solutions for all TCE HDC activity analysis presented herein were not buffered. Reported TOF values are an average of at least three replicate experiments with a relative standard deviation (rsd) ≤ ~20%.

The activity of Pd-on-Au NPs was compared to those of Pd NPs and Pd/Al_2O_3 (1 wt% Pd, Sigma-Aldrich). Pd NPs (d ~ 4 nm)[9] were synthesized similarly to 3 nm Au NPs by substituting the chloroauric acid solution with a 0.32 mM $PdCl_4^{2-}$ solution (12 mL of 2.39 mM $PdCl_4^{2-}$ diluted with 68 mL H_2O). All Pd sols were heated to boiling for ~25 min prior to air-cooling to room temperature.

Approximately 1 mL of ~4 nm Pd NPs was injected into the sealed bottles (final Pd concentration in reactor = 0.18 ppm; 1.7×10^{-6} M). The Pd/Al_2O_3 was injected as a water suspension (20 mg of powder in 1 mL of H_2O) into the batch reactor (final Pd

concentration in reactor = 1.16 ppm; 1.1×10^{-5} M). Pd NPs have a calculated dispersion value (percentage of the total atoms that are surface atoms) of ~27%,[11] and Pd/Al_2O_3 had a measured dispersion of 38.5%. Reported TOF values for Pd NPs and Pd/Al_2O_3 are the average of at least three replicate experiments with a relative standard deviation (rsd) ≤ ~20%.

2.2.5 Characterization Methods.

Transmission Electron Microscopy (TEM): Particle sizes were analyzed using transmission electron microscopy (TEM) images collected using a JEOL 2010 transmission electron microscope operating at 100 kV. Au NPs were deposited onto 200-mesh carbon/Formvar grids by evaporating a drop of NP sol at room temperature (23 °C). The number-average size distribution for each sample was determined by measuring 400+ particles using *ImageJ* Software. TEM images of Au NPs following Pd deposition were obtained, but no significant differences in the average size or in size distribution were observed.

Scanning Transmission Electron Microscopy (STEM): Pd-on-Au NPs with 70 and 150 SC% were immobilized onto carbon, and the resulting particles were deposited onto a holey carbon grid. The images were collected on a probe-corrected FEI STEM Titan at 300 kV in the Environmental Molecular Sciences Laboratory at the Pacific Northwest National Laboratory. The NPs that were analyzed were either ones that had fallen off of the carbon supports and directly on to the thin holey carbon, or a piece of carbon support that extended into a hole of the holey carbon grid to ensure the highest signal to noise ratio necessary to see the lighter Pd atoms on the surface of the Au particles. The resulting images were not processed in any way.

Ultraviolet-Visible Spectroscopy (UV-Vis): Pure Au and Pd-on-Au NP sols were analyzed through ultraviolet-visible absorption spectroscopy (Shimadzu UV-2401 PC spectrophotometer). Spectra of the NP sols were collected between wavelengths of 400 and 900 nm. Polystyrene cuvettes (Sarstedt AG & Co.) with a path length of 1 cm were used.

Inductively Coupled Plasma Optical Emission Spectroscopy (ICP-OES): Inductively coupled plasma optical emission spectroscopy (ICP-OES) (Perkin-Elmer Optima 4300 DV) was used to confirm deposition of Pd onto the different-sized Au NPs. Pd-on-Au NPs with 30, 70, and 110 SC% were concentrated via ultracentrifugation and decantation. Concentrated hydrochloric acid and nitric acid were added then to completely dissolve the NPs. The resulting solutions were syringe-filtered (Millex GP 0.25 μm) and diluted to <20 ppm with 1 wt% HNO_3 prior to analysis.

X-ray Absorption Spectroscopy (XAS): NPs were supported on carbon powder for all extended X-ray absorption fine-structure (EXAFS) and X-ray absorption near edge structure (XANES) analyses. Carbon powder was added to each NP suspension (monometallic Au NPs, monometallic Pd NPs, different-sized Pd-on-Au NPs with 30, 50, 70, 90, 110, and 150 SC%) such that the calculated Pd content of the dried powder was ~1 wt%. Following vigorous stirring for ~8-12 h, suspensions were centrifuged to concentrate the carbon-supported suspensions and boiled for ~20 min to remove excess water. The recovered carbon-supported NP (NP/C) samples were dried under vacuum at 70 °C for ~24 hr to produce the final powders. This immobilization method should not significantly alter the NP atomic structure (NP size and distribution of Pd and Au atoms).[11,44,45]

XAS measurements were conducted on the insertion and bending magnet devices (10-ID and 10-BM) of the Materials Research Collaborative Access Team (MRCAT) at the Advanced Photon Source at Argonne National Laboratory. All measurements were made in transmission mode and were simultaneously acquired with a Au or Pd foil spectrum for energy calibration. The ionization chambers were optimized to give the maximum current with linear response (~10^{10} photons per second) by using a nitrogen-helium mixture in the incident X-ray detector and an argon-nitrogen mixture in the transmission X-ray detector. Details of the instrumentation used can be found in our previous publication.[11]

All NP/C samples were loaded into a cylindrical holder and pressed to form a pellet with a total absorbance (μx) at the Au L_{III} (11.918 keV) and Pd K (24.350 keV) edges of 2.0 and an edge step of 0.5. The cylindrical holder was loaded into a continuous flow reactor cell (glass tube, length 18 in., diameter 0.75 in.) fitted at both ends with polyimide windows and stainless steel valves.

All measurements were made at room temperature. Each as-prepared, immobilized sample was first analyzed under air at room temperature. Following *in situ* reduction at 200 °C for ~30 min in 4% H_2/He, each sample was then analyzed under He at room temperature. Our previous XAS measurements showed that, under these reduction conditions, oxidized Pd can be reduced without altering the NP size or structure.[11] The reduced particles were purged with He gas to decompose any Pd-H that could have formed and to desorb chemisorbed hydrogen. Measurements of the reduced sample were required to determine fractions of oxidized Pd in the as-prepared samples handled under air.

Reference compounds used to evaluate experimental phase shifts and back-scattering amplitudes were $Pd(NH_3)_4(NO_3)_2$ (purchased from Aldrich), Pd foil, and Au foil. Pd and Au foil experimental data were used to determine the best fit of Debye-Waller factor (DWF's) and amplitude reduction factors (S_0) for the FEFF fitting phase shifts and back-scattering amplitudes for Pd-Pd, Au-Au, Pd-Au, and Au-Pd bonds. The data was extracted using standard procedures based on WINXAFS97 software. A base square fit in k- and R-space of the nearest neighbor, k^2-weighted Fourier transform data (k: photoelectron wavenumber) was used to obtain coordination parameters. The data fit equally well using k^1 and k^3 weightings. For all bimetallic NPs, the EXAFS fittings from both Pd and Au edges were within error, leading to the same bond distances, DWF's, and self-consistent coordination numbers (CN's) for Pd-Au and Au-Pd bonds.

Fractions of oxidized Pd (Pd^{2+}) on the pure Pd NPs and Pd-on-Au NP samples were estimated by fitting the data with PdO, $PdCl_2$, and the reduced catalyst spectra. Fitting of the oxide peaks was complicated since they overlapped with large Pd-Pd and Pd-Au metallic peaks. To eliminate this contribution, we subtracted EXAFS spectra of reduced samples from spectra of the as-prepared, oxidized sample leaving only the Pd^{2+} peaks (which could be reliably fit as either Pd-Cl or Pd-O depending on the phase and bond distance). The fraction of oxidized Pd^{2+} was then calculated by dividing the fit coordination number by 4 (since CN for Pd-Cl and Pd-O in $PdCl_2$ and PdO, respectively, is 4). Generally, the fraction of oxidized Pd from XANES and EXAFS were in agreement.

2.3 Results and Discussion.

2.3.1 Au Nanoparticle and Pd-on-Au Nanoparticle Synthesis.

To generate three different sized Au NPs, we used the tannic acid-citrate method developed by Slot and Geuze in which the final particle size is determined by the tannic acid concentration.[40] Three Au NP sols were synthesized using final tannic acid concentrations of 1.5 mM, 0.15 mM, and 3.0 µM, respectively. TEM analysis of over 400 particles for each sample indicated mean NP diameters of 3.0, 7.0, and 10 nm, respectively (Fig. 2.1).

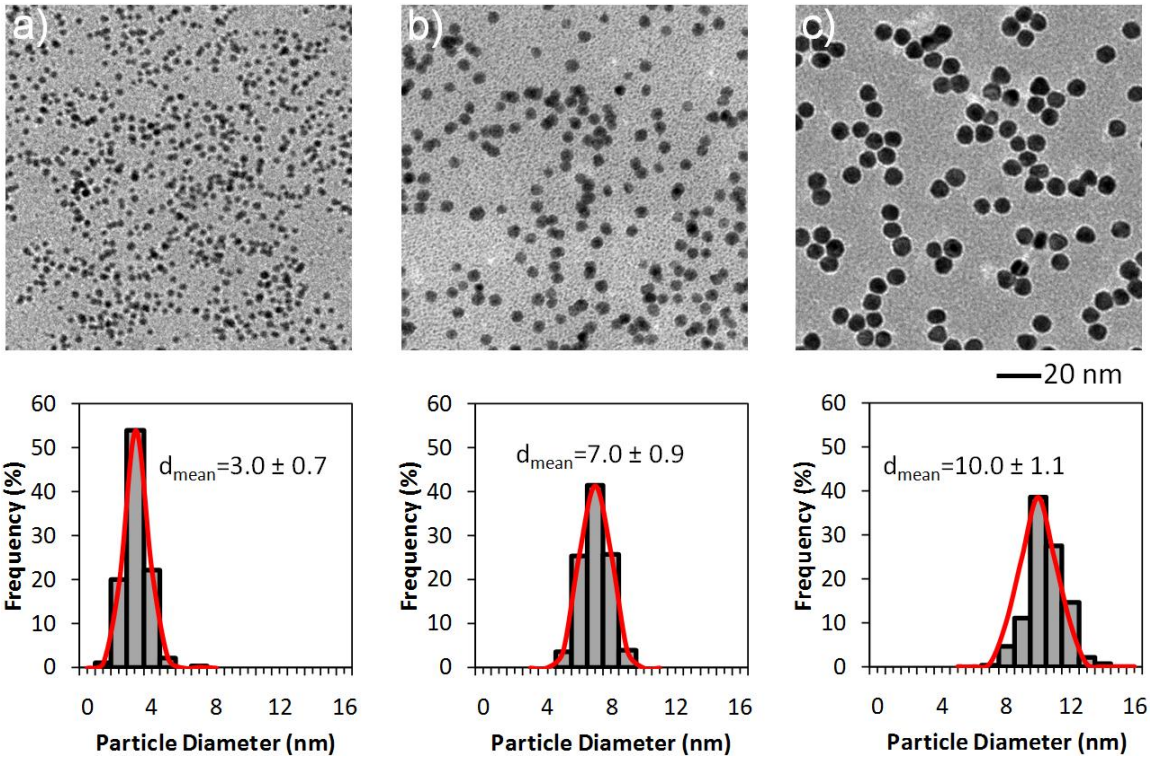

Figure 2.1. TEM images and particle size distributions of (a) 3 nm, (b) 7 nm, and (c) 10 nm Au NPs. Red curves are Gaussian curve fits to the particle size histograms.

The 3, 7, and 10 nm Au NP sols had unimodal size distributions with relative standard deviations (rsd) of 23%, 13%, and 11%, respectively. All three Au NP size distributions

could be fit as Gaussian functions, though the size distribution of the 10 nm Au NPs was slightly positively skewed.

The color of the Au sols changed from brown (3 nm Au NPs) to red (10 nm Au NPs), due to the size-dependent shift of the surface plasmon resonance (SPR) peak and also to the higher tannic acid concentrations used for the smaller particles (Fig. 2.2). Tannic acid absorbed over the same wavelengths as the Au NPs, overwhelming the absorbance of the 3 nm Au NP sol itself.[9]

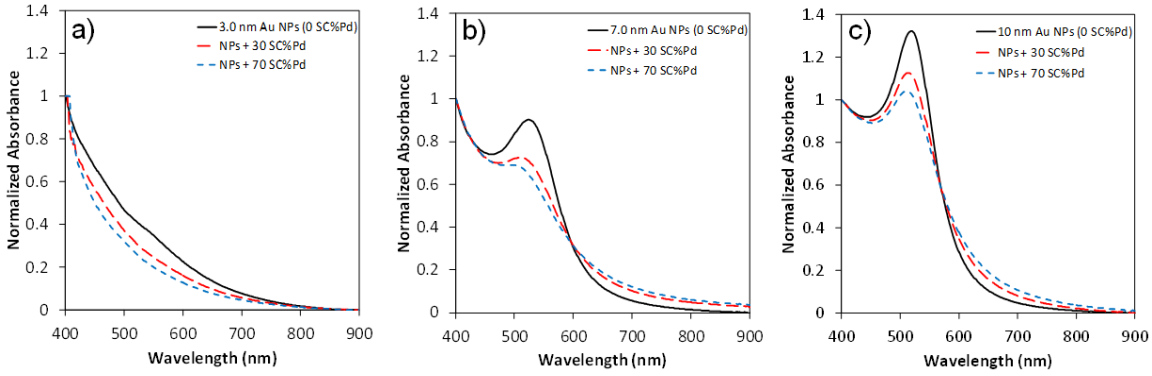

Figure 2.2. UV-Vis absorbance spectra of (a) 3 nm, (b) 7 nm, and (c) 10 nm Au NPs with Pd SC's of 30 and 70 SC%.

Deposition of Pd^0 onto the surface of Au NPs is expected since heterogeneous nucleation is energetically favored over homogeneous nucleation (which leads to Pd NP formation).[46] UV-Vis spectra of the Pd-on-Au samples following Pd deposition showed that Pd deposition on Au NPs occurred, as evidenced by the decreased Au NP SPR peak intensity with increasing Pd SC (Fig. 2.2).[47-49] Elemental analysis via ICP-OES of 3, 7, and 10 nm Au NPs with 30, 70, and 110 SC% (Table 2.1) confirmed that actual Pd contents were similar to calculated values (~10%). Pd surface coverages were calculated from ICP-OES assuming monodisperse NP dispersions and deposition of Pd in monolayers in accordance with the magic cluster model. No significant change in particle

size was observed following Pd deposition, according to TEM analysis, and so henceforth 3 nm, 7 nm, and 10 nm Au NPs coated with Pd atoms are referred to as "3 nm Pd-on-Au NPs," "7 nm Pd-on-Au NPs," and "10 nm Pd-on-Au NPs," respectively.

Table 2.1. Comparison of calculated and measured Pd surface coverages.

Au NP Diameter (nm)	Calculated, Theoretical Pd Surface Coverage (SC%)	Pd Surface Coverage Calculated from ICP-OES (SC%)[a]
3	30	24.6
	70	66.3
	110	103.4
7	30	30.0
	70	66.7
	110	98.6
10	30	31.5
	70	68.9
	110	111.4

[a]Assuming Pd atoms deposit as a monolayer

2.3.2 TCE HDC Activity of Pd-on-Au Nanoparticles.

Batch reactor kinetic studies showed that the TCE HDC activity of the Pd-on-Au NP sols varied with (i) Au NP size and (ii) Pd SC (Fig. 2.3). The catalytic activity of all Pd-on-Au NPs greatly exceeded the activities of Pd NPs (TOF = 0.042 mol-TCE·mol-Pd^{-1}·s^{-1}) and Pd/Al_2O_3 (TOF = 0.021 mol-TCE·mol-Pd^{-1}·s^{-1}). These results are in good agreement with our previous measurements of TCE HDC activity exhibited by pure Pd NPs and Pd/Al_2O_3.[9] Pd-on-Au NPs with 0 SC% (Au NPs) did not catalyze TCE HDC regardless of NP size.

Pd-on-Au NPs, Pd NPs, and Pd/Al_2O_3 exhibited high selectivity to ethane and ethene (mol% ~ 90%), in good agreement with our previous study which also showed that ethane was the dominant specie.[9] Trace amounts of vinyl chloride, dichloroethene isomers (1,1-, cis-1,2-, and trans-1,2-), butane, and butenes were observed for Pd NPs, Pd/Al_2O_3, and Pd-on-Au NPs, regardless of Au NP size or Pd SC (Fig. A1).

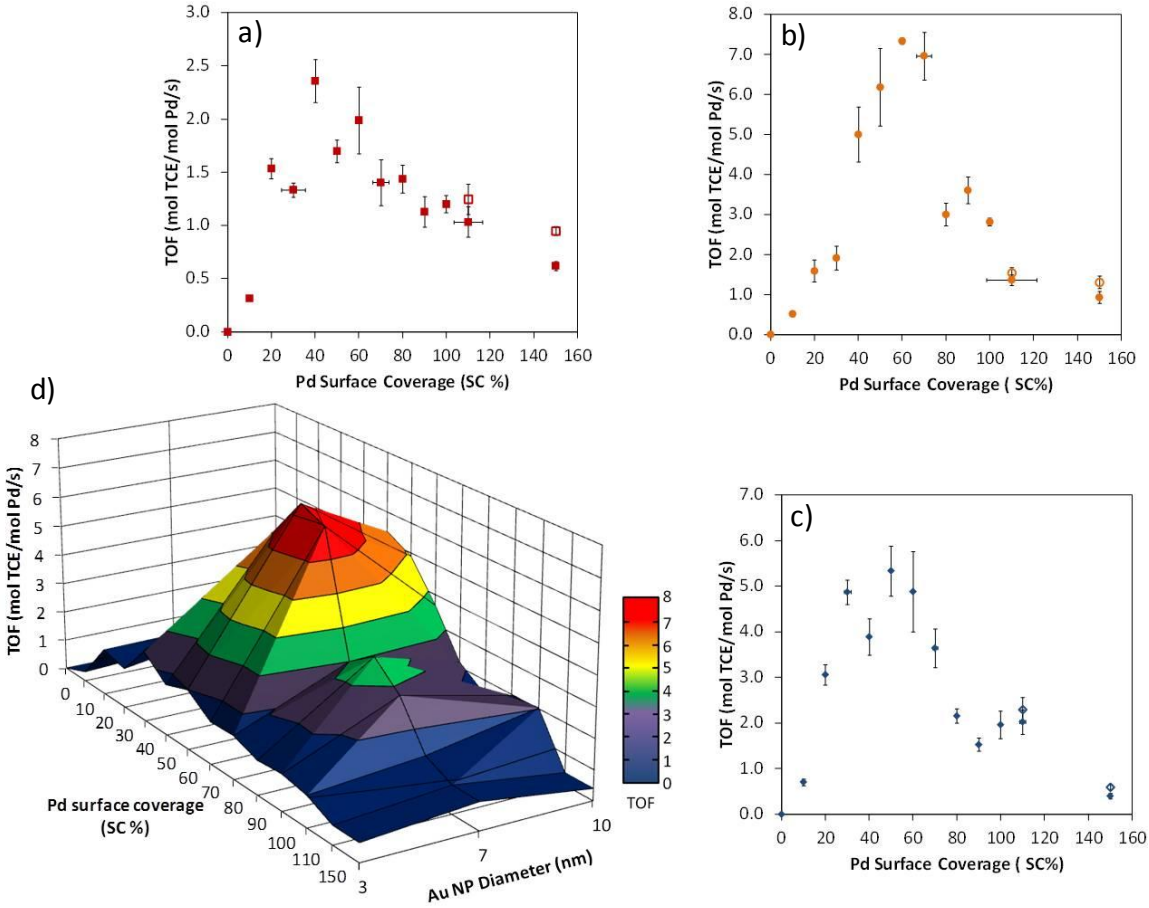

Figure 2.3. TOF's of (a) 3 nm, (b) 7 nm, and (c) 10 nm synthesized citrate/tannic acid Au NPs with Pd SC's between 0 and 150% (100 SC% = 1 monolayer of Pd atoms on the Au NP surface). Panel (d) is a 3-D combined plot of panels (a)-(c) showing the combined effects of Au NP diameter and Pd surface coverage on the TOF of the Pd-on-Au NPs. Horizontal error bars (some are visible) for panels (a)-(c) are based on ICP-OES measurements shown in Table 2.1. Open (unfilled) data points for Pd SC's >100% are surface-Pd-based TOF values (mol TCE/mol $Pd_{surface}$/s).

The activity of Pd-on-Au NPs synthesized with 3 nm Au NPs samples exhibited a volcano shape dependence on Pd SC (Fig. 2.3a). Maximum TCE HDC activity (TOF ~ 2.4 s^{-1}) was measured at 40 SC%, though the peak of the volcano curve appeared to lie between 40 and 60 SC%. The TOF values and peak location were somewhat similar to those of Pd-on-Au NPs synthesized with 4 nm Au NPs described in our earlier work.[9]

Above 100 SC%, Pd dispersion was expected to be less than 100%. Calculated using total surface Pd atoms, the samples at 110 and 150 SC% had TOF values of 1.3 and

0.95 mol-TCE·mol-$Pd_{surface}^{-1}s^{-1}$, respectively, which were higher than those of Pd NPs (0.12 mol-TCE·mol-$Pd_{surface}^{-1}s^{-1}$) and Pd/Al_2O_3 (0.057 mol-TCE·mol-$Pd_{surface}^{-1}s^{-1}$).

Pd-on-Au NPs synthesized with 7 nm Au NPs showed the highest TCE HDC activity (TOF = ~7.3 s^{-1}), with the volcano curve peaking between 60-70 SC% (Fig. 2.3b). The samples at 110 and 150 SC% had surface-Pd-normalized TOF values of 1.5 and 1.3 mol-TCE·mol-$Pd_{surface}^{-1}\cdot s^{-1}$, respectively, somewhat similar to values for the 3 nm NPs with >100 SC%.

Pd-on-Au NPs synthesized with 10 nm Au NPs had maximum activity at 50 SC% (TOF ~ 5.3 s^{-1}), with the volcano peak centered roughly between 30 and 60 SC% (Fig 2.3c). The samples at 110 and 150 SC% had surface-Pd-normalized TOF values of 2.3 and 0.6 mol-TCE·mol-$Pd_{surface}^{-1}\cdot s^{-1}$, respectively. The large difference between these $TOF_{Pdsurface}$ values could be due to an artifact of the magic cluster model or a real difference in Pd dispersion or oxidation state at the highest Pd coverage for the 10 nm case.

Regardless of NP size, the activity of the Pd-on-Au NPs varied with a volcano-shape dependence upon the Pd surface coverage (Fig 2.3d). The variation in the TOF with Pd SC indicated that the surface Pd atoms were not isolated from each other as "monomers." If they were isolated from one another at all Pd SC's, then the particle TOF should not change as a function of Pd SC. As we proposed previously, the observed volcano curves could be due to the formation of 2-D and 3-D Pd ensembles on the NP surface formed with increasing Pd SC.[9] Particle activity increased with Pd SC due to the increased population of highly active 2-D Pd ensembles and decreased as 3-D Pd ensembles formed, reducing access to all Pd content, *i.e.*, lower Pd dispersion. As shown

in Fig 2.3d, the larger NPs (7 and 10 nm) likely exhibit higher maximum activities than the smaller NPs due to the formation of more dispersed (*i.e.*, smaller) 2-D Pd islands on the NP surface. We next used X-ray absorption spectroscopy (XAS) to verify the Pd-rich shell/Au-rich core structure for Pd-on-Au NPs of all Au sizes and representative Pd surface coverages, and to infer information about the catalytically active sites on these NPs.

2.3.3 XAS Analysis of 3 nm Pd-on-Au Nanoparticles.

XAS is a powerful spectroscopic technique that provides atomic-scale structure information of materials (Pd-on-Au NPs, in our case) by examining how X-rays are absorbed and how photoelectrons are scattered by neighboring atoms after being ejected from the absorbing atomic element by impinging X-rays.[39,50-54] All Pd-on-Au NPs were supported on carbon powder for analysis. The scattering paths analyzed for each sample in the 3 nm Pd-on-Au NP series were Au-Au, Au-Pd, Pd-Cl, Pd-O, Pd-Pd, and Pd-Au (notation: first atom is the absorber; second atom is the scatterer). The bond distances, coordination numbers, Debye-Waller factors (DWF's), and threshold absorption energies are reported in Tables A5-A6. All of these values are in good agreement with our previous XAS study of 4 nm Pd-on-Au NPs with 60 SC%.[11]

The coordination numbers (CN's) for the two Pd scattering paths (Pd-Au and Pd-Pd) indicate how many Au atoms (Pd-Au CN) and Pd atoms (Pd-Pd CN) each Pd atom contacts, on average, for a given Pd-on-Au NP sample. Similarly, the CN's for the two Au scattering paths (Au-Pd and Au-Au) indicate how many Pd atoms (Au-Pd CN) and Au atoms (Au-Au CN) each Au atom contacts. It is noted that the Au-Pd CN's do not necessarily equal the Pd-Au CN's. Both values describe extent of Au and Pd atom

coordination, except the Au-Pd CN represents the number of Pd atoms in contact with one Au atom, and the Pd-Au CN represents the number of Au atoms in contact with one Pd atom.

Conceptually, Pd atoms can deposit on top of the Au surface atoms (Fig. 2.4a) or into the first layer of Au surface atoms to form a PdAu surface alloy (Fig. 2.4b). The latter comes from the place-exchange of deposited Pd atoms with Au atoms at edge dislocations, which has been observed in room-temperature STEM surface studies of Pd-on-Au films.[31] The lower coordination and bond strength of Au atoms at a dislocation make such a surface defect an entry point for deposited Pd atoms migrating into and under the Au surface layer. This migration is thought to minimize overall surface stress/energy and is possible at the defects due to the similar atomic radius and lattice constants of Pd and Au.[30,31] If the surface were that of Au(111), the maximum Pd-Au CN values are 3, 9, and 12 for a Pd adatom, surface atom, or subsurface atom, respectively. If the surface were that of a Au NP, Pd atoms can have Pd-Au CN values of 5 and 7 for corner (vertex) and edge sites, respectively.[55]

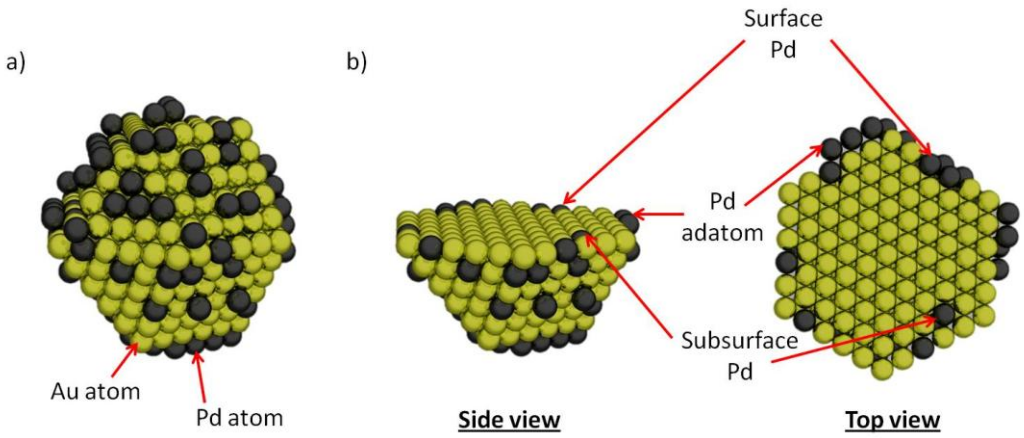

Figure 2.4. Representations of (a) a whole 3 nm Pd-on-Au NP and (b) side and top views of a NP cross-section to show the three possible configurations of Pd atoms after Pd salt reduction and deposition on the Au NP surface.

Coordination Number Results: XAS spectra were obtained for roughly half the NP samples tested for TCE HDC, before and after hydrogen treatment at 200 °C, and were analyzed in terms of CN's. The Pd-Au CN of untreated 3 nm Pd-on-Au NPs decreased uniformly from ~9 (30 SC%) to ~4.5 (150 SC%) with increasing Pd SC (Fig. 2.5a, open squares). This trend was consistent with each Pd atom coming into contact with a relatively decreasing number of Au atoms, on average, as the Pd SC increased. Following hydrogen treatment at 200 °C, a small increase (*i.e.*, within error) in the Pd-Au CN was seen at most Pd SC's (Fig. 2.5a, filled squares).

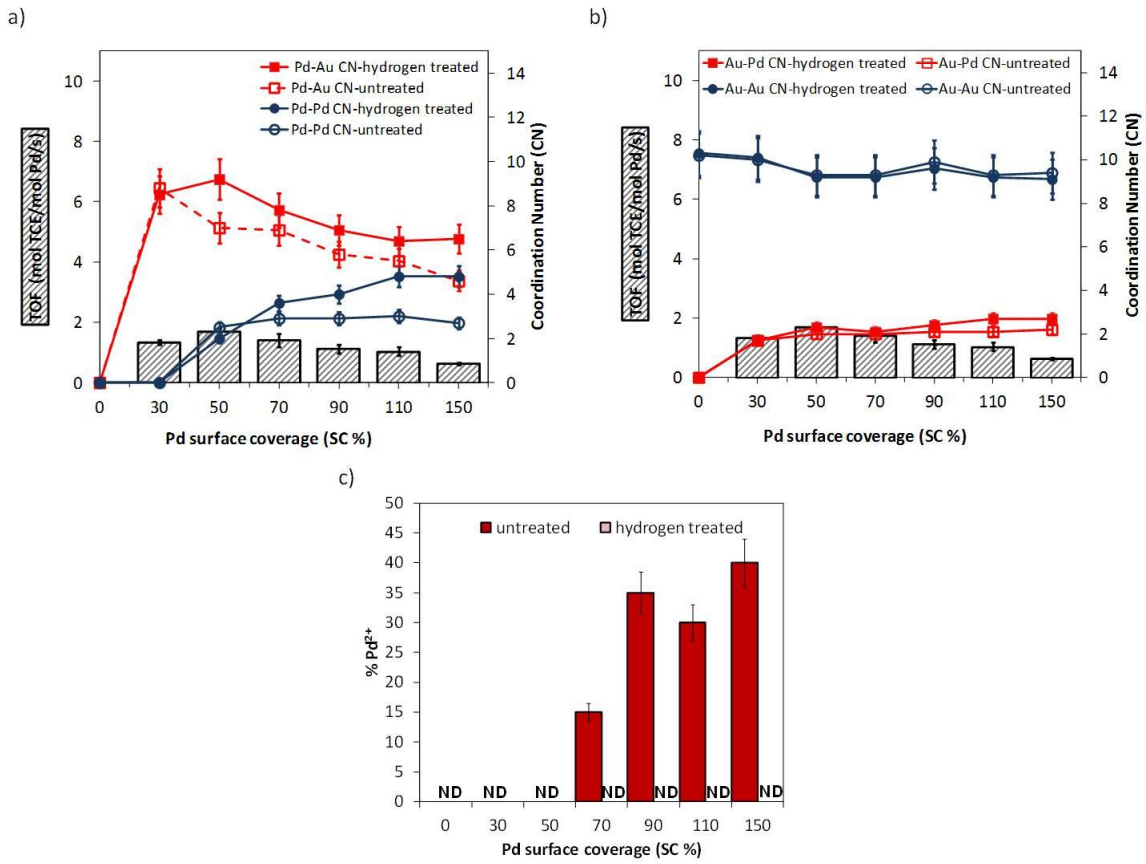

Figure 2.5. Changes in (a) Pd-Au and Pd-Pd CN's and (b) Au-Pd and Au-Au CN's as a function of Pd SC for 3 nm Pd-on-Au NPs, before and after hydrogen treatment at 200 °C. Catalytic activity data (TOF) is shown as rectangular bars. (c) Percentage of oxidized Pd (% Pd^{2+}) at different Pd SC's. "ND" = no detection of scattering signal.

The Pd-Pd CN was roughly constant at ~3 above 30 SC% for the untreated NPs (Fig. 2.5a, open circles). Following H_2 treatment, the Pd-Pd CN slightly decreased to ~2 (though within error) at 50 SC% and increased up to ~5 above 50 SC% (Fig. 2.5a, filled circles). The Pd-Pd CN at 30 SC% was not detected due to the Pd-Pd scattering signal being too small to analyze, indicating the Pd content of this particular carbon-supported Pd-on-Au NP sample was in the form of either isolated Pd atoms and/or small 2-D Pd ensembles in undetectable quantities. Close to this 30 SC% value is the maximum Pd surface coverage on a Au(111) surface at which all Pd are exclusively isolated Pd atoms (~25 SC%).

The Au-Au CN of untreated 3 nm Pd-on-Au NPs did not change with Pd SC, as expected (Fig 2.5b, open circles). The Au-Au CN (~9-10) corresponded to an average NP size of ~5.6 nm (larger than measured 3 nm), based on TEM-EXAFS size correlations previously developed for supported Au materials.[11,56] Hydrogen treatment at 200 °C did not change the Au-Au CN's, indicating the NPs' size did not change (Fig 2.5b, filled circles). The Au-Pd CN of untreated NPs increased with increasing Pd SC, from ~2 (at 30 SC%) to ~3 (at 150 SC%), which was consistent with increased contact by Au atoms with Pd atoms (Fig. 2.5b, open squares) due to the increased number of deposited Pd atoms. Following hydrogen treatment, no significant change in the Au-Pd CN's was observed at any Pd SC (Fig. 2.5b, filled squares).

Pd Oxidation State Results: The fraction of Pd atoms in the +2 oxidation state (as PdO or $PdCl_2$) in untreated NP samples was detectible in all samples except those with 0, 30 and 50 SC% Pd coverage (Fig. 2.5c). Hydrogen treatment at 200 °C reduced all oxidized Pd atoms in all the samples, coincident with the increase in Pd-Pd CN's. The $\%Pd^{2+}$ at 70, 90, 110, and 150 SC% corresponded to values of 15, 35, 30, and 40% of the total Pd atoms that were oxidized, respectively. These values were consistent with our previous experiments showing that unreduced 4 nm Pd-on-Au NPs with 60 SC% had 20% of the surface Pd atoms in oxidized form.[11] As a comparison, unreduced 4 nm Pd NPs had ~100% of all surface Pd atoms in oxidized form.[11]

Taking the Pd oxidation state and coordination number data together, we propose that Pd-Pd CN's is a reasonable measure of metallic Pd ensemble size. No Pd^{2+} was detected in Pd-on-Au NPs with 30 SC% and Pd-Pd CN = 0, indicating the Pd content was mostly in the form of isolated, metallic Pd atoms (before and after hydrogen treatment).

Direct contact of Pd atoms with the Au NP surface appears to prevent Pd oxidation, which has been experimentally observed by others.[57-60]

The sample of Pd-on-Au NPs with 50 SC% was unlike the others. Before or after H_2 treatment, Pd^{2+} was also not detected. The Pd content was in the form of Pd ensembles, as indicated by a non-zero Pd-Pd CN of ~3, which did not significantly change in size after H_2 treatment. Untreated Pd-on-Au NPs with >50 SC% contained Pd^{2+} species and Pd ensembles (Pd-Pd CN ~ 3), which then became larger due to Pd^{2+} reduction after H_2 treatment.

We conclude that untreated Pd-on-Au NPs with >50 SC% contain partially oxidized 3-D Pd ensembles, in which the topmost Pd atoms are oxidized. We infer that untreated Pd-on-Au NPs with 50 SC% contain metallic 2-D Pd ensembles, and that untreated Pd-on-Au NPs with 30 SC% contain isolated, metallic Pd atoms.

Pd-shell/Au-core Structure: Additional analysis of the metal CN's confirmed the Pd-shell/Au-core structure of the NPs through a comparison of the measured Au and Pd CN's with calculated values of theoretically alloyed PdAu NPs of the same particle size and metal composition (or equivalently, the total Au CN and total Pd CN).[11] To assess the Pd-on-Au NP structure in a convenient manner, we use a "Punnett square" representation of the measured and calculated CN's (Fig. 2.6). As an example, the measured CN values of 3 nm Pd-on-Au NPs with 70 SC% from Fig. 5 are shown in Punnett square format (Fig. 2.6a). The total Au CN is 9.2 + 2.1 = 11.3, and the total Pd CN 7.8 + 3.6 = 11.4.

a)

XAS Measured CN's

Absorbing atom	Scattering atom: **Au**	Scattering atom: **Pd**
Au	9.2	2.1
Pd	7.8	3.6

b)

Calculated Alloy CN's

Absorbing atom	Scattering atom: **Au**	Scattering atom: **Pd**
Au	7.9	3.4
Pd	8.0	3.4

Figure 2.6. (a) XAS-measured CN's for 3 nm Pd-on-Au NPs with 70% Pd SC and (b) calculated CN's for alloyed Pd-Au NPs with the same metal content (30.2 mol% Pd), total Au CN (11.3), and total Pd CN (11.4). Experimental CN's were those of NPs after hydrogen reduction at 200 °C.

The CN's of alloyed PdAu NPs are calculated using the total Au and total Pd CN's and metal molar composition using Equations 2.5-2.8 (Fig. 2.6b).[11]

$$\text{Au-Au}_{\text{alloy}}\ \text{CN} = \text{total Au CN} \times \text{mol\% Au} = 7.9 \qquad (2.5)$$

$$\text{Au-Pd}_{\text{alloy}}\ \text{CN} = \text{total Au CN} \times \text{mol\% Pd} = 3.4 \qquad (2.6)$$

$$\text{Pd-Pd}_{\text{alloy}}\ \text{CN} = \text{total Pd CN} \times \text{mol\% Pd} = 3.4 \qquad (2.7)$$

$$\text{Pd-Au}_{\text{alloy}}\ \text{CN} = \text{total Pd CN} \times \text{mol\% Au} = 8.0 \qquad (2.8)$$

The 9.2 value for the measured Au-Au CN is larger than the 7.9 value for Au-Au_{alloy} CN, and the 7.8 value for the measured Au-Pd is slightly smaller than the 8.0 value for Au-Pd_{alloy} CN, which indicates that our 3 nm Pd-on-Au NPs have a Au-rich core. The 3.6 value for the measured Pd-Pd CN is slightly larger than the 3.4 value for Pd-Pd_{alloy} CN, and the 2.1 value for the measured Pd-Au CN is smaller than the 3.4 value for Pd-Au_{alloy} CN, which indicates that our NPs have a Pd-rich surface.[11] Analysis of NPs with other Pd SC's (before and after hydrogen treatment at 200 °C) led to the same general nanostructure conclusion. The differences in measured and calculated Pd-Au and Pd-Pd CN's for NPs with 30 SC% were small, which can be interpreted as the particle

surface being a PdAu alloy (Fig. A2). Such surface alloying of deposited Pd atoms onto Au(111) surfaces has been observed by others using STEM analysis.[30,61]

Correlation to Catalytic Activity: We hypothesize that 2-D Pd ensembles are responsible for the catalytic activity peak (~50 SC%) for 3 nm Pd-on-Au NPs. The Pd atoms of these ensembles are metallic, are in direct contact with the supporting Au surface, and are all exposed, accessible, and active for TCE HDC reaction (*i.e.*, 100% Pd dispersion). Lower SC's favor the formation of isolated Pd atoms, which are 100% dispersed but have lower per-atom activity. 2-D ensembles could also be present at these low Pd SCs below the XAS detection limit. Between Pd surface coverages of 50 and 100 SC%, the Pd dispersion is definitively <100% due to the presence of 3-D ensembles, which can partially explain the decrease in TOF values above 50 SC%. In addition, the decrease in TOF values could be due to the presence of oxidized Pd atoms, which are presumably less active than metallic Pd. Above 100 SC%, the effect of <100% Pd dispersion on TOF values can be accounted by using the magic cluster model. There are currently no experimental measured values for Pd dispersion at any SC, such as those from carbon monoxide adsorption infrared spectroscopy, which would give truer TOF values.

2.3.4 XAS analysis of 7 nm Pd-on-Au Nanoparticles.

The 7 nm Pd-on-Au NPs were at least twice as active as the 3 nm ones, particularly at 50-70 SC% (Fig. 2.3). XAS data confirmed the Pd-shell/Au-core structure for the 7 nm NPs and pointed to several atomic-level differences (Fig. 2.7, Tables A7-A8). "Punnett square" analysis confirmed the Pd shell/Au core structure of the NPs.

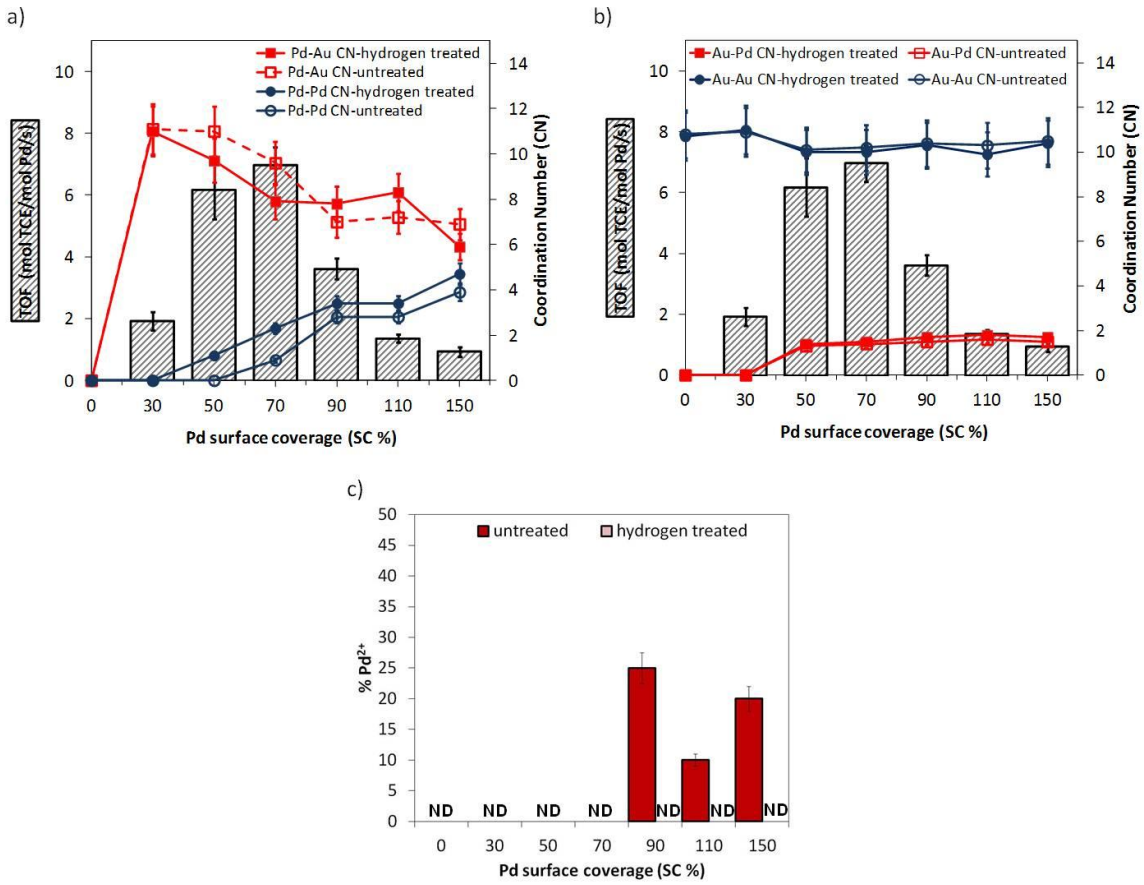

Figure 2.7. Changes in (a) Pd-Au and Pd-Pd CN's and (b) Au-Pd and Au-Au CN's as a function of Pd SC for 7 nm Pd-on-Au NPs, before and after hydrogen treatment at 200 °C. Catalytic activity data (TOF) is shown as rectangular bars. (c) Percentage of oxidized Pd (% Pd^{2+}) at different Pd SC's. "ND" = no detection of scattering signal.

The Pd-Au CN value of ~11 at 30 SC% indicated a large proportion of Pd atoms were detectible as subsurface atoms. The generally higher Pd-Au CN's than those of the 3 nm NPs (before and after H_2 treatment) suggested that subsurface Pd atoms were present. Subsurface Pd atoms have maximum contact with Au atoms, and do not oxidize (Fig. 2.7c).

Untreated and treated 7 nm NPs with 30 SC% had a Pd-Pd CN of 0, like the 3 nm NP case. However, unlike the untreated 3 nm NPs (in which Pd-Pd CN was constant at ~3), Pd-Pd CN = 0 at 50 SC% and slowly increased from ~1 at 70 SC% to ~4 at 150 SC%. This indicated the 7 nm NPs had smaller-sized Pd ensembles than those in 3 nm

NPs at the lower Pd surface coverages. After hydrogen treatment at 200 °C, the Pd-Pd CN of 7 nm NPs increased for all surface coverages. This increase corresponded somewhat to the reduction of Pd^{2+}. The relatively large increase in Pd-Pd CN at 50 and 70 SC% could be due to migration of subsurface Pd atoms to Pd ensembles at the particle surface, corresponding to the observed decrease in Pd-Au CN's or could be due to reduction of XAS-undetectable Pd^{2+}. The Pd-Pd CN's in the 90-150 SC% range (~3-5) and presence of oxidized Pd were indicative of 3-D Pd ensembles.

The Au-Au CN of the 7 nm NPs did not vary with Pd SC or hydrogen treatment (Fig. 2.7b). This CN value of ~10.8 corresponded to 7.0 nm,[11,56] agreeing with the 7 nm NP diameter determined from TEM analysis. The Au-Pd CN of untreated and hydrogen treated NPs was constant at ~2, from 50 SC% to 150 SC%. The CN value was smaller than the CN value for 3 nm NPs (~3), indicating the average Au atom in larger Au particles contacted a smaller number of Pd atoms. Larger Au NPs have a larger fraction of Au atoms that do not contact Pd atoms, leading to a smaller Au-Pd CN value. The Au-Pd CN can be zero even though Pd is present, as is the case of Pd-on-Au NPs with 30 SC% (Table 2.1).

The 7 nm Pd-on-Au NPs generally had less oxidized Pd compared to the 3 nm NPs. No oxidized Pd was detected on 7 nm NPs with 70 SC%, unlike the 3 nm case (Fig. 2.7c). The 7 nm particles with 110 SC% sample had much less oxidized Pd compared to the 90 and 150 SC% cases (somewhat similar to the 3 nm samples), but the reason is not clear. Hydrogen treatment at 200 °C reduced all oxidized Pd.

We propose that 7 nm Pd-on-Au NPs with 70 SC% are the most active due to the presence of smaller 2-D Pd ensembles and absence of oxidized Pd. The Pd-Pd CN for

NPs with 70 SC% was ~1, indicating smaller Pd ensembles than those of the most active 3 nm Pd-on-Au NPs at 50 SC% (which had Pd-Pd CN of ~3). The Pd dispersion is <100%, suggesting the true TOF value is underestimated.

2.3.5 XAS analysis of 10 nm Pd-on-Au Nanoparticles.

The 10 nm NPs had TCE HDC activities between those of the 3 nm and 7 nm NPs (Fig. 2.3). XAS analysis confirmed the Pd-shell/Au-core structure (Tables A9-A10).

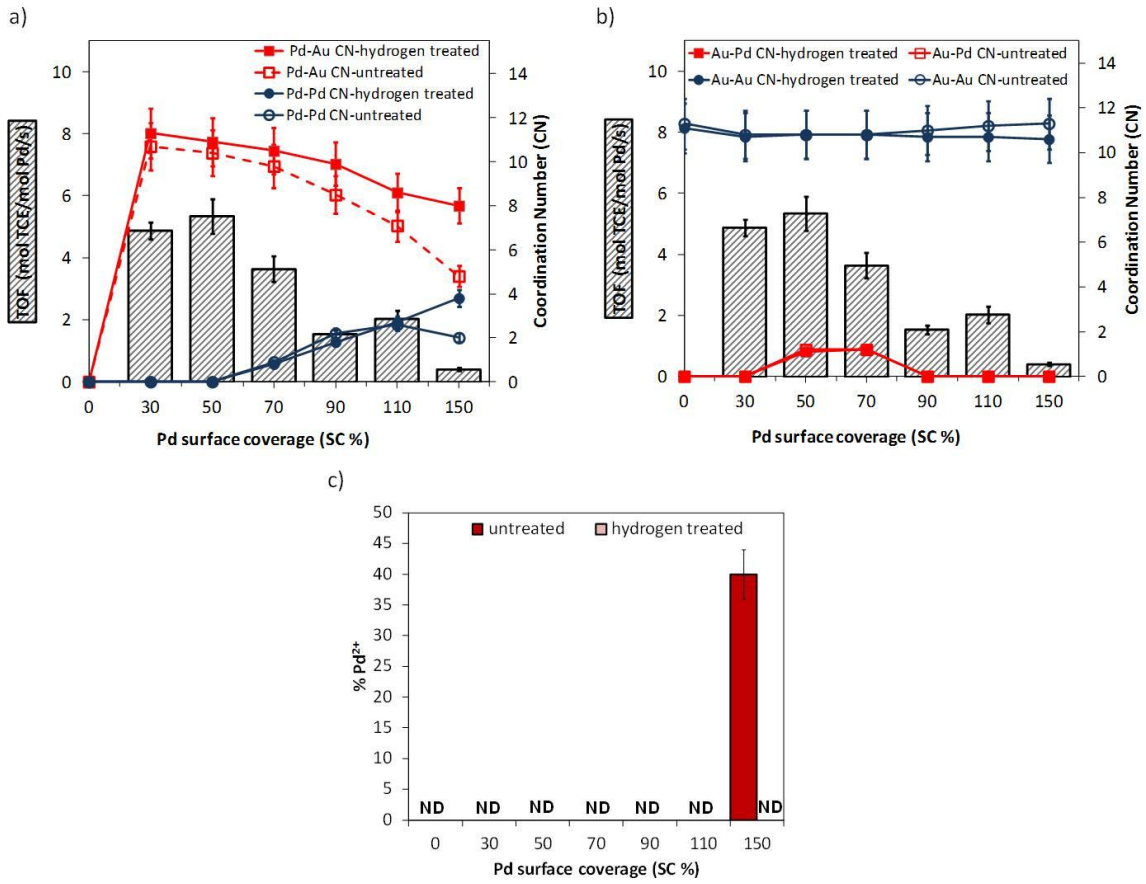

Figure 2.8. Changes in (a) Pd-Au and Pd-Pd CN's and (b) Au-Pd and Au-Au CN's as a function of Pd SC for 10 nm Pd-on-Au NPs, before and after hydrogen treatment at 200 °C. Catalytic activity data (TOF) is shown as rectangular bars. (c) Percentage of oxidized Pd (% Pd^{2+}) at different Pd SC's. "ND" = no detection of scattering signal.

The larger Au NPs led to some differences from the 7 nm NPs, especially for the NPs with 150 SC%. Subsurface Pd atoms were present, indicated by the high Pd-Au CN

values and consistent with the lack of oxidized Pd (Fig. 2.8c). These CN values increased slightly (*i.e.*, within error) after the NPs were hydrogen treated. The Pd-Pd CN values of untreated 10 nm particles were similar to those of untreated 7 nm NPs. Unlike the latter case though, the Pd-Pd CN values did not change after hydrogen treatment (Fig. 2.8a). For NPs with 150 SC%, almost 40% of the Pd atoms were oxidized, and their reduction after hydrogen treatment corresponded to the Pd-Au CN increasing from ~5 to ~8 and the Pd-Pd CN increasing from ~2 to ~4.

The Au-Au CN of 10 nm NPs also did not change significantly with Pd SC or hydrogen treatment (Fig. 2.8b). This CN value of ~11.3 corresponded to 8.0 nm, which was less than the TEM measured diameter of 10.0 nm, and can be attributed to Au-Au CN values not being accurate for particle sizing at the larger diameters.[11,56] Only NPs with Pd SCs of 50 and 70 SC% had detectable Au-Pd CN's, before or after hydrogen treatment (Fig. 2.8b). Compared to the 3 and 7 nm cases, the 10 nm Au core has an even larger fraction of Au atoms that do not contact Pd atoms, which was responsible for the small-to-zero Au-Pd CN values.

The correlation of Pd structure to catalysis was not as clear for the 10 nm case as for the other two particle sizes. This could be due to distortion of the XAS Pd surface scattering path signals due to the large particle size.[62,63] This could also be due to limitations of our magic cluster model calculations at the larger particle sizes, which are based on the assumption of 0% size distribution of the actual Au NPs and the use of a Au atom diameter value of 0.270 nm. Concerning the latter point, a Au atom diameter value of 0.288 nm is often used also.[64] For a magic cluster to approximate a 10 nm Au particle, the total number of atoms/NP decreases from 21126 atoms/NP (using the 0.270 nm

value) to 17855 atoms/NP (using the 0.288 nm value). For a magic cluster to approximate a 7 nm particle, the total number of atoms/NP decreases from 8217 to 6525. The total number of atoms/NP remains the same for a magic cluster of 3 nm. The small difference in Au atom size thus leads to differences in calculated Au NP sizes and Pd surface coverages that accentuates for the larger particle sizes.

Having considered the aforementioned effects, we concluded that the 150 SC% sample has 3-D Pd ensembles based on a relatively large Pd-Pd CN and the presence of oxidized Pd. The 110 SC% could be concluded to have 2-D Pd ensembles because there is no oxidized Pd and the Pd-Pd CN is >2. Decreasing the surface coverage below 110 SC%, the average Pd ensembles became smaller as Pd-Pd CN's decreased. HDC TCE activity had the highest value at 50 SC%, however. To be consistent with the 3 and 7 nm cases, we suggest that 2-D Pd ensembles are responsible for the peak activity at 50 SC% even though Pd-Pd CN = 0. It may be that a significant amount of isolated Pd atoms are present as subsurface Pd atoms and/or in a surface alloy with Au, and that there are XAS-undetectible 2-D ensembles that provide the high catalytic activity.

2.3.6 STEM Analysis.

We performed aberration-corrected STEM analysis to visualize the Pd surface structures of the most catalytically active (7 nm Pd-on-Au NPs with 70 SC%) and a less-active material with the same particle size and a Pd surface coverage in excess of 100% (7 nm Pd-on-Au NPs with 150 SC%). Representative images of individual NPs at the two different coverages are shown in Fig. 2.9.

Spread over the surface of the 70 SC% material were isolated Pd atoms and small clusters of Pd atoms (Fig. 2.9a,b). Determining the number of atoms within a cluster and

identifying subsurface Pd atoms were not possible. The 150 SC% material had few single Pd surface atoms but more clusters of Pd atoms (Fig. 2.9c,d). These Pd structures, observed at the periphery of the Au particles, presumably cover the rest of the particle surface (but are unobservable in transmission images). These are the first STEM images that illustrate the differences in Pd metal structure above and below 1 calculated monolayer of Pd atoms.

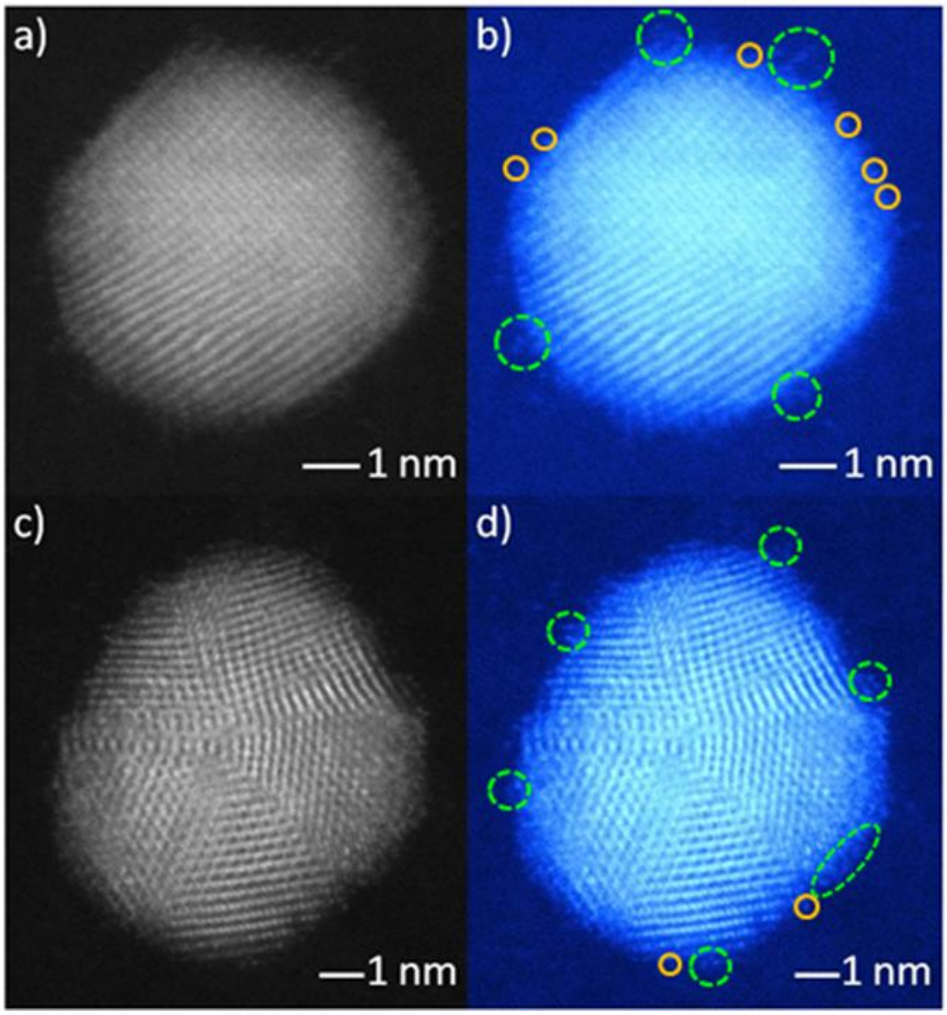

Figure 2.9. STEM images of 7 nm Pd-on-Au NPs with Pd surface coverages of (a,b) 70 and (c,d) 150 %. Panels (a) and (c) are shown in pseudo-colored versions (b and d, respectively) to enhance the image contrast between Pd and Au atoms. No other image processing was performed. Some individual Pd atoms (solid orange circles) and Pd ensembles (dashed green circles) are marked.

The observed STEM structures are in reasonably good agreement with EXAFS analysis. The Pd-Pd CN and Pd-Au CN of the NPs with 70 SC% are ~1 and ~10, respectively, consistent with the observed small, dispersed Pd ensembles located on the Au surface. The presence of isolated and different-sized clusters of Pd atoms is compatible with these CN's, which represent the average coordination environment for all atoms of a given element. The Pd clusters observed in the 150 SC% material is good evidence of the Pd 3-D ensembles implicated by the larger Pd-Pd and Pd-Au CN values of ~4 and ~7, respectively.

2.4 Conclusions.

Batch-reactor studies showed that all Pd-on-Au NPs exhibited hydrodechlorination activity ~1-2 orders of magnitude higher than pure Pd NPs and the conventional Pd/Al_2O_3 HDC catalyst. The NPs exhibited volcano-shape catalytic activity dependence on both Au particle size and Pd surface coverage. The 7 nm Pd-on-Au NPs with Pd SC of ~70% were most active due to the presence of metallic 2-D Pd ensembles consisting of ~2-3 Pd atoms in contact with ~8-10 Au atoms. The 3 nm Pd-on-Au NPs were most active with a Pd SC of ~50 SC% due also to metallic 2-D Pd ensembles, though these ensembles were larger and less active than those of the most active 7 nm NPs. The 10 nm Pd-on-Au NPs had maximum catalytic TCE HDC activity with Pd SC of ~50 SC%, speculated to be from XAS-undetectible 2-D ensembles. 2-D ensembles were detected at a Pd SC of ~110 SC%, matching a second, smaller volcano peak. As the Pd SC increased on the Au NPs, XAS analysis revealed that the oxidation state and dispersion of Pd changed from isolated, metallic Pd atoms to metallic 2-D Pd ensembles of varying coordination numbers or sizes, and finally to partially oxidized 3-D Pd ensembles. STEM

analysis of 7 nm NPs with 70 and 150 SC% directly confirmed the presence of isolated and clusters of Pd atoms. This evolution of Pd species occurred regardless of particle size, but the Au NP size affected the Pd SC at which these transitions occurred and the size/dispersion of these Pd ensembles. At a given Pd SC, the 7 nm Au NPs had smaller/more disperse Pd surface ensembles compared to the 3 nm NPs, and the 10 nm NPs had more subsurface Pd atoms. This evidence of Au particle size affecting the nature of Pd surface species of Pd-on-Au NPs illustrates a new approach to control and modify metal active sites of bimetallic NP catalysts.

2.5 Acknowledgements.

This chapter is reprinted from the *Journal of Catalysis*, Vol. 298, Pretzer, L.A.; *et al.*; "Hydrodechlorination Catalysis of Pd-on-Au Nanoparticles Varies with Particle Size." Pgs. 206-217, copyright (2013), with permission from Elsevier. I thank my co-authors Ms. H. J. Song, Dr. Y. Fang, Mr. Z. Zhao, Dr. N. Guo, Dr. T. Wu, Dr. I. Arslan, Dr. J. T. Miller, and Dr. M. S. Wong. We gratefully acknowledge the Welch Foundation (C-1676) and the National Science Foundation (CBET-1134535, CHE-1214092, EEC-0118007) for financial support. We thank Dr. W. Guo for assisting in the collection of TEM images; Mr. J. Velazquez and Dr. S. Leekumjorn, for assistance with the collection and analysis of GC-MS data; and Dr. H. G. Bagaria, Dr. G. C. Kini, and Dr. N. Soultanidis, for helpful discussions. Use of the Advanced Photon Source was supported by the U. S. Department of Energy, Office of Science, Office of Basic Energy Sciences, under Contract No.DE-AC02-06CH11357. A portion of the research was performed using EMSL, a national scientific user facility sponsored by the Department of Energy's Office of Biological and Environmental Research and located at Pacific Northwest National

Laboratory. PNNL is operated by Battelle for the U.S. Department of Energy under contract DE-AC05-76RL01830.

2.6 Supporting Information Available in Appendix A.

Detailed synthesis methods of Pd-on-Au NPs (Tables A1-A3), magic cluster of Au NPs (Table A4), details of XAS fitting and results (Tables A5-A10), Pd-on-Au NP TCE HDC selectivity (Fig. A1), and XAS "Punnett square" core-shell structure analysis for 3 nm Pd-on-Au NPs with 30% Pd SC (Fig. A2).

2.7 References.

(1) Lee, A. F.; Hackett, S. F. J.; Hutchings, G. J.; Lizzit, S.; Naughton, J.; Wilson, K. *Catal. Today* **2009**, *145*, 251.

(2) Hermans, S.; Devillers, M. *Catal. Lett.* **2005**, *99*, 55.

(3) Chen, M. S.; Kumar, D.; Yi, C. W.; Goodman, D. W. *Science* **2005**, *310*, 291.

(4) Jirkovsky, J. S.; Panas, I.; Ahlberg, E.; Halasa, M.; Romani, S.; Schiffrin, D. J. *J. Am. Chem. Soc.* **2011**, *133*, 19432.

(5) Baddeley, C. J.; Ormerod, R. M.; Stephenson, A. W.; Lambert, R. M. *J. Phys. Chem.* **1995**, *99*, 5146.

(6) Bonarowska, M.; Burda, B.; Juszczyka, W.; Pielaszek, J.; Kowalczyk, Z.; Karpinski, Z. *Appl. Catal., B* **2001**, *35*, 13.

(7) Kibler, L. A. *Electrochim. Acta* **2008**, *53*, 6824.

(8) Maroun, F.; Ozanam, F.; Magnussen, O. M.; Behm, R. J. *Science* **2001**, *293*, 1811.

(9) Nutt, M. O.; Heck, K. N.; Alvarez, P.; Wong, M. S. *Appl. Catal., B* **2006**, *69*, 115.

(10) Wong, M. S.; Alvarez, P. J. J.; Fang, Y.-l.; Ackin, N.; Nutt, M. O.; Miller, J. T.; Heck, K. N. *J. Chem. Technol. Biotechnol.* **2009**, *84*, 158.

(11) Fang, Y.-L.; Miller, J. T.; Guo, N.; Heck, K. N.; Alvarez, P. J. J.; Wong, M. S. *Catal. Today* **2011**, *160*, 96.

(12) Fuggle, J. C.; Hillebrecht, F. U.; Zeller, R.; Zolnierek, Z.; Bennett, P. A.; Freiburg, C. *Phys. Rev. B* **1983**, *27*, 2145.

(13) Moran, M. J.; Zogorski, J. S.; Squillace, P. J. *Environ. Sci. Technol.* **2007**, *41*, 74.

(14) Rowe, B. L.; Toccalino, P. L.; Moran, M. J.; Zogorski, J. S.; Price, C. V. *Environ. Health Perspect.* **2007**, *115*, 1539.

(15) "Assessing the Human Health Risks of Trichloroethylene: Key Scientific Issues," National Research Council of the National Academies, 2006.

(16) Scott, C. S.; Cogliano, V. J. *Environ. Health Perspect.* **2000**, *108*, 159.

(17) "Sources, Emission, and Exposure for Trichloroethylene and Related Chemicals," U.S. Environmental Protection Agency, 2001.

(18) "Contaminants in the Subsurface: Source Zone Assessment and Remediation," Committee on Source Removal of Contaminants in the Subsurface-National Research Council, 2005.

(19) Crittenden, J. C.; Trussell, R. R.; Hand, D. W.; Howe, K. J.; Tchobanoglous, G. *Water Treatment Principles and Design*, 2nd ed.; John Wiley & Sons: Hoboken, N.J., 2005.

(20) "Cost-effective Design of Pump and Treat Systems," U.S. Environmental Protection Agency, 2005.

(21) Alonso, F.; Beletskaya, I. P.; Yus, M. *Chem. Rev.* **2002**, *102*, 4009.

(22) McNab, W. W.; Ruiz, R.; Reinhard, M. *Environ. Sci. Technol.* **2000**, *34*, 149.

(23) Schuth, C.; Kummer, N. A.; Weidenthaler, C.; Schad, H. *Appl. Catal., B* **2004**, *52*, 197.

(24) Chaplin, B. P.; Reinhard, M.; Schneider, W. F.; Schuth, C.; Shapley, J. R.; Strathmann, T. J.; Werth, C. J. *Environ. Sci. Technol.* **2012**, *46*, 3655.

(25) Chen, N.; Rioux, R. M.; Ribeiro, F. H. *J. Catal.* **2002**, *211*, 192.

(26) Munakata, N.; Reinhard, M. *Appl. Catal., B* **2007**, *75*, 1.

(27) Chaplin, B. P.; Shapley, J. R.; Werth, C. J. *Environ. Sci. Technol.* **2007**, *41*, 5491.

(28) Nutt, M. O.; Hughes, J. B.; Wong, M. S. *Environ. Sci. Technol.* **2005**, *39*, 1346.

(29) Heck, K. N.; Nutt, M. O.; Alvarez, P.; Wong, M. S. *J. Catal.* **2009**, *267*, 97.

(30) Baber, A. E.; Tierney, H. L.; Sykes, E. C. H. *ACS Nano* **2010**, *4*, 1637.

(31) Casari, C. S.; Foglio, S.; Siviero, F.; Li Bassi, A.; Passoni, M.; Bottani, C. E. *Phys. Rev. B* **2009**, *79*, 195402.

(32) Andersin, J.; Honkala, K. *Phys. Chem. Chem. Phys.* **2011**, *13*, 1386.

(33) Jugnet, Y.; Bertolini, J. C.; Barbosa, L.; Sautet, P. *Surf. Sci.* **2002**, *505*, 153.

(34) Barbosa, L.; Sautet, P. *J. Catal.* **2002**, *207*, 127.

(35) Shan, B.; Wang, L. G.; Yang, S.; Hyun, J.; Kapur, N.; Zhao, Y. J.; Nicholas, J. B.; Cho, K. *Phys. Rev. B* **2009**, *80*, 035404.

(36) Yuan, D. W.; Gong, X. G.; Wu, R. Q. *Phys. Rev. B* **2008**, *78*.

(37) Atanasov, I.; Hou, M. *Surf. Sci.* **2009**, *603*, 2639.

(38) van Bokhoven, J. A.; Miller, J. T. *J. Phys. Chem. C* **2007**, *111*, 9245.

(39) Frenkel, A. I.; Hills, C. W.; Nuzzo, R. G. *J. Phys. Chem. B* **2001**, *105*, 12689.

(40) Slot, J. W.; Geuze, H. J. *Eur. J. Cell Biol.* **1985**, *38*, 87.

(41) Fang, Y. L.; Heck, K. N.; Alvarez, P. J. J.; Wong, M. S. *ACS Catal.* **2011**, *1*, 128.

(42) Moshfegh, A. Z. *J. Phys. D: Appl. Phys.* **2009**, *42*, 30.

(43) Aiken, J. D.; Finke, R. G. *J. Mol. Catal., A* **1999**, *145*, 1.

(44) Liu, H. B.; Pal, U.; Medina, A.; Maldonado, C.; Ascencio, J. A. *Phys. Rev. B* **2005**, *71*, 0754303.

(45) Liu, H. B.; Pal, U.; Perez, R.; Ascencio, J. A. *J. Phys. Chem. B* **2006**, *110*, 5191.

(46) Kashchiev, D.; van Rosmalen, G. M. *Cryst. Res. Technol.* **2003**, *38*, 555.

(47) Kan, C. X.; Cai, W. P.; Li, C. C.; Zhang, L. D.; Hofmeister, H. *J. Phys. D: Appl. Phys.* **2003**, *36*, 1609.

(48) Fang, P. P.; Li, J. F.; Yang, Z. L.; Li, L. M.; Ren, B.; Tian, Z. Q. *J. Raman. Spectrosc.* **2008**, *39*, 1679.

(49) Toshima, N. *Pure Appl. Chem.* **2000**, *72*, 317.

(50) Bazin, D. C.; Sayers, D. A.; Rehr, J. J. *J. Phys. Chem. B* **1997**, *101*, 11040.

(51) Chen, C. H.; Sarma, L. S.; Chen, J. M.; Shih, S. C.; Wang, G. R.; Liu, D. G.; Tang, M. T.; Lee, J. F.; Hwang, B. J. *ACS Nano* **2007**, *1*, 114.

(52) Shekhar, M.; Wang, J.; Lee, W.-S.; Williams, W. D.; Kim, S. M.; Stach, E. A.; Miller, J. T.; Delgass, W. N.; Ribeiro, F. H. *J. Am. Chem. Soc.* **2012**, *134*, 4700.

(53) Thomson, J. W.; Cademartiri, L.; MacDonald, M.; Petrov, S.; Calestani, G.; Zhang, P.; Ozin, G. A. *J. Am. Chem. Soc*. **2010**, *132*, 9058.

(54) Cuenya, B. R.; Croy, J. R.; Mostafa, S.; Behafarid, F.; Li, L.; Zhang, Z.; Yang, J. C.; Wang, Q.; Frenkel, A. I. *J. Am. Chem. Soc.* **2010**, *132*, 8747.

(55) Qu, Y.; Sutherland, A. M.; Lien, J.; Suarez, G. D.; Guo, T. *J. Phys. Chem. Lett.* **2010**, *1*, 254.

(56) Miller, J. T.; Kropf, A. J.; Zha, Y.; Regalbuto, J. R.; Delannoy, L.; Louis, C.; Bus, E.; van Bokhoven, J. A. *J. Catal.* **2006**, *240*, 222.

(57) Venezia, A. M.; La Parola, V.; Nicoli, V.; Deganello, G. *J. Catal.* **2002**, *212*, 56.

(58) Gao, F.; Wang, Y.; Goodman, D. W. *J. Phys. Chem. C* **2009**, *113*, 14993.

(59) Beck, A.; Horvath, A.; Schay, Z.; Stefler, G.; Koppany, Z.; Sajo, I.; Geszti, O.; Guczi, L. *Top. Catal.* **2007**, *44*, 115.

(60) Davis, R. J.; Boudart, M. *J. Phys. Chem.* **1994**, *98*, 5471.

(61) Baber, A. E.; Tierney, H. L.; Lawton, T. J.; Sykes, E. C. H. *Chemcatchem* **2011**, *3*, 607.

(62) Tew, M. W.; Miller, J. T.; van Bokhoven, J. A. *J. Phys. Chem. C* **2009**, *113*, 15140.

(63) Bond, G. C. *Metal-Catalysed Reactions of Hydrocarbons*; Springer, 2005.

(64) Hostetler, M. J.; Wingate, J. E.; Zhong, C. J.; Harris, J. E.; Vachet, R. W.; Clark, M. R.; Londono, J. D.; Green, S. J.; Stokes, J. J.; Wignall, G. D.; Glish, G. L.; Porter, M. D.; Evans, N. D.; Murray, R. W. *Langmuir* **1998**, *14*, 17.

Chapter 3

Three-dimensional Pd Surface Ensembles Improve Au Nanoparticle Catalysis for Nitroarene Reduction

3.1 Introduction.

The catalytic reduction of the nitro-group of nitroaromatics is a rapidly expanding field of study. Aromatic amines produced from such reactions have widespread industrial application, being used to synthesize medicines, dyes and stains, rubbers, pesticides, and explosives.[1-3] Either Bechamp reduction or catalytic hydrogenation of nitroaromatics is currently used for commercial synthesis of aromatic amines.[1,4-7] Using Bechamp reduction, the nitroaromatic is mixed with an acidic slurry of metallic iron (Fe^0) and heated to ~75-100°C such that the nitro-group is reduced and iron is oxidized to iron oxide.[8] A noted drawback of Bechamp reduction is that ~4 mol of undesired metal oxide waste is produced per mole of aromatic amine.[1,5,7] Alternatively, using catalytic hydrogenation, the nitroaromatic is reduced by hydrogen in the presence of a metal catalyst (such as Pt, Pd, or Rh) typically under pressure (~20-60 atm) and high temperature T ≤100- 110°C.[6]

Reduction of 4-nitrophenol (4-NL) to 4-aminophenol by aqueous sodium borohydride is a model nitroaromatic reduction reaction used to evaluate the potential of catalytic materials for nitroarene reduction(Eqn. 3.1).[9-11]

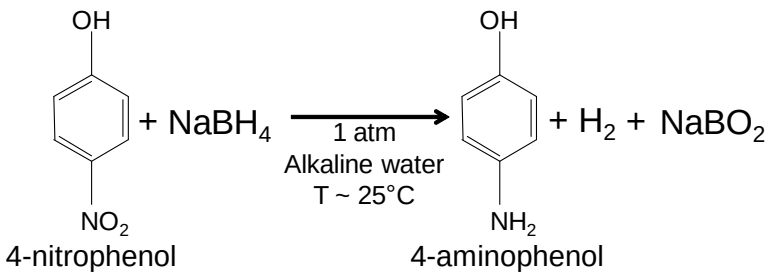

(3.1)

This reaction is catalyzed under ambient conditions (room temperature and atmospheric pressure) and is usually monitored by following the absorption of 4-aminophenol and 4-nitrophenol with an ultraviolet-visible spectrophotometer. Several studies have shown that 4-aminophenol is the only aromatic product synthesized[10,12,13] and that the reaction does not significantly occur without a catalyst (under the specified reaction conditions) due to kinetic restraints.[14,15]

Unsupported and supported monometallic nanocatalysts, such as Pd, Au, Cu, Pt, and Ag, have been used to catalyze 4-nitrophenol reduction.[1,14-20] In general, bimetallic nanomaterials, such as Pt-Ni,[19] Au-Ag,[21] Pd-Ag,[22] and Pd-Au,[23] exhibit higher catalytic activity than monometallics. The enhanced activity of bimetallics has been ascribed to electron donation between the two metals, creation of electron-rich bimetallic interfaces, and the unique structure of aggregated surface atoms.[19,24-26] Kaiser *et al.* recently showed that the surface composition of alloyed Pd-Au NPs influenced their 4-nitrophenol catalytic activity.[11] In their study, Pd-Au alloy NPs with 75 mol% Au and 25 mol% Pd exhibit ~10x higher activity than pure Pd and pure Au NPs. The size of the pure Pd, pure Au, and Pd-alloy NPs was different which could have influenced the activity results obtained. The authors postulate that the Pd-Au NPs exhibit higher activity due to a much higher reactivity of adsorbed reactants caused by structure-related electronic surface properties.[11]

In this work, we explore how the arrangement of surface Pd ensembles on 3 nm Pd-on-Au NPs affects their ability to catalyze 4-nitrophenol reduction. This work extends prior studies and provides further insight into the structure-activity properties of bimetallic nanocatalysts for 4-nitrophenol reduction. By increasing the Pd surface

coverage of the NPs from 30-150%, we have previously shown that one-dimensional (1D), 2-D, and 3-D Pd ensembles progressively form on the Au NP surface.[27] Two-dimensional Pd ensembles consist of at least two Pd atoms which extend in two directions. Alternatively, three-dimensional Pd ensembles are surface Pd atom aggregates which extend in three directions with the topmost Pd atoms being oxidized. The dispersion of the Pd atoms and oxidation state was previously shown to affect the NPs activity for trichloroethene hydrodechlorination.[27-29] NPs with 2-D Pd ensembles were observed to exhibit the highest activity. [27,30,31] Using density functional theory calculations, Andersin and Honkala showed that the enhanced activity of these 2-D Pd ensembles could be explained by their unique TCE and H_2 adsorption energies.[32]

In this work, batch reactor studies reveal a volcano-shape dependence of Pd-on-Au NP activity on the Pd surface coverage, such that NPs with partially oxidized 3-D Pd ensembles (~150% Pd SC) exhibit a maximum TOF of ~3.7 s^{-1}. Further activation energy analysis of the NPs confirm that pure Pd NPs, pure Au NPs, and Pd-on-Au NPs with Pd SC<175% exhibit compensation behavior, which occurs as a consequence of the Langmuir-Hinshelwood kinetics of the reaction. The compensation behavior by the particles suggests that the surface coverage and adsorption enthalpy of reactants likely influences their activity. We infer that 3-D Pd surface ensembles enhance the activity of 3 nm Au NPs due to structure-related electronic properties that influence reactant adsorption and reactivity of adsorbed reactants. Lastly, X-ray absorbance spectroscopy analysis of NPs with 200% Pd SC reveals that at Pd SC>150% Pd SC, 3-D Pd ensemble growth and increased Pd-Au surface alloying occurs. Collectively, these results provide

further insight into the design and structure-activity properties of bimetallic catalysts for nitroarene reduction reactions.

3.2 Experimental Methods.

3.2.1 Materials.

Palladium(II) chloride ($PdCl_2$; >99.99%), gold (III) chloride trihydrate ($HAuCl_4 \cdot 3H_2O$, 99%), tannic acid (>99.5%), potassium carbonate (>99.5%), and 4-nitrophenol (>99%), were purchased from Sigma-Aldrich. Sodium citrate dihydrate (>99.5%) was obtained from Fischer Scientific. Sodium borohydride (>98%) was purchased from Acros (Lot number: B0116503). Sodium hydroxide (1.0M ±0.001) was obtained from EMD Chemicals. Amorphous carbon powder (Vulcan XC-72 and Monarch 700) was purchased from Cabot. Ultra-high purity argon gas, nitrogen gas, and hydrogen gas were obtained from Matheson Tri-gas. Deionized water from a Barnstead NANOpure Diamond purifier (resistivity > 18 MΩ/cm) was used for all experiments. All chemicals were used as-received unless otherwise noted.

3.2.2 Au Nanoparticle Synthesis.

The Slot and Gueze method was used to synthesize the 3 nm Au NPs as previously described.[27,33] Briefly, a 0.32 mM chloroauric acid ($HAuCl_4$) solution was added to a second reducing solution (1.5 mM tannic acid, 7.0 mM trisodium citrate dihydrate, and 6.3 mM potassium carbonate for the 3 nm NPs) at 60 °C. The resulting brown sol was vigorously stirred and heated to boiling. After boiling for two minutes the sol was cooled to room temperature and the total sol volume was adjusted to 100 mL with water. The size of the NPs was verified using transmission electron microscopy.[27] Au NPs were stored up to 1 week at 4 °C.

3.2.3 Pd-on-Au Nanoparticle Synthesis.

Pd-on-Au NPs with Pd SCs between 10 and 200% were synthesized by reducing aliquots (13-265 μL) of a 2.47 mM chloropalladic (II) acid (H_2PdCl_4) solution with hydrogen gas onto the Au NP sols under ambient conditions as previously described (see Table C1).[27] The volume of 2.47 mM H_2PdCl_4 needed for a specific Pd SC was calculated using the magic cluster model, in which each Au NP is viewed as a central Au atom surrounded by consecutive shells of Au atoms.[28,34,35] A 3 nm Au NP, for example, would consist of 5 consecutive Au shells, 561 total Au atoms, and 252 surface Au atoms (see Table C2). The Pd SC of 100% would be modeled as a 6th consecutive shell on the NP since Pd and Au atoms are nearly the same size. Pd SCs>100% were modeled as filling the subsequent 7th consecutive shell of the NP, such that at 200% Pd SC each Pd-on-Au NP consisted of 7 consecutive shells (*i.e.,* 5 Au shells + 2 consecutive Pd shells).[27]

The concentration of NPs in the 3 nm Au NP sol was calculated to be 2.7×10^{14} NPs/mL assuming complete $HAuCl_4$ reduction (previously verified by elemental analysis).[27] We have verified reduction and deposition of H_2PdCl_4 (>90%) on the Au NPs using elemental analysis.[27] TEM confirmed no significant change in particle size (*i.e.*, beyond the initial Au particle size distribution) or size distribution when Pd was deposited on the Au NP surface.[27]

3.2.4 Pd Nanoparticle Synthesis.

The activity of Pd-on-Au NPs was compared to those of pure 3 nm and 4 nm Pd NPs. Pd NPs (d ~ 4 nm)[28] were synthesized similarly to the Au NPs except that a 0.32 mM $PdCl_4^{2-}$ solution (12 mL of 2.39 mM $PdCl_4^{2-}$ diluted with 68 mL H_2O) was used. Pd sols were

heated to boiling for ~25 min prior to cooling to room temperature under ambient conditions.[27]

3.2.5 Catalytic Testing.

A 10 mM 4-nitrophenol stock solution was made by adding 41.7 mg of 4-NL to 30 mL of water and sonicating for 20 min. An alkaline 0.1 M $NaBH_4$ stock solution was made by dissolving 0.038 g of $NaBH_4$ in 10 mL of an ice-cold 0.1 mM NaOH solution (100 uL of 0.01 M NaOH diluted with 9.9 mL water). A fresh $NaBH_4$ stock solution was made every 3 h. Catalytic testing was conducted using cuvette batch reactors. A screw-cap quartz cuvette (1 cm pathlength) with 2.7 mL water, 30 uL of 10 mM 4-NL stock solution, and 200 uL of 0.1 M $NaBH_4$ stock solution was sealed with a PTFE-silicone septum. The sealed cuvette was purged with an inert gas (either Ar or N_2) for 1 min to displace dissolved oxygen and fill the headspace (~1 atm). An aliquot (51 uL) of as-prepared 3 nm Pd-on-Au NP sols was diluted with 9.94 mL of water to prepare a diluted NP sol (total Au concentration = 1.3×10^{-6} M; 0.26 ppm and total Pd concentration = 8.4×10^{-8} M; 0.0089 ppm - 1.7×10^{-6} M; 0.18 ppm). After purging, 100 µL of diluted NP sol was injected into the quartz cuvette at t = 0 min. The final concentration of Pd-on-Au NPs in the reactor was 4.5×10^{10} NPs/mL. No UV-Vis absorbance by the NPs was detected at this concentration. The final concentration of total Au in the reactor was 4.2×10^{-8} M while the total concentration of Pd ranged from 2.7×10^{-9} M to 5.5×10^{-8} M, depending on the NP surface coverage.

Monitoring of 4-NL reduction was started 30 sec. after NP injection by following the absorbance of the nitro group of 4-NL at λ=400 nm (red-shifted from ~313 nm due to basic reaction conditions).[36] Initial concentrations of 4-NL and $NaBH_4$ in the quartz

cuvette reactor were 9.7×10^{-2} mM (~13.5 ppm) and 6.5 mM (~246 ppm), respectively. These initial reactant concentrations were selected based on prior studies.[9-12] All reactions were monitored for total t = 26.5 min using a Shimadzu 2450 UV-Vis spectrophotometer. Sample reaction spectra were acquired every 2 min. Between spectra scans, the quartz cuvette was vortexed using a Fisher Scientific mini vortexor set at ~7.

Since the concentration of $NaBH_4$ greatly exceeds (~65×) that of 4-NL, the reaction rate constants were calculated from the pseudo-first order rate law with respect to 4-NL, as previously reported:[9,10,12,21,37]

$$-dC_{4\text{-NL}}/dt = k_{meas}C_{4\text{-NL}} \qquad (3.2)$$

where $C_{4\text{-NL}}$ is the 4-NL concentration in the cuvette reactor and k_{meas} is the measured pseudo-first-order rate constant. According to previous studies, the reaction proceeds via a Langmuir-Hinshelwood type mechanism in which adsorbed 4-nitrophenol and borohydride species react to form 4-aminophenol, metaborate (BO_2^-), and hydrogen.[11,12,38,39] Catalyst turnover frequency (TOF) was calculated by normalizing the measured rate to the total concentration of surface Au atoms ($C_{Au\ surface\ atoms}$) and total concentration of surface Pd atoms ($C_{Pd\ surface\ atoms}$):

$$TOF = (k_{meas}\ C_{4\text{-NL}}/[(C_{Pd\ surface\ atoms})+(C_{Au\ surface\ atoms})]) \qquad (3.3)$$

For Pd SC<100%, the $C_{Pd\ surface\ atoms}$ comes from the number of Pd atoms in the 6th shell of the magic cluster model. The $C_{Au\ surface\ atoms}$ is based on the number of Au atoms in the 5th shell that are theoretically covered by the Pd atoms in the 6th shell. For Pd SC> 100%, $C_{Pd\ surface\ atoms}$ depends on the number of Pd atoms in the 7th shell and the Pd atoms in the 6th shell that are not covered by the Pd atoms in the 7th shell. The concentration of Pd and Au surface atoms used for reported TOFs is provided in Table C3. We verified that the

observed reaction rate constants varied linearly with respect to the concentration of Pd and Au surface atoms used for our studies (Fig. C1-C4). The pH of the reaction solution (~10.4) did not change during the reaction. No reaction was observed in the absence of catalyst NPs.

Control experiments with monometallic Pd and Au NPs were performed as follows. Approximately 100 µL of a diluted~4 nm Pd NP sol (446 µL as prepared Pd NP sol diluted with 9.54 mL H_2O) was injected into the sealed quartz reactor (final Pd concentration in reactor = 4.4×10^{-7} M; 0.047 ppm). A diluted 3 nm Au NP sol (206 µL as prepared Au NP sol diluted with 9.78 mL H_2O) was prepared and 100 µL of the diluted sol was injected into the quartz reactor (final Au concentration in reactor = 1.7×10^{-7} M; 0.034 ppm). At these particle concentrations, no significant UV-Vis absorbance by the NPs was detected.

3.2.6 Activation Energy Analysis.

An activation energy analysis of pure 3 nm NPs, pure 4 nm Pd NPs, and representative 3 nm Pd-on-Au NPs was conducted by measuring the reaction rate of each catalyst at 30 °C, 40 °C, 50 °C, and 60 °C. The sample chamber in the UV-Vis can be temperature-controlled using an external water bath. The maximum variation of the temperature in the batch reactor during the reaction was ± 1 °C. Thermal equilibration between the batch reactor and sample chamber occurred within ~30 sec. No significant change in batch reactor temperature (>1 °C) was observed due to vortexing between scans. The activation energy and frequency factor of each catalyst was determined using the Arrhenius equation.

3.2.7 XAS Analysis.

X-ray absorption spectroscopy of carbon-supported 200% Pd NPs was conducted at the Advanced Photon Source at Argonne National Laboratory. Details concerning the XAS experiment protocol used can be found in our previous publications and will not be described here.[27,29]

3.3 Results and Discussion.

3.3.1 4-nitrophenol Reduction Activity of Pd-on-Au Nanoparticles.

UV-Vis absorbance spectra of 3 nm Au NPs, 4 nm Pd NPs, and Au NPs with 150% Pd SC are shown in Figure 3.1. No change in 4-NL absorbance was observed in the absence of metal nanoparticles.

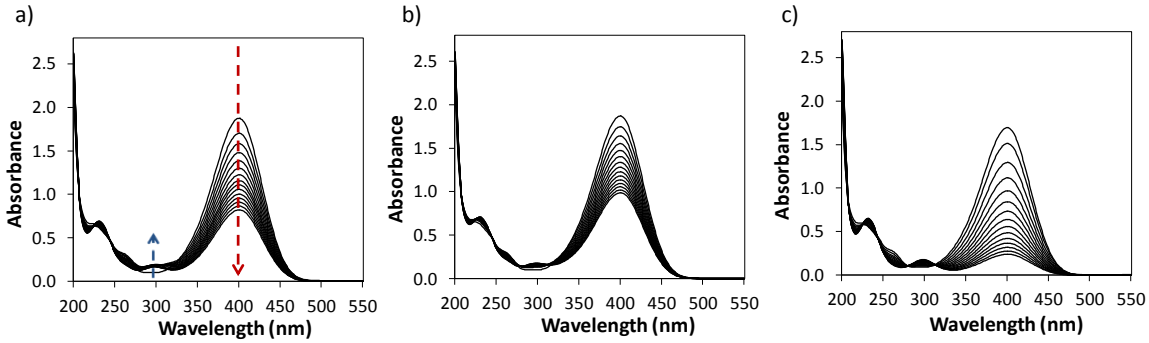

Figure 3.1. UV-Vis absorbance spectra of (a) pure 3 nm Au NPs, (b) pure 4 nm Pd NPs, and (c) 3 nm Pd-on-Au NPs with 150% Pd SC. The red and blue arrows in panel a show the decreasing absorbance of 4-NL and increasing absorbance of 4-AP, respectively, as the reaction progresses.

Spectra were collected every 2 min for a total reaction time of 26.5 min. All three spectra exhibit isobestic points at ~280nm, ~240 nm, and ~220 nm. The principal absorbance wavelengths of 4-nitrophenol and 4-aminophenol are 400 nm and 293 nm, respectively. The absorption coefficient of 4-aminophenol is significantly lower than 4-nitrophenol leading to significantly lower 4-aminophenol absorbance. Several studies have confirmed that isobestic points in the UV-Vis spectra indicate the selective

formation of 4-aminophenol.[10,12,13,19] Similar UV-Vis spectra were observed for the other Pd-on-Au NPs tested. Unlike previous studies, no induction time was observed for any of our catalysts. This strongly suggests that no rearrangement of the particles' structure occurs.[12,40]

To verify that the reaction was not diffusion-limited under our experiment conditions, we calculated the Damköhler number, D_a, as shown in Equation 3.4:

$$D_a = \frac{kC_{4NL}^{n-1}}{\beta\, a} \qquad (3.4)$$

where k is the reaction rate constant (1/s), n the reaction order, β is the mass transport coefficient, and a is the interfacial area.[40,41] The mass transport coefficient is given by the molecular diffusion coefficient of 4-NL (~6.92×10^{-10} m^2/s at 20 °C in water)[40,42] divided by the characteristic length scale, δ, over which mass transport occurs.[40] The interfacial areas of pure 3 nm Au NPs, 3 nm Pd-on-Au NPs, and 4 nm Pd NPs were calculated as 5.2×10^{-3} m^{-1}, 1.3×10^{-3} $1/m^{-1}$, and 9.4×10^{-3} m^{-1}, respectively. Even if a value of 300 nm is used for δ, the D_a of all the NPs tested is $<1\times10^{-17}$. This indicates that under our experiment conditions, the reaction is not diffusion-limited and the rate-limiting step is the surface chemical reaction.[40,41]

The catalytic activity of 3 nm Pd-on-Au NPs for 4-NL reduction and the overall structure of the NPs is shown in Figure 3.2. The structures of the Pd-on-Au NPs with Pd SC<150% is based on XAS analysis that we previously published.[27] The structure of the Pd-on-Au NPs with Pd SC = 200% is based on the XAS structural analysis which we describe below.

The activity of the NPs varies with a volcano-shape dependence on Pd surface coverage (SC) at Pd SC≥90%, such that NPs with partially oxidized 3-D Pd ensembles

displayed higher activity. The activity of 3 nm NPs with Pd SC> 70% exceeded that of pure Pd NPs (TOF ~ 0.28 mol 4-NL mol $Pd_{surface\ atoms}^{-1}$ s^{-1}) and pure Au NPs (TOF ~ 0.67 mol 4-NL mol $Au_{surface\ atoms}^{-1}$ s^{-1}). The catalytic activity of NPs with Pd SC≤70% did not vary significantly with Pd SC and was similar to the activity of pure Au NPs. The highest activity (TOF~3.7 s^{-1}) was exhibited by Pd-on-Au NPs that have partially oxidized 3-D Pd ensembles, consisting of ~4-5 Pd atoms (Pd SC=150%). At Pd SC>150%, the TOF of the NPs decreased with increasing Pd SC to ~2.0 s^{-1} at 200% Pd SC. The TOFs of our NPs (pure Au, pure Pd, and Pd-on-Au) are within the range of TOFs previously reported for similar nanoparticles (Tables C4-C5). The activity of additional 3 nm Pd-on-Au NPs was also measured to verify the activity trends shown in Figure 3.2 (Figure C5). Studies using 7 nm Pd-on-Au NPs also support these activity trends and indicate that quantum size effects do not significantly influence Au particle catalysis for 4-nitrophenol reduction (Appendix D).

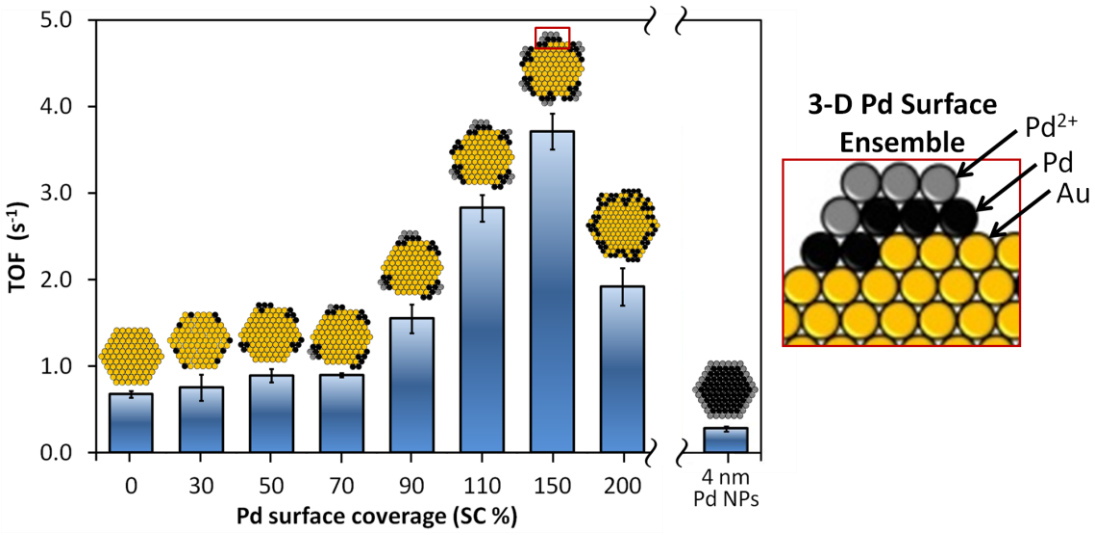

Figure 3.2. Turnover frequencies (TOFs) of 3 nm Pd-on-Au NPs with Pd surface coverages from 0 to 200% Pd SC. Representative schematics of overall NP structures are shown. NPs with 0% Pd SC are pure 3 nm Au NPs. The TOF of pure 4 nm Pd NPs is included for comparison. Error bars represent the standard deviation of at least three replicate experiments.

The enhanced activity of NPs with partially oxidized 3-D Pd ensembles is likely due moreso to the spatial arrangement (dispersion) of the surface Pd atoms than the presence of oxidized Pd. The majority of the surface Pd atoms of the pure 4 nm Pd NPs are oxidized[27,29]; hence, if simply the presence of Pd oxide resulted in significantly higher activity, we would expect the pure 4 nm Pd NPs to exhibit maximum activity. While it is thermodynamically possible for Pd oxide to be reduced by borohydride under our experimental conditions (see Eqn. C1-C3),[43] we do not believe that significant particle structure changes occur since we do not observe any induction time.

3.3.2 XAS Analysis of Pd-on-Au NPs with 200% Pd SC.

Here, we report the XAS analysis of the 200% Pd-on-Au NPs which was used to determine the structure of these NPs as shown in Figure 3.2. A detailed explanation of this XAS analysis can be found in our previous publication.[27] The structure of the Pd-on-Au NPs is based on the XAS-measured Pd and Au coordination numbers. The Punnett square analysis of the NPs with 200% Pd SC is shown in Figure 3.3. The coordination numbers, bond distances, threshold absorption energies, and Debye-Waller factors (DWF's) for 3 nm Pd-on-Au NPs with 200% Pd SC is provided in Tables C6-C7. The NPs with 200% Pd SC did not have any XAS-detectible Pd^{2+}, which indicates that likely no 3-D Pd ensembles are present.[27]

a)

XAS Measured CN's

Absorbing atom	Scattering atom: **Au**	Scattering atom: **Pd**
Au	9.1	2.1
Pd	7.8	3.6

b)

Calculated Alloy CN's

Absorbing atom	Scattering atom: **Au**	Scattering atom: **Pd**
Au	4.9	6.3
Pd	5.0	6.4

Figure 3.3. (a) XAS-measured CN's for 3 nm Pd-on-Au NPs with 200% Pd SC and (b) calculated CN's for alloyed Pd-Au NPs (see Eqn. C4-C7) with the same metal content (56.3 mol% Pd), total Au CN (Au-Au CN + Au-Pd CN = 11.2), and total Pd CN (Pd-Pd CN + Pd-Au CN = 11.4). Experimental CN's are those of as-prepared nanoparticles.

The Pd-Au, Pd-Pd, Au-Pd, and Au-Au CN (first atom is the absorber second atom is the scatterer) of theoretical alloy particles were calculated based on the total Pd and total Au CN and the mol% of Pd and mol% of Au in the particle (see Eqn. C4-C7).[27] A relative comparison of the measured and calculated alloy coordination numbers provides insight into the average structure of the NPs.[27,29] The measured Au-Au CN (~9.1) is higher than the calculated alloy Au-Au CN (~4.9) while the measured Au-Pd CN is lower (~ 2.1) than the calculated alloy Au-Pd CN (~6.3). Alternatively, the measured Pd-Pd CN (~3.6) is lower than the calculated alloy Pd-Pd CN (~6.4) while the measured Pd-Au CN is ~7.8 which is higher than the calculated alloy Pd-Au CN (~5.0). These results indicate that the general nanostructure of the NPs with 200% Pd SC is a Pd-rich surface and Au-rich core, which is consistent with the other Pd-on-Au NPs. The Pd CN results for the NPs with 200% Pd SC indicate that the surface of the NPs, while more rich in Pd than the core, is likely a PdAu surface alloy. The Pd-on-Au NPs with 30% Pd SC have a similar PdAu surface alloy.[27]

The XAS structural analysis provides further insight into the way that the structure of the Pd surface ensembles varies with the Pd surface coverage. We hypothesize that once the Pd surface coverage exceeds 150%, the 3-D Pd surface ensembles begin to coalesce and grow. Coalescence and growth of Pd ensembles (or islands) on Au surfaces has been previously observed through STEM and is a known method of ensemble/island growth.[44,45] As such ensembles grow, Pd-Au interdiffusion/alloying can concomitantly occur and has been experimentally observed even at room-temperature.[44,46] Indeed, Pd-Au alloy formation has been experimentally observed when 5 ML of Pd was deposited on Au surfaces.[46] This alloy formation can occur due to place-exchange between deposited Pd atoms and Au surface atoms. The migration of Pd either into or under the Au surface layer is thought to minimize overall surface stress/energy and is possible at surface defects because Pd and Au have similar atomic radii and lattice constants.[44,47] Several experimental studies have shown that direct contact between Pd and Au atoms can prevent oxidation of surface Pd due to electronic effects of Au.[48-51] As a result of such Pd-Au surface alloying and island growth, the activity of the 3 nm NPs with Pd SC>150% likely decreases becoming more similar to the activity of pure Au and Pd NPs.

3.3.3 Activation Energy Analysis of Pd-on-Au NPs.

Herves *et al.* previously observed that the measured activation energy of metal nanoparticles for 4-nitrophenol reduction can be influenced by temperature-dependent reactant surface coverages of reactants or changing adsorption enthalpies.[39] According to Wunder *et al.*, such a change in reactant surface coverage with temperature is a consequence of the Langmuir-Hinshelwood kinetics of catalyzed 4-nitrophenol

reduction.[40] A consequence of this phenomenon is that the activation energy and frequency factors of many metal nanoparticles for 4-nitrophenol reduction have been shown to display a compensation effect, in which an empirical linear relationship is observed between the lnA and the measured activation energy[39,52] (Eqn. 3.5),

$$\ln A = aE_a + b \qquad (3.5)$$

where a and b are constants.[53]

To determine if our metal NPs display such compensation behavior, we measured the pseudo-first order rate constant (k_{meas}) of the pure 3 nm Au NPs, pure 4 nm Pd NPs, and representative Pd-on-Au NPs at 30°C, 40°C, 50°C, and 60°C. The measured activation energy and frequency factors were calculated using the logarithmic form of the Arrhenius equation (Eqn. 3.6):

$$\ln k_{meas} = \ln A - (E_a/RT) \qquad (3.6)$$

in which A is the frequency factor, E_a the measured activation energy, R the molar gas constant (8.31 $Jmol^{-1}K^{-1}$), and T is the temperature (K). No induction time was observed for any of the NPs at the reaction temperatures tested. We recently observed that the structure of similar 4 nm Pd-on-Au NPs supported on carbon powder does not change after being exposed to an alkaline aqueous solution (pH~13) at 60 °C for ~2h.[54] Therefore, we do not expect the structure of the NPs to change at the experiment temperatures used.

The Arrhenius plots of the pure 3 nm Au NPs, pure 4 nm Pd NPs, and Pd-on-Au NPs with 150% Pd SC are shown in Figure 3.4. The natural log of the measured rate constant (ln k_{meas}) varied with a linear dependence on the inverse reaction temperature (1/T). This behavior was observed for all NPs tested (see Fig. C6).

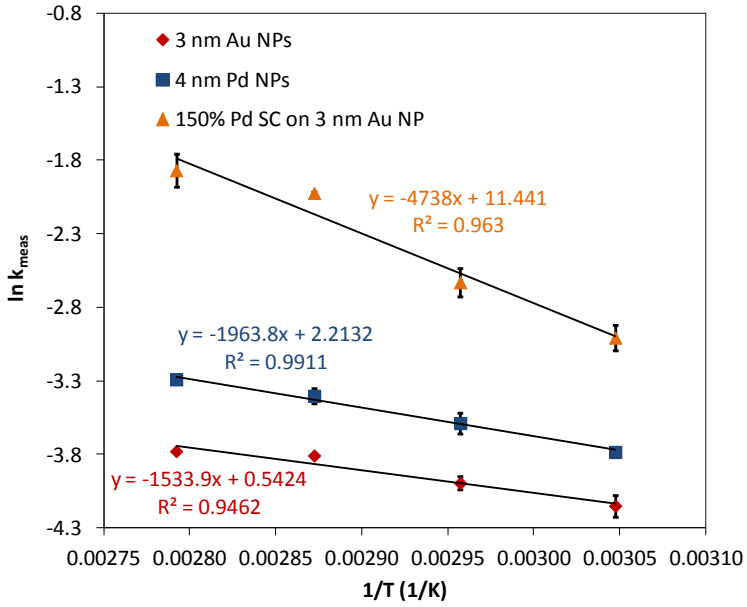

Figure 3.4. Arrhenius plot ($\ln k_{meas}$ as a function of 1/T) of 3 nm Au NPs, 4 nm Pd NPs, and Pd-on-Au NPs with 150% Pd SC. Error bars represent the standard deviation of at least three replicate experiments.

The measured activation energies are within the range of activation energies (7.5 kJ/mol – 115 kJ/mol) reported in previous studies.[9,10,16,39,55-57]

As shown in Figure 3.5, we plotted the lnA of our NPs as a function of their measured E_a to determine if they exhibit compensation behavior.

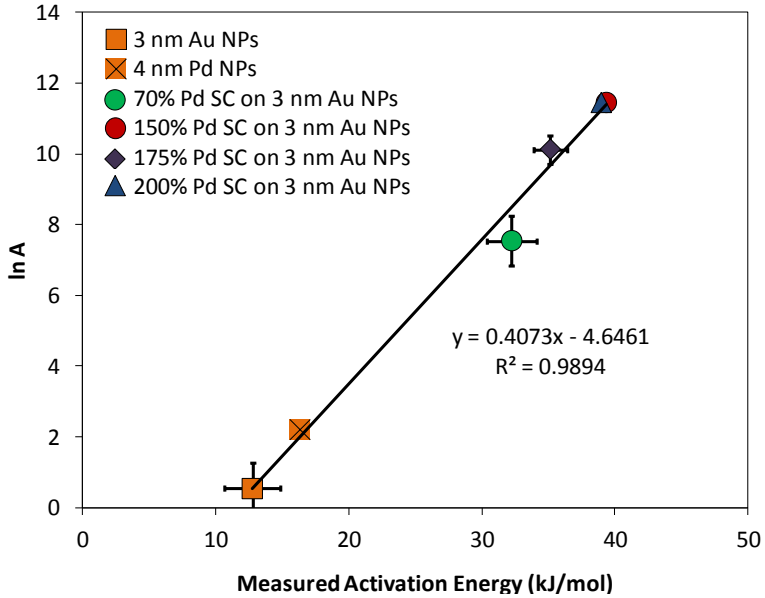

Figure 3.5. Compensation effect of 3 nm Au NPs, 4 nm Pd NPs, and representative Pd-on-Au NPs. The particles' activation energy and frequency factors were experimentally determined using the Arrhenius equation. Horizontal and vertical error bars represent the standard deviation of at least three replicate experiments.

A compensation effect was observed for pure 3 nm Au NPs, pure 4 nm Pd NPs, and Pd-on-Au NPs with Pd SC ≤ 175% Pd SC. This suggests that the surface reaction on these NPs follow Langmuir-Hinshelwood kinetics similar to other metal nanoparticles that have been tested for 4-nitrophenol reduction.[39,40] We can infer that the measured activation energies for our NPs likely differ significantly from the true activation energy because the reactant surface coverages of reactants or adsorption enthalpies are changing.[39,52] With exception of the Pd-on-Au NPs with 70% Pd SC and pure Pd NPs, the nanoparticles that exhibit higher catalytic activity typically have higher measured values of lnA and E_a. This suggests that the surface coverage and adsorption enthalpies of reactants may influence the catalytic activity of our NPs.

The 3 nm Pd-on-Au NPs with 200% Pd SC did not display a compensation effect. The pre-exponential factor of the NPs with 200% Pd SC remains the same as the particles

with 150% Pd SC but their activation energy decreases. We explain these effects by inferring that these NPs have electronic properties different than the other Pd-on-Au NPs which affect the reaction kinetics.[52,58] These altered electronic properties are likely related to the alloyed surface structure of these NPs.

3.3.4 Explanation for Catalytic Effect of 3-D Pd Surface Ensembles.

We propose that the 3-D Pd surface ensembles increase the catalytic activity of Au NPs due to structure-related electronic properties that affect the adsorption affinity and reactivity of reactants. Kaiser *et al.* previously reported that the adsorption equilibrium constants of nitrophenol (K_{Nip}) and borohydride (K_{BH4}) for pure Pd, pure Pt, pure Au, and $Au_{75}Pd_{25}$ alloy NPs differ, but are of the same order of magnitude and cannot explain their different catalytic activities.[11] Kaiser *et al.* ascribe the ~10× higher activity of $Au_{75}Pd_{25}$ NPs' to structure-related electronic properties that enhance the reactivity of adsorbed reactants.[11]

It is well known that the dispersion of Pd atoms deposited on Au surfaces influences their electronic properties, such as the d-band density of states (DOS), which affects their catalytic activity.[32,59-61] Using density functional theory calculations, Liu and Nørskov show that with increasing neighboring Au atoms, the d-band states of a Pd atom move away from the bulk Pd Fermi level and decrease in energy.[62] Interestingly, Escaño *et al.* recently predicted that dissociative adsorption of borohydride increasingly occurs as a 3d transition metal's d-band DOS approaches the Fermi level.[63] Such dissociative adsorption of borohydride would be necessary for 4-nitrophenol reduction and is predicted to occur on Pd(111) but not on pure Au(111) or alloyed Au (111) surfaces.[63,64] Tanaka *et al.* and Erol *et al.* alternatively demonstrated that 4-NL adsorption on Ag

particles is a Coulombic interaction in which electron density is transferred from the Ag surface to the 4-NL molecule. Stronger adsorption of 4-NL would be expected with increasing d-band DOS near the catalyst Fermi level. However, Corma *et al.* suggests that if the nitro group of a nitroarene binds too strongly to a catalyst, the adsorbed molecule will not react.[65] The d-band DOS resulting from the 3-D Pd ensembles likely results in 4-NL adsorption such that catalyst surface poisoning is minimized. Erol *et al.* also recently showed that the orientation of nitrophenol (*i.e.*, perpendicular *vs.* parallel to the surface) adsorbed on silver nanoparticles depends on the nitrophenol surface coverage.[66] Changing the adsorbed 4-NL orientation likely affects the reaction between adsorbed nitrophenol and adsorbed borohydride species. Hence the adsorption affinity of 4-NL on 3-D Pd ensembles could result in 4-NL binding configurations more suitable for 4-NL reduction to occur.

3.4 Conclusions.

We have used model Pd-on-Au NPs of controlled size and surface composition to probe how the surface structure of a bimetallic nanomaterial influences its ability to catalyze 4-nitrophenol reduction. The activity of 3 nm Pd-on-Au NPs with Pd SCs between 10 and 200 % varies with a volcano-shape dependence as a function of Pd SC, with maximum activity (TOF ~3.7 s^{-1}) being exhibited by NPs with 3-D Pd ensembles (~150% Pd SC). We infer that 3-D Pd ensembles enhance the activity of Au NPs by affecting the adsorption efficiency and reactivity of adsorbed reactants due to their unique structure-related electronic properties. Extended X-ray absorption fine-structure spectroscopy of the 200% Pd on Au NPs provided insight into the role of Pd surface at Pd SC >150%. At these surface coverages, we provide strong evidence that alloying of the Pd-on-Au NP

surface occurs. The collective results from this study provide further insight into the structure-activity relationship of bimetallic catalysts for nitroarene reduction reactions. Particularly for industrial applications where nitroaromatics are used, improving catalyst activity through structure control would be economically and environmentally advantageous.

3.5 Acknowledgements.

I thank my co-authors Mr. S. S. Kim, Dr. Y. Fang, Mr. Z. Zhao, Dr. N. Guo, Dr. T. Wu, Dr. J. T. Miller, and Dr. M. S. Wong. We gratefully acknowledge the Welch Foundation (C-1676) and Sabic for financial support. We thank Dr. J. C. Foursythe, Dr. Z. Schaefer, Dr. N. Soultanidis, Dr. G. C. Kini, Ms. S. Gullapalli, and Mr. J. Velazquez are acknowledged for helpful discussions. Use of the Advanced Photon Source was supported by the U. S. Department of Energy, Office of Science, Office of Basic Energy Sciences, under Contract No.DE-AC02-06CH11357.

3.6 Supporting Information Available In Appendices C and D.

Detailed synthesis methods of Pd-on-Au NPs (Table C1), magic cluster of Au NPs (Table C2), surface atom concentrations of NPs (Tables C3), TOFs of Pd, Au, and Pd-Au catalysts studied by others (Tables C4-C5), details of XAS fitting and results for 3 nm NPs with 200% Pd SC (Tables C6-C7), Au, Pd, and Pd-on-Au NP concentration studies (Fig. C1-C4), TOFs of additional Pd-on-Au NPs studied (Fig. C5; Appendix D), Arrhenius plot of Pd-on-Au NPs (Fig. C6), chemical equations for reduction of PdO(s) by BH_4^-(aq) (Eqn. C1-C3), and equations used to calculate the alloy coordination numbers of 3 nm Pd-on-Au NPs with 200% Pd SC (Eqn. C4-C7).

3.7 References.

(1) Saha, S.; Pal, A.; Kundu, S.; Basu, S.; Pal, T. *Langmuir* **2010**, *26*, 2885.

(2) Radomski, J. L. *Ann. Rev. Pharmacol. Toxicol.* **1979**, *19*, 129.

(3) Pinheiro, H. M.; Touraud, E.; Thomas, O. *Dyes and Pigments* **2004**, *61*, 121.

(4) Kantam, M. L.; Chakravarti, R.; Pal, U.; Sreedhar, B.; Bhargava, S. *Adv. Synth. Catal.* **2008**, *350*, 822.

(5) Mukhopadhyay, S.; Gandi, G. K.; Chandalia, S. B. *Org. Proc. Res. Develop.* **1999**, *3*, 201.

(6) Mitchell, S. C.; Waring, R. H. Aminophenols. In *Van Nostrand's Encyclopedia of Chemistry*; 5 ed.; Considine, G. D., Ed.; Wiley, John & Sons Inc., 2005.

(7) Bond, G. C.; Webb, G. *Catalysis*; Royal Society of Chemistry, 1983.

(8) Kiss, A.; Potor, A.; Hell, Z. *Catal. Lett.* **2008**, *125*, 250.

(9) Kuroda, K.; Ishida, T.; Haruta, M. *J. Molec. Catal. A* **2009**, *298*, 7.

(10) Mei, Y.; Lu, Y.; Polzer, F.; Ballauff, M.; Drechsler, M. *Chem. Mater.* **2007**, *19*, 1062.

(11) Kaiser, J.; Leppert, L.; Welz, H.; Polzer, F.; Wunder, S.; Wanderka, N.; Albrecht, M.; Lunkenbein, T.; Breu, J.; Kuemmel, S.; Lu, Y.; Ballauff, M. *Phys. Chem. Chem. Phys.* **2012**, *14*, 6487.

(12) Wunder, S.; Polzer, F.; Lu, Y.; Mei, Y.; Ballauff, M. *J. Phys. Chem. C* **2010**, *114*, 8814.

(13) Prucek, R.; Kvitek, L.; Panacek, A.; Vancurova, L.; Soukupova, J.; Jancik, D.; Zboril, R. *J. Mater. Chem.* **2009**, *19*, 8463.

(14) Pradhan, N.; Pal, A.; Pal, T. *Langmuir* **2001**, *17*, 1800.

(15) Esumi, K.; Isono, R.; Yoshimura, T. *Langmuir* **2004**, *20*, 237.

(16) Arora, S.; Kapoor, P.; Singla, M. L. *Reac. Kinet. Mech. Catal.* **2010**, *99*, 157.

(17) Lu, W.; Ning, R.; Qin, X.; Zhang, Y.; Chang, G.; Liu, S.; Luo, Y.; Sun, X. *J. Hazard. Mater.* **2011**, *197*, 320.

(18) Li, H.; Han, L.; Cooper-White, J.; Kim, I. *Green Chem.* **2012**, *14*, 586.

(19) Ghosh, S. K.; Mandal, M.; Kundu, S.; Nath, S.; Pal, T. *Appl. Catal. A: Gen.* **2004**, *268*, 61.

(20) Pradhan, N.; Pal, A.; Pal, T. *Coll. Surf. A-Physicochem. Eng. Aspects* **2002**, *196*, 247.

(21) Jiang, H.-L.; Akita, T.; Ishida, T.; Haruta, M.; Xu, Q. *J. Am. Chem. Soc.* **2011**, *133*, 1304.

(22) Kim, K.; Kim, K. L.; Shin, K. S. *J. Phys. Chem. C* **2011**, *115*, 14844.

(23) Tang, S.; Vongehr, S.; He, G.; Chen, L.; Meng, X. *J. Colloid Interface Sci.* **2012**, *375*, 125.

(24) Huang, J.; Vongehr, S.; Tang, S.; Lu, H.; Shen, J.; Meng, X. *Langmuir* **2009**, *25*, 11890.

(25) Zhao, D.; Chen, X.; Liu, Y.; Wu, C.; Ma, R.; An, Y.; Shi, L. *J. Colloid Interface Sci.* **2009**, *331*, 104.

(26) Tang, S.; Vongehr, S.; Zheng, Z.; Meng, X. *J. Colloid Interface Sci.* **2010**, *351*, 217.

(27) Pretzer, L. A.; Song, H. J.; Fang, Y.-L.; Zhao, Z.; Guo, N.; Wu, T.; Arslan, I.; Miller, J. T.; Wong, M. S. *J. Catal.* **2013**, *298*, 206.

(28) Nutt, M. O.; Heck, K. N.; Alvarez, P.; Wong, M. S. *Appl. Catal., B* **2006**, *69*, 115.

(29) Fang, Y.-L.; Miller, J. T.; Guo, N.; Heck, K. N.; Alvarez, P. J. J.; Wong, M. S. *Catal. Today* **2011**, *160*, 96.

(30) Fang, Y. L.; Heck, K. N.; Alvarez, P. J. J.; Wong, M. S. *ACS Catal.* **2011**, *1*, 128.

(31) Heck, K. N.; Nutt, M. O.; Alvarez, P.; Wong, M. S. *J. Catal.* **2009**, *267*, 97.

(32) Andersin, J.; Honkala, K. *Phys. Chem. Chem. Phys.* **2011**, *13*, 1386.

(33) Slot, J. W.; Geuze, H. J. *Eur. J. Cell Biol.* **1985**, *38*, 87.

(34) Moshfegh, A. Z. *J. Phys. D-Appl. Phys.* **2009**, *42*, 233001.

(35) Aiken, J. D.; Finke, R. G. *J. Mol. Catal., A* **1999**, *145*, 1.

(36) Harish, S.; Mathiyarasu, J.; Phani, K. L. N.; Yegnaraman, V. *Catal. Lett.* **2009**, *128*, 197.

(37) Endo, T.; Kuno, T.; Yoshimura, T.; Esumi, K. *J. Nanosci. Nanotechnol.* **2005**, *5*, 1875.

(38) Nemanashi, M.; Meijboom, R. *J. Colloid Interface Sci.* **2013**, *389*, 260.

(39) Herves, P.; Perez-Lorenzo, M.; Liz-Marzan, L. M.; Dzubiella, J.; Lu, Y.; Ballauff, M. *Chem. Soc. Rev.* **2012**, *41*, 5577.

(40) Wunder, S.; Lu, Y.; Albrecht, M.; Ballauff, M. *ACS Catal.* **2011**, *1*, 908.

(41) Vannice, A. *Kinetics of Catalytic Reactions*; Springer, 2005.

(42) Bielejewska, A.; Bylina, A.; Duszczyk, K.; Fialkowski, M.; Holyst, R. *Anal. Chem.* **2010**, *82*, 5463.

(43) *Standard Potentials in Aqueous Solution*; Bard, A. J.; Parsons, R.; Jordan, J., Eds.; Marcel Dekker Inc.: New York, 1985, pp 195.

(44) Casari, C. S.; Foglio, S.; Siviero, F.; Li Bassi, A.; Passoni, M.; Bottani, C. E. *Phys. Rev. B* **2009**, *79*, 195402.

(45) Robins, J. L. *Thin Solid Films* **1976**, *32*, 151.

(46) Gong, J. L. *Chem. Rev.* **2012**, *112*, 2987.

(47) Baber, A. E.; Tierney, H. L.; Sykes, E. C. H. *ACS Nano* **2010**, *4*, 1637.

(48) Venezia, A. M.; La Parola, V.; Nicoli, V.; Deganello, G. *J. Catal.* **2002**, *212*, 56.

(49) Gao, F.; Wang, Y.; Goodman, D. W. *J. Phys. Chem. C* **2009**, *113*, 14993.

(50) Beck, A.; Horvath, A.; Schay, Z.; Stefler, G.; Koppany, Z.; Sajo, I.; Geszti, O.; Guczi, L. *Top. Catal.* **2007**, *44*, 115.

(51) Davis, R. J.; Boudart, M. *J. Phys. Chem.* **1994**, *98*, 5471.

(52) Ponec, V.; Bond, G. C. The Catalytic Cycle. In *Catalysis by Metals and Alloys*; Elsevier: New York, 1995; Vol. 95; pp 276.

(53) Bligaard, T.; Honkala, K.; Logadottir, A.; Norskov, J. K.; Dahl, S.; Jacobsen, C. J. H. *J. Phys. Chem. B* **2003**, *107*, 9325.

(54) Zhao, Z.; Arentz, J.; Pretzer, L. A.; Clomburg, J.; Gonzalez, R.; Schweitzer, N.; Wu, T.; Miller, J. T.; Wong, M. S. *J. Am. Chem. Soc.* **(in preparation)**.

(55) Bhandari, R.; Knecht, M. R. *ACS Catal.* **2011**, *1*, 89.

(56) Panigrahi, S.; Basu, S.; Praharaj, S.; Pande, S.; Jana, S.; Pal, A.; Ghosh, S. K.; Pal, T. *J. Phys. Chem. C* **2007**, *111*, 4596.

(57) Schrinner, M.; Polzer, F.; Mei, Y.; Lu, Y.; Haupt, B.; Ballauff, M.; Goeldel, A.; Drechsler, M.; Preussner, J.; Glatzel, U. *Macromolec. Chem. Phys.* **2007**, *208*, 1542.

(58) Allison, E. G.; Bond, G. C. *Catal. Rev.-Sci. Eng.* **1972**, *7*, 233.

(59) Gao, F.; Goodman, D. W. *Chem. Soc. Rev.* **2012**, *41*, 8009.

(60) Yuan, D.; Gong, X.; Wu, R. *J. Phys. Chem. C* **2008**, *112*, 1539.

(61) Yuan, D. W.; Liu, Z. R.; Xu, S. *Phys. Lett. A* **2012**, *376*, 3432.

(62) Liu, P.; Norskov, J. K. *Phys. Chem. Chem. Phys.* **2001**, *3*, 3814.

(63) Escano, M. C. S.; Gyenge, E.; Arevalo, R. L.; Kasai, H. *J. Phys. Chem. C* **2011**, *115*, 19883.

(64) Arevalo, R. L.; Escano, M. C. S.; Wang, A. Y.-S.; Kasai, H. *Dalton Trans.* **2013**, *42*, 770.

(65) Corma, A.; Serna, P.; Garcia, H. *J. Am. Chem. Soc.* **2007**, *129*, 6358.

(66) Erol, M.; Han, Y.; Stanley, S. K.; Stafford, C. M.; Du, H.; Sukhishvili, S. *J. Am. Chem. Soc.* **2009**, *131*, 7480.

Chapter 4

Light-triggered Biocatalysis Using Thermophilic Enzyme-Au Nanoparticle Complexes

4.1 Introduction.

Gold (Au) nanoparticles have been used in a wide-variety of biological applications to date, including drug/oligonucleotide delivery, bioimaging, gene therapy, and photothermal therapy.[1-6] The most prominent properties of Au nanoparticles that can be exploited to achieve these applications are their ease of surface functionalization, their biocompatibility, and their surface plasmon-derived optical properties.[1,7,8] Plasmonic Au nanoparticles such as Au nanorods (NRs) have collective electronic oscillations that can be utilized to convert optical energy to thermal energy with high efficiency upon resonant optical illumination.[7,9] This photothermal response is tunable, based on nanoparticle size and geometric configuration, and is particularly important for biological applications because the particles can be designed to have an absorption efficiency in the near-infrared region (NIR) (690−900 nm).[8] Biological reactions and cells are maximally transparent in this "water window", and light can penetrate to depths of several centimeters, even in more complex tissues.[10]

Thermophilic enzymes are obtained from thermophiles, archaea or eubacteria that thrive at high temperatures (*i.e.*, 50-120 °C).[11] These organisms survive due to proteins that have been highly selected for robust functioning in this elevated temperature range. Many thermophilic enzymes are heat-responsive, in other words, they have dramatically lower activity at ambient temperatures than standard enzymes and increase in function up to or beyond their native temperature(s). When combined with plasmonic nanoparticles, the resulting enzyme-nanoparticle complex should be light-triggerable: the local heating

induced by resonant illumination of the nanoparticle will activate the attached heat-responsive enzymes.

Currently, control of biochemical pathways, *in vivo* or *in vitro*, is largely achieved by the addition of chemical/biochemical signals or constituents that are difficult to remove once added.[12] Biomolecule-nanoparticle complexes that are designed to be responsive to light could provide an easy means of controlling a biochemical reaction in a less intrusive manner than traditional biochemical signals, simply by illuminating with an appropriate light source. To turn off the reaction, one would simply remove the light source. This latter attribute is a critical feature, since the remote control of biological reactions could be useful in a multitude of applications. Potential uses would include minimizing operations for industrial biological products, or modulating biochemical pathways *in vivo* for therapeutic outcomes. With current conventional approaches, the use of chemical/biochemical signals to control reaction rates can be invasive, more readily introducing contaminating agents such as certain gases or infectious particles into the reactor, or resulting in the unwanted synthesis of dangerous byproducts. Indeed, remote control of biological systems inside or outside of cells through the use of nanotechnology has been a novel and exciting forefront of recent studies.[13-17]

In this study, we describe the fabrication of light-responsive, thermophilic enzyme-photothermal gold nanoparticle complexes (TE-PGNs) useful for the light-dependent activation of a biochemical reaction under traditional bulk reaction temperatures (~50 °C). This extends previous studies involving confined heating of DNA with nanoparticles[18,19] and is in direct contrast to recent studies, including elegant ones employing the use of magnetic nanoparticles and magnetic fields that activate

biochemical pathways through bulk heating.[13,16,17] The goal here is to minimize such bulk heating so that we can provide proof of concept that could eventually lead to remote triggering of biochemical reactions under standard nonthermophilic conditions utilizing thermophilic enzyme nanoparticle complexes. Our particles consist of a Au nanoparticle core with a monolayer coating of thiol-conjugated heat-responsive enzyme. Au NRs (~30 × 10 nm) were chosen for their optical response in the desired 'water window' (800 nm), while our chosen model thermophilic enzyme is *Aeropyrum pernix* glucokinase (Glk), a key enzyme in sugar degradation *via* the glycolysis pathway in bacteria and eukarya.[20] The TE-PGNs were encapsulated in a calcium alginate matrix to sequester the heat generated by the Au NR cores excited by a continuous wave laser, such as those used in medical practice. As a result, a temperature gradient sufficient to increase the temperature in the nanometer scale vicinity of the enzyme and activate it without significantly affecting the bulk temperature of the system is formed. The concept of light-dependent activation of a biochemical reaction utilizing our novel encapsulated thermophilic enzyme-photothermal gold nanoparticles is demonstrated in Fig. 4.1.

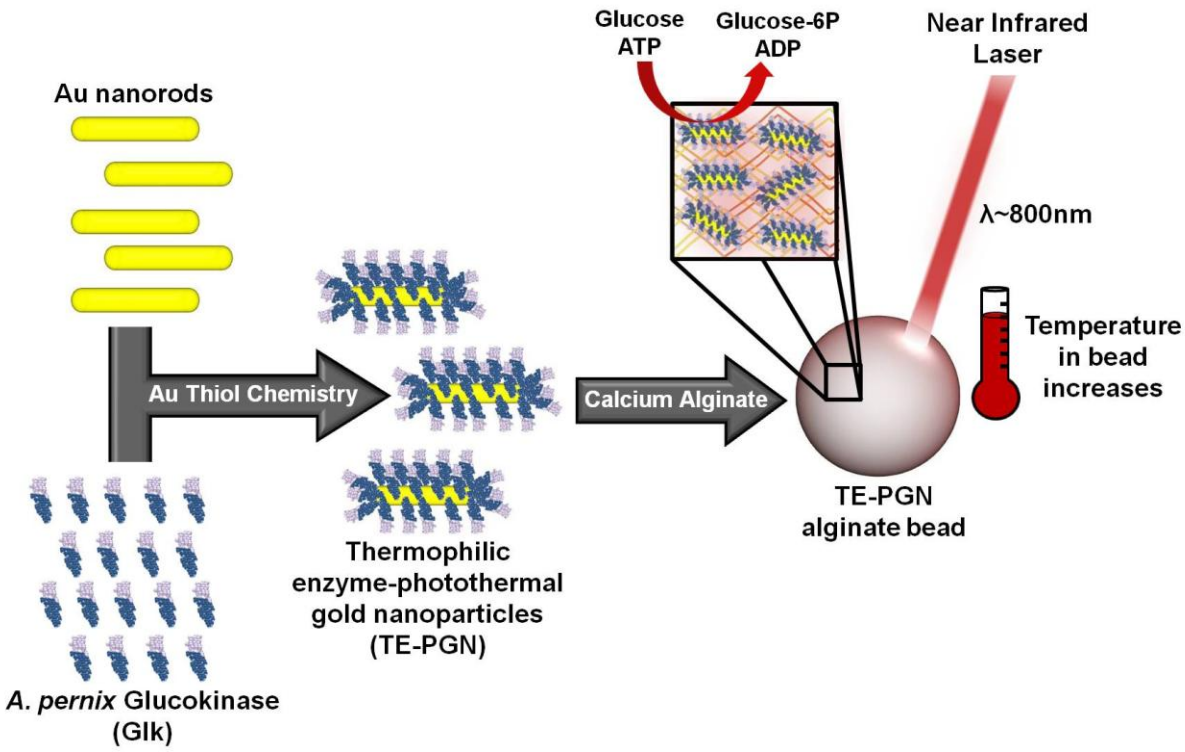

Figure 4.1. Schematic of thermophilic enzyme-photothermal gold nanoparticles (TE-PGNs) synthesis and laser-induced activation.

Gold-thiol chemistry provides both a robust and highly convenient means of binding thermophilic enzymes to Au nanoparticles, with high bond strengths of ~45 kcal/mol and thermal resistances well past 100 °C.[21] It is already well known that Au nanoparticle surfaces can be readily functionalized with a wide variety of thiolated molecules including oligonucleotides,[1] chemotherapeutic agents,[22] and polypeptides.[23] Attachment is as straightforward as mixing reduced sulfur moieties with the nanoparticles. While many types of functional Au nanocomplexes have been reported, including those with proteins, attachment of a heat-responsive (thermophilic) enzyme has not previously been reported.

4.2 Experimental Methods.

4.2.1. Cloning of A. pernix *Glk With N-terminal Tags.*

Genomic DNA of *A. pernix* (NBRC 100138G) was obtained from NITE Biological Resource Center, Japan. PCR amplification of *glk* was performed with the following primers:5-TACCATGGGTTGCGGTGGTCATCATCATCATCATCACGGTGGTGGTG TGGCGGAGGTTGTTGCT-3 and 5-GCAAGCTTGCTGCTAGAAGATTGGGAGGT-3 in which the forward primer contained additional coding information for both a N-terminal cysteine (Cys) residue tag and a His_6 tag. After digestion of the ends with NcoI and HindIII (New England Biolabs, the PCR product was cloned into the pET28a expression vector (Novagen). After restriction and sequencing analysis, the resulting pET28a-*cyshis*$_6$*glk*^{AP} vector was transformed into the BL21(DE3) expression strain (Novagen). All techniques were performed according to the manufacturer or as previously described.[24,25]

4.2.2. Preparation of Cell Extracts and Purification of A. pernix *Tagged Glk.*

E. coli BL21(DE3) [pET28a-*cyshis*$_6$*glk*^{AP}] cells were aerobically grown in 75 mL of Luria-Bertani medium containing 40 μg/mL of kanamycin at 37 °C to an optical density at 600 nm of ~0.8 at which expression of the *cyshis*$_6$*glk*^{AP} gene was initiated with the addition of 1 mM IPTG. After 3 h of further growth, the cells were pelleted (160 OD equivalents) by centrifugation at 4 °C and stored at −80 °C. Cell extracts were prepared from the pellets by cell disruption with a Disruptor Genie (Scientific Industries, Inc.) of cell suspensions in 4 mL of NPI-10 buffer (Qiagen) containing 5 mM β-mercaptoethanol (0.5 g glass beads + 1 mL cells in a 1.5 microcentrifuge tube, 4 total). After centrifugation (16,000 × g for 10 min at 4 °C), the solution was heat precipitated at 85 °C

for 25 min and centrifuged again at 4 °C. A near homogeneous Cys-His_6-Glk^{AP} enzyme preparation was achieved by use of affinity Ni-NTA resin spin columns at 15 °C according to the manufacturer's protocol for native conditions (Qiagen) with a final suspension volume of 400 µL in NPI-500. When necessary, dialysis against PBS buffer was performed once overnight at 4 °C to remove the imidazole using Slide-A-Lyzer dialysis cassettes (7,000 MWCO, Thermo Scientific). If warranted, eluate was stored at 4 °C. Under these conditions, activity remained constant for several days. Protein concentration was determined by the use of the Lowry assay with BSA as the standard. Analysis of protein expression was performed *via* sodium dodecyl sulfate-polyacrylamide gel electrophoresis (SDS-PAGE) using NuPAGE® Novex 12% Bis-Tris 10-well gels (Invitrogen), as described by the manufacturer. Once electrophoresis was completed, the gel was washed and stained with SimplyBlue TM SafeStain (Invitrogen), according to the manufacturer protocol.

4.2.3 Gold Nanorod Fabrication.

***Materials Used for Au NR Synthesis*:** Gold (III) chloride trihydrate ($HAuCl_4 \cdot 3H_2O$, 99%) and L-ascorbic acid (99+%) were purchased from Sigma-Aldrich. Cetyltrimethylammonium bromide (CTAB, ≥96%) was purchased from Fluka and sodium borohydride ($NaBH_4$) was obtained from Acros. Silver nitrate ($AgNO_3$, ≥99%) was purchased from Strem Chemicals. Deionized water from a Barnstead NANOpure Diamond system (resistivity ≥18 MΩ/cm) was used for Au NR synthesis. All chemicals were used as-received unless otherwise noted.

Au NR Synthesis: Au NRs were synthesized using the method of Sau *et al.*[26] Briefly, a 127 mM $HAuCl_4$ stock solution was prepared by dissolving 5 g of $HAuCl_4 \cdot 3H_2O$ in 95

mL of water. A 0.01 M $HAuCl_4$ solution was prepared by diluting 0.79 mL of the $HAuCl_4$ stock solution with 9.21 mL of nanopure water. A stock 0.10 M CTAB solution was prepared by dissolving 2.19 g of CTAB with vigorous stirring and low heat in 60 mL of water. An ice-cold 0.01 M $NaBH_4$ solution was prepared by diluting an ice-cold 0.1 M $NaBH_4$ solution (0.038 g of $NaBH_4$ in 10 mL of ice-cold water). The Au seed sol was synthesized by adding 0.60 mL of ice-cold 0.01 M $NaBH_4$ to a vigorously stirred solution of 0.32 mM $HAuCl_4$ (0.25 mL of 0.01 M $HAuCl_4$ solution) and 96.8 mM CTAB (7.5 mL of 0.1 M CTAB). The seed sol was vigorously stirred for 2 min following addition of $NaBH_4$ and was stored in a 27 °C water bath for no more than 10 min. Au NR growth solution was prepared by first adding 0.30 mL of a 0.01 M $AgNO_3$ solution (0.017 g of $AgNO_3$ in 10 mL of water) to a gently stirred solution of 0.40 mM $HAuCl_4$ (2 mL of 0.01 M $HAuCl_4$ solution) and 96.0 mM CTAB (47.5 mL of 0.1 M CTAB). The resulting solution was vigorously stirred and 0.32 mL of a 0.1 M ascorbic acid (0.18 g ascorbic acid in 10 mL water) was quickly added to make the final NR growth solution. The NR growth solution was equilibrated in a 27 °C water bath and 0.38 mL of the Au seed sol was added. The resulting Au NR (Au NR) sol was gently stirred for ~4 h at 27 °C. The final Au NR sol was washed twice by centrifuging at 12,000 rpm for 10 min. The cleaned sol was diluted such that the absorbance of the Au NR longitudinal surface plasmon (λ ~770 nm) was 1.41.

4.2.4 Enzyme Functionalization of Au Nanorods.

Conjugation of Cys-His_6-Glk^{AP} to the gold NRs was initiated immediately after Ni-NTA spin column elution (to prevent any disulfide bond formation). Briefly, 375 µL of extract was added to 1,425 µL of NRs in a microcentrifuge tube, gently mixed, and placed in a

rotisserie shaker overnight at room temperature. The next morning, the conjugates were pelleted at 13,400 x g for 30 min and the pellet was washed 3 times with 1 mL of PBS buffer to remove all free, unbound enzyme. To resuspend the pellet, 4 brief sonication pulses were performed with a Branson Sonifier 250 at the lowest settings with a final suspension volume of between 50-200 µL. The resulting conjugates were kept at room temperature throughout the day with intermittent vortexing where the activity remained constant.

4.2.5 Enzyme Entrapment in Calcium Alginate Beads.

Cys-His_6-Glk^{AP} or the Cys-His_6-Glk^{AP} functionalized Au NRs were entrapped in Ca-alginate beads by mixing equal volumes of the enzyme or conjugates with 1.5 % w/v of medium viscosity sodium alginate salt (MP Biomedicals, LLC). The mixture was vortexed and 10 µL was pipetted and dropped into 15 mL of 0.5 M $CaCl_2$ solution at an appropriate height so that spherical Ca-alginate beads were formed. After a minimum of 10 min of hardening in the same solution, the $CaCl_2$ solution was removed and replaced with Tris buffer (pH 7.5). The beads were stable for at least several days.

4.2.6 Enzyme Assay for Glucokinase Activity and Laser Setup.

The Cys-His_6-Glk^{AP} activity (glucose + ATP → G6P + ADP) was measured by coupling the ATP-dependent formation of glucose-6-phosphate (G6P) to the reduction of $NADP^+$ *via* G6P dehydrogenase (GPD) from yeast as previously reported.[20] Briefly, the initial assay mixture (500 µL) contained 100 mM Tris-HCl (pH 6.2, 90 °C), 5 mM glucose, 2 mM ATP, and 4 mM $MgCl_2$. After preincubation in a microcentrifuge tube, the reaction was started with the addition of the free enzyme, conjugates, or beads. This mixture was then incubated anywhere from 1 min to 25 min at the temperature of interest or irradiated

with the laser (see below), and the reaction was quenched by addition of EDTA to a final concentration of 10 mM and cooling in ice water for a minimum of 2 min. In the secondary reaction, the G6P concentration was quantified by addition of 0.6 mM $NADP^+$ and 0.5 units of GPD in 100 mM Tris (pH 7.5) to a final volume of 1 mL and incubation at 40 °C. The reduction of $NADP^+$ at 365 nm was determined 5 min later. This coupled assay was used as the basis for all activity work determined in this study.

For all laser studies and respective controls, a constant temperature quartz cuvette (Starna Cells, Inc.) with a nominal volume of 825 µL (not including neck volume), a 13 mm sample chamber diameter, and a depth/path length of 10 mm, connected to a water bath/immersible pump when appropriate, was used. The laser utilized was an 800 ± 20 nm Diomed 15 Plus model. The end of the fiber was placed vertically above both focusing lenses and the cuvette (laid sideways, water surface tension in the neck prevented spillage) to provide a spot size the same as the cuvette window (power 15 W, spot size diameter = 13 mm, optical intensity = power/beam cross section = 11 W/cm^2). Temperatures were monitored by a thermocouple. Mixing was achieved with a 2 mm spherical stir bar placed in the cuvette spun with a magnetic stir plate at 1500 RP (Sunset Model, IKA works). After laser treatment of 850-900 µL samples, a 500 µL aliquot was taken for each and processed as above for the thermal reactions. For diagram of laser setup see Figure 4.4.

4.2.7 Physical Characterization Methods.

***Ultraviolet-Visible Spectroscopy (UV-Vis)*:** The absorbance of cleaned Au NR sols and prepared Au NR-protein conjugates between wavelengths of 400 and 900 nm was

measured on a Shimadzu UV-2401 PC spectrophotometer. Polystyrene cuvettes (Fischer Scientific) with a path length of 1 cm were used.

***Transmission Electron Microscopy (TEM)*:** The length and width of Au NRs was determined using transmission electron microscopy (TEM) images collected on a JEOL 2010 transmission electron microscope operating at 100 kV. The NR sol was deposited onto 200-mesh carbon/Formvar grids by evaporating a drop of sol at room temperature (23 °C). The number-average size distribution for each sample (width and length) was determined by measuring 400+ particles using *ImageJ* Software.

***Inductively Coupled Plasma Optical Emission Spectroscopy (ICP-OES)*:** Inductively coupled plasma optical emission spectroscopy (ICP-OES) (Perkin-Elmer Optima 4300 DV) of the AuNR-protein conjugates was used to determine the total Au concentration so that the AuNR:protein ratio of the conjugates could be calculated. AuNR-protein conjugates were dissolved in 2 mL of concentrated aqua regia for at least 1 h. The resulting solution was syringe-filtered (VWR 0.2 µm polypropylene) and diluted with water to a volume of 5 mL such that the total Au concentration was <20 ppm Au.

***Thermogravimetric Analysis (TGA)*:** Thermogravimetric analysis of Au-protein conjugate calcium alginate beads was done using a Q600 TA instrument to verify water content in alginate beads. All TGA experiments were done using air (Matheson Trigas, flow rate = 40 mL/min) with a temperature ramp rate of 10 °C/min from ~ 30 °C to 700 °C.

***Scanning Electron Microscopy (SEM)*:** The structure of TE-PGN Ca-alginate beads was analyzed using a JEOL 6500F scanning electron microscope with the electron gun

operating at 15 kV. The beads were dried at 60 °C under vacuum, placed on an aluminum stub, and sputter-coated with 20 nm of Au prior to analysis.

4.3 Results.

4.3.1 Cloning, Purification, and Characterization of A. pernix *Glk.*

The model thermophilic enzyme we chose to use in this proof of principle study is the *Aeropyrum pernix* glucokinase (Glk).[20] Glucokinase can serve as an initial and key enzyme (glucose + ATP → G6P + ADP) in glucose degradation *via* the glycolysis pathway found in nearly all bacteria and eukarya, including humans.[27] Besides its central position in an important metabolic pathway, *A. pernix* glucokinase has many ideal characteristics that permit its use in creating TE-PGNs, including: O_2 insensitivity, monomeric character, excellent heat response and very high temperature resistance, low sulfur content, stability in reducing agents, the ability to be heated and cooled repeatedly, and the ability to harbor N-terminal modifications[20] (demonstrated in this study).

Genomic DNA of *A. pernix* was obtained and the glucokinase (*glk*) gene was PCR amplified. The forward PCR primer contained additional coding information for an optimal ATG start codon, a His_6 tag, and a sulfur-containing cysteine (Cys) residue. These latter elements would permit affinity purification on Ni^{+2} columns and N-terminal gold-thiol attachment, respectively. The $cyshis_6glk^{AP}$ PCR product was subsequently cloned into pET28a vector and expressed in an appropriate *E. coli* host. Cell extracts were prepared *via* cell disruption in the presence of β-mercaptoethanol to maintain reduced sulfur groups (cysteines) for later gold-thiol chemistry. Subsequently, the heat precipitation of native nonthermophilic *E. coli* proteins and metal ion affinity purification utilizing the His_6 tag were performed. As seen in Figure 4.2a (middle column), a high

specific activity (μmol mg^{-1} min^{-1} for glucose-6P formation) at 80 °C was obtained after the affinity purification step.

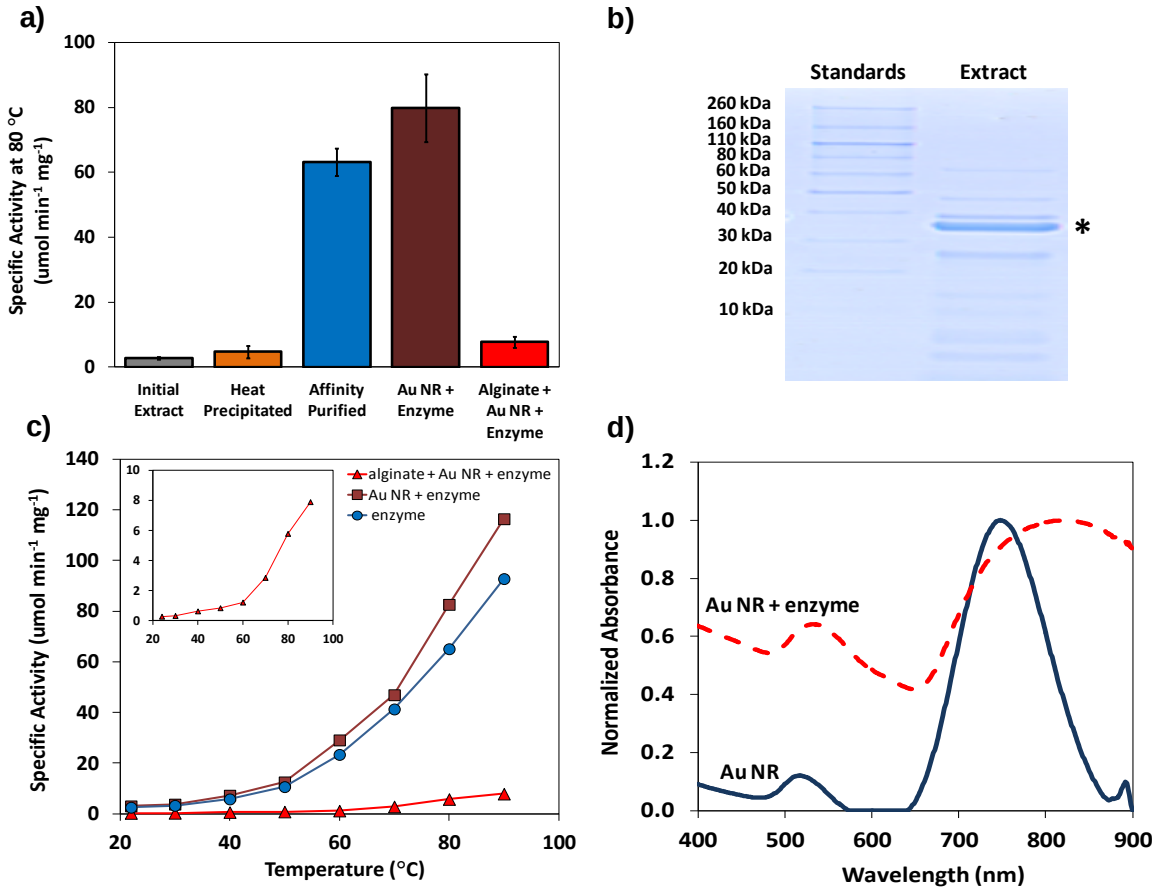

Figure 4.2. Thermal characterization of purified and TE-PGN-conjugated *A. pernix* glucokinase activity. (a) Specific Glk^{AP} activity at 80 °C for successive stages of enzyme purification, after TE-PGN formation (Au NR + enzyme), and of Ca-alginate encapsulated TE-PGNs. Error bars denote standard deviation of 3 replicates each. (b) SDS-PAGE showing purity of *A. pernix* glucokinase (Glk^{AP}, 35.19 kDa) in extracts after Ni^{+2} affinity chromatography. (c) Specific activity *vs.* bulk temperature kinetics of Glk^{AP} either nonconjugated (circles), in TE-PGNs (squares), or in Ca-alginate encapsulated TE-PGNs (triangles). Inset displays the encapsulated TE-PGNs data at a smaller scale. (d) UV-Vis absorbance spectra of Au NRs (NR) and TE-PGNs (Au NR + enzyme).

While the heat precipitation step did not yield large increases in purification, it had the added benefit of inactivating native proteases that could inhibit TE-PGN activity in subsequent use. In agreement with the activity obtained after Ni^{+2} affinity chromatography, SDS-PAGE showed that the major polypeptide constituent in the

purified extract was at or near the 35.19 kDa expected size of the Cys-His_6-Glk^{AP} protein (for ease referred to as Glk^{AP} here out) (Fig. 4.2b). Furthermore, the affinity-purified Glk^{AP} displayed the desired heat responsiveness for TE-PGN synthesis, with lower activity from room temperature to ~50°C where larger exponential increases occur in response to rising temperatures (Fig. 4.2c). It was observed that Glk^{AP} was not active at 4 °C and the observed kinetics were nearly identical to those previously reported.[20] With adequate purity of Glk^{AP} achieved, this final extract was used in the functionalization of Au NRs to create thermophilic enzyme-photothermal gold nanoparticles.

4.3.2 Attachment of Glucokinase to Au NRs and Characterization of the Resulting Conjugates.

Au NRs (33 nm x 10.4 nm) were fabricated by standard wet chemistry methods and functionalized with thermophilic Glk^{AP} polypeptides *via* gold-thiol bond formation. The cleaned Au NRs were incubated with the reduced Glk^{AP} extract overnight at room temperature. After centrifugation and washing the resulting pellet to remove all free, unbound enzyme, the TE-PGNs were resuspended by brief sonication and diluted so that the absorbance at 800 nm for a 1/6 dilution was 1.1. The concentration of the NRs in the TE-PGN suspension was 4.2±0.06 x 10^{12} NRs/mL, calculated using the average dimensions NR dimensions from TEM and total Au concentration in the TE-PGN suspension measured *via* ICP-OES. A protein loading efficiency of 20±4% was achieved resulting in a TE-PGN protein concentration of 0.210±0.02 mg/mL. With these concentrations and an Au NR surface area of ~1,250 nm^2, around 850 Glk^{AP} polypeptides (35.19 kDa) are conjugated to the Au NR surface. This agrees with theoretical calculations assuming average specific protein density (0.73 cm^3/g),[28] cubic geometry or

spherical geometry, and a linear N-terminus linker of 10 to 20 amino acids (*i.e*,. Cys-His_6 residues) for 100% surface coverage with protein.

Characterization of the localized surface plasmon resonance shift (LSPR) of the Au NRs before and after protein functionalization was performed by UV-Vis spectroscopy and the extinction spectra of TE-PGNs and Au NRs in solution are shown in Figure 4.2d. The large LSPR shift observed is consistent with a dense protein monolayer functionalized to the Au NR surface.

While the resonance wavelengths for the transverse plasmon is similar to that for Au NRs and the TE-PGNs (~520 nm), the higher longitudinal resonance wavelength (~750-850 nm, from the increased aspect ratio) is substantially broader/flatter for the TE-PGNs. This broadening of the longitudinal resonance wavelength and overall increase in absorbance could be due to electronic coupling between the TE-PGN's at the longitudinal wavelength and/or to some aggregation of TE-PGN's in suspension. Indeed, over time, the TE-PGN's are observed to visibly aggregate; however, this is easily reversed by gentle vortexing prior to use.

Thermal, non-laser testing of these novel thermophilic enzyme-photothermal gold nanoparticles revealed robust specific activity. At 80 °C, the TE-PGNs displayed ~20% greater specific glucose phosphorylation activity than the unbound free enzyme (Fig. 4.2a, for assay see Experimental Methods). This increased activity was also evident in the activity *vs.* temperature profile where the TE-PGN's displayed similar enzymatic kinetics to the unbound Glk^{AP} (Fig. 4.2c). The increased specific activity of the TE-PGNs could reflect a gold-thiol binding selection for more properly folded Glk^{AP} amongst the total pool of Glk^{AP} and minor contaminating polypeptides. Another possibility is that Au NR

bound Glk^{AP} *vs.* unbound enzyme could more readily adopt the right conformation for activity in response to heat by virtue of being conjugated to a scaffold.

4.3.3 Encapsulation of TE-PGNs in Ca-alginate Matrix.

To make the TE-PGNs compatible with continuous wave (cw) laser excitation, we encapsulated concentrated amounts of TE-PGNs in a Ca-alginate matrix to sequester the complexes and enhance the temperature gradient between the nanoparticle-enzyme complex and the bulk solution. Enzyme entrapment within a calcium alginate gel is recognized as a versatile method for not only enhancing stability, but also allowing enzyme reuse and separation from the reaction mixture.[29-31]

To encapsulate the complexes, 1.5 % w/v sodium alginate and the TE-PGNs were mixed in a 1:1 ratio and dropped in 10 µL aliquots into a solution of 0.5 M $CaCl_2$. This resulted in consistent and uniform TE-PGN Ca-alginate beads (average diameter = 1.9 ± 0.1 mm) easily visible due to their crimson color (Fig. 4.3a).

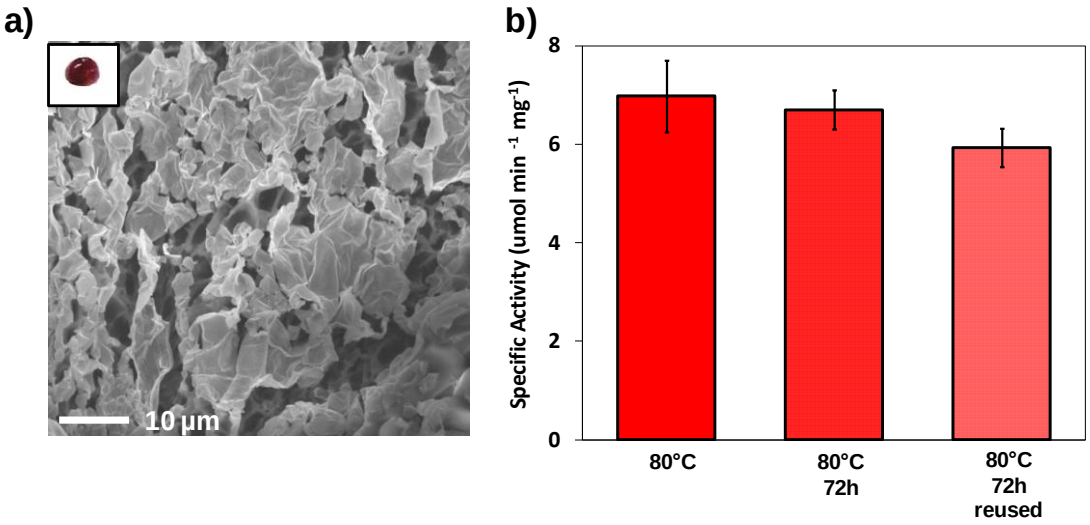

Figure 4.3. Characterization of thermophilic enzyme-photothermal gold nanoparticles encapsulated in a Ca-alginate matrix. (a) Scanning electron microscopy (SEM) image of the TE-PGN Ca-alginate bead surface. Inset shows visual image of LTNB Ca-alginate bead. (b) Specific Glk^{AP} activity of the LTNB Ca-alginate beads at 80 °C for freshly prepared beads *vs.* untested and reused beads 72 h later. Error bars denote the standard deviation of 3 replicate experiments.

Scanning electron microscopy (SEM) revealed the TE-PGN loaded Ca-alginate beads were indeed porous (Fig. 4.3a), with a pore size of a few µm instead of 10-30 nm:[31,32] however, it is possible that the pores were enlarged due to changes induced during sample preparation prior to imaging. This larger-than-expected enhanced porosity could be advantageous since porosity is critical for the transfer of reactants and products to and from the TE-PGNs. Thermogravimetric analysis revealed that ~90 wt% of the beads consisted of water, which agrees with the porosity seen in the SEM analysis (Figure E1).

The TE-PGN alginate beads (5 beads/rxn) were enzymatically active under bulk heating with the glucokinase specific activity displaying the expected heat-responsive kinetics (Fig. 4.2a,c). The specific activity was ~8-fold lower than the unencapsulated TE-PGNs, however, which may well be due to the mass transfer limitations of the Ca-alginate matrix. Possible heat transfer limitations into the matrix could also be a factor, as the Ca-alginate encapsulation was performed to reduce bulk heat flow and sustain high

temperatures at the TE-PGNs (see below). This lowered specific activity would not be critical for industrial use since this limitation would be offset by the benefit of repeated enzyme bead use. To test re-usability, TE-PGN stability and reuse was examined over a 3-day period, and no significant change in enzyme activity was observed (Fig. 4.3b). Furthermore, the TE-PGN alginate beads retained their color, shape, and consistency over multiple weeks, further suggesting their stability and reuse potential.

4.3.4 Laser-dependent activation of the encapsulated TE-PGNs.

To test whether TE-PGN complexes could control a biochemical reaction *via* light activation while maintaining standard nonthermophilic bulk temperatures, the experimental geometry diagrammed in Figure 4.4 was employed (see also Experimental Methods).

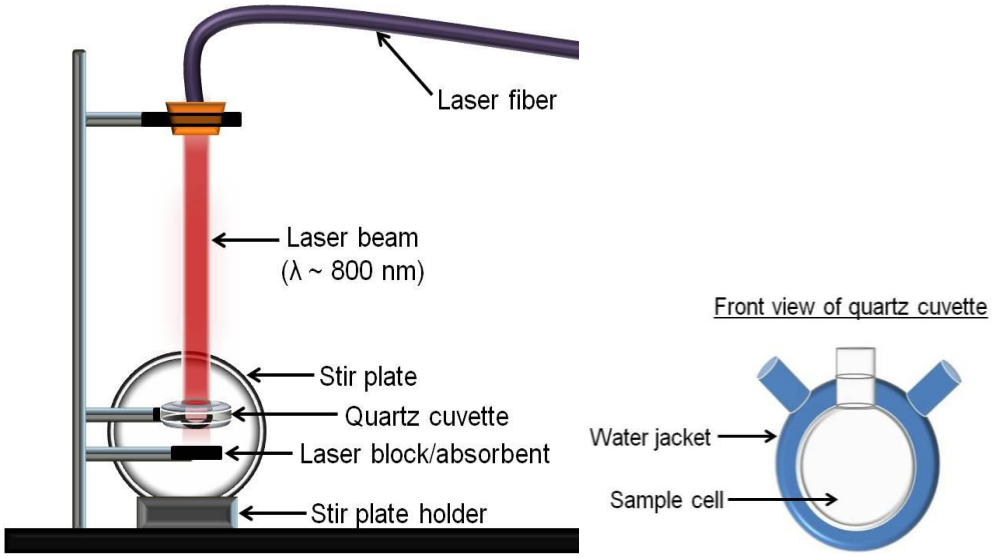

Figure 4.4. Schematic of laser setup used in this study (further details in the method section).

Laser treatment consisted of placing 5 TE-PGN-Ca-alginate beads into the cuvette containing reaction buffer and illuminating the stirred sample with a continuous wave NIR laser (λ = 800 ± 20 nm, 15 W). Calcium-alginate beads (5) containing only

nonconjugated *glk*^{AP}, reaction buffer, or pure Au nanorods were also analyzed as controls. The laser wavelength chosen for illumination was near the peak longitudinal plasmon resonance of the Au NR TE-PGN core (Fig. 4.2d). An integrated water jacket of the cuvette, connected to a water bath/immersible pump, was used to maintain bulk reaction temperatures at standard conditions (i.e nonthermophilic, 35-50 °C). We chose working temperatures of 40-45 °C, since this range was just slightly cooler than the temperature range where the larger Glk^{AP} displays a strong, exponentially increasing temperature-dependent activity response (Fig. 4.2c). Following laser irradiation, the samples were aliquoted and the reactions quenched with EDTA and put on ice until they could be measured. As seen in Figure 4.5a, laser-treated Ca-alginate beads encapsulating enzyme only (enzyme + alginate, left two bars) did not display any laser-dependent activity: the observed glucokinase activity matched the activity of bulk temperature controls.

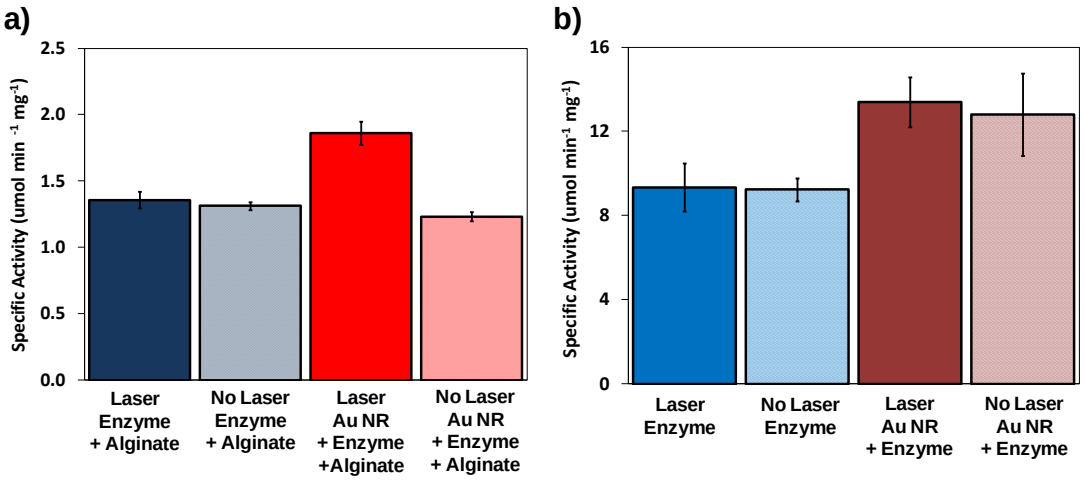

Figure 4.5. Laser activation of the encapsulated thermophilic enzyme-photothermal gold nanoparticles. (a) Specific activity of glucokinase Ca-alginate beads (enzyme + alginate) and the TE-PGN Ca-alginate beads (Au NR + enzyme + alginate) with laser irradiation *vs.* no laser irradiation (respective bulk temperature controls). 5 beads were used per reaction run. (b) Specific activity of unencapsulated glucokinase only (enzyme) and the TE-PGNs (Au NR + enzyme) with laser irradiation *vs.* no laser irradiation (respective bulk temperature controls). For both panels, error bars denote the standard deviation from 3 replicates. Bulk temperatures were 42 °C for all enzyme experiments and 44 °C for all TE-PGN experiments. The laser power was 15 W for all laser irradiation experiments. Au NR-only and reaction buffer-only controls (with and without Ca-alginate) were also run, showing no laser-induced or bulk thermal activity (Specific activities = 0).

No activity was observed for NP-only and buffer-only Ca-alginate beads, as expected. In contrast, for the laser-irradiated TE-PGN Ca-alginate beads, the observed glucokinase activity substantially exceeded the analogous bulk temperature controls, showing a 60% increase (Fig. 4.5a, Au NR + enzyme + alginate, right two bars). This laser-dependent increase in enzyme activity shows that Ca-alginate encapsulation of the complexes is critical to this response, most likely due to heat trapping by the alginate matrix which assists in the formation of a temperature gradient around the illuminated NR-enzyme complexes.

To further investigate the role of the Ca-alginate matrix, catalytic amounts of unencapsulated enzyme or TE-PGNs (1/100 dilution, absorbance at 800 nm of 0.066) were tested under the same laser conditions as above. As seen in Figure 4.5b, no laser-

dependent activation of the TE-PGNs was seen; both the laser irradiated unbound enzyme (enzyme, left two bars) and TE-PGNs (Au NR + enzyme, right two bars) displayed the same specific activity as their respective bulk temperature controls. For the unencapsulated TE-PGNs, we suspect that a nanoscale temperature gradient was not being established (*i.e.*, the heat from the Au NR core surface is diffusing to the surrounding media such that Glk^{AP} is not significantly activated[33]) (See Discussion).

4.4 Discussion.

In this study, we investigated the process of light-induced activation of a heat-responsive, thermophilic enzyme to remotely control a biochemical reaction while maintaining mesophilic bulk temperatures of ~20-50 °C. This is in contrast with some conventional photothermal applications where the photothermal response of Au nanoparticles is used for bulk heating.[1,7,16,34] To achieve our goal, we created thermophilic enzyme-photothermal gold nanoparticle complexes by conjugating a heat-responsive enzyme, *A. pernix* glucokinase, to plasmonic Au NRs, then encapsulating the TE-PGNs in a Ca-alginate matrix. Here the goal was to retain the photothermal heat generated from the Au NR cores such that the temperature around the NP surface is sufficient to activate the attached Glk^{AP} peptides while bulk heating of the reactor volume was minimized. Ultimately, when the TE-PGN Ca-alginate beads were laser irradiated with a continuous wave laser, their glucokinase activity exceeded the analogous bulk temperature controls by 60% showing validity of the light-activation concept.

Encapsulation of the TE-PGNs in Ca-alginate provided an initial means of validating our thermophilic enzyme-photothermal gold nanoparticles using a continuous wave laser amenable to industrial and practical applications. Two recent studies have

successfully encapsulated unfunctionalized Au-NRs in Ca-alginate,[32,35] such that the desired properties of the Ca-alginate matrix and Au-NRs were retained. In one of these studies,[35] single Au NR Ca-alginate clusters were continuously irradiated and successfully heated from 25 °C to over 60 °C using a laser irradiation regime similar to that employed in this study. Importantly, the collective effect of heating nanoparticle clusters, similar to our conjugates encapsulated in calcium alginate, has been observed previously and provided local temperature increases of several tens of degrees over that of the bulk temperature.[36,37] For our observed 60% increase in glucokinase activity, it can be inferred from Fig. 4.2c that, at a minimum, a ~20 °C temperature differential (*i.e.*, ~64 °C inside the beads) was achieved between the TE-PGN Ca-alginate bead and the bulk solution, approaching the 35 °C seen by Jo *et al*.[35] Our setup ensured that the encapsulated TE-PGN's remained submerged during the experiments, thus allowing uniform mass and heat-transfer between the bead and the bulk water. The bulk temperature was observed to increase from 42 °C (water bath temperature) to 44 °C following laser irradiation of the encapsulated TE-PGNs.

We observed a 60% increase in glucokinase activation when the encapsulated TE-PGNs were laser irradiated, but the activation was below the maximum of ≥8-fold activation based on the activity *vs.* temperature profiles (Fig. 4.2c). The encapsulation does introduce inherent complications that could limit enzyme activity, despite successful photothermal heating. For example, establishing a higher temperature gradient by sequestering the TE-PGNs together could have a negative impact on mass transfer of reactants and products. The separate ~8-fold lower specific activity the TE-PGN Ca-alginate beads display over the unencapsulated TE-PGNs in bulk thermal studies suggest

this (see Fig. 4.2a,c). However, these bulk thermal studies could also present heat transfer limitations, in that, here the insulation effects of the Ca-alginate could work opposite to the desired direction seen when photothermal heating occurs. However, we attempted to minimize this effect by allowing bulk thermal controls to equilibrate at the desired temperature. The lowered specific activity could also be compounded further during photothermal heating as the beads shrink somewhat due to an expulsion of air and water (which may also indicate inhibition of mass transfer of reactants to the enzymes). As stated earlier, the lower specific activity due to encapsulation would not be a significant drawback, since the Ca-alginate encapsulate beads are reusable multiple times.

The principal limitation of unencapsulated TE-PGNs in this application is the creation of a proper nanoscale temperature gradient originating from the gold surface, permitting enzyme activation. Theoretical and semi-empirical modeling suggest achieving a high temperature gradient (>10 °C) at the gold nanoparticle surface may require high optical densities, on the order of 10^4-10^5 W/cm^2.[7,34,38,39] Our experimental regime and use of a continuous wave laser at 15W provides an optical density at least 1,000-fold below this, which explains the lack of any observed laser-dependent activation without encapsulation. It should be noted that many conventional applications of Au nanoparticles (*i.e.*, tumor treatment) are believed to exploit relatively small temperature gradients compared to the bulk temperature.[34,40] These sustained, albeit small, temperature gradients can rapidly produce high bulk temperatures if enough Au-nanoparticles are irradiated. Since focusing the beam size down to micron levels is not desirable for a biochemical reactor application, the best approach for light-dependent activation of unencapsulated TE-PGNs may be to employ pulsed lasers sources.[39,41]

However, use of such lasers provides unique challenges as the pulse energy, duration, and frequency must be fine tuned so that the gold-thiol bonds are not broken and the Au NR cores, as well as the attached proteins, are not fragmented.[41,42] Conversely, the pulses would have to be frequent enough to sustain a permanent temperature gradient, enabling the attached enzyme in the TE-PGNs to achieve and maintain an active conformation.

Encapsulation, which enables the use of a simple cw laser source, is appealing in its simplicity; however, our current fabrication method provides beads not amenable to *in vivo* use due to their size. Thus fabrication methods involving microfluidics, and/or other encapsulation materials would be warranted to greatly reduce the current dimensions. Perhaps, more ideally, the encapsulation material could be eliminated and TE-PGN clusters could be possibly made through molecular-protein linkers to provide the needed heat generation using a cw laser with completely nanoscale materials. Future fine tuning of all parameters including: encapsulation materials/bead coating, heat generation/type of laser employed, transfer limitations, as well as mixing could significantly improve TE-PGN performance and eventually shrink our current system to the nanoscale for *in vivo* use.

4.5 Conclusions.

Thermophilic enzyme-photothermal gold nanoparticle complexes have the potential to be used in a wide variety of ground-breaking applications. For example, TE-PGNs using a thermophilic polymerase (*i.e., Taq* polymerase) could further refine the concept of "laser-assisted" PCR.[43] Engineering TE-PGNs for the incorporation of thermophilic hydrogenases could take advantage of the thermodynamic benefits of elevated temperature (from Gibbs equation $\Delta G = \Delta H - T\Delta S$) for the production of an important

biofuel, H_2, under more standard nonthermophilic temperatures (≤50 °C).[44,45] Ultimately, remote light-driven control of an entire biological system could be achieved using TE-PGNs, utilizing a global regulator after subsequent incorporation of TE-PGNs *in vivo*. With a plethora of thermophilic enzymes available and being discovered,[46] the applications are nearly limitless. Extension of this study to other thermophilic enzymes, materials, fabrication techniques, and/or lasers (such as pulsed) could result in the synthesis of additional TE-PGNs that would significantly change how biochemical pathways are studied and controlled in the future.

4.6 Acknowledgements.

This chapter is reprinted with permission from *ACS Nano*, Vol. 7, Blankschien, M.D.; Pretzer, L.A.; *et al.*; "Light-triggered Biocatalysis Using Thermophilic Enzyme-gold Nanoparticle Complexes." Pgs. 654-663, copyright (2013), American Chemical Society. I thank my co-first author Dr. M. D. Blankschien and co-authors Dr. R. Huschka, Dr. N. J. Halas, Dr. R. Gonzalez, and Dr. M. S. Wong. We gratefully acknowledge financial support from the Peter and Ruth Nicholas Postdoctoral Fellowship Program (M.D.B.), the Robert A. Welch Foundation under Grants C-1676 (M.S.W.) and C-1220 (N.J.H.), the National Security Science and Engineering Faculty Fellowship (NSSEFF, N00244-09-1-0067; N.J.H.), the Defense Threat Reduction Agency (DTRA, HDTRA1-11-1-0040; N.J.H.); the Air Force Office of Scientific Research (AFOSR, FA9550-10-1-0469; N.J.H.), the National Science Foundation (CBET-1134535, CHE-1214092; M.S.W.), the Rice University Institute of Biosciences and Bioengineering (IBB) Hamill Innovations Award Program (M.S.W., R.G.), and the Rice University Faculty Initiatives Fund (R.G.,

M.S.W.). We also acknowledge the help of J. M. Clomburg, M. Rodríguez-Moyá, and J. Forsythe for their technical expertise.

4.7 Supporting Information Available in Appendix E.

Thermogravimetric analysis of alginate beads (Figure E1). Glucokinase specific activity values of Figure 4.5, shown in table format (Figure E2). This material is available free of charge via the Internet at http://pubs.acs.org.

4.8 References.

(1) Huschka, R.; Zuloaga, J.; Knight, M. W.; Brown, L. V.; Nordlander, P.; Halas, N. J. *J. Am. Chem. Soc.* **2011**, *133*, 12247.

(2) Bardhan, R.; Chen, W.; Bartels, M.; Perez-Torres, C.; Botero, M. F.; McAninch, R. W.; Contreras, A.; Schiff, R.; Pautler, R. G.; Halas, N. J.; Joshi, A. *Nano. Lett.* **2010**, *10*, 4920.

(3) Sharrna, P.; Brown, S.; Walter, G.; Santra, S.; Moudgil, B. *Adv. Colloid Interfac. Sci.* **2006**, *123*, 471.

(4) Huschka, R.; Neumann, O.; Barhoumi, A.; Halas, N. J. *Nano. Lett.* **2010**, *10*, 4117.

(5) Dreaden, E. C.; Alkilany, A. M.; Huang, X.; Murphy, C. J.; El-Sayed, M. A. *Chem. Soc. Rev.* **2012**, *41*, 2740.

(6) Pallaoro, A.; Braun, G. B.; Moskovits, M. *PNAS* **2011**, *108*, 16559.

(7) Govorov, A. O.; Richardson, H. H. *Nano Today* **2007**, *2*, 30.

(8) Alkilany, A. M.; Thompson, L. B.; Boulos, S. P.; Sisco, P. N.; Murphy, C. J. *Adv. Drug Deliv. Rev.* **2012**, *64*, 190.

(9) Guerrero-Martinez, A.; Grzelczak, M.; Liz-Marzan, L. M. *ACS Nano* **2012**, *6*, 3655.

(10) Weissleder, R. *Nat. Biotechnol.* **2001**, *19*, 316.

(11) Turner, P.; Mamo, G.; Karlsson, E. N. *Microb Cell Fact* **2007**, *6*, 9.

(12) Sambrook, J.; Russell, D. W. *CSH Prot.* **2006**, *1*.

(13) Stanley, S. A.; Gagner, J. E.; Damanpour, S.; Yoshida, M.; Dordick, J. S.; Friedman, J. M. *Science* **2012**, *336*, 604.

(14) Schroeder, A.; Goldberg, M. S.; Kastrup, C.; Wang, Y.; Jiang, S.; Joseph, B. J.; Levins, C. G.; Kannan, S. T.; Langer, R.; Anderson, D. G. *Nano. Lett.* **2012**, *12*, 2685.

(15) Lee, S. E.; Liu, G. L.; Kim, F.; Lee, L. P. *Nano. Lett.* **2009**, *9*, 562.

(16) Miyako, E.; Nagata, H.; Hirano, K.; Hirotsu, T. *Lab on a Chip* **2009**, *9*, 788.

(17) Knecht, L. D.; Ali, N.; Wei, Y.; Hilt, J. Z.; Daunert, S. *ACS Nano* **2012**.

(18) Stehr, J.; Hrelescu, C.; Sperling, R. A.; Raschke, G.; Wunderlich, M.; Nichtl, A.; Heindl, D.; Kurzinger, K.; Parak, W. J.; Klar, T. A.; Feldmann, J. *Nano. Lett.* **2008**, *8*, 619.

(19) Buchkremer, A.; Linn, M. J.; Reismann, M.; Eckert, T.; Witten, K. G.; Richtering, W.; von Plessen, G.; Simon, U. *Small* **2011**, *7*, 1397.

(20) Hansen, T.; Reichstein, B.; Schmid, R.; Schonheit, P. *J. Bacteriol.* **2002**, *184*, 5955.

(21) Nuzzo, R. G.; Zegarski, B. R.; Dubois, L. H. *J. Am. Chem. Soc.* **1987**, *109*, 733.

(22) Thierry, B. *Curr. Drug Delivery* **2009**, *6*, 391.

(23) Huang, H.-C.; Koria, P.; Parker, S. M.; Selby, L.; Megeed, Z.; Rege, K. *Langmuir* **2008**, *24*, 14139.

(24) Sambrook, J.; Russell, D. W. *Molecular Cloning: A Laboratory Manual*; Cold Spring Harbor Laboratory Press: New York, 2001.

(25) Miller, J. H. *A Short Course in Bacterial Genetics: A Laboratory Manual and Handbook for* Escherichia coli *and Related Bacteria*; Cold Spring Harbor Laboratory Press: New York, 1992.

(26) Sau, T. K.; Murphy, C. J. *Langmuir* **2004**, *20*, 6414.

(27) Solomon, K. V.; Moon, T. S.; Ma, B.; Sanders, T. M.; Prather, K. L. J. *ACS Synth. Biol.* **2012**.

(28) Harpaz, Y.; Gerstein, M.; Chothia, C. *Structure* **1994**, *2*, 641.

(29) Bhushan, I.; Parshad, R.; Qazi, G. N.; Gupta, V. K. *J. Bioact. Compact. Pol.* **2008**, *23*, 552.

(30) Gombotz, W. R.; Wee, S. F. *Adv. Drug Delivery Rev.* **1998**, *31*, 267.

(31) Fundueanu, G.; Nastruzzi, C.; Carpov, A.; Desbrieres, J.; Rinaudo, M. *Biomat.* **1999**, *20*, 1427.

(32) Mitamura, K.; Imae, T.; Saito, N.; Takai, O. *J. Phys. Chem. C* **2008**, *112*, 416.

(33) Huehn, D.; Govorov, A.; Gil, P. R.; Parak, W. J. *Adv. Funct. Mater.* **2012**, *22*, 294.

(34) Richardson, H. H.; Carlson, M. T.; Tandler, P. J.; Hernandez, P.; Govorov, A. O. *Nano. Lett.* **2009**, *9*, 1139.

(35) Jo, W.; Freedman, K.; Yi, D. K.; Bose, R. K.; Lau, K. K. S.; Solomon, S. D.; Kim, M. J. *Biofabrication* **2011**, *3*.

(36) Govorov, A. O.; Zhang, W.; Skeini, T.; Richardson, H.; Lee, J.; Kotov, N. A. *Nanoscale Res. Lett.* **2006**, *1*, 84.

(37) Hrelescu, C.; Stehr, J.; Ringler, M.; Sperling, R. A.; Parak, W. J.; Klar, T. A.; Feldmann, J. *J. Phys. Chem. C* **2010**, *114*, 7401.

(38) Baffou, G.; Quidant, R.; Javier Garcia de Abajo, F. *ACS Nano* **2010**, *4*, 709.

(39) Baffou, G.; Quidant, R.; Girard, C. *Appl. Phys. Lett.* **2009**, *94*.

(40) Bardhan, R.; Lal, S.; Joshi, A.; Halas, N. J. *Acc. Chem. Res.* **2011**, *44*, 936.

(41) Link, S.; Burda, C.; Nikoobakht, B.; El-Sayed, M. A. *J. Phys. Chem. B* **2000**, *104*, 6152.

(42) Braun, G. B.; Pallaoro, A.; Wu, G.; Missirlis, D.; Zasadzinski, J. A.; Tirrell, M.; Reich, N. O. *ACS Nano* **2009**, *3*, 2007.

(43) Kim, H.; Dixit, S.; Green, C. J.; Faris, G. W. *Optics Express* **2009**, *17*, 218.

(44) Baker, S. E.; Hopkins, R. C.; Blanchette, C. D.; Walsworth, V. L.; Sumbad, R.; Fischer, N. O.; Kuhn, E. A.; Coleman, M.; Chromy, B. A.; Letant, S. E.; Hoeprich, P. D.; Adams, M. W. W.; Henderson, P. T. *J. Am. Chem. Soc.* **2009**, *131*, 7508.

(45) Verhaart, M. R. A.; Bielen, A. A. M.; van der Oost, J.; Stams, A. J. M.; Kengen, S. W. M. *Environ. Technol.* **2010**, *31*, 993.

(46) Mehta, M. P.; Baross, J. A. *Science* **2006**, *314*, 1783.

Chapter 5

Controlled Growth of Sub-10 nm Gold Nanoparticles Using Carbon Monoxide Reductant

5.1 Introduction.

Au nanoparticles (NPs) have been synthesized for centuries.[1] They are made by physically breaking bulk Au and by reducing molecular or ionic Au precursors to Au^0 atoms,[1-5] with the latter method leading to more monodisperse NPs.[2,6] The general approaches to the liquid-phase synthesis of monodisperse Au NPs by reducing molecular or ionic Au precursors involve homogeneous nucleation and heterogeneous nucleation. Well controlled particle size distributions are readily achieved if nucleation (*i.e.*, formation of ultrasmall particles or nuclei consisting of a few Au atoms) is relatively slow; if subsequent particle growth is fast; and if these processes are sequential and separated from one another in time.[7-9] For homogeneous nucleation routes, this is accomplished by nucleating and growing NPs in one pot at specific temperatures, reactant and stabilizing agent concentrations, and synthesis time.[1] For heterogeneous nucleation (also called seeded-growth) routes, monodisperse Au NPs are produced by carefully reducing gold salt onto smaller, monodisperse NPs (commonly referred to as seeds).[10,11] Post-synthesis approaches to narrow a particle size distribution include centrifugation,[12,13] electrophoresis,[14,15] etching,[16,17] chromatography,[18,19] and "digestive ripening," in which alkanethiol-coated Au NPs with a broad size distribution are refluxed in toluene.[20,21]

The controlled synthesis of Au NPs in the 1-10 nm range is desirable, since the most significant particle size effects appear in this range,[1,22-25] leading to unique optical, electronic, and chemical properties potentially useful in catalytic, sensing, electronic, and

medical applications.[26-30] Sub-10 nm Au NPs (hereafter referred to as "small" NPs) are often synthesized through homogeneous nucleation methods, such as the Brust method, in which chloroauric acid, $HAuCl_4$, is reduced by sodium borohydride in the presence of an alkanethiol in a nonpolar organic solvent. The thiols covalently bind to the NP as surface ligands through the sulfur head, and the hydrocarbon tails extend from the surface to sterically stabilize the suspended NPs.[1,23,30,31]

In addition to their hydrophobic form, small Au NPs can be synthesized in water, using amino acids,[32] thiol-containing molecules,[15,33-35] polymers,[26,29,36] phosphonium ligands,[37,38] polyphenols,[39] dendrimers,[24,40] and citrate[41,42] as surface ligands. A recent report indicated that monodisperse and stable NPs (d = 3.2-5.2 nm) were synthesized through the reduction of gold chloride using sodium borohydride.[43] Resulting sols were stable for approximately one year without requiring stabilizing agents. Several groups have demonstrated that such small colloidal Au NPs can be catalytically active,[44-47] while others have conducted catalytic studies using small Au NPs either modified with a second metal and/or deposited on a support.[1,48-53]

The seeded-growth approach has been used to prepare Au NPs in various solvents,[28,54] with a limited number of reports on aqueous-based synthesis of Au NPs in the 1-10 nm range. Jana *et al.* reported in 2001 that ~3.5 nm Au seeds formed by reducing $HAuCl_4$ with ascorbic acid in the presence of cetyltrimethylammonium bromide (CTAB) can grow into Au NPs in the 5-40 nm size range.[23] Tsunoyama *et al.* later reported the use of ~1.3 nm Au seeds stabilized by poly(N-vinyl-2-pyrrolidone) (PVP) to grow into NPs with diameters in the 2-10 nm range, by reducing $AuCl_4^-$ with Na_2SO_3 and adding excess PVP.[26] The synthesis took ~3 h and required freeze-pump-thaw cycles,

dialysis, and a N_2 atmosphere. These NPs were found to be catalytically active for the aerobic oxidation of benzylic alcohols. Henglein and co-workers alternatively used γ-radiation to reduce $KAu(CN)_2$ onto ~2 nm Au NPs to grow NPs in the 10 nm size range.[55,56] The irradiation step was conducted in a nitrous oxide atmosphere for 3 h, and ion-exchange was required post-synthesis to remove excess cyanide ions.

In this work, we report a new water-based synthesis method for small Au NPs with tunable particle sizes in a relatively broad range (d = 3 – 12 nm) using a seeded-growth approach. Gold hydroxide-chloride ions are reduced onto Au seeds, using carbon monoxide gas (CO) as the reducing agent. While not commonly used as a reducing agent in the preparation of NPs[57] (*e.g.*, Au,[58-61] Pd,[62] and Pt[63] NPs), CO is used to prepare submicron-sized Au-coated silica particles called Au nanoshells.[64-67] We find that our synthesis method can be carried out at room temperature and atmospheric pressure to generate Au sols that are colloidally stable for at least 1 month, even though no additional surface ligands are used. Ultraviolet-visible absorbance spectroscopy and small angle X-ray scattering of the sols and transmission electron microscopy of the dried NPs were used to determine particle diameters and size distributions, which were consistent with values predicted from magic cluster modeling. We propose a formation mechanism in which the Au seeds catalyze the oxidation of CO into CO_2 and, in the process, Au hydroxide-chloride ions reduce and deposit onto the seed surface as Au^0 atoms.

5.2 Experimental Methods.

5.2.1 Materials.

All chemicals were used as received unless otherwise noted. Tetrakis(hydroxymethyl)phosphonium chloride (THPC, 80% aqueous solution by

weight), gold (III) chloride trihydrate ($HAuCl_4 \bullet 3H_2O$, 99%), and anhydrous potassium carbonate (K_2CO_3, ACS reagent) were obtained from Sigma-Aldrich. Sodium hydroxide solution (NaOH, 1 M) was purchased from Fisher Scientific. Carbon monoxide gas (99%) was obtained from Specialty Chemical Products. Deionized water from a Barnstead NANOpure Diamond system (resistivity > 18 MΩ/cm) was used for all experiments.

5.2.2 Synthesis of Au Seeds.

The method used to synthesize the Au seeds has been reported elsewhere.[37,65] Briefly, a 1 wt% (~25 mM) chloroauric acid ($HAuCl_4$) solution was made by diluting 2.7 mL of a 127 mM solution (~5 g of $HAuCl_4 \cdot 3H_2O$ in 95 mL of H_2O) with 10.8 mL of H_2O. 1.2 mL of a 1M NaOH solution and 4 mL of a 1.2 mM THPC solution (0.4 mL of 80% THPC solution diluted in 33 mL of H_2O) were added to 180 mL of water with vigorous stirring. After 5 min, 6.75 mL of the 1 wt% $HAuCl_4$ solution was quickly added and the resulting liquid immediately turned brown indicating that NPs were formed. Stirring was continued for another 10 min after the noted color change. The entire synthesis was carried out at room temperature (23 °C). The resulting sol was kept at room temperature for three weeks prior to any use; it was subsequently kept in a refrigerator at 4 °C for storage. The concentration of NPs was calculated to be ~9.6×10^{17} NP/L = ~0.002 mM, assuming all the Au salt reduced to metal and modeling the 2.8 nm Au NPs as a ~3.0 nm "magic cluster" containing 561 Au atoms.[68]

5.2.3 Growth of Au Seeds.

A Au salt solution (pH ~ 7.5) was prepared by dissolving 50 mg of K_2CO_3 in 203 mL of a 0.38 mM $HAuCl_4$ solution (3 mL of 1 wt% $HAuCl_4$ diluted with 200 mL H_2O), and aging

for at least 24 h before use.[65] Ten samples with 0.05 mL of the seed sol and different volumes (0.30-3.0 mL) of the Au salt solution were prepared and diluted with water such that the total volume of each sample was 3.05 mL and the total Au^{3+} concentration increased by ~0.04 mM with increasing sample number. Deaerated water was not necessary for successful growth of Au seeds. The final Au NP concentration of each sample was estimated to be ~2.0×10^{16} NP/L or ~0.03 μM; the salt:seed molar ratios are listed in Table 1. Subsequently, CO was bubbled into each sample at an average flow rate of 3.3 mL/sec for 30 sec. The gas was bubbled into each sample for 30 sec again, 1 hr later, to ensure complete reduction of the Au salt. The samples were analyzed no earlier than 1 hr after the second CO bubbling step. Each sample was synthesized at least three times, to ensure reproducibility of synthesis and to assess any batch-to-batch variations. *Caution: CO is toxic and all experiments should be performed in a ventilated hood.*

Table 5.1. Molar ratio of Au salt ions to Au NP seeds prior to CO treatment.

Sample number	**Au salt concentration (mM)**	**Au salt/Au NP molar ratio**	**Total Au atom/Au NP molar ratio (n_{tot})[a]**
1	0.04	1415	1976
2	0.07	2829	3390
3	0.11	4243	4804
4	0.15	5658	6219
5	0.19	7072	7633
6	0.22	8486	9047
7	0.26	9901	10462
8	0.30	11315	11876
9	0.34	12729	13290
10	0.37	14144	14705

[a] Calculated total number of Au atoms per particle after CO treatment

5.2.4 Control Experiments.

To determine if particle growth could occur without the Au seeds, ten samples were prepared in the same manner as indicated earlier, but water (0.05 mL) was used instead of

the Au seed sol. To determine if particle growth could occur without the CO, ten additional control samples were prepared as indicated earlier, but CO bubbling steps were not carried out.

5.2.5 Characterization of Au Sols.

UV-Vis absorption spectra (UV-Vis) of the samples were collected from 400 to 900 nm using a Shimadzu UV-2401 PC spectrophotometer; polystyrene cuvettes (Sarstedt AG & Co.) with a path length of 1 cm were used. Transmission electron microscopy (TEM) images were collected using a JEOL 2010 transmission electron microscope operating at 100 kV. Au NPs were deposited onto 200-mesh carbon/formvar grids by evaporating ~8 µL of a sample at room temperature. The number-average size distributions of 400+ particles were determined for each sample using *ImageJ* Software. For small angle X-ray scattering (SAXS), sample sols were sealed in borosilicate glass capillaries (1 mm diameter and 10 µm wall thickness) and analyzed using a Riguku SmartLab X-ray Diffractometer (CuKα radiation, λ = 1.54 Å). All measurements were taken in transmission mode at maximum power (40 kV and 44 mA). Number-average particle sizes and distributions were determined by simulating the particle scattering profiles from 2θ values of 0.2 to 4.0 degrees using Nanosolver software (Rigaku). The pH of NP suspensions was measured at room temperature using a Phoenix Co. 5533501 pH electrode.

5.3 Results and Discussion.

5.3.1 Size Analysis of Au Sols.

UV-Vis spectroscopy can provide size information about the Au NPs while they are in suspension. The UV-Vis spectra for each sample showed a systematic increase in

absorbance, correlated to the amount of Au salt available for chemical reduction (Fig. 5.1). Three separate batches were prepared and analyzed for each sample. The nearly overlapping absorbance spectra for each sample indicated the seeded-growth procedure was robust and repeatable. The sols produced did not require additional stabilizing agents and were stable for at least one month.

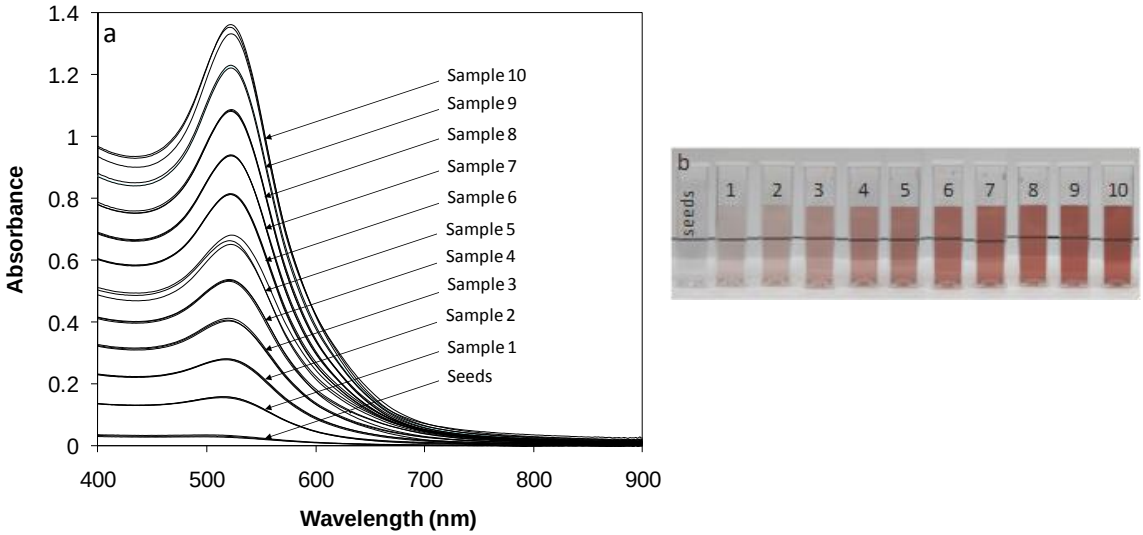

Figure 5.1. (a) UV-Vis absorbance spectra and (b) corresponding photograph of Au sol samples after CO treatment. Each sample was prepared three times and an absorbance spectra of each batch was collected.

By accounting for the particle size effect on the conduction electron mean free path in gold, one can accurately determine average Au NP size using surface plasmon resonance (SPR) peak position and absorbance. For Au NPs with diameters in the 35-110 nm range, Haiss *et al.* developed the following correlation (with an error of 3%) between experimental absorbance results for citrate-stabilized Au NPs and Mie scattering theory:

$$D = \ln[(\lambda_{SPR}-512)/6.53]/0.0216 \qquad (5.1)$$

where D is the mean NP diameter from TEM measurements and λ_{SPR} is the SPR peak position (ranging from 525 to 585 nm).[69] More appropriate for our study was the

following size correlation (with an error of 11%) based on the relative absorbance for Au NPs in the 5-80 nm size range:

$$D = \exp([B_1 \times (A_{spr}/A_{450})] - B_2) \qquad (5.2)$$

where A_{SPR} is the absorbance of the SPR peak, A_{450} is the absorbance at 450 nm, and B_1 (= 3.00) and B_2 (= 2.20) are fitted parameters using experimental data.[69]

Application of Eqn. 5.2 provided mean NP diameters that ranged from 2.5 nm for the seed particles to 8.6 nm for the Au NPs of Sample 10 (Table 5.2). Standard error propagation analysis based on the triplicate syntheses of each sample indicated high reproducibility, with the maximum error, or relative standard deviation, found to be 7% (one standard deviation divided by mean diameter = relative standard deviation = RSD). The diameters of the seed particles and NPs of Samples 1 and 2 were outside the operational range of Eqn. 5.2, and so these extrapolated UV-Vis-derived sizes, while precise, may not be accurate.

Table 5.2. Sample particle diameters (nm) determined through different methods.

Sample #	UV-Vis[a]	Predicted[c]	TEM Mean[d]	TEM Mode	SAXS Mean[d]	SAXS Mode
Seed particles	2.4 (4.0%)[b]	3.0	3.0 ± 0.9	2.8	3.6 ± 1.3[e]	3.1
1	4.0 (5.0%)[b]	4.5	–	–	5.7 ± 2.0	4.9
2	4.7 (2.0%)[b]	5.4	–	–	6.1 ± 2.2	5.3
3	5.3 (3.0%)	6.1	–	–	6.8 ± 2.5	5.8
4	5.9 (1.0%)	6.6	–	–	7.2 ± 2.6	6.2
5	6.7 (7.0%)	7.1	7.3 ± 1.6	7.1	7.7 ± 2.8[e]	6.7
6	7.0 (1.0%)	7.5	–	–	8.5 ± 3.1	7.3
7	7.4 (1.0%)	7.9	–	–	8.6 ± 3.2	7.5
8	7.9 (1.0%)	8.2	–	–	9.2 ± 3.4	7.9
9	8.3 (1.0%)	8.6	–	–	9.4 ± 3.4	8.1
10	8.6 (1.0%)	8.9	11.9 ± 4.6	10.1	9.7 ± 3.6[e]	8.3

[a] Sizes calculated from absorbance spectra using Eqn. 5.2. RSDs (%) represent experimental error between three separate syntheses.
[b] Values outside the size range for Eqn. 5.2.
[c] Sizes predicted using a power fit to the magic cluster model, Eqn. 5.4.
[d] Size distributions represent one standard deviation.
[e] Particle sizes and distributions averaged for three separate syntheses.

These absorbance-derived size values were compared with particle sizes predicted using the magic cluster model. With this model,[25,70,71] a Au NP is approximated as a single Au atom surrounded by closed shells of Au atoms,[68] such that the total number of atoms, n_{tot}, is exactly known for a magic cluster of n_s number of closed shells: $n_{tot} = (10n_s^3+15n_s^2+11n_s+3)/3$.[68] With a Au atom diameter of 0.27 nm, an analytical relationship between magic cluster diameter D_{mc} and $n_{tot,}$ can be derived (Eqn. 5.3), which simplifies to a power-law equation showing a 1/3 dependence of diameter on

number of atoms (Eqn. 5.4):

$$D_{mc} = 0.27\times(1+2n_s), \text{ where } n_s = (0.265\times f - 4.41)/(f - 0.5) \text{ and}$$

$$f = [8{,}100\times n_{tot}+30\times(5{,}145+72{,}900\times n_{tot}^{2})^{1/2}]^{1/3} \quad (5.3)$$

$$D_{mc} \approx 0.359\times n_{tot}^{0.334} \quad (5.4)$$

Interestingly, Eqn. 5.4 correlates well with the expected relationship between particle diameter and total number of atoms for a fcc-packed metal atom. Assuming that all of the Au salt precursor for a given sample completely reduces and deposits onto the Au seeds after CO treatment, the Au salt/Au NP molar ratio (Table 5.1) represents the *additional* atoms added to one seed particle and the Au atom/Au NP molar ratio is the *total* atoms per particle after growth is complete. As shown in Table 5.2, the absorbance-derived diameters of sample sols were in good agreement with the diameters predicted by Eqn. 5.3 in which each seed particle is assumed to consist of 561 Au atoms (D_{mc} = 2.97 nm).

Having determined the size of the different Au NPs from their absorbance spectra, we estimated the NP concentration in NP/mL, N, in our samples using another fit developed by Haiss *et al.*,

$$N = (A_{450} \times 10^{14}) / (d^2 \times [-0.295 + 1.36\exp(-((d-96.8)/78.2)^2)] \quad (5.5)$$

where d is the NP diameter (nm).[69] Application of Eqn. 5.5 gave NP concentrations that ranged from 2.6×10^{13} (for Au seeds) to 1.5×10^{13} (for sample 10) NP/mL, with the apparent concentration differences being within error (Table 5.3). These results are also within error of the estimated concentration of Au seeds (~2.0×10^{16} NP/L) assuming complete reduction of gold chloride to form monodisperse ~3.0 nm Au seeds.

Table 5.3. Sample particle concentrations estimated from NP diameter and absorbance.[a]

Sample	NP Concentration ($\times 10^{16}$ NP/L)
Seed particles	2.6 ± 0.7
1	2.2 ± 0.3
2	2.3 ± 0.4
3	2.2 ± 0.7
4	2.0 ± 0.5
5	1.7 ± 2.3
6	1.7 ± 0.3
7	1.7 ± 0.3
8	1.6 ± 0.7
9	1.5 ± 0.7
10	1.5 ± 2.8

[a] Absorbance measured at 450 nm.

TEM was performed on selected samples to quantify the Au particles in the dried state (Fig. 5.2). The seed particles had a mean diameter of 3.0 nm and a mode diameter (*i.e.*, the most frequent diameter exhibited by the particles) of 2.4 nm. The seeds were unimodal in size but were broadly distributed, with a RSD of 30%, which is close to previously reported values.[37] Samples 5 and 10 showed systematic growth in diameter size, after CO treatment (Table 5.2). The RSD's (22% and 39%, respectively) were variable and moderately large, which could be due to the broad size distribution of seed NPs or drying effects and electron beam damage during TEM analysis.[72] The mean diameters were at least 17% larger than the mode diameters for these 3 suspensions, indicating a positive skew to the size distributions for all samples.

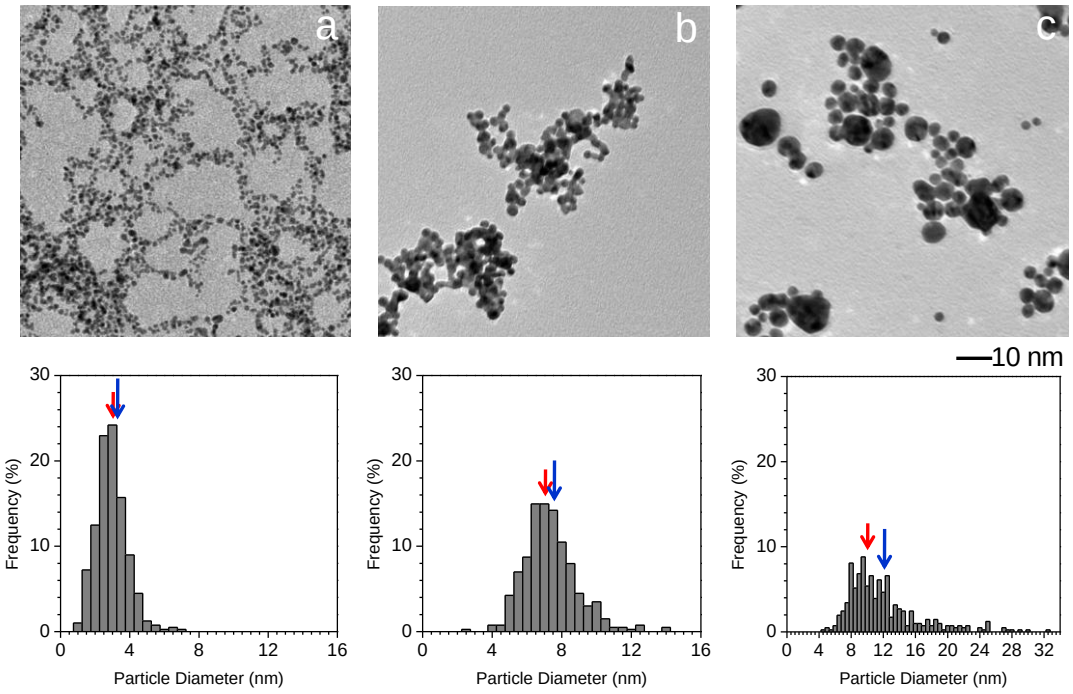

Figure 5.2. TEM images and size distributions of (a) the Au seed particles, and (b,c) the resulting Au NPs of Samples 5 and 10 after CO treatment. Short red and long blue arrows represent the mode and mean NP diameters, respectively. Au salt/Au NP molar ratio was 7,072 for Sample 5 and 14,144 for Sample 10. At least 400 particles of each sample were measured.

Small-angle X-ray scattering (SAXS) was used to determine the diameter and size distribution of the NPs dispersed in water (Fig. 5.3). A small aliquot of our samples was sealed in a glass capillary tube and irradiated with X-rays. With the particles having a higher electron density than water, the collected scattered X-ray spectra contain information about the number-average size and shape of the NPs, which can be extracted by comparison with simulated scattering spectra of model NP suspensions.[73,74] Reliability factor (R factor) values between 1 and 10% indicate an acceptable match with lower values (<10%) being preferred. For all of our samples, the R factors were ~3-4% between the experimental and simulated scattering data (Fig. 5.3).

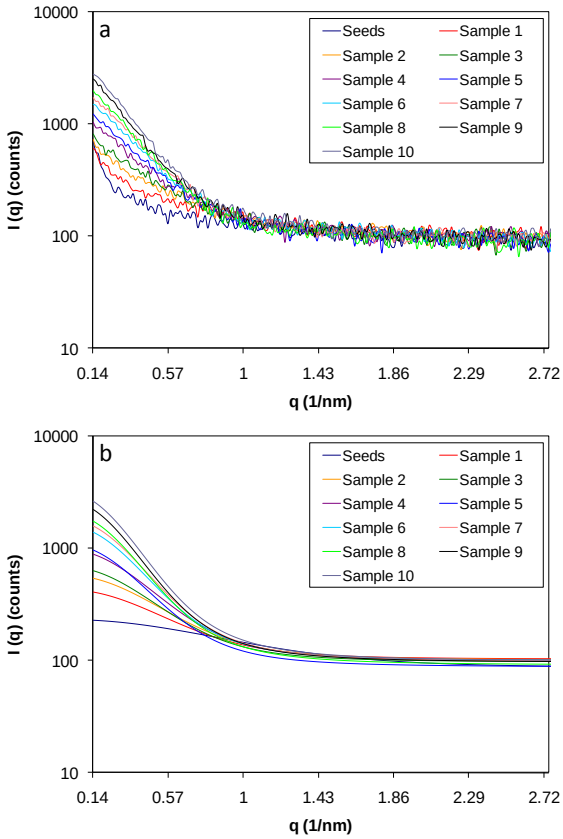

Figure 5.3. (a) Experimental and (b) simulated SAXS scattering profiles of seed NPs and selected samples.

The diameters of our NPs and their associated size distributions determined from SAXS analysis are provided in Table 5.2. For all of the sample sols, the RSDs were ~37% which was in good agreement with the reported RSD of the seed sol (~38%).[37] The mean diameters were ~14% larger than the mode diameters for all samples, agreeing with the positive skew of the size distributions determined via TEM.

Figure 5.4 shows the comparison of the diameters determined from UV-Vis, SAXS, and TEM analyses with predicted values in relation to the total number of Au atoms per particle (n_{tot}). Overall, SAXS mode diameters matched predicted diameters the best, followed by the UV-Vis mean diameters and then TEM mode diameters. Because of the presence of larger particles giving the positive skew to the distribution, the SAXS-

derived and TEM-derived mean diameters deviated the most from the other values. Nonetheless, these size measurements indicated the seeded growth of Au NPs was accomplished reproducibly in the size range of 4-12 nm, with a resolution of ~0.5 nm.

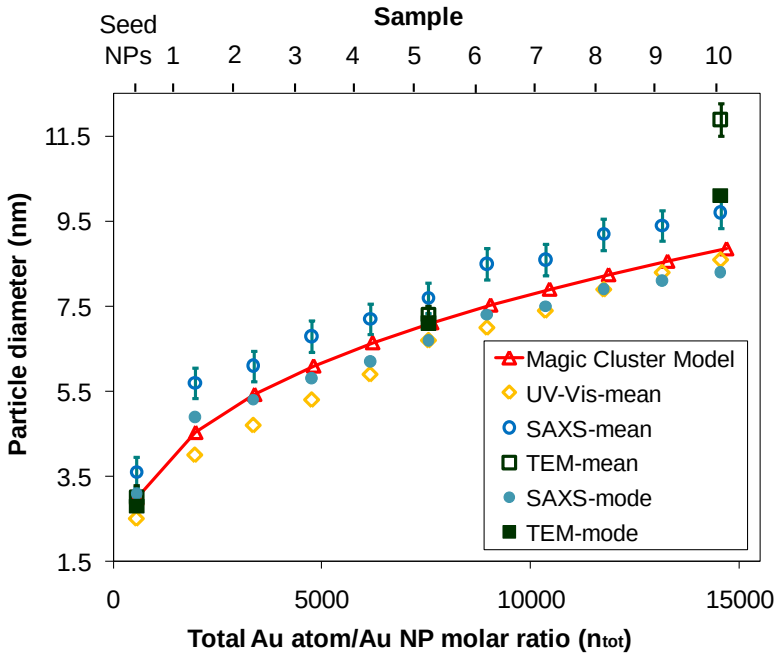

Figure 5.4. Calculated and measured diameters of sample Au NPs. Error bars for SAXS and TEM measurements represent RSD values. Error bars for UV-Vis measurements are not visible.

5.3.2 Chemistry of Au^{3+} Reduction Using CO.

The speciation of the Au in the Au salt precursor solution is more complicated than what is typically assumed in Au nanomaterial synthesis chemistry.[23,65,75,76] Specifically, the $AuCl_4^-$ ionic species can form gold hydroxide-chloride species depending on solution pH.[77,78] Visually, the $HAuCl_4/K_2CO_3$ solution (pH~7.5) appears colorless after 24 h as compared to the pure $HAuCl_4$ solution aged for the same time (Fig. F1).[79,80] $AuCl_4^-$ absorbs in the UV-violet range in a ligand-to-metal charge transfer process, and substitution of the chloride ligands by hydroxide groups decreases this absorption.[81]

The high pH resulting from the potassium carbonate induces $AuCl_4^-$ hydrolysis, as established through Raman,[82] extended X-ray absorbance fine structure[83] and UV-Vis spectroscopies,[79,81] and ion chromatography studies[84]:

$$AuCl_4^- + OH^- \leftrightarrow AuCl_3(OH)^- + Cl^- \quad (\log K = 7.9) \quad (5.6)^{77}$$

$$AuCl_3(OH)^- + OH^- \leftrightarrow AuCl_2(OH)_2^- + Cl^- \quad (\log K = 6.9) \quad (5.7)^{77}$$

$$AuCl_2(OH)_2^- + OH^- \leftrightarrow AuCl(OH)_3^- + Cl^- \quad (\log K = 6.0) \quad (5.8)^{77}$$

$$AuCl(OH)_3^- + OH^- \leftrightarrow Au(OH)_4^- + Cl^- \quad (\log K = 5.7) \quad (5.9)^{77}$$

The different hydrolyzed forms of $AuCl_4^-$ are collectively referred to here as gold hydroxide-chloride, $[AuCl_{4-x}(OH)_x]^-$. At pH 7.5, ~90% of these Au salt species are present as $AuCl_2(OH)_2^-$ (x = 2) and $AuCl(OH)_3^-$ (x = 3) in roughly equal amounts, such that x = 2.5 on average. The remaining ~10% are in the form of $AuCl_3OH^-$ (x = 1) and $Au(OH)_4$ (x = 4) species.[79,85]

The reduction of gold hydroxide-chloride species by CO can be written as

$$2[AuCl_{4-x}(OH)_x]^- + 3CO + 3H_2O \rightarrow 2Au^0 + 3CO_2 + 6H^+ + 2xOH^- + 2(4-x)Cl^- \quad (5.10)$$

The reaction is thermodynamically favored, according to its standard reduction potential of E° = 0.64 V calculated using the following half-reactions [77]:

$$[AuCl_{4-x}(OH)_x]^- + 3e^- \rightarrow Au^0 + (4-x)Cl^- + xOH^- \quad (E° = 0.53\ V)^{84} \quad (5.11)$$

$$CO_2 + 2H^+ + 2e^- \rightarrow CO + H_2O \quad (E° = -0.106\ V)^{86} \quad (5.12)$$

A control study in which CO was introduced into the gold salt solution without seed particles indicated that the reduction reaction can occur without the seeds to produce Au NPs (Fig. F2-F4). In contrast, though, these particles had larger average sizes and wider size distributions than the corresponding NP samples prepared using seed particles (Table F1). For example, Sample 5 (with Au seeds) had a mean diameter of 7.3±1.6 nm

(Table 5.2) and the absence of seeds led to Au NPs with a mean diameter of 23.9±6.1 nm (Table F1). Sample #10 (with Au seeds) had a mean diameter of 11.9±4.6 nm (Table 5.2) and the absence of seeds led to Au NPs with a mean diameter of 19.4±5.6 nm (Table F1).

This observation of homogeneous nucleation and growth of Au NPs indicated that formation of new particles could have occurred during our seeded growth experiments. Our rough calculations of Au NP concentrations did not support this possibility though (Table 5.3). One argument for this is that the activation energy for Au metal deposition onto a pre-existing Au surface is smaller than that for the creation of a Au surface, *i.e.*, heterogeneous nucleation is energetically favored over homogeneous nucleation.[68,87] In other words, the growth rate dominates over the nucleation rate. Another argument follows the Watzky and Finke work on iridium NP formation.[8] They proposed that Ir seed NPs autocatalyze the reduction of Ir salt species, thereby causing the growth rate to be faster than the nucleation rate. The seeded-growth of Au NPs may involve the autocatalytic reduction of Au salt also.

Seeded Growth Mechanism: The seeded-growth of gold NPs using CO is proposed to proceed through a series of surface reactions that involve the gold-catalyzed oxidation of CO to CO_2 in water (Fig. 5.5). CO_2 was detected through gas chromatography after the seeded-growth synthesis was carried out (Appendix 6).

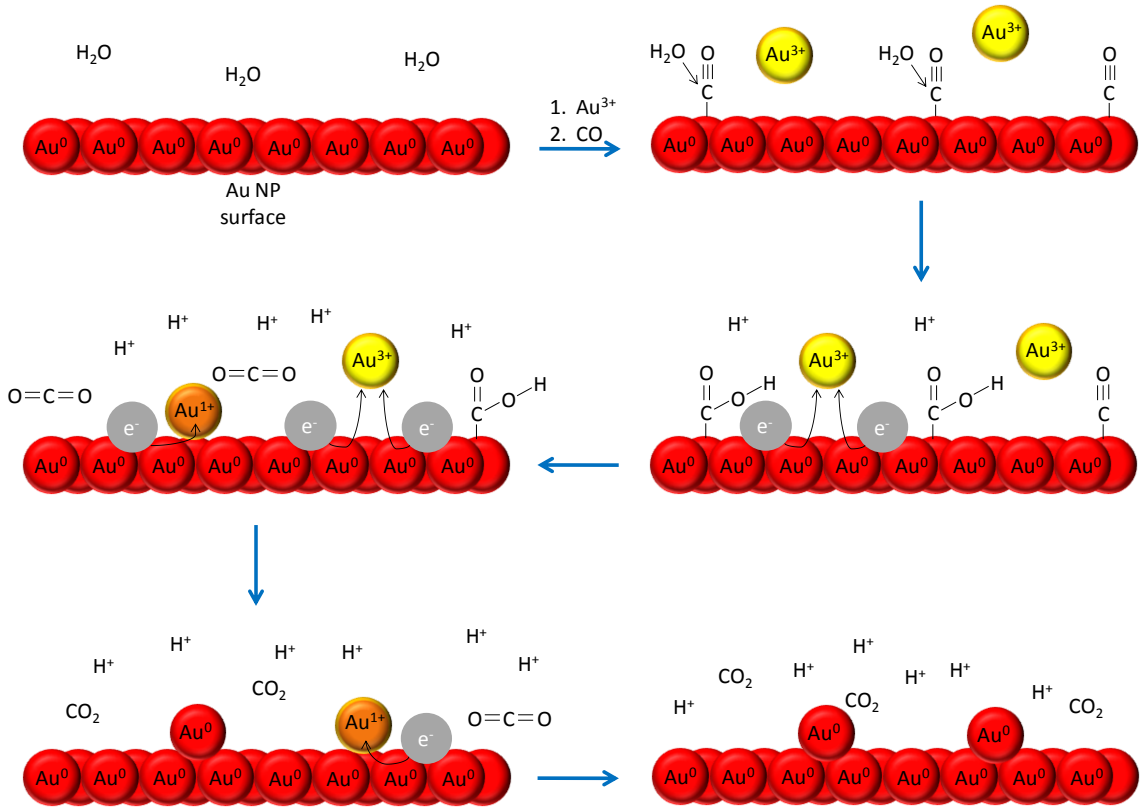

Figure 5.5. Reaction schematic for the seeded growth of Au NPs by reducing gold hydroxide-chloride species with CO. Reduced gold atoms are represented as Au^0 while $[AuCl_{4-x}(OH)_x]^-$ and intermediate gold (I) species are shown as Au^{3+} and Au^{1+}, respectively without the ligands.

The mechanism of CO oxidation in water on a Au electrode and supported Au NPs has been debated.[88-91] It is hypothesized that either a water molecule and/or its hydroxyl form can react with adsorbed CO.[88,90] Given the dearth of experimental evidence for water oxidation on gold electrodes to form hydroxyl surface species, we follow the mechanism proposed by Weaver and coworkers in which a water molecule is involved in CO oxidation.[91] A H_2O molecule reacts with a CO species weakly adsorbed[92,93] on the Au seed surface to form a carboxyhydroxyl species, free proton, and an electron which is donated to the Au NP. Au NPs can temporarily store and release electron charge.[94,95]

To balance the reaction stoichiometry for the CO reduction of Au salt (Eqn. 5.10), three CO molecules are needed to adsorb to the surface of a NP. Reaction of two CO with two free water molecules creates two carboxyhydroxyl species, two protons, and two electrons.[88,90] The two free electrons migrate to the NP and then to one physisorbed $[AuCl_{4-x}(OH)_x]^-$ species to form a Au^{1+} intermediate. While Au^{2+} could be formed, it is a rare[96] and unstable[97,98] gold oxidation state, and therefore quickly reduces further to form the more stable Au^{1+}. One of the carboxyhydroxyl species dissociates to give CO_2, a proton, and an electron. This single electron transfers to the adsorbed Au^{1+} intermediate to complete the reduction to Au^0.[97] The formation of CO_2 from the other carboxyhydroxyl species releases another electron. The third CO reacts with one H_2O molecule to generate a proton, an electron, and a carboxyhydroxyl that, in turn, generates CO_2, another proton, and another electron. The three electrons allow for the reduction of a second $[AuCl_{4-x}(OH)_x]^-$ species. The gold atoms reduced are added to seed NPs so that reduction of $[AuCl_{4-x}(OH)_x]^-$ controllably increases the size of the seed NPs.

This proposed mechanism is not meant to indicate a particular sequence of reaction events, but rather, to show the minimum number of surface reaction steps needed to reduce two Au^{3+} species (*i.e.*, $[AuCl_{4-x}(OH)_x]^-$) stoichiometrically with three CO and three H_2O molecules. The mechanism assumes that CO oxidizes into CO_2 via the formation and subsequent decomposition of carboxyhydroxyl surface species. The Au NPs can thus be thought to catalyze the Au^{3+} reduction by acting as a conduit for electron flow from CO (as it converts into CO_2) to the Au salt during the NP growth process. A control experiment in which no CO was introduced to a seed NP/Au salt solution

confirmed that Au salt reduction was not possible in the absence of CO (Fig. F5-F8; Table F2).

The seeded growth process is expected to be accompanied by a pH change, depending on the extent of chloride substitution by hydroxyl ligands in the Au salt (Eqn. 5.10). If $x < 3$, the pH would decrease because more protons are generated than hydroxyl anions. The pH for all ten samples prior to Au salt reduction was less than 7.5, and so it was expected that $x < 2.5$ for the Au salt in all samples and therefore the pH would lower after Au reduction. Indeed, the pH of sample sols was observed to decrease after contact with CO (Table F3). As a note, CO_2 formed during Au salt reduction suspension could also lower the suspension pH due to formation of carbonic acid (and bicarbonate and carbonate species) in water:

$$CO_2(aq) + H_2O \leftrightarrow H_2CO_3 \qquad (pK = 2.89) \qquad (5.13)$$

$$H_2CO_3 + H_2O \leftrightarrow HCO_3^- + H_3O^+ \qquad (pK_a = 3.8) \qquad (5.14)$$

$$HCO_3^- + H_2O \leftrightarrow CO_3^{2-} + H_3O^+ \qquad (pK_a = 10.3) \qquad (5.15)$$

Due to the low pK of Eqn. 5.13 and the small amount of CO_2 formed, an even smaller amount would be present as carbonic acid; CO_2 would not be expected to be a major contributor to lowering the pH after seeded growth.

5.4 Conclusions.

Stable water suspensions of gold NPs with controlled particle sizes were successfully synthesized in the 3 to 12 nm range by using 2.8 nm Au NPs as seeds and by controlling the reduction chemistry of gold(III) hydroxide-chloride species using CO as the reductant. Compared to TEM and UV-Vis measurements, SAXS provided particle sizes closest to predicted values. A detailed reaction mechanism for the growth process was

presented, in which the high-pH hydrolysis of chloroauric acid and stoichiometry among the reactants were considered. Compared to other reducing agents used to generate metallic NPs, CO can be used at room temperature and its oxidized form does not interfere with the colloidal stability of the NPs. This seeded method of growing NPs should be extendable to other monometallic and multimetallic compositions and shapes, and can be improved by using seed particles with a narrower size distribution.

5.5 Acknowledgements.

This chapter is reprinted with permission from *The Journal of Physical Chemistry C*, Vol. 114, Pretzer, L.A.; *et al.*; "Controlled Growth of Sub-10 nm Gold Nanoparticles Using Carbon Monoxide Reductant." Pgs. 21226-21233, copyright (2010), American Chemical Society. I thank my co-authors Mr. Q. Nguyen and Dr. M. S. Wong. We gratefully acknowledge the National Science Foundation (CBEN, EEC-0118007; IGERT, DGE-0504425) and the Welch Foundation (C-1676) for financial support. We thank Mr. A. Orbaek, Mr. A. Prakash, and Mr. R. Crouse for collection and analysis of SAXS data, and Dr. W. Guo, Mr. G. C. Kini, and Dr. H. G. Bagaria for collection of TEM images.

5.6 Supporting Information Available in Appendix F.

Method for detecting CO_2 after seeded growth experiment, overview of SAXS data analysis, Table F1 (Particle diameters for controls with no seed), Table F2 (Particle diameters for controls with no CO), Table F3 (pH of sample sols before and after CO bubbling), Figure F1 (UV-Vis spectra of the 0.375mM $HAuCl_4$ solution with no K_2CO_3 and the Au salt solution ~24h after preparation), Figure F2 (UV-Vis spectra of controls with Au salt solution bubbled with CO and no seed NPs), Figure F3 (TEM images and size distributions of controls with Au salt solution bubbled with CO and no seed NPs),

Figure F4 (SAXS spectra of controls with Au salt solution bubbled with CO and no seed NPs), Figure F5 (UV-Vis spectra of controls with Au salt solution and seed NPs but no CO), Figure F6 (TEM images and size distributions of controls with Au salt solution and seed NPs but no CO), and Figure F7 (SAXS spectra of controls with Au salt solution and seed NPs but no CO). This information is available free of charge via the Internet at http://pubs.acs.org.

5.7 References.

(1) Daniel, M.-C.; Astruc, D. *Chem. Rev.* **2004**, *104*, 293.

(2) Toshima, N.; Yonezawa, T. *New J. Chem.* **1998**, *22*, 1179.

(3) Yu, Y. Y.; Chang, S. S.; Lee, C. L.; Wang, C. R. C. *J. Phys. Chem. B* **1997**, *101*, 6661.

(4) Ashkarran, A. A.; Zad, A. I.; Mahdavi, S. M.; Ahadian, M. M.; Nezhad, M. R. H. *Appl. Phys. A* **2009**, *96*, 423.

(5) Neddersen, J.; Chumanov, G.; Cotton, T. M. *Appl. Spectrosc.* **1993**, *47*, 1959.

(6) Schmid, G. *Chem. Rev.* **1992**, *92*, 1709.

(7) Skrabalak, S. E.; Xia, Y. A. *ACS Nano* **2009**, *3*, 10.

(8) Watzky, M. A.; Finke, R. G. *J. Am. Chem. Soc.* **1997**, *1198*, 10382.

(9) Yu, H.; Gibbons, P. C.; Kelton, K. F.; Buhro, W. E. *J. Am. Chem. Soc.* **2001**, *123*, 9198.

(10) Park, J.; Joo, J.; Kwon, S. G.; Jang, Y.; Hyeon, T. *Angew. Chem. Int. Ed.* **2007**, *46*, 4630.

(11) Wilcoxon, J. P.; Provencio, P. P. *J. Am. Chem. Soc.* **2004**, *126*, 6402.

(12) Lee, J. S.; Stoeva, S. I.; Mirkin, C. A. *J. Am. Chem. Soc.* **2006**, *128*, 8899.

(13) Svedberg, T.; Nichols, J. B. *J. Am. Chem. Soc.* **1923**, *45*, 2910.

(14) Peterson, R. R.; Cliffel, D. E. *Anal. Chem.* **2005**, *77*, 4348.

(15) Schaaff, T. G.; Knight, G.; Shafigullin, M. N.; Borkman, R. F.; Whetten, R. L. *J. Phys. Chem. B* **1998**, *102*, 10643.

(16) Schaaff, T. G.; Whetten, R. L. *J. Phys. Chem. B* **1999**, *103*, 9394.

(17) Wilcoxon, J. P.; Provencio, P. *J. Phys. Chem. B* **2003**, *107*, 12949.

(18) Jimenez, V. L.; Georganopoulou, D. G.; White, R. J.; Harper, A. S.; Mills, A. J.; Lee, D. I.; Murray, R. W. *Langmuir* **2004**, *20*, 6864.

(19) Tsunoyama, H.; Negishi, Y.; Tsukuda, T. *J. Am. Chem. Soc.* **2006**, *128*, 6036.

(20) Stoeva, S.; Klabunde, K. J.; Sorensen, C. M.; Dragieva, I. *J. Am. Chem. Soc.* **2002**, *124*, 2305.

(21) Prasad, B. L. V.; Stoeva, S. I.; Sorensen, C. M.; Klabunde, K. J. *Langmuir* **2002**, *18*, 7515.

(22) Miller, J. T.; Kropf, A. J.; Zha, Y.; Regalbuto, J. R.; Delannoy, L.; Louis, C.; Bus, E.; van Bokhoven, J. A. *J. Catal.* **2006**, *240*, 222.

(23) Jana, N. R.; Gearheart, L.; Murphy, C. J. *Langmuir* **2001**, *17*, 6782.

(24) Kim, Y. G.; Oh, S. K.; Crooks, R. M. *Chem. Mater.* **2004**, *16*, 167.

(25) Moshfegh, A. Z. *J. Phys. D: Appl. Phys.* **2009**, *42*.

(26) Tsunoyama, H.; Sakurai, H.; Negishi, Y.; Tsukuda, T. *J. Am. Chem. Soc.* **2005**, *127*, 9374.

(27) Zhao, W. A.; Gonzaga, F.; Li, Y. F.; Brook, M. A. *Adv. Mater.* **2007**, *19*, 1766.

(28) Yang, Y.; Yan, Y.; Wang, W.; Li, J. R. *Nanotechnology* **2008**, *19*.

(29) Hussain, I.; Graham, S.; Wang, Z. X.; Tan, B.; Sherrington, D. C.; Rannard, S. P.; Cooper, A. I.; Brust, M. *J. Am. Chem. Soc.* **2005**, *127*, 16398.

(30) Warner, M. G.; Reed, S. M.; Hutchison, J. E. *Chem. Mater.* **2000**, *12*, 3316.

(31) Brust, M.; Walker, M.; Bethell, D.; Schiffrin, D. J.; Whyman, R. *Chem. Commun.* **1994**, 801.

(32) Selvakannan, P. R.; Mandal, S.; Phadtare, S.; Pasricha, R.; Sastry, M. *Langmuir* **2003**, *19*, 3545.

(33) Templeton, A. C.; Chen, S. W.; Gross, S. M.; Murray, R. W. *Langmuir* **1999**, *15*, 66.

(34) Manea, F.; Bindoli, C.; Polizzi, S.; Lay, L.; Scrimin, P. *Langmuir* **2008**, *24*, 4120.

(35) Yonezawa, T.; Sutoh, M.; Kunitake, T. *Chem. Lett.* **1997**, 619.

(36) Teranishi, T.; Kiyokawa, I.; Miyake, M. *Adv. Mater.* **1998**, *10*, 596.

(37) Duff, D. G.; Baiker, A.; Edwards, P. P. *Langmuir* **1993**, *9*, 2301.

(38) Huang, C. C.; Liao, H. Y.; Shiang, Y. C.; Lin, Z. H.; Yang, Z.; Chang, H. T. *J. Mater. Chem.* **2009**, *19*, 755.

(39) Slot, J. W.; Geuze, H. J. *Eur. J. Cell Biol.* **1985**, *38*, 87.

(40) Esumi, K.; Goino, M. *Langmuir* **1998**, *14*, 4466.

(41) Grabar, K. C.; Allison, K. J.; Baker, B. E.; Bright, R. M.; Brown, K. R.; Freeman, R. G.; Fox, A. P.; Keating, C. D.; Musick, M. D.; Natan, M. J. *Langmuir* **1996**, *12*, 2353.

(42) Kimling, J.; Maier, M.; Okenve, B.; Kotaidis, V.; Ballot, H.; Plech, A. *J. Phys. Chem. B* **2006**, *110*, 15700.

(43) Martin, M. N.; Basham, J. I.; Chando, P.; Eah, S.-K. *Langmuir* **2010**, *26*, 7410.

(44) Esumi, K.; Houdatsu, H.; Yoshimura, T. *Langmuir* **2004**, *20*, 2536.

(45) Tsunoyama, H.; Ichikuni, N.; Sakurai, H.; Tsukuda, T. *J. Am. Chem. Soc.* **2009**, *131*, 7086.

(46) Zhu, Y.; Qian, H. F.; Drake, B. A.; Jin, R. C. *Angew. Chem. Int. Ed.* **2010**, *49*, 1295.

(47) Comotti, M.; Della Pina, C.; Matarrese, R.; Rossi, M. *Angew. Chem. Int. Ed.* **2004**, *43*, 5812.

(48) Yen, C. W.; Lin, M. L.; Wang, A. Q.; Chen, S. A.; Chen, J. M.; Mou, C. Y. *J. Phys. Chem. C* **2009**, *113*, 17831.

(49) Turner, M.; Golovko, V. B.; Vaughan, O. P. H.; Abdulkin, P.; Berenguer-Murcia, A.; Tikhov, M. S.; Johnson, B. F. G.; Lambert, R. M. *Nature* **2008**, *454*, 981.

(50) Della Pina, C.; Falletta, E.; Prati, L.; Rossi, M. *Chem. Soc. Rev.* **2008**, *37*, 2077.

(51) Hou, W. B.; Dehm, N. A.; Scott, R. W. J. *J. Catal.* **2008**, *253*, 22.

(52) Scott, R. W. J.; Wilson, O. M.; Oh, S. K.; Kenik, E. A.; Crooks, R. M. *J. Am. Chem. Soc.* **2004**, *126*, 15583.

(53) Long, C. G.; Gilbertson, J. D.; Vijayaraghavan, G.; Stevenson, K. J.; Pursell, C. J.; Chandler, B. D. *J. Am. Chem. Soc.* **2008**, *130*, 10103.

(54) Pastoriza-Santos, I.; Liz-Marzan, L. M. *Adv. Func. Mater.* **2009**, *19*, 679.

(55) Henglein, A. *Langmuir* **1999**, *15*, 6738.

(56) Hodak, J. H.; Henglein, A.; Hartland, G. V. *J. Chem. Phys.* **2000**, *112*, 5942.

(57) Kang, Y.; Ye, X.; Murray, C. *Angew. Chem. Int. Ed.* **2010**, *49*, 6156.

(58) Milligan, W. O.; Morriss, R. H. *J. Am. Chem. Soc.* **1964**, *86*, 3461.

(59) Kopple, K.; Meyerstein, D.; Meisel, D. *J. Phys. Chem.* **1980**, *84*, 870.

(60) Weiser, H. B. Reduction With Gaseous Reducing Agents. In *Inorganic Colloid Chemistry*; J. Wiley & Sons, Inc.: New York, 1933; pp 41.

(61) Guo, S.; Shi, F.; Gu, Y. L.; Yang, J.; Deng, Y. Q. *Chem. Lett.* **2005**, *34*, 830.

(62) Grigg, R.; Zhang, L. X.; Collard, S.; Ellis, P.; Keep, A. *J. Organomet. Chem.* **2004**, *689*, 170.

(63) Mucalo, M. R.; Cooney, R. P. *Chem. Commun.* **1989**, *2*, 94.

(64) Bardhan, R.; Mukherjee, S.; Mirin, N. A.; Levit, S. D.; Nordlander, P.; Halas, N. J. *J. Phys. Chem. C* **2009**, *114*, 7378.

(65) Brinson, B. E.; Lassiter, B. J.; Levin, C. S.; Bardhan, R.; Mirin, N.; Halas, N. J. *Langmuir* **2008**, *24*, 14166.

(66) Knight, M. W.; Wu, Y. P.; Lassiter, J. B.; Nordlander, P.; Halas, N. J. *Nano Lett.* **2009**, *9*, 2188.

(67) Knight, M. W.; Fan, J.; Capasso, F.; Halas, N. J. *Opt. Express*, *18*, 2579.

(68) Nutt, M. O.; Heck, K. N.; Alvarez, P.; Wong, M. S. *Appl. Catal., B* **2006**, *69*, 115.

(69) Haiss, W.; Thanh, N. T. K.; Aveyard, J.; Fernig, D. G. *Anal. Chem.* **2007**, *79*, 4215.

(70) Aiken, J. D.; Finke, R. G. *J. Mol. Catal., A* **1999**, *145*, 1.

(71) Watzky, M. A.; Finke, R. G. *Chem. Mater.* **1997**, *9*, 3083.

(72) D'Souza, L.; Suchopar, A.; Richards, R. M. *J. Colloid Interface Sci.* **2004**, *279*, 458.

(73) Prakash, A.; Zhu, H. G.; Jones, C. J.; Benoit, D. N.; Ellsworth, A. Z.; Bryant, E. L.; Colvin, V. L. *ACS Nano* **2009**, *3*, 2139.

(74) Sasaki, A. *The Rigaku Journal* **2005**, *22*, 31.

(75) Brown, K. R.; Walter, D. G.; Natan, M. J. *Chem. Mater.* **2000**, *12*, 306.

(76) Lee, J. H.; Kamada, K.; Enomoto, N.; Hojo, J. *J. Colloid Interface Sci.* **2007**, *316*, 887.

(77) Baes, C. F. J.; Mesmer, R. E. Hydroxide-Chloride Complexes. In *Hydrolysis of Cations*; Krieger Publishing Company: Malabar, 1986; pp 284.

(78) Harada, A.; Yuzawa, A.; Kato, T.; Kojima, C.; Kono, K. *J. Polym. Sci. Part A: Polym. Chem.* **2010**, *48*, 1391.

(79) Usher, A.; McPhail, D. C.; Brugger, J. *Geochim. Cosmochim. Acta* **2009**, *73*, 3359.

(80) Zhang, H.; Xu, J.-J.; Chen, H.-Y. *J. Phys. Chem. C* **2008**, *112*, 13886.

(81) Peck, J. A.; Tait, C. D.; Swanson, B. I.; Brown, G. E. *Geochim. Cosmochim. Acta* **1991**, *55*, 671.

(82) Murphy, P. J.; LaGrange, M. S. *Geochim. Cosmochim. Acta* **1998**, *60*, 1849.

(83) Yang, J. H.; Henao, J. D.; Costello, C.; Kung, M. C.; Kung, H. H.; Miller, J. T.; Kropf, A. J.; Kim, J. G.; Regalbuto, J. R.; Bore, M. T.; Pham, H. N.; Datye, A. K.; Laeger, J. D.; Kharas, K. *Appl. Catal., A* **2005**, *291*, 73.

(84) Wang, S.; Qian, K.; Bi, X.; Huang, W. *J. Phys. Chem. C* **2009**, *113*, 6505.

(85) Goia, D. V.; Matijevic, E. *Colloids Surf. A* **1999**, *146*, 139.

(86) Galus, Z. Carbon, Silicon, Germanium, Tin, and Lead. In *Standard Potentials in Aqueous Solution*; Bard, A. J., Parsons, R., Jordan, J., Eds.; Marcel Dekker Inc.: New York, 1985; pp 189.

(87) Kashchiev, D.; van Rosmalen, G. M. *Cryst. Res. Technol.* **2003**, *38*, 555.

(88) Kim, W. B.; Voitl, T.; Rodriguez-Rivera, G. J.; Evans, S. T.; Dumesic, J. A. *Angew. Chem. Int. Ed.* **2005**, *44*, 778.

(89) Ketchie, W. C.; Murayama, M.; Davis, R. J. *Top. Catal.* **2007**, *44*, 307.

(90) Beltramo, G. L.; Shubina, T. E.; Koper, M. T. M. *Chem. Phys. Chem.* **2005**, *6*, 2597.

(91) Edens, G. J.; Hamelin, A.; Weaver, M. J. *J. Phys. Chem.* **1996**, *100*, 2322.

(92) Ponec, V.; Bond, G. C. Structure and Properties of Metals and Alloys. In *Catalysis by Metals and Alloys*; Elsevier: New York, 1995; Vol. 95; pp 42.

(93) Thomas, J. M.; Thomas, J. W. Fischer Tropsch Catalysis. In *Principles and Practice of Heterogeneous Catalysis*; VCH Verlagsgesellschaft: New York, 1997; pp 535.

(94) Novo, C.; Funsten, A. M.; Mulvaney, P. *Nature Lett.* **2008**, *3*, 598.

(95) Sardar, R.; Funston, A. M.; Mulvaney, P.; Murray, R. W. *Langmuir* **2009**, *25*, 13840.

(96) Cotton, F. A.; Wilkinson, G.; Murillo, C. A.; Bochmann, M. Compounds of Gold(II), d^9. In *Advanced Inorganic Chemistry*; 6 ed.; John Wiley & Sons, Inc.: New York, 2003.

(97) Schmid, G. M. Gold. In *Standard Potentials in Aqueous Solution*; Bard, A. J., Parsons, R., Jordan, J., Eds.; Marcel Dekker, Inc: New York, 1985; pp 313.

(98) Eustis, S.; Hsu, H. Y.; El-Sayed, M. A. *J. Phys. Chem. B* **2005**, *109*, 4811.

Chapter 6
Summary and Recommendations for Future Work

6.1 Research Summary.

This work investigates the relationships between structure and catalytic properties of synthesized Au and Pd-on-Au model transition metal nanocatalysts, even Au-enzyme biocatalysts. In Chapters 2 and 3, catalysis of aqueous trichloroethene hydrodechlorination (TCE HDC) and 4-nitrophenol (4-NL) reduction by Pd-on-Au nanoparticles (NPs) of specific size and surface composition was found to depend on the dispersion and oxidation state of surface Pd atoms. In-depth scanning transmission electron microscopy (STEM) and extended X-ray absorption fine-structure spectroscopy (EXAFS) structural analyses of the Pd-on-Au NPs revealed that Pd surface coverage and Au particle size directly influence Pd surface atom aggregation and oxidation. The Au NP size affected the Pd surface coverage (SC) at which metallic Pd monomers, metallic two-dimensional (2-D) and partially oxidized 3-D Pd ensembles were formed, thus changing the Pd dispersion and oxidation state. Correlation of Pd-on-Au NP activity and structural analyses provide strong evidence that 2-D Pd surface ensembles are important for TCE HDC whilst partially oxidized 3-D Pd ensembles are important for 4-nitrophenol reduction. The use of Au particle size to control the nature of Pd surface species of Pd-on-Au NPs illustrates a new approach to control and modify active sites of bimetallic NP catalysts.

In Chapter 4, the light-triggered biocatalysis of model thermophilic enzyme-photothermal gold nanorod complexes (TE-PGNs) was demonstrated as a means to control biochemical reactions in a less intrusive manner than traditional biochemical signals. The activity of alginate-encapsulated TE-PGNs exposed to a laser beam (λ~800

nm) was ~60% higher than the activity of analogous controls that were not illuminated. The encapsulated TE-PGNs were reusable and stable for several days, making them commercially viable. This approach could significantly improve how biochemical pathways are controlled for *in vitro* and, quite possibly, *in vivo* use.

In Chapter 5, Au NP sols with particle diameters of 3 nm to 12 nm were prepared using a new CO oxidation seeded-growth synthesis method. Particle size was controlled by varying the initial concentration of gold(III) hydroxide-chloride ions ($[AuCl_{4-x}(OH)_x]^-$) and was confirmed using three independent analytical techniques (Ultraviolet-visible spectroscopy (UV-Vis), small-angle x-ray scattering (SAXS), and transmission electron microscopy (TEM)). This synthesis method could be done under ambient conditions and did not require additional stabilizing agents. This seeded method of growing NPs should be extendable to other monometallic and multimetallic compositions and shapes and can be improved by using seed particles with a narrower size distribution.

Collectively, the studies presented in this work provide further insight into structure-activity properties of Au and Pd-on-Au nanocatalysts, thereby enabling the design and preparation of more efficient transition metal (T-metal) catalysts. The synthesis and characterization techniques used in these studies should be extendable to other t-metal nanomaterials. The correlations observed between particle structure and activity are anticipated to serve as a guide to design highly active nanocatalysts for similar chemical reactions. Tuning the activity of a T-metal nanocatalyst by altering its structure is an expedient means of obtaining desired catalytic properties. Transition metal catalyzed chemical reactions are already key processes in environmental, medicinal, petrochemical, and electrical/optics fields. Hence, methods to improve the activity and

lifetime of transition metal nanocatalysts should yield significant economic and environmental rewards.

6.2 Recommendations for Future Work.

6.2.1. X-ray Absorption Near-Edge Spectroscopy (XANES) of Pd-on-Au Nanoparticles.

In Chapter 2, EXAFS was used to show that the dispersion and oxidation state of Pd surface atoms changes as a function of the Pd surface Au particle size. Further insight into the reason that NPs with 2-D and 3-D Pd surface ensembles exhibit high catalytic activity can be provided by probing the XANES spectra, specifically of the L_{III} Pd and Au absorption edges. The L_{III} edge occurs when incident X-rays have sufficient energy to excite core p electrons to unoccupied valence d states (2p to 4d; ~3,157 eV for Pd and 2p to 5d; ~11,918 eV for Au).[1-3] While the electronic configuration of a Pd and Au atom is $4d^{10}5s^{0}$ and $5d^{10}6s^{1}$, respectively, orbital hybridization in the pure bulk metals results in a Pd electronic configuration of $4d^{10-x}5s^{0+x}$ and Au electronic configuration of $5d^{10-x}6s^{1+x}$, such that unoccupied d states are present.[4,5] The intensity of the L_{III} edge varies directly with the unoccupied density of d-states, or number of d-holes.[1,6]

Several studies have shown that the Au L_{III} edge white-line intensity (first sharp feature of the rising edge)[4] of bimetallic Pd-Au NPs has a lower intensity than pure Au nanoparticles.[2,5-7] Dash *et al.* reported that the Au L_{III} edge intensity of Pd-Au NPs decreased with increasing Pd content but similar studies by Reifsnyder and Lamb and Davis *et al.* showed that the Au L_{III} edge intensity did not significantly change with Pd content.[2,8,9] Nahm *et al.* noted that the Pd L_{III} edge white-line intensity decreases as the Au content in Pd-Au alloys is increased.[5] These changes have been ascribed to both charge transfer between Pd and Au atom valence orbitals and intra-atomic valence orbital

rehybridization.[2,6] According to electronic structure calculations, intra-atomic d band rehybridization is the main cause for the observed Pd and Au L_{III} edge changes.[2,10]

Our study will extend prior studies by probing how the geometry of specific Pd ensembles (*i.e.,* 2-D *vs.* 3-D Pd ensembles) on Au NPs influences the d-band of Pd and Au atoms comprising Pd-on-Au NPs. In this manner, we can further explore the geometric and electronic effects of the ensembles on catalyst activity, which is anticipated to result in the synthesis of more efficient bimetallic nanocatalysts. We have already collected XANES spectra of the L_{III} Au edge (Fig. 6.1) showing that the edge shape changes with the addition of Pd and that the white-line intensity of the 3 nm Pd-on-Au NPs is slightly lower than pure Au NPs and bulk Au. XANES spectra of the Pd L_{III} edge of representative 3 nm Pd-on-Au NPs has been collected and is currently being analyzed by Dr. Randall J. Meyer at the University of Illinois at Chicago and Dr. Jeffrey T. Miller at Argonne National Laboratory.

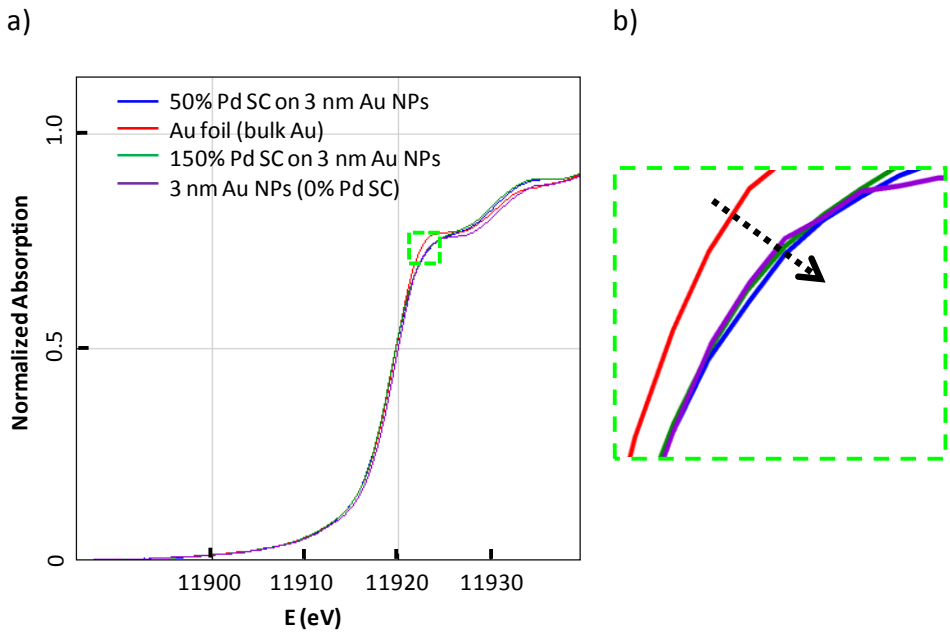

Figure 6.1. (a) XANES spectra of the Au L_{III} edge of bulk Au (Au foil), pure 3 nm Au NPs, and representative Pd-on-Au NPs. (b) Magnification of the edge white-line intensity showing the lowered intensity of the Pd-on-Au NPs in comparison to the bulk Au and pure Au NPs (marked by dotted arrow).

6.2.2. In-Situ X-ray Absorption Spectroscopy of Pd-on-Au Nanocatalysts.

An advantage of XAS over other characterization methods, such as x-ray photoelectron spectroscopy (XPS), is that measurements can be acquired under the conditions of a chemical reaction (in-situ XAS).[11] In-situ XAS analysis of several nanocatalysts, such as Au (water-gas shift reaction),[12] NiPt (ethylene glycol reforming),[13] CoNi (oxidative steam reforming of ethanol),[14] and Pd and PdBi (liquid phase oxidation of 1-phenylethanol)[15] has been performed under a variety of reaction conditions. In-situ XAS of Pd-on-Au NPs under either TCE HDC or nitrophenol reduction reaction conditions would provide further insight into the catalyzed reaction mechanisms. A reaction cell has already been designed by Dr. Jeffrey T. Miller and his research team at Argonne National Laboratory for such experiments (Fig. 6.2).

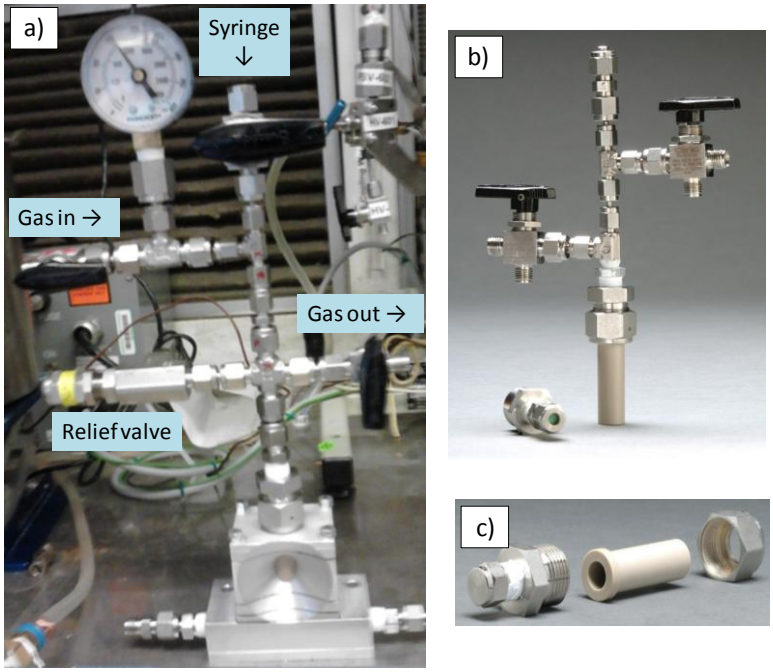

Figure 6.2. (a) Picture of the polyether ether ketone (PEEK) reactor and holder (can be connected to temperature-controlled bath) for future in-situ XAS experiments. b) Picture of the reactor and inlet/outlet ports. (c) Close-up picture of the reactor and fittings. The reactor and holder were designed and assembled by Dr. Jeffrey T. Miller and his research team at Argonne National Laboratory.

Specifically, by monitoring the L_{III} absorption edge of Pd and Au, the interaction between NP surface atoms and adsorbates could be explored. Following adsorption of an adsorbate, changes in the L_{III} metal edges can occur due to charge transfer, orbital rehybridization, metal-adsorbate scattering, and differences in metal-metal scattering.[1] Surface enhanced raman spectroscopy (SERS) could be used as a complimentary independent analytical technique to verify/clarify the XANES results obtained. Previously, the hydrodechlorination of dichloroethene was successfully monitored over Pd-on-Au nanoshells using SERS.[16] SERS has also been used to investigate adsorption of 4-nitrophenol on Ag powders and films.[17,18] Collectively, these XANES and SERS analyses could further clarify the reaction mechanisms of Pd-on-Au NP catalyzed TCE HDC and 4-NL reduction.

6.2.3. Au-Metal Carbide Nanocatalysts for TCE HDC and 4-NL Reduction.

Pd-on-Au bimetallic NPs have previously been demonstrated to be more cost-effective than pure Pd NPs (particularly for TCE HDC).[19] Nevertheless, the development of less expensive, yet highly active catalysts is desirable. Metal carbides, such as molybdenum carbide, have been shown to have electronic and catalytic properties similar to Pt-group metals.[20] Recently, Schweitzer *et al.* showed that the ability of Pt particles to catalyze the water-gas-shift reaction significantly improves when they are supported on molybdenum carbide (Mo_2C).[21] Consuegra *et al.* recently showed that Mo_2C supported on SiO_2 exhibited high catalytic activity (52.8 $mol_{Cl}mol_{Mo_2C}^{-1}h^{-1}$) for the gas-phase hydrodechlorination of chlorobenzene.[22] Metal carbides are significantly less expensive than Pt-group metals but synthesizing nano-sized metal carbides in a systematic and scalable fashion is challenging.[23] Recent studies, summarized in a review article by Giordano and Antonietti, show that metal carbide and metal nitride NPs (diameter <50 nm) can be synthesized using sol-gel chemistry and provide motivation for further study.[23]

The substitution of the Pd in the Pd-on-Au NPs with metal carbides, such as Mo_2C, is an interesting idea. Potapenka *et al.* demonstrated that Mo_2C nanoparticles (d ~5 nm) could be deposited on a Au(111) surface and used to catalyze cyclohexene dehydrogenation.[24,25] Using periodic density functional calculations, Florez *et al.* propose that Au nanoparticles on ZrC would be able to dissociatively adsorb hydrogen, an important adsorption process for TCE HDC.[26] Perret *et al.* alternatively demonstrated that Au supported on Mo_2C could be used to catalyze the gas-phase reduction of the nitro groups of nitroarenes (para-chloronitrobenzene and meta-dinitrobenzene) to their

respective aromatic amines.[27] The synthesis of Au-metal carbide nanoparticles (d~1-50 nm) has not yet been reported but such catalysts would be expected to exhibit unusual, and, perhaps, highly efficient catalytic activity for both TCE HDC and 4-NL reduction.

6.2.4 Preparation of Pd-carbide Nanoparticles

EXAFS of the 4 nm Pd nanoparticle controls (see in Chapters 2 and 3 for further details) suggests that such particles consist of Pd-carbide. This conclusion is supported by preliminary EXAFS analysis. For EXAFS experiments, the tannic acid-citrate Pd particle sols were immobilized on carbon powder as described in Chapter 2. As shown in Table A6 (Appendix A), the Pd-Pd bond length of as-prepared and hydrogen-treated (at 200 °C) carbon-supported Pd particles is ~2.79 Å. This is larger than the expected bond length between Pd-Pd atoms in bulk Pd (~2.74 Å).[6] Incorporation of carbon atoms in the Pd lattice to form Pd-carbide could explain the increased Pd-Pd bond length observed. If such Pd-carbide were formed, Pd hydride formation should not significantly occur.

To evaluate the particles' propensity to form Pd-hydride, the carbon-supported samples were treated with hydrogen gas at 400 °C. After this high temperature treatment, the samples were cooled to room temperature and analyzed under H_2 gas. Under these conditions, Pd hydride should be formed if Analogous control experiments were conducted using He. As shown in Table 6.1, the Pd-Pd bond length did not significantly change after treatment under hydrogen at 400 °C.

Table 6.1 4 nm Pd NPs EXAFS fit parameters-Pd Edge.[a]

Treatment	Analysis Conditions[b]	Scattering Path	CN[c] (±10%)	R, Å[d] (±0.02 Å)	DWF[e] ($\times 10^3$ Å^2)	E_0, eV[f]
H_2, 400°C	H_2, RT	Pd-Pd	9.9	2.81	2.0	1.4
	He, RT	Pd-Pd	9.8	2.80	2.0	0.7
He, 400°C	H_2, RT	Pd-Pd	10.0	2.81	2.0	1.6
	He, RT	Pd-Pd	9.9	2.80	2.0	1.6

a. 4 nm Pd NP sol supported on carbon powder
b. Gas and temperature under which EXAFS analysis was conducted
c. CN:coordination number
d. R: bond distance
e. DWF: Debye-waller factor
f. E_0: threshold absorption edge energy

Furthermore, the Pd-Pd bond length under hydrogen was similar to analogous controls under He. The Pd-Pd CN of the samples treated at 400 °C was slightly higher than those analyzed at 200 °C, possibly due to particle sintering (particle diameter increased to ~5.5 nm after treatments under H_2 and He at 400 °C). These EXAFS results are consistent with Pd-carbide formation. Further EXAFS experiments should be conducted to further verify this conclusion and explore the possible role of the carbon support in Pd-carbide formation.

6.2.5. BioHydrogen Production Using Thermophilic Enzyme-Photothermal Gold Nanoparticle Complexes

There is a current global need for the development of more clean, sustainable energy sources. Hydrogen has been proposed as a viable alternative to fossil fuels as it has the highest gravimetric energy density of any fuel, could be compatible with current energy conversion processes, and would not generate undesired carbon-based emissions.[28] Currently, most hydrogen is synthesized through electrolysis of water or methane steam reforming. The production of hydrogen using microorganisms is an attractive alternative given the wide range of renewable resources (*i.e.,* plant-derived) that these organisms can potentially use to make hydrogen.[28]

Hyperthermophiles are microorganisms, typically from *Archae* or *Bacteria*, that optimally grow at temperatures >80 °C.[29] Enzymes from such organisms, or thermophilic enzymes, are stable at relatively high reaction temperatures and have recently been used to produce biofuels, such as hydrogen, ethanol, and methane.[29,30] Thermophilic hydrogenase enzymes can catalyze the reversible reduction of protons to hydrogen using renewable sources, such as glucose, starch, and lignocellulose.[31,32] For these experiments, the bulk reaction temperature had to exceed 50 °C (~70-100°C) which can limit this technology's industrial scalability.

Light-triggered activation of thermophilic hydrogenases conjugated to photothermal Au nanorods would be an interesting and viable alternative to this problem. In Chapter 4, it was demonstrated that a thermophilic glucokinase conjugated to Au nanorods can be activated at non-thermophilic bulk reaction temperatures (<50 °C) through localized surface plasmon resonance heating in the presence of a suitable light source (λ~ 800 nm).[33] By conjugating thermophilic hydrogenase enzymes to photothermal gold nanorods and exposing to a laser (λ ~800 nm), biohydrogen could conceivably be generated from biomass at bulk reaction temperatures <50 °C. Operation at lower reaction temperatures would improve the energy efficiency of the overall biohydrogen synthesis process. Furthermore, encapsulation of the thermophilic enzyme-gold complexes in alginate would simplify post-reaction catalyst sequestration and likely decrease enzyme degradation, making this technology more commercially viable.

6.3. References.

(1) Tew, M. W.; Miller, J. T.; van Bokhoven, J. A. *J. Phys. Chem. C* **2009**, *113*, 15140.

(2) Reifsnyder, S. N.; Lamb, H. H. *J. Phys. Chem. B* **1999**, *103*, 321.

(3) Pretzer, L. A.; Song, H. J.; Fang, Y.-L.; Zhao, Z.; Guo, N.; Wu, T.; Arslan, I.; Miller, J. T.; Wong, M. S. *J. Catal.* **2013**, *298*, 206.

(4) Miller, J. T.; Kropf, A. J.; Zha, Y.; Regalbuto, J. R.; Delannoy, L.; Louis, C.; Bus, E.; van Bokhoven, J. A. *J. Catal.* **2006**, *240*, 222.

(5) Nahm, T. U.; Jung, R.; Kim, J. U.; Park, W. G.; Oh, S. J.; Park, J. H.; Allen, J. W.; Chung, S. M. *Phys. Rev. B* **1998**, *58*, 9817.

(6) Gao, F.; Goodman, D. W. *Chem. Soc. Rev.* **2012**, *41*, 8009.

(7) Dash, P.; Dehm, N. A.; Scott, R. W. J. *J. Mol. Catal., A* **2008**, *286*, 114.

(8) Davis, R. J.; Boudart, M. *J. Phys. Chem.* **1994**, *98*, 5471.

(9) Dash, P.; Bond, T.; Fowler, C.; Hou, W.; Coombs, N.; Scott, R. W. J. *J. Phys. Chem. C* **2009**, *113*, 12719.

(10) Weinberger, P.; Szunyogh, L.; Bennett, B. I. *Phys. Rev. B* **1993**, *47*, 10154.

(11) Russell, A. E.; Rose, A. *Chem. Rev.* **2004**, *104*, 4613.

(12) Deng, W.; Frenkel, A. I.; Si, R.; Flytzani-Stephanopoulos, M. *J. Phys. Chem. C* **2008**, *112*, 12834.

(13) Tupy, S. A.; Karim, A. M.; Bagia, C.; Deng, W.; Huang, Y.; Vlachos, D. G.; Chen, J. G. *ACS Catal.* **2012**, *2*, 2290.

(14) Andonova, S.; de Avila, C. N.; Arishtirova, K.; Bueno, J. M. C.; Damyanova, S. *Appl. Catal. B: Environ.* **2011**, *105*, 346.

(15) Keresszegi, C.; Grunwaldt, J. D.; Mallat, T.; Baiker, A. *J. Catal.* **2004**, *222*, 268.

(16) Heck, K. N.; Janesko, B. G.; Scuseria, G. E.; Halas, N. J.; Wong, M. S. *J. Am. Chem. Soc.* **2008**, *130*, 16592.

(17) Merklin, G. T.; Griffiths, P. R. *Langmuir* **1997**, *13*, 6159.

(18) Perry, D. A.; Son, H. J.; Cordova, J. S.; Smith, L. G.; Biris, A. S. *J. Colloid Interface Sci.* **2010**, *342*, 311.

(19) Wong, M. S.; Alvarez, P. J. J.; Fang, Y.-l.; Ackin, N.; Nutt, M. O.; Miller, J. T.; Heck, K. N. *J. Chem. Technol. Biotechnol.* **2009**, *84*, 158.

(20) Kelly, T. G.; Chen, J. G. *Chem. Soc. Rev.* **2012**, *41*, 8021.

(21) Schweitzer, N. M.; Schaidle, J. A.; Ezekoye, O. K.; Pan, X.; Linic, S.; Thompson, L. T. *J. Am. Chem. Soc.* **2011**, *133*, 2378.

(22) Consuegra, A. D.; Patterson, P. M.; Keane, M. A. *Appl. Catal. B: Environ.* **2006**, *65*, 227.

(23) Giordano, C.; Antonietti, M. *Nano Today* **2011**, *6*, 366.

(24) Potapenko, D. V.; Horn, J. M.; White, M. G. *J. Catal.* **2005**, *236*, 346.

(25) Horn, J. M.; Song, Z.; Potapenko, D. V.; Hrbek, J.; White, M. G. *J. Phys. Chem. B* **2005**, *109*, 44.

(26) Florez, E.; Gomez, T.; Rodriguez, J. A.; Illas, F. *Phys. Chem. Chem. Phys*. **2011**, *13*, 6865.

(27) Perret, N.; Wang, X.; Delannoy, L.; Potvin, C.; Louis, C.; Keane, M. A. *J. Catal.* **2012**, *286*, 172.

(28) Levin, D. B.; Pitt, L.; Love, M. *Int. J. Hydro. Energy* **2004**, *29*, 173.

(29) Atomi, H.; Sato, T.; Kanai, T. *Curr. Opinion Biotechnol.* **2011**, *22*, 618.

(30) Barnard, D.; Casanueva, A.; Tuffin, M.; Cowan, D. *Environ. Technol.* **2010**, *31*, 871.

(31) Baker, S. E.; Hopkins, R. C.; Blanchette, C. D.; Walsworth, V. L.; Sumbad, R.; Fischer, N. O.; Kuhn, E. A.; Coleman, M.; Chromy, B. A.; Letant, S. E.; Hoeprich, P. D.; Adams, M. W. W.; Henderson, P. T. *J. Am. Chem. Soc.* **2009**, *131*, 7508.

(32) de Vrije, T.; Bakker, R. R.; Budde, M. A. W.; Lai, M. H.; Mars, A. E.; Claassen, P. A. M. *Biotechnol. Biofuels* **2009**, *2*, 12.

(33) Blankschien, M. D.; Pretzer, L. A.; Huschka, R.; Halas, N. J.; Gonzalez, R.; Wong, M. S. *ACS Nano* **2012**, *7*, 654.

Appendix A

Supporting Information for Chapter 2

A1 Tables.

Table A1. Volumes of $PdCl_4^{2-}$ used to synthesize 3 nm Pd-on-Au NPs.[a]

Pd surface coverage (SC%)	Volume of $PdCl_4^{2-}$ precursor (µL)[b]	Pd metal content (mol%)[c]
10	13	6.1
20	27	11.4
30	40	16.2
40	53	20.5
50	66	24.4
60	80	27.9
70	89	30.2
80	106	34.0
90	119	36.7
100	133	39.2
110	146	41.5
150	199	49.2

[a] All calculations are based on the magic cluster model.
[b] Volumes shown are for a 2.47 mM $PdCl_4^{2-}$ solution added to 2 mL of Au NP sol.
[c] Composition of one nanoparticle.

Table A2. Volumes of $PdCl_4^{2-}$ used to synthesize 7 nm Pd-on-Au NPs.[a]

Pd surface coverage (SC%)	Volume of $PdCl_4^{2-}$ precursor (µL)[b]	Pd metal content (mol%)[c]
10	5	2.3
20	10	4.6
30	15	6.7
40	20	8.7
50	25	10.7
60	29	12.5
70	33	13.8
80	39	16.0
90	44	17.7
100	49	19.3
110	54	20.8
150	74	26.4

[a] All calculations are based on the magic cluster model.
[b] Volumes shown are for a 2.47 mM $PdCl_4^{2-}$ solution added to 2 mL of Au NP sol.
[c] Composition of one nanoparticle.

Table A3. Volumes of $PdCl_4^{2-}$ used to synthesize 10 nm Pd-on-Au NPs.[a]

Pd surface coverage (SC %)	Volume of $PdCl_4^{2-}$ precursor (µL)[b]	Pd metal content (mol%)[c]
10	4	1.7
20	7	3.3
30	11	4.9
40	14	6.4
50	18	7.9
60	21	9.3
70	24	10.3
80	28	12.0
90	32	13.3
100	35	14.6
110	39	15.8
150	53	20.4

[a] All calculations are based on the magic cluster model.
[b] Volumes shown are for a 2.47 mM $PdCl_4^{2-}$ solution added to 2 mL of Au NP sol.
[c] Composition of one nanoparticle.

Table A4. Calculated gold magic cluster sizes.

Shell number (n)	Number of atoms in shell (n_{atom})[a]	Total number of atoms per NP (n_{tot})[b]	Calculated diameter (nm)
	1	1	0.27
1	12	13	0.81
2	42	55	1.35
3	92	147	1.89
4	162	309	2.43
5	252	561	2.97
6	362	923	3.51
7	492	1415	4.05
8	642	2057	4.59
9	812	2869	5.13
10	1002	3871	5.67
11	1212	5083	6.21
12	1442	6525	6.75
13	1692	8217	7.29
14	1962	10179	7.83
15	2252	12431	8.37
16	2562	14993	8.91
17	2892	17885	9.45
18	3242	21127	9.99
19	3612	24739	10.53
20	4002	28741	11.07

[a] $n_{atom} = 10n^2 + 2$

[b] $n_{tot} = (10n^3 + 15n^2 + 11n + 3)/3$

Table A5. 3 nm Pd-on-Au NPs EXAFS fit parameters-Au Edge.

Pd Surface Coverage (%)	Treatment	Scattering Path	CN[a] (±10%)	R, Å[b] (±0.02 Å)	DWF[c] (×10^3 $Å^2$)	E_0, eV[d]
0	Air, RT	Au-Au	10.2	2.87	1.0	-0.4
	H_2, 200°C	Au-Au	10.3	2.86	1.0	-0.5
30	Air, RT	Au-Au	10.0	2.85	0.5	-0.1
		Au-Pd	1.7	2.80	0.5	3.5
	H_2, 200°C	Au-Au	10.1	2.85	0.5	-0.1
		Au-Pd	1.7	2.80	0.5	3.3
50	Air, RT	Au-Au	9.3	2.85	0.0	-1.6
		Au-Pd	2.0	2.79	0.0	5.5
	H_2, 200°C	Au-Au	9.2	2.84	0.0	-0.8
		Au-Pd	2.3	2.79	0.0	4.3
70	Air, RT	Au-Au	9.3	2.85	0.0	-1.2
		Au-Pd	2.0	2.79	0.0	5.0
	H_2, 200°C	Au-Au	9.2	2.86	0.0	-0.5
		Au-Pd	2.1	2.79	0.0	5.1
90	Air, RT	Au-Au	9.9	2.85	0.0	-1.2
		Au-Pd	2.1	2.79	0.0	5.0
	H_2, 200°C	Au-Au	9.6	2.86	0.0	-2.3
		Au-Pd	2.4	2.79	0.0	5.3
110	Air, RT	Au-Au	9.3	2.86	0.0	-1.2
		Au-Pd	2.1	2.79	0.0	4.3
	H_2, 200°C	Au-Au	9.2	2.86	0.0	-1.3
		Au-Pd	2.7	2.79	0.0	4.9
150	Air, RT	Au-Au	9.4	2.86	0.0	-1.8
		Au-Pd	2.2	2.79	0.0	5.2
	H_2, 200°C	Au-Au	9.1	2.86	0.0	-1.1
		Au-Pd	2.7	2.79	0.0	4.3

a. CN:coordination number
b. R: bond distance
c. DWF: Debye-waller factor
d. E_0: threshold absorption edge energy

Table A6. 3 nm Pd-on-Au NPs EXAFS fit parameters-Pd Edge.

Pd Surface Coverage (%)	Treatment	Scattering Path	CN[a] (±10%)	R, Å[b] (±0.02 Å)	DWF[c] ($\times 10^3$ Å^2)	E_0, eV[d]
30	Air, RT	Pd-Au	8.8	2.79	0.5	-5.6
	H_2, 200°C	Pd-Au	8.5	2.80	0.5	-4.4
50	Air, RT	Pd-Pd	2.7	2.80	1.0	-1.1
		Pd-Au	7.0	2.80	1.0	-4.3
	H_2, 200°C	Pd-Pd	2.0	2.80	1.0	-1.5
		Pd-Au	9.2	2.80	1.0	-4.4
70	Air, RT	Pd-Pd	2.9	2.76	0.5	-5.4
		Pd-Au	6.9	2.81	0.5	-2.7
		Pd-O	0.5	2.05	1.0	1.0
	H_2, 200°C	Pd-Pd	3.6	2.76	0.5	-5.3
		Pd-Au	7.8	2.81	0.5	-2.6
90	Air, RT	Pd-Pd	2.9	2.76	0.5	-3.4
		Pd-Au	5.8	2.81	0.5	-1.9
		Pd-Cl	0.5	2.29	1.0	-1.7
		Pd-O	0.7	2.05	1.0	4.5
	H_2, 200°C	Pd-Pd	4.0	2.76	0.5	-2.7
		Pd-Au	6.9	2.81	0.5	-2.0
110	Air, RT	Pd-Pd	3.0	2.76	0.5	-3.2
		Pd-Au	5.5	2.81	0.5	-1.4
		Pd-Cl	1.1	2.3	1.0	-1.0
	H_2, 200°C	Pd-Pd	4.8	2.76	0.5	-3.2
		Pd-Au	6.4	2.81	0.5	-2.1
150	Air, RT	Pd-Pd	2.7	2.79	1.0	-1.5
		Pd-Au	4.6	2.80	1.0	-3.4
		Pd-Cl	1.2	2.3	1.0	-0.1
	H_2, 200°C	Pd-Pd	4.8	2.76	0.5	-2.7
		Pd-Au	6.5	2.81	0.5	-2.1
[e]Pd NPs	Air, RT	Pd-Pd	8.2	2.79	2.0	-0.2
		Pd-O	0.5	2.05	1.0	2.0
	H_2, 200°C	Pd-Pd	9.1	2.79	2.0	0.2

a. CN:coordination number
b. R: bond distance
c. DWF: Debye-waller factor
d. E_0: threshold absorption edge energy
e. 4 nm Pd NP sol supported on carbon powder

Table A7. 7 nm Pd-on-Au NPs EXAFS fit parameters-Au Edge.

Pd Surface Coverage (%)	Treatment	Scattering Path	CN[a] (±10%)	R, Å[b] (±0.02 Å)	DWF[c] ($\times 10^3$ Å^2)	E_0, eV[d]
0	Air, RT	Au-Au	10.8	2.86	1.0	-0.3
	H_2, 200°C	Au-Au	10.7	2.86	1.0	-0.4
30	Air, RT	Au-Au	10.9	2.86	0.5	-0.8
	H_2, 200°C	Au-Au	11.0	2.86	0.5	-0.7
50	Air, RT	Au-Au	10.2	2.86	0.0	-0.7
		Au-Pd	1.4	2.81	0.0	5.5
	H_2, 200°C	Au-Au	10.0	2.86	0.0	-0.7
		Au-Pd	1.4	2.81	0.0	5.7
70	Air, RT	Au-Au	10.1	2.86	0.0	-1.1
		Au-Pd	1.3	2.80	0.0	5.9
	H_2, 200°C	Au-Au	10.0	2.86	0.0	-0.7
		Au-Pd	1.5	2.80	0.0	4.9
90	Air, RT	Au-Au	10.4	2.86	0.0	-1.0
		Au-Pd	1.5	2.79	0.0	4.8
	H_2, 200°C	Au-Au	10.3	2.86	0.0	-1.0
		Au-Pd	1.7	2.79	0.0	4.7
110	Air, RT	Au-Au	10.3	2.86	0.0	-0.5
		Au-Pd	1.6	2.80	0.0	5.2
	H_2, 200°C	Au-Au	9.9	2.86	0.0	-0.8
		Au-Pd	1.8	2.79	0.0	2.7
150	Air, RT	Au-Au	10.5	2.86	0.0	-1.1
		Au-Pd	1.5	2.80	0.0	5.0
	H_2, 200°C	Au-Au	10.4	2.86	0.0	-1.1
		Au-Pd	1.7	2.79	0.0	5.3

a. CN:coordination number
b. R: bond distance
c. DWF: Debye-waller factor
d. E_0: threshold absorption edge energy

Table A8. 7 nm Pd-on-Au NPs EXAFS fit parameters-Pd Edge.

Pd Surface Coverage (%)	Treatment	Scattering Path	CN[a] (±10%)	R, Å[b] (±0.02 Å)	DWF[c] ($\times 10^3$ Å^2)	E_0, eV[d]
30	Air, RT	Pd-Au	11.1	2.81	0.0	-3.4
	H_2, 200°C	Pd-Au	11.0	2.81	0.0	-3.2
50	Air, RT	Pd-Au	11.0	2.80	0.5	-5.3
	H_2, 200°C	Pd-Pd	1.1	2.79	1.0	-1.6
		Pd-Au	9.7	2.81	1.0	-4.4
70	Air, RT	Pd-Pd	0.9	2.79	1.0	-1.4
		Pd-Au	9.6	2.81	1.0	-3.8
	H_2, 200°C	Pd-Pd	2.3	2.76	0.5	-4.5
		Pd-Au	7.9	2.81	0.5	-3.3
90	Air, RT	Pd-Pd	2.8	2.76	0.5	-6.0
		Pd-Au	7.0	2.81	0.5	-3.5
		Pd-O	0.9	2.05	1.0	1.0
	H_2, 200°C	Pd-Pd	3.4	2.76	0.5	-5.7
		Pd-Au	7.8	2.81	0.5	-3.1
110	Air, RT	Pd-Pd	2.8	2.76	0.5	-5.9
		Pd-Au	7.2	2.81	0.5	-3.1
		Pd-Cl	0.4	2.30	1.0	-3.0
	H_2, 200°C	Pd-Pd	3.4	2.76	0.5	-4.6
		Pd-Au	8.3	2.81	0.5	-3.3
150	Air, RT	Pd-Pd	3.9	2.76	0.5	-3.4
		Pd-Au	6.9	2.81	0.5	-2.9
		Pd-Cl	0.4	2.30	1.0	-0.8
		Pd-O	0.4	2.05	1.0	-0.04
	H_2, 200°C	Pd-Pd	4.7	2.76	0.5	-3.0
		Pd-Au	5.9	2.81	0.5	-2.4

a. CN:coordination number
b. R: bond distance
c. DWF: Debye-waller factor
d. E_0: threshold absorption edge energy

Table A9. 10 nm Pd-on-Au NPs EXAFS fit parameters-Au Edge.

Pd Surface Coverage (%)	Treatment	Scattering Path	CN[a] (±10%)	R, Å[b] (±0.02 Å)	DWF[c] ($\times 10^3$ Å^2)	E_0, eV[d]
0	Air, RT	Au-Au	11.3	2.87	1.0	-0.3
	H_2, 200°C	Au-Au	11.1	2.87	1.0	-0.2
30	Air, RT	Au-Au	10.8	2.86	0.5	-0.7
	H_2, 200°C	Au-Au	10.7	2.86	0.5	-0.9
50	Air, RT	Au-Au	10.8	2.86	0.0	-0.4
		Au-Pd	1.2	2.81	0.0	6.4
	H_2, 200°C	Au-Au	10.8	2.86	0.0	-0.8
		Au-Pd	1.1	2.81	0.0	6.1
70	Air, RT	Au-Au	10.8	2.86	0.0	-0.6
		Au-Pd	1.2	2.81	0.0	5.6
	H_2, 200°C	Au-Au	10.8	2.86	0.0	-0.5
		Au-Pd	1.2	2.81	0.0	5.5
90	Air, RT	Au-Au	11.0	2.87	1.0	-0.5
	H_2, 200°C	Au-Au	10.7	2.86	1.0	-0.8
110	Air, RT	Au-Au	11.2	2.87	1.0	-0.4
	H_2, 200°C	Au-Au	10.7	2.86	1.0	-0.6
150	Air, RT	Au-Au	11.3	2.87	1.0	-0.4
	H_2, 200°C	Au-Au	10.6	2.86	1.0	-0.5

a. CN:coordination number
b. R: bond distance
c. DWF: Debye-waller factor
d. E_0: threshold absorption edge energy

Table A10. 10 nm Pd-on-Au NPs EXAFS fit parameters-Pd Edge.

Pd Surface Coverage (%)	Treatment	Scattering Path	CN[a] (±10%)	R, Å[b] (±0.02 Å)	DWF[c] ($\times 10^3$ Å^2)	E_0, eV[d]
30	Air, RT	Pd-Au	10.7	2.82	0.0	-2.7
	H_2, 200°C	Pd-Au	11.3	2.82	0.0	-2.6
50	Air, RT	Pd-Au	10.4	2.80	1.0	-5.1
	H_2, 200°C	Pd-Au	10.9	2.80	0.5	-5.9
70	Air, RT	Pd-Pd	0.9	2.80	1.0	-2.2
		Pd-Au	9.8	2.80	1.0	-5.5
	H_2, 200°C	Pd-Pd	0.8	2.79	1.0	-1.5
		Pd-Au	10.5	2.80	1.0	-5.4
90	Air, RT	Pd-Pd	2.2	2.76	0.5	-3.5
		Pd-Au	8.5	2.81	0.5	-1.4
	H_2, 200°C	Pd-Pd	1.8	2.76	0.5	-3.5
		Pd-Au	9.9	2.81	0.5	-1.6
110	Air, RT	Pd-Pd	2.6	2.76	0.5	-4.4
		Pd-Au	7.1	2.81	0.5	-1.9
	H_2, 200°C	Pd-Pd	2.7	2.76	0.5	-3.2
		Pd-Au	8.6	2.81	0.5	-1.8
150	Air, RT	Pd-Pd	2.0	2.76	0.5	-4.5
		Pd-Au	4.8	2.81	0.5	-3.6
		Pd-O	1.6	2.05	1.0	3.5
	H_2, 200°C	Pd-Pd	3.8	2.76	0.5	-5.6
		Pd-Au	8.0	2.81	0.5	-2.4

a. CN:coordination number
b. R: bond distance
c. DWF: Debye-waller factor
d. E_0: threshold absorption edge energy

A2 Figures.

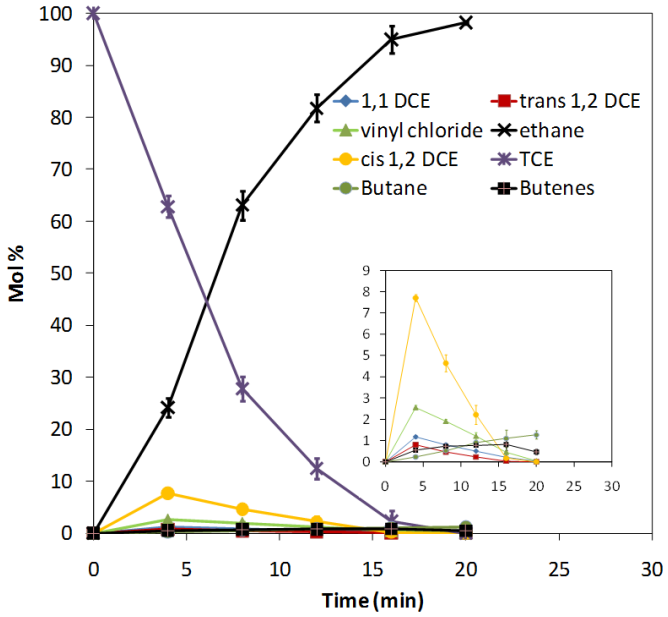

Figure A1. Typical product concentration-time profiles for 10 nm Pd-on-Au NPs with 50% Pd SC. DCE is dichloroethene and TCE is trichloroethene.

A) **XAS Measured CN's**

Absorbing atom	Scattering atom: Au	Scattering atom: Pd
Au	10.1	8.5
Pd	1.7	0.0

B) **Calculated Alloy CN's**

Absorbing atom	Scattering atom: Au	Scattering atom: Pd
Au	9.9	7.1
Pd	1.6	1.4

Figure A2. (A) XAS-measured CN's for 3 nm Pd-on-Au NPs with 30% Pd SC and (B) calculated CN's for alloyed PdAu NPs with the same metal content (16.2 mol% Pd), total Au CN (11.8), and total Pd CN (8.5). Experimental CN's were those of NPs after hydrogen reduction at 200 °C.

Appendix B

Overview of Extended X-ray Absorption Fine-Structure Spectroscopy (EXAFS)

B1 General Introduction to X-ray Absorption Spectroscopy (XAS).

XAS is a powerful spectroscopic technique that provides atomic-scale structure information of materials by examining how X-rays are absorbed and how photoelectrons are scattered by neighboring atoms after being ejected from the absorbing atomic element by impinging X-rays.[1-4] XAS has several advantages; namely, it can be performed under extreme pressure or temperature conditions, is independent of the physical state of the absorbing element (*i.e.,* can be used to analyze gases, liquids, and solids), and can be measured for the majority of the elements (those lighter than phosphorous are usually analyzed under vacuum).[5,6] Depending on the energy of the X-ray beam, core-level electrons are either excited to higher unoccupied valence electron states or to an ionization continuum such that a photoelectron is generated.[7-9] Core-level excitation of electrons makes it possible to use XAS to distinguish between different elements. XAS is therefore classified as an element-specific technique.[10] When the energy of the X-ray beam equals the binding energy of the relevant core-electron, a significant increase in X-ray absorption occurs. This increase in absorption is often referred to as an absorption edge and corresponds to photoelectron generation.[6,8]

Absorption edges are distinguished from each other based on the principle quantum number of the core electron that is being excited. For example, a K absorption edge refers to excitation of a core electron with n=1, L edge refers to excitation of a core electron with n=2, and M edge refers to excitation of a core electron with n=3.[6] The edge may not be perfectly smooth and can have multiple absorption peaks due to spin- orbit coupling.[11] The kinetic energy of the photoelectron is the difference between the binding

energy of the electron and the energy of the incident X-ray photon. As the energy of the X-ray beam is increased beyond the binding energy of the electron, the generated photoelectron has increasing kinetic energy.

Once the photoelectron has excess kinetic energy it can interact with surrounding atoms. Such interaction results in constructive and destructive interference between the photoelectron wave going out from the X-ray absorbing atom and the same wave scattered by neighboring atoms.[5,6,12] These interferences directly affect the absorption of X-rays by the absorbing atom resulting in quasiperiodic oscillations of X-ray absorbance as a function of X-ray beam energy.[12] The nature of the interferences between the outgoing and scattered photoelectron wave varies with the identity of the absorbing and scattering atoms and their relative spatial configuration. By analyzing the quasiperiodic oscillations of the X-ray absorbance resulting from these interferences, it is possible to determine structural information, such as the number and identity of neighboring atoms and the bond lengths between these atoms and the X-ray absorbing atom.[5,6,12]

B2 Description of Transmission XAS Measurement.

The absorption of an X-ray beam by a given sample can be determined by measuring the intensity of the incoming and transmitted X-rays with ion beam chambers.[8] The typical set-up of such transmission XAS is provided in Figure B1.

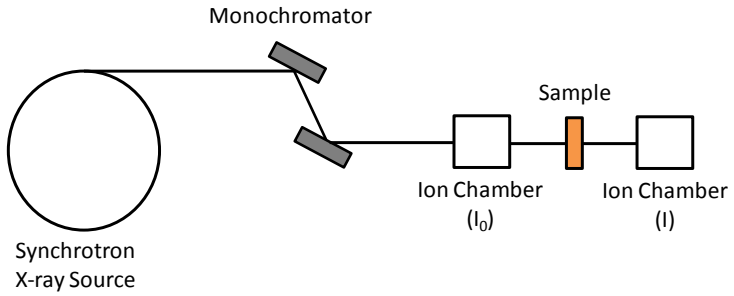

Figure B1. Schematic of the general experimental set-up for transmission XAS.[5,7]

Each ion beam chamber consists of parallel plate capacitor that is filled with inert gas and has a high-voltage across it.[7] A monochromator is used to select specific X-ray wavelengths.[8] Crystalline silicon monochromators are often used since they provide high energy resolution (~1 keV at 10 keV).[5,7] The detection limit of transmission XAFS is ~500 ppm.[6] This detection limit can be lowered by measuring the fluorescence of X-rays by the sample instead of absorption. Further details concerning this XAS technique will not be discussed here but can be found elsewhere.[6,7] Sample absorption is typically quantified as the absorption coefficient, μ, which is calculated using Beer's Law (Eqn. B1),[7,13]

$$\ln\left(\frac{I_0}{I}\right) = \mu t \qquad \text{(B1)}$$

where I_0 and I are the intensities incoming and transmitted X-rays, respectively, and t is the sample thickness (cm). As shown in Eqn. B2, the absorption coefficient strongly depends on the sample's atomic mass, A, atomic number, Z, density, ρ, and the X-ray beam energy, E.[7]

$$\mu \approx \frac{\rho Z^4}{AE^3} \qquad \text{(B2)}$$

For elements with Z >18, the K or L edge is evidenced at X-ray beam energies between 3 and 35 keV, which is within the range of most synchrotron X-ray sources.[7]

A synchrotron X-ray source is required to generate the intense energy-tunable X-rays required for XAS. A synchrotron source generates X-ray radiation ~10^5 to 10^6 times more intense than a conventional Mg or Al source.[8] A synchrotron is a circular particle accelerator consisting of an electron source, linear accelerator, booster ring, and storage ring (Fig. B2).[5,8]

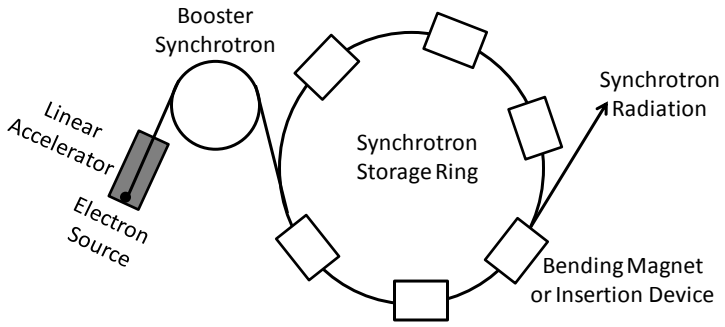

Figure B2. Representation of the general set-up of a synchrotron (Adapted from Ref. 5).

Synchrotron X-ray radiation is generated when electrons traveling at relativistic energies in a circular trajectory are passed through a magnetic field.[5,6] As shown in Eqn. B3, the intensity, Γ, of the generated X-ray radiation depends on the accelerated particle's mass, m, and energy, E_p and on the velocity of light, c (~3.0×10^8 m/s).[5]

$$\Gamma = \frac{E_p}{mc^2} \qquad \text{(B3)}$$

For a given energy, the intensity of the X-ray radiation is highest when particles with very small masses, such as electrons or positrons, are accelerated. The energies to which electrons are accelerated varies between synchrotrons.[5,6,8] The energy specifications described below are specific to the synchrotron at the Advanced Photon Source (APS) at Argonne National Laboratory. This information is readily available on the APS website (http://www.aps.anl.gov/About/APS_Overview/index.html).

Synchrotron generation of X-ray radiation involves the generation of electrons, which are subsequently accelerated by a linear particle accelerator prior to acceleration in the synchrotron booster and storage rings. At the APS, electrons are first generated by a cathode that is heated to ~1100 °C and injected into a linear particle accelerator. The linear particle accelerator consists of alternating electric fields that accelerate the electrons up to an energy of 450 MeV (at 450 MeV the electrons are traveling at > 99.999% the speed of light). The electrons are then introduced into the booster synchrotron ring where they are accelerated to 7 GeV in 0.5 sec by a ring of electromagnets. These electrons are injected into the storage ring which consists of more than 1,000 electromagnets that cause the electron beam to curve. The diameter of the storage ring at APS is ~1104 m, which is similar to most synchrotron storage rings.[6] X-ray radiation is generated tangential to the electron beam and can be extracted at the straight sections of the storage ring between the electromagnets.[5] Extraction points are referred to as beamlines. Such beamlines have equipment for various X-ray analyses such as XAS, X-ray diffraction, X-ray photoemission spectroscopy, and small angle X-ray scattering (SAXS). Each beamline is enclosed in an experiment hutch. At the APS, the spacing between the electromagnets is such that ~40 beamlines can be positioned around the storage ring. These beamlines and their experiment hutches are housed in the experiment hall, which surrounds the synchrotron storage ring.

The intensity and energy range of the X-ray radiation obtained at a given beamline can vary depending on the type of electromagnet used. The storage ring electromagnets are either bending magnets or insertion devices.[5] The X-ray beam generated when insertion devices are used has higher intensity and energy range than X-

ray radiation that is generated with a bending magnet. Two common types of insertion devices are wigglers and undulators. Wigglers consist of ~3-5 superconducting magnets which cause the electrons to travel in a local radius shorter than that of dipole bending magnets. This increases the energy of the X-rays generated from the electrons. An undulator is a multipole wiggler that uses either a transverse sinusoidal or helical magnetic field to accelerate electrons. The resulting X-ray radiation that is generated has the highest spectral intensity and power density.[5]

A typical XAS absorbance spectrum is provided in Figure B3. To simplify interpretation, the spectra are separated into two regions: X-ray absorption near-edge spectroscopy (XANES) and Extended X-ray absorption fine structure spectroscopy.[6,7]

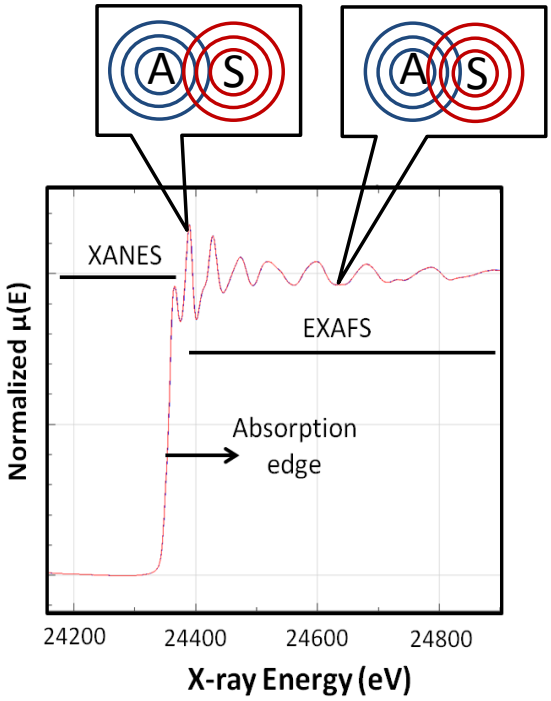

Figure B3. Example of typical XAS spectra in which the normalized absorption coefficient (μ) is plotted as a function of the X-ray beam energy (eV). XANES is X-ray absorption near-edge spectroscopy and EXAFS is extended X-ray absorption fine-structure spectroscopy. The callouts show the constructive and destructive interference between the photoelectron wave going out from absorbing atom, A, and the incoming photoelectron wave scattered by surrounding atom, S.[7]

The XANES region extends to X-ray beam energies within ~20-50 keV of the absorption edge.[6,7] The absorption in this region can be used to probe vacant orbitals and provide information concerning oxidation state and site symmetry of the absorbing atom. [10,14,15] The EXAFS region consists of absorbance at X-ray beam energies greater than 40 keV above the absorption edge.[5] In this region, quasiperiodic oscillations of X-ray absorbance occur due to interferences between the outgoing and scattered photoelectron wave. EXAFS provides information about the atomic number, coordination numbers, and interatomic bond distances of the atoms surrounding the X-ray absorbing atoms.[14,15] XANES analysis is generally qualitative while EXAFS analysis provides quantitative structural parameters.[6,7] A detailed explanation concerning the extraction of these structural parameters from EXAFS data is provided in the following section.

B3 Brief Overview of the Theory of EXAFS.

X-ray absorption by a given sample can be described using the Beer-Lambert law (Eqn. B1). The photoelectron wave vector, k, describes the photoelectron wave and can be expressed in terms of the kinetic energy, E_k, of the photoelectron as shown in Eqn. B4:[12]

$$k = \frac{(2m_e E_k)^{1/2}}{\hbar} \qquad \text{(B4)}$$

where m_e is the mass of the electron (~9.1×10^{-31} kg) and ħ is the reduced Planck's constant. Equation B5 shows that the kinetic energy of the photoelectron is the difference between the energy of the incoming photon ($E_{x\text{-}ray}$) and the binding energy of the core-level electron (E_b).

$$E_k = E_{X-ray} - E_b \qquad \text{(B5)}$$

The reduced Planck's constant (ħ) is calculated by dividing Planck's constant ($h \sim 6.6 \times 10^{-34}$ J/s) by 2π (Eqn. B6).

$$\hbar = \frac{h}{2\pi} \qquad \text{(B6)}$$

The photoelectron wave vector is proportional to the photoelectron momentum ($m_e\upsilon$) where υ is the velocity of the photoelectron wave. The de Broglie wavelength, λ, of the photoelectron is inversely proportional to the photoelectron momentum as shown in Equation B7.[16]

$$\lambda = \left(\frac{h}{m_e \upsilon}\right) \qquad \text{(B7)}$$

The absorption coefficient of an absorbing atom in the sample and the same absorbing atom in a free state (background absorption coefficient, μ_0) are functions of the wave vector, k, as shown in Eqn. B8.[5,8,12] The photoelectron function, $\chi(k)$, is a mathematical expression that refers only to the quasiperiodic modulations of the absorption coefficient, μ, so that only the EXAFS region of the XAS spectrum is considered.[16]

$$\chi(k) = \frac{\mu - \mu_0}{\mu_0} \qquad \text{(B8)}$$

The increase in μ at the edge, which is referred to as the step height, is proportional to the background absorption coefficient, μ_0. The step height is the difference between the minimum and maximum μ values at the same energy corresponding to the onset of the edge.[12] The absorption coefficient, μ_0, is approximated by fitting a spline function through the EXAFS data (quartic or cubic).[6] Further details concerning this analysis are available in reference 16.

As shown in Eqn. B9, the scattering of the absorbing atom's ejected photoelectron by surrounding coordinated atoms is mathematically expressed by the photoelectron function, $\chi(k)$, as:[5-8,12]

$$\chi(k) = \sum_j A_j(k) \sin\left[2kR_j + 2\delta_j(k)\right] \qquad \text{(B9)}$$

j indicates the number of coordination shells over which the function is summed, R_j is the distance between the central absorbing atom and scattering atoms in the j^{th} shell, $\delta_j(k)$ is the phase shift which can occur when electrons are scattered, and $A_j(k)$ is the amplitude for a given j coordination shell.[12] This amplitude is expressed (Eqn. B10) as:

$$A_j(k) = \left(\frac{N_j}{kR_j^2}\right) F_j(k) \exp(-2k^2\sigma_j^2) \qquad \text{(B10)}$$

where N_j is the number of atoms in the j^{th} coordination shell, σ_j is the root mean square deviation of R_j, and F_j is a factor accounting for the inelastic scattering and backscattering of electrons. The function exp $(-2k^2\sigma_j^2)$ is the Debye-waller factor, which accounts for the dampening effects of vibrational motion and structural disorder.[12] A consequence of these dampening effects is that EXAFS information is limited to atoms 4-5 Å from the X-ray absorbing atom.[6] EXAFS data is typically collected at low temperatures to minimize temperature-dependent vibration described by σ_j^2.[16] As seen in Eqn. B11, the factor, F_j, is element specific and is expressed as:[12]

$$F_j(k) = f(k) \times \exp\left(\frac{-2R_j}{\lambda_f}\right) \qquad \text{(B11)}$$

where f(k) is the inherent back-scattering amplitude of the X-ray absorbing atom and λ_f is the mean free path for photoelectron inelastic scattering.[16] These scattering factors are

typically calculated using the EXAFS data analysis programs described below. Such programs use *ab initio* calculations.[7]

By taking the Fourier transform of Eqn. B9, the radial structure function shown in Eqn. B12 can be derived.[12]

$$\emptyset_n(R) = \left(1/2\,\pi\right)^{1/2} \int_{k_{min}}^{k_{max}} k^n\,\chi(k)\exp(-2ikR)\,dk \qquad \text{(B12)}$$

R refers to the distance from the central absorbing atom, k^n is introduced to weight the data (n=1-3)) and compensate for the dampening effects expressed by the Debye-waller factor,[16] and k_{min} and k_{max} are the minimum and maximum k values, respectively, from the data.[12]

The EXAFS function, $\chi(k)$, is typically multiplied by the Hanning window function (HW) to account for termination errors which occur due to taking the Fourier transform over a limited range of k values (Eqn. B13). Only the regions of the EXAFS function corresponding to k values in the first and last 10% of the range of k values considered are multiplied with the Hanning window function.[12]

$$HW = \left(1/2\left\{1 - \cos 2\pi\left[\frac{(k - k_{min})}{(k_{max} - k_{min})}\right]\right\}\right) \qquad \text{(B13)}$$

The EXAFS contribution of a particular coordination shell can be ascertained by taking the inverse Fourier transform of the radial structure function over a range of R values corresponding to the desired coordination shell. For example, if the first coordination shell is considered to have R values between R_1'-ΔR and R_1' + ΔR then the inverse Fourier transform of Eqn. B12 would yield the EXAFS function $k^n \times \chi(k)$ for the first coordination shell as shown in Eqn. B14.[12]

$$k^n\chi_1(k) = \left(\frac{2}{\pi}\right)^{1/2} \int_{R_1-\Delta R}^{R_1+\Delta R} \emptyset_n(R)\exp(2ikR)dR \qquad \text{(B14)}$$

Using the expression for $\chi_1(k)$ in Eqn. B9, the EXAFS function $k^n\chi(k)$ can be written as (Eqn. B15):[12]

$$\chi_1(k) = k^n A_1(k)\sin[2kR_i + 2\delta_i(k)] \qquad \text{(B15)}$$

The phase shift, δ_1, is a function (k) as shown below in Eqn. B16:

$$\delta_1(k) = b + ak + a'k^2 + a''k^3 \qquad \text{(B16)}$$

As seen in Eqn. B17, the amplitude, $A_1(k)$ for the first coordination shell is expressed as:

$$A_1(k) = \left(\frac{N_1}{kR_1^2}\right)F_1(k)\exp(-2k^2\sigma^2) \qquad \text{(B17)}$$

The EXAFS signal for the first coordination shell is typically stronger than other coordination shells. This occurs because of the inverse dependence of the scattering amplitude on the distance, R, between the absorbing atom and scattering atoms.

The parameters in the last two equations are determined using an iterative least squares procedure to fit the theoretical EXAFS function, $k^n\chi_1(k)$ expressed by Eqn. B14, to the experimentally derived EXAFS function. Using this fitting method, the EXAFS function, $\chi_1(k)$, is expanded about a set of assumed parameters. Parameter variation terms higher than first order from the assumed parameter values are not included. The least squares condition (minimization of the residual sum) is then used to determine the parameter variations about the assumed value which give the best fit of the EXAFS function derived from the data.[6,7,12] There are currently more than 20 programs available that can be used to perform this calculation. The three most widely used programs are

FEFF, EXCURVE, and GNXAS. These programs use *ab initio* calculations to determine the scattering parameters.[6]

B4 References.

(1) Frenkel, A. I.; Hills, C. W.; Nuzzo, R. G. *J. Phys. Chem. B* **2001**, *105*, 12689.

(2) Bazin, D. C.; Sayers, D. A.; Rehr, J. J. *J. Phys. Chem. B* **1997**, *101*, 11040.

(3) Shekhar, M.; Wang, J.; Lee, W.-S.; Williams, W. D.; Kim, S. M.; Stach, E. A.; Miller, J. T.; Delgass, W. N.; Ribeiro, F. H. *J. Am. Chem. Soc.* **2012**, *134*, 4700.

(4) Thomson, J. W.; Cademartiri, L.; MacDonald, M.; Petrov, S.; Calestani, G.; Zhang, P.; Ozin, G. A. *J. Am. Chem. Soc.* **2010**, *132*, 9058.

(5) Lifshin, E. *X-ray Characterization of Materials*; Wiley, 2008.

(6) Penner-Hahn, J. E. X-ray Absorption Spectroscopy. In *eLS*; John Wiley & Sons, Ltd, 2001.

(7) Newville, M. Fundamentals of XAFS. In *Consortium for Advanced Radiation Sources* University of Chicago, Chicago, IL, 2004.

(8) Hollas, J. M. *Modern Spectroscopy*, Fourth ed.; Wiley, 2007.

(9) Van Grieken, R.; Markowicz, A. *Handbook of X-Ray Spectrometry*, Second ed.; Taylor & Francis, 2001.

(10) Singh, J.; Lamberti, C.; van Bokhoven, J. A. *Chem. Soc. Rev.* **2010**, *39*, 4754.

(11) Marx, S.; Baiker, A. *J. Phys. Chem. C* **2009**, *113*, 6191.

(12) Via, G. H.; Drake, K. F.; Meitzner, G.; Lytle, F. W.; Sinfelt, J. H. *Catal. Lett.* **1990**, *5*, 25.

(13) Skoog, D. A.; Holler, F. J.; Nieman, T. A. *Principles of Instrumental Analysis*, Fifth ed.; Thomson Learning, Inc. Brooks/Cole: Bangalore, 2005.

(14) Ferrando, R.; Jellinek, J.; Johnston, R. L. *Chem. Rev.* **2008**, *108*, 845.

(15) Toshima, N.; Yonezawa, T. *New J. Chem.* **1998**, *22*, 1179.

(16) Que, L. *Physical Methods in Bioinorganic Chemistry: Spectroscopy and Magnetism*; Univ. Science Book, 2000.

Appendix C

Supporting Information for Chapter 3

C1 Tables.

Table C1. Synthesis and Pd metal content of 3 nm Pd-on-Au NPs.[a]

Pd surface coverage (SC%)	Volume of $PdCl_4^{2-}$ precursor (µL)[b]	Pd metal content (mol%)[c]
10	13	6.1
30	40	16.2
50	66	24.4
70	89	30.2
90	119	36.7
100	133	39.2
110	146	41.5
150	199	49.2
175	232	53.0
200	265	56.3

[a] All calculations are based on the magic cluster model.
[b] Volumes shown are for addition of a 2.47 mM $PdCl_4^{2-}$ solution to 2 mL of Au NP sol.
[c] Pd metal content of one nanoparticle.

Table C2. Magic cluster model calculations for different sized Au particles.

Shell number (n)	Number of atoms in shell (n_{atom})[a]	Total number of atoms per NP (n_{tot})[b]	Calculated particle diameter (nm)
	1	1	0.27
1	12	13	0.81
2	42	55	1.35
3	92	147	1.89
4	162	309	2.43
5	252	561	2.97
6	362	923	3.51
7	492	1415	4.05
8	642	2057	4.59
9	812	2869	5.13
10	1002	3871	5.67
11	1212	5083	6.21
12	1442	6525	6.75
13	1692	8217	7.29
14	1962	10179	7.83
15	2252	12431	8.37

[a] $n_{atom} = 10n^2 + 2$

[b] $n_{tot} = (10n^3 + 15n^2 + 11n + 3)/3$

Table C3. Concentration of Pd and Au surface atoms of nanocatalysts.[a]

Pd surface coverage (SC%)	Concentration of Au surface atoms ($\times 10^{-8}$M)[b]	Concentration of Pd surface atoms ($\times 10^{-8}$M)[b]
0[c]	7.6	-
10	1.6	0.26
30	1.3	0.77
50	0.90	1.3
70	0.59	1.7
90	0.18	2.3
100	-	2.5
110	-	2.6
150	-	2.9
175	-	3.1
200	-	3.5
Pure 4 nm Pd NP control[d]	-	14.8

[a] All calculations are based on the magic cluster model.
[b] Concentrations shown were used to calculate reported catalyst TOF values.
[c] A larger volume of as-prepared particle sol (~206 µL) was used for the pure Au NP control.
[d] A larger volume of the as-prepared sol (~446 µL) was used for the pure Pd NP control.

Table C4. Reported Au nanomaterial activity for 4-nitrophenol (4-NL) reduction.

Reference	Sample	Turnover Frequency[a] (mol 4-NL/mol surface atom/min)
This work	3 nm Au NPs	40.3
Kuroda, *et al.*; *J. Molec. Catal. A* 298, (2009) 7.	6.9 nm Au NPs on PMMA beads[b]	31.7
Panigrahi, *et al.*; *J. Phys. Chem. C* 111, (2007) 4596.	Au NPs on resin beads	8 nm Au NPs: 0.22 20 nm Au NPs: 0.32 55 nm Au NPs: 0.17
Damato, *et al.; Langmuir* web published	Au NPs on TiO_2 particles	12.2 nm Au NPs: 4.6 19.3 nm NPs: 7.4
Feng, *et al., Colloid Polym. Sci.* web published	2.45 nm Au NPs inPAMAM dendrimers[b]	Gen. 1-37.3
Nemanashi, *et al. J. Colloid Interface Sci.* 389, (2013), 260.	3.1 nm Au NPs in PAMAM dendrimers[b]	402.3
Li, *et al. J. Mater. Chem.* 22, (2012), 8426.	16 nm Au NPs in Au/graphene hydrogel	4.3
Jan, *et al. Langmuir* 27, (2011), 2834.	5 nm Au NPs on mesoporous silica tubular nanostructures	16.7
Huang, *et al. J. Phys. Chem. C* 113, (2009), 13636.	Cyclodextrin-capped Au NPs	11 nm Au NPs: 11.0 20 nm Au NPs: 14.6 26 nm Au NPs: 16.2
Liu, *et al. Chem. Eur. J.* 12, (2006), 2131.	Glucose-stabilized 8 nm Au NPs	2.0
Lu, *et al. J. Hazard. Mater.* 197, (2011), 320.	Au NPs on graphene oxide nanosheets	6 nm Au NPs: 1.7 15 nm Au NPs: 4.1
Zeng, *et al. Nano Lett.* 10, (2010), 30.	Au NP suspensions from Ted Pella	5 nm Au NPs: 63.2 50 nm Au NPs: 52.4
Lee, *et al. Adv. Mater.* 20, (2008), 1523.	Au NPs in Au@SiO_2 yolk/shell structures	104 nm Au NPs: 103.8 67 nm Au NPs: 248.4 43 m Au NPs: 426.6

[a] All calculations are based on the magic cluster model.
[b] PMMA = poly (methyl methacrylate); PAMAM = Poly(amido amine)

Table C5. Reported Pd and Pd-Au NP activity for 4-nitrophenol reduction.

Reference	Sample	Turnover Frequency[a] (mol 4-NL/mol surface atom/min)
This work	4 nm Pd NPs	16.7
This work	3 nm Au NPs with 150% Pd surface coverage	222.4
Arora, *et al.*; *Reac. Kinet. Mech. Catal.* 99, (2010), 157.	6.0 nm Pd NPs on Al_2O_3	0.87
Bhandari, *et al.*; *ACS Catal.* 1, (2011), 89.	2.6 nm Pd NPs in peptide	4.9
Mei, *et al. Chem. Mater.* 19, (2007), 1062.	2.4 nm Pd NPs in polyelectrolyte brushes	2.4 nm Pd NPs: 0.50
Xue, *et al. J. Colloid Interface Sci.* 379, (2012), 89.	2-4 nm Pd NPs in nanocapsules[b]	44.6
Yuan, *et al. Polymer* 53, (2012), 43.	2.5 nm Pd NPs on polymer brushes	273.5
Behrens, *et al. Adv. Mater.* 21, (2009), 3515.	2.85 nm Pd NPs in protein complexes	11.8
Esumi, *et al. Langmuir* 20, (2004), 237.	1.6 nm Pd NPs in Gen.4 PAMAM dendrimers[c]	1.7
Morère, *et al. J. Supercrit. Fluids* 56, (2011), 213.	6.0 nm Pd NPs in mesoporous silica	4.4
Lu, *et al. J. Mater. Chem.* 22, (2012), 12723.	2.0 nm Pd NPs on polypyrrole-TiO_2 nanofibers	4.4
Li, *et al. Green Chem.* 14, (2012), 586.	Pd NPs on carbon nanotubes	2.7 nm Pd NPs: 14.1 51 nm Pd NPs: 192.78
Tang, *et al. J. Colloid Interface Sci.* 375 (2012), 125.	4 nm Pd-Au NPs on carbon nanocomposites	0.174
Zhao, *et al. J. Colloid Interface Sci.* 331 (2009), 104.	6 nm Pd-Au NP on polymer nanocomposites	7.9

[a] All calculations are based on the magic cluster model.
[b] Nanoparticles were modeled as 3 nm Pd NPs.
[c] PAMAM = Poly(amido amine)

Table C6. 3 nm Pd-on-Au NPs with 200% Pd SC EXAFS fit parameters-Au Edge.

Treatment	Scattering Path	CN[b] (±10%)	R, Å[c] (±0.02 Å)	DWF[d] ($\times 10^3$ Å^2)	E_0, eV[e]
H_2, RT[a]	Au-Au	9.1	2.85	0	-0.1
	Au-Pd	2.1	2.78	0	4.0
H_2, 200°C	Au-Au	8.9	2.84	0	0.3
	Au-Pd	2.4	2.78	0	3.1

[a] No change in structure occurs under these conditions.[1]
[b]CN:coordination number
[c] R: bond distance
[d] DWF: Debye-waller factor
[e] E_0: threshold absorption edge energy

Table C7. 3 nm Pd-on-Au NPs with 200% Pd SC EXAFS fit parameters-Pd Edge.

Treatment	Scattering Path	CN[a] (±10%)	R, Å[b] (±0.02 Å)	DWF[c] ($\times 10^3$ Å^2)	E_0, eV[d]
H_2, RT	Pd-Pd	3.6	2.72	-1.0	-6.2
	Pd-Au	7.8	2.78	-1.0	-3.7
H_2, 200°C	Pd-Pd	4.0	2.72	-1.0	-4.1
	Pd-Au	7.6	2.78	-1.0	-3.5

[a] CN:coordination number
[b] R: bond distance
[c] DWF: Debye-waller factor
[d] E_0: threshold absorption edge energy

C2 Figures.

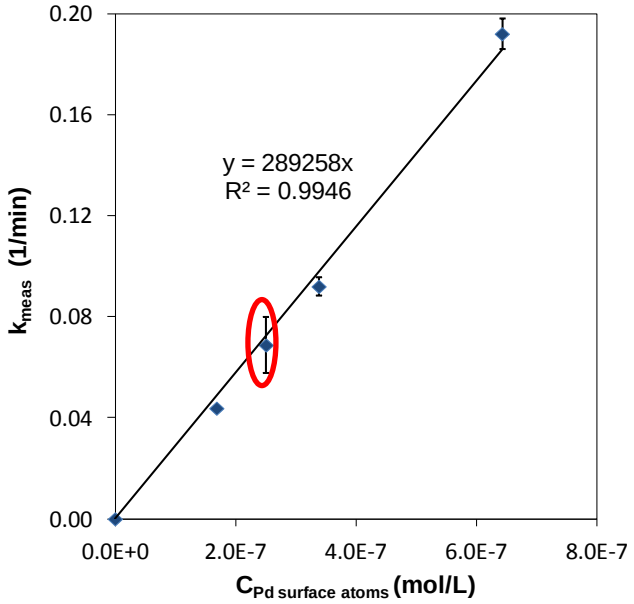

Figure C1. Observed pseudo-first order rate constant (k_{meas}) of pure 4 nm Pd NPs as a function of the concentration of Pd surface atoms (mol/L). The circle denotes the surface concentration in the cuvette when 446 µL of as-prepared sol is used to prepare the diluted sol. Error bars represent the standard deviation of at least three replicate experiments.

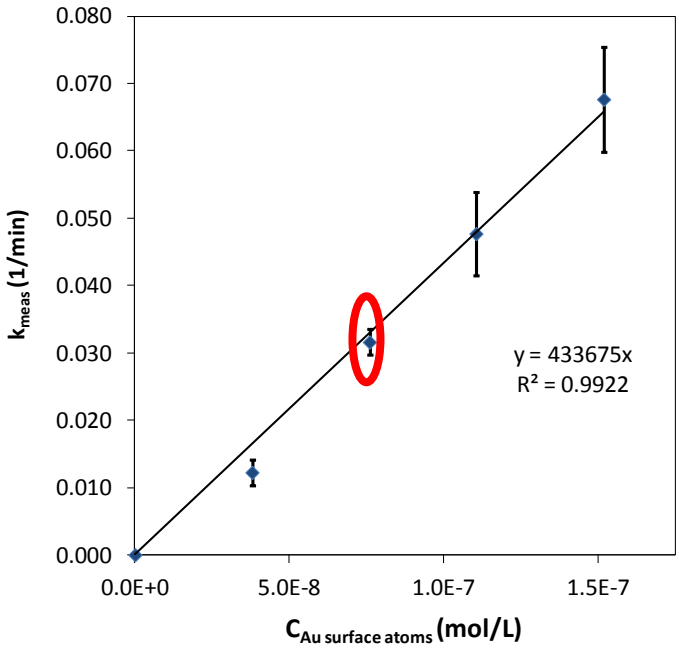

Figure C2. Observed pseudo-first order rate constant (k_{meas}) of pure 3 nm Au NPs as a function of the concentration of Au surface atoms (mol/L). The circle denotes the surface concentration in the cuvette when 206 µL of as-prepared sol is used to prepare the diluted sol. Error bars represent the standard deviation of at least three replicate experiments.

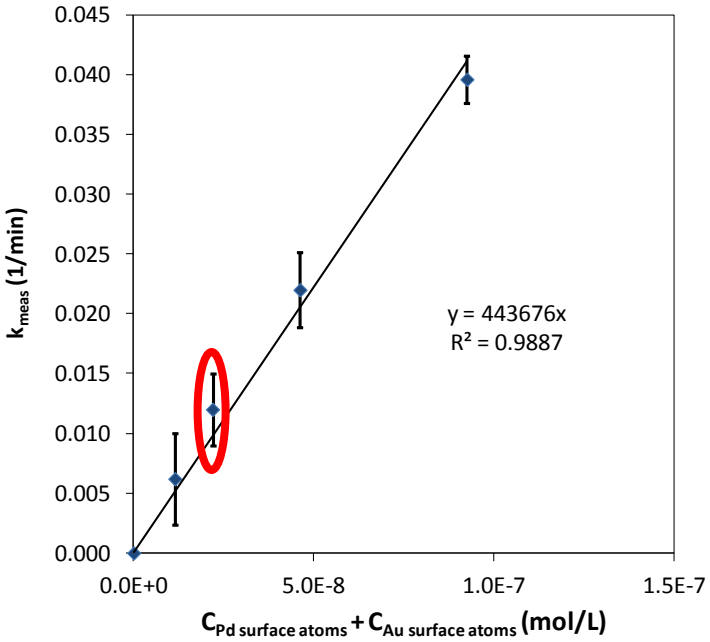

Figure C3. Observed pseudo-first order rate constant (k_{meas}) of 3 nm Pd-on-Au NPs with 50% Pd SC as a function of the concentration of Pd and Au surface atoms (mol/L). The circle denotes the surface concentration in the cuvette when 51 µL of as-prepared sol is used to prepare the diluted sol. This was the as-prepared sol volume used for all 3 nm Pd-on-Au NP experiments. Error bars represent the standard deviation of at least three replicate experiments.

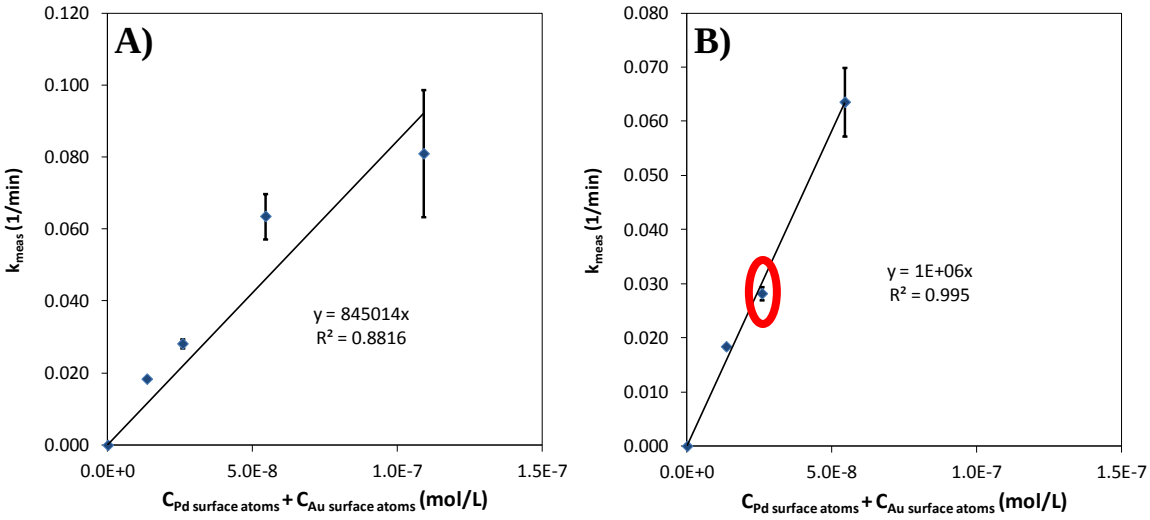

Figure C4. (A) Observed pseudo-first order rate constant (k_{meas}) of 3 nm Pd-on-Au NPs with 100 % Pd SC as a function of the concentration of Pd and Au surface atoms (mol/L). (B) Panel a replotted showing linearity between total surface atom concentrations of 1.4×10^{-8} M and 5.4×10^{-8}M. The circle denotes the surface concentration in the cuvette when 51 µL of as-prepared sol is used to prepare the diluted sol. This was the as-prepared sol volume used for all 3 nm Pd-on-Au NP experiments. Error bars represent the standard deviation of at least three replicate experiments.

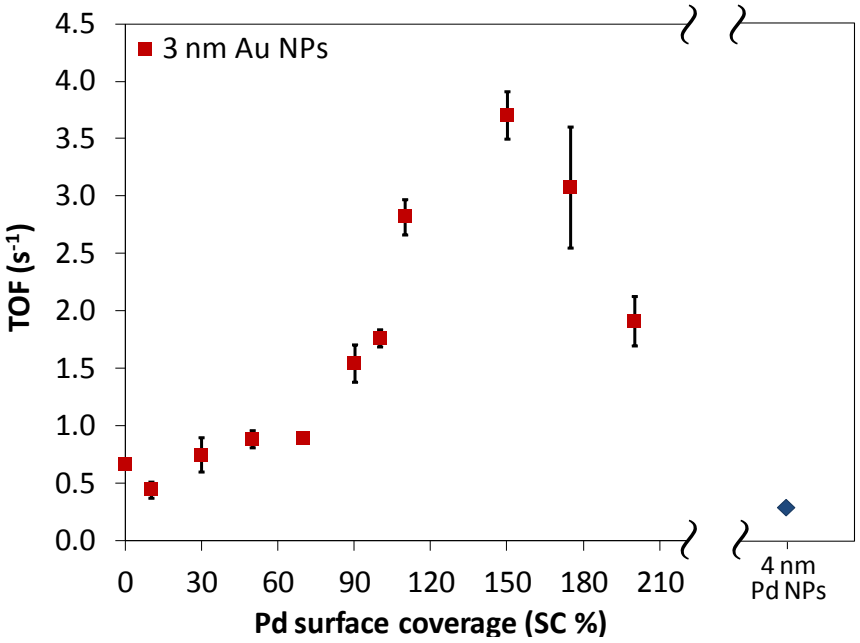

Figure C5. TOF's of 3 nm Pd-on-Au NPs with Pd surface coverages from 0 to 200% Pd SC. NPs with 0% Pd SC are pure 3 nm Au NPs. The TOF of pure 4 nm Pd NPs is included for comparison. Error bars represent the standard deviation of at least three replicate experiments.

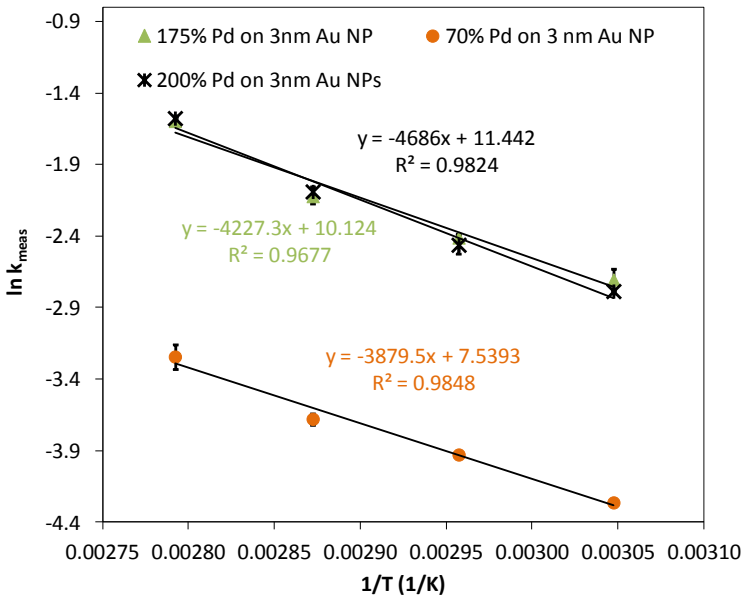

Figure C6. Arrhenius plot ($\ln k_{meas}$ as a function of 1/T) of Pd-on-Au NPs with Pd SC of 70%, 175%, and 200%. Error bars represent the standard deviation of at least three replicate experiments.

C3 Equations.

$$BH_4^-(aq) + 8OH^-(aq) \rightarrow BO_2^-(aq) + 6H_2O(l) + 8e^- \quad (E° = 1.241V) \quad (C1)^2$$

$$4PdO(s) + 8H^+(aq) + 8e^- \rightarrow 4Pd(s) + 4H_2O(l) \quad (E° = 0.79\ V) \quad (C2)^2$$

$$BH_4^-(aq) + 4PdO(s) \rightarrow 4Pd(s) + BO_2^-(aq) + 2H_2O(l) \quad (E° = 0.45\ V) \quad (C3)$$

Equations C4-C7 were used to calculate alloy particle coordination numbers.[1,3]

$$Au\text{-}Au_{alloy}\ CN = \text{total Au CN} \times \text{mol\% Au} = 4.9 \quad (C4)$$

$$Au\text{-}Pd_{alloy}\ CN = \text{total Au CN} \times \text{mol\% Pd} = 6.3 \quad (C5)$$

$$Pd\text{-}Pd_{alloy}\ CN = \text{total Pd CN} \times \text{mol\% Pd} = 6.4 \quad (C6)$$

$$Pd\text{-}Au_{alloy}\ CN = \text{total Pd CN} \times \text{mol\% Au} = 5.0 \quad (C7)$$

C4 References.

(1) Fang, Y.-L.; Miller, J. T.; Guo, N.; Heck, K. N.; Alvarez, P. J. J.; Wong, M. S. *Catal. Today* **2011**, *160*, 96.

(2) *Standard Potentials in Aqueous Solution*; Bard, A. J.; Parsons, R.; Jordan, J., Eds.; Marcel Dekker Inc.: New York, 1985, pp 195.

(3) Pretzer, L. A.; Song, H. J.; Fang, Y.-L.; Zhao, Z.; Guo, N.; Wu, T.; Arslan, I.; Miller, J. T.; Wong, M. S. *J. Catal.* **2013**, *298*, 206.

Appendix D

Influence of Size on Catalysis of Pd-on-Au Nanoparticles for Nitroarene Reduction

D1 Introduction.

We have previously demonstrated through x-ray absorbance spectroscopy (XAS) that Pd-on-Au nanoparticles (NPs) can be synthesized with controlled size and surface composition.[1] XAS analysis of 3, 7, and 10 nm Pd-on-Au NPs with Pd surface coverages (Pd SCs) between 30 and 150% showed that Pd surface atom dispersion and oxidation state change as a function of Pd surface coverage and Au particle size.[1] As the Pd surface coverage increases, one-dimensional (1-D), 2-D, and 3-D Pd ensembles progressively form; however, at a given Pd SC, Pd ensembles on larger NPs are more disperse and metallic.

In Chapter 3, we conclude that 3-D Pd ensembles on 3 nm Au NPs enhance the catalytic activity of Au nanoparticles for 4-nitrophenol (4-NL) reduction. Here, we further explore this conclusion by testing the activity of 7 nm Pd-on-Au NPs. Since the Pd ensembles are more disperse and metallic on these NPs, we expect their catalytic activity to be lower than similar 3 nm Pd-on-Au NPs. Comparing the activity of the pure 3 nm and pure 7 nm Au NPs also provides insight concerning the role of quantum size effects on the catalytic activity of Au NPs.

D2 Experimental Section.

Details concerning the synthesis of the 7 nm Pd-on-Au NPs can be found in Chapter 2. The same general experiment procedure used for the 3 nm Pd-on-Au NP 4-NL reduction experiments reported in Chapter 3 are used here for the 7 nm NPs. For 7 nm Pd-on-Au NP studies, 212 uL of as-prepared Pd-on-Au NP sols were diluted with 9.78 mL of H_2O to prepare a diluted NP sol (total Au concentration = 5.4×10^{-6} M; 1.0 ppm and total Pd

concentration = 6.4×10^{-7} M; 0.13 ppm – 2.6×10^{-6} M; 0.51 ppm). An aliquot (~100 µL) of the diluted sol was injected into the reactor as previously reported for the 3 nm Pd-on-Aui NPs. The final concentration of Pd-on-Au NPs in the reactor was 1.3×10^{13} NPs/mL. No UV-Vis absorbance by the NPs was detected at this concentration. The final concentration of total Au in the reactor was 1.7×10^{-7} M while the total concentration of Pd ranged from 2.1×10^{-8} M to 8.4×10^{-8} M, depending on the Pd surface coverage.

As a control, a diluted 7 nm Au NPs sol (552 µL as prepared Au NP sol diluted with 9.45 mL H_2O) was prepared and 100 µL of the diluted sol was injected into the quartz reactor (final Au concentration in reactor = 4.5×10^{-7} M; 0.89 ppm). No UV-Vis absorbance by the NPs was detected at this concentration. The concentration of Pd and Au surface atoms used for the reported 7 nm Au NP and Pd-on-Au NP turnover frequencies (TOFs) are provided in Table D1.

Table D1. Concentration of Pd and Au surface atoms of 7 nm Pd-on-Au NPs.[a]

Pd surface coverage (SC%)	Concentration of Au surface atoms ($\times10^{-8}$M)[b]	Concentration of Pd surface atoms ($\times10^{-8}$M)[b]
0[c]	9.3	-
50	1.8	2.0
70	1.2	2.8
90	0.36	3.7
100	-	4.15
110	-	4.2
150	-	4.4
175	-	4.6
200	-	4.8

[a] All calculations are based on the magic cluster model.
[b] Concentrations shown were used to calculate reported catalyst TOF values.
[c] A larger volume of the as-prepared particle sol (~552 µL) was used for the pure Au NP control.

As shown in Figures D1-D3, the measured pseudo-first order rate constant (k_{meas}) for 4-nitrophenol reduction varied linearly with the concentration of Pd and Au surface

atoms for pure 7 nm Au NPs and representative Pd-on-Au NPs. TOFs of 7 nm pure Au NPs and Pd-on-Au NPs were therefore calculated as previously described Chapter 3.

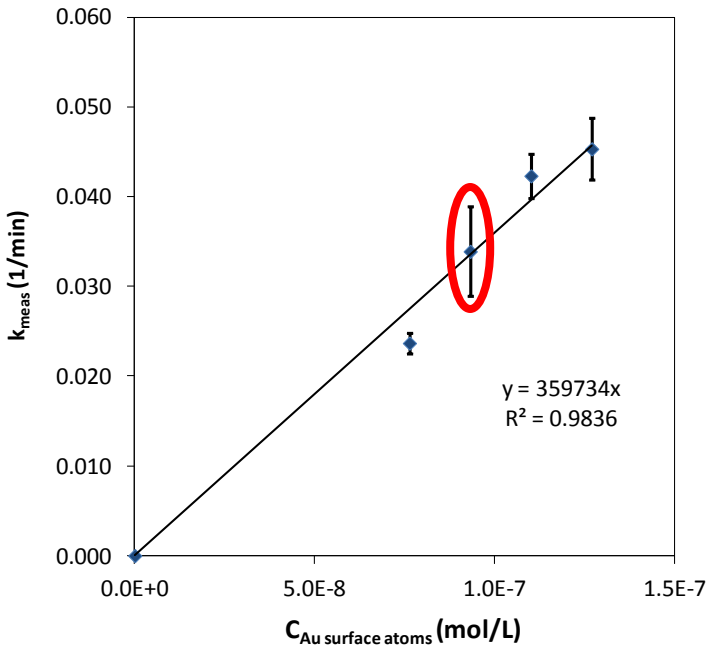

Figure D1. Observed pseudo-first order rate constant (k_{meas}) of pure 7 nm Au NPs as a function of the concentration of Au surface atoms (mol/L). The circle denotes the surface concentration in the cuvette when 552 µL of as-prepared sol is used to prepare the diluted sol. Error bars represent the standard deviation of at least three replicate experiments.

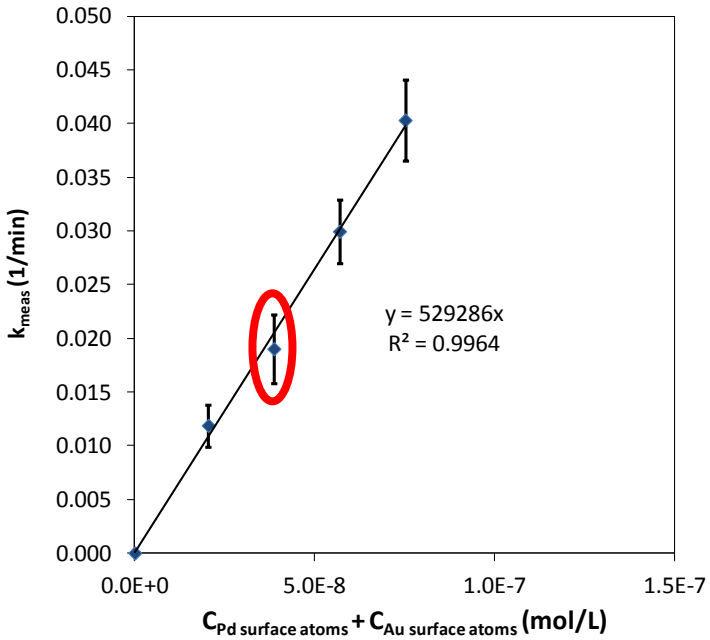

Figure D2. Observed pseudo-first order rate constant (k_{meas}) of 7 nm Pd-on-Au NPs with 50% Pd SC as a function of the concentration of Pd and Au surface atoms (mol/L). The circle denotes the surface concentration in the cuvette when 212 µL of as-prepared sol is used to prepare the diluted sol. This was the as-prepared sol volume used for all 7 nm Pd-on-Au NP experiments. Error bars represent the standard deviation of at least three replicate experiments.

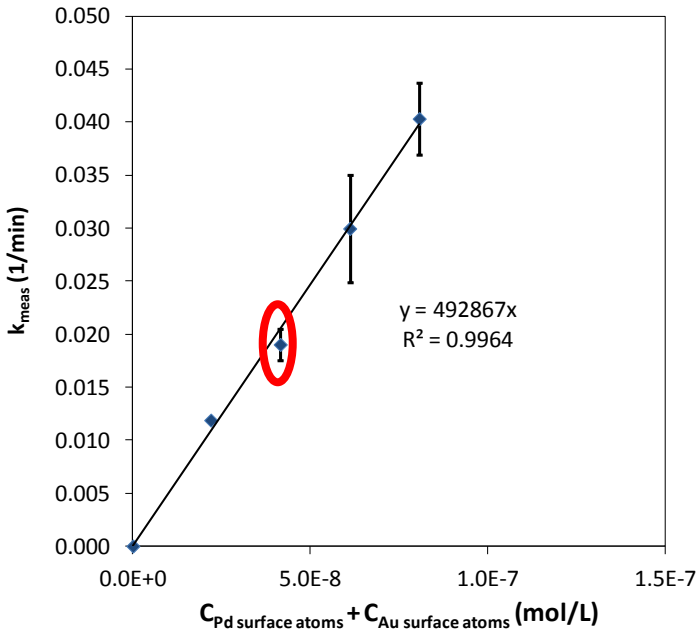

Figure D3. Observed pseudo-first order rate constant (k_{meas}) of 7 nm Pd-on-Au NPs with 100% Pd SC as a function of the concentration of Pd and Au surface atoms (mol/L). The circle denotes the surface concentration in the cuvette when 212 µL of as-prepared sol is used to prepare the diluted sol. This was the as-prepared sol volume used for all 7 nm Pd-on-Au NP experiments. Error bars represent the standard deviation of at least three replicate experiments.

D3 Results and Discussion.

To qualitatively test if 3-D Pd ensembles are important for 4-nitrophenol reduction, we analyzed the catalytic activity of larger 7 nm Pd-on-Au NPs since more disperse Pd ensembles with less oxidized Pd are formed on these NPs at Pd SC >70% (in comparison to similar 3 nm Pd-on-Au NPs).[1] The UV-Vis absorbance spectra for the 7 nm Au NPs and Pd-on-Au NPs were similar to the spectra reported in Chapter 3 for 3 nm NPs. The Damköhler number of the 7 nm NPs was calculated as shown in Eqn. 3.4 in Chapter 3. The Damköhler number of all the 7 nm NPs was $<1\times10^{-17}$ which indicates that the reaction is not diffusion-limited.

The catalytic activity of 7 nm Pd-on-Au NPs varied with Pd SC such that the TOF of NPs with Pd SC ≥90% exceeded that of NPs with Pd SC≤70% (Figure D4). The

activity of the 7 nm Pd-on-Au NPs does not exhibit the same volcano-shape dependence on Pd surface coverage as the 3 nm Pd-on-Au NPs. This is ascribed to the difference in the dispersion and oxidation of the Pd surface ensembles at a given Pd surface coverage which occurs as a consequence of particle size. The similar activity exhibited by pure 3 nm and 7 nm Au NPs (TOF ~ $0.6 s^{-1}$) indicates that quantum size effects do not significantly affect catalysis of Au nanoparticles for 4-nitrophenol reduction.

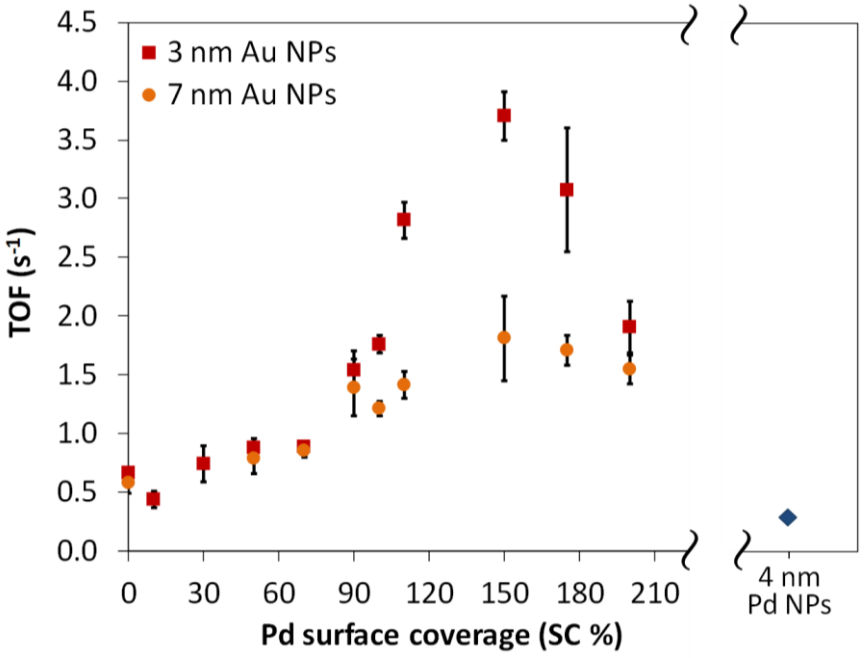

Figure D4. TOF's of 3 nm and 7 nm Pd-on-Au NPs with Pd surface coverages from 0 to 200% Pd SC. NPs with 0% Pd SC are pure 3 nm and pure 7 nm Au NPs. The TOF of pure 4 nm Pd NPs is included for comparison. Error bars represent the standard deviation of at least three replicate experiments.

The catalytic activity of NPs with Pd SC≤70% did not vary significantly with Pd SC and was similar to that of analogous 3 nm NPs. The TOF of 7 nm NPs with Pd SC>70% (~ $1.8 s^{-1}$) exceeded that of pure Pd NPs and pure 3 nm and 7 nm Au NPs. At Pd SC between 90 and 175%, the 7 nm Pd-on-Au NPs exhibited a much lower TOF than analogous 3 nm Pd-on-Au NPs. The slightly higher activity of the 7 nm Pd-on-Au NPs at Pd SC >90% than pure 7 nm Au NPs is likely due to the formation of 3-D Pd ensembles;

however these ensembles are more disperse and have less oxidized Pd than analogous 3-D ensembles on 3 nm Pd-on-Au NPs. Therefore, the activity of 7 nm Pd-on-Au NPs with Pd SC~90-150% is lower than the activity of similar 3 nm Pd-on-Au NPs. The similar activity of 7 nm and 3 nm Pd-on-Au NPs with 200% could indicate that surface Pd and Au atom alloying begins to occur at this surface coverage on 7 nm Pd-on-Au NPs. Such activity trends qualitatively support our hypothesis that the more aggregated 3-D Pd ensembles formed on 3 nm Pd-on-Au NPs with Pd SC between 90 and 150% are important for the catalytic reduction of 4-nitrophenol.

D4 Conclusions and Future Works.

The activity exhibited by 7 nm Pd-on-Au NPs agrees with our conclusion in Chapter 3 that the 3-D Pd ensembles on the surface of 3nm Pd-on-Au NPs with Pd SC~90-150% enhance the catalytic activity of Au for 4-nitrophenol reduction. The pure 3 nm and pure 7 nm Au NPs exhibit similar activity, which strongly suggests that quantum size effects do not significantly influence the catalytic activity of Au NPs for 4-nitrophenol reduction. The similar activity exhibited by 7 nm and 3 nm Pd-on-Au NPs with Pd SC <70% indicates that the presence of Pd monomers and two-dimensional Pd ensembles do not significantly improve Au nanoparticle activity for nitrophenol reduction. The activity of 7 nm Pd-on-Au NPs with Pd SC~90-150% is lower than similar 3 nm Pd-on-Au NPs. This agrees with our prediction that the 7 nm Pd-on-Au NPs will exhibit lower activity because of the higher dispersion of Pd ensembles formed on the 7 nm NPs. It would be interesting to analyze the activation energy of 7 nm Pd-on-Au NPs to see if these nanoparticles exhibit compensation behavior analogous to the 3 nm Pd-on-Au NPs.

Furthermore density functional theory calculations to compare the surface d-band center of 3 nm and 7 nm Pd-on-Au NPs would provide further insight into the results obtained.

D5 References.

(1) Pretzer, L. A.; Song, H. J.; Fang, Y.-L.; Zhao, Z.; Guo, N.; Wu, T.; Arslan, I.; Miller, J. T.; Wong, M. S. "Hydrodechlorination Catalysis of Pd-on-Au Nanoparticles Varies with Particle Size" *J. Catal.* **2013**, *298*, 206-217.

Appendix E

Supporting Information for Chapter 4

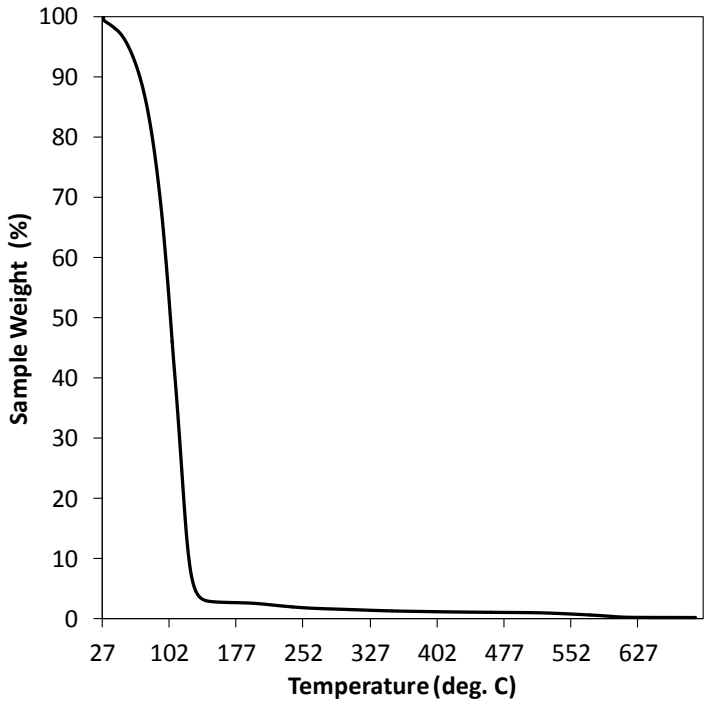

Figure E1. Thermogravimetric analysis of as-prepared alginate beads.

A)

Specific Activity of Enzyme or TE-PGN Alginate Beads

	Enzyme + Alginate	Au NR + Enzyme + Alginate
Laser	1.4 ± 0.055	1.9 ± 0.087
No Laser	1.3 ± 0.031	1.2 ± 0.035

B)

Specific Activity of Enzyme or TE-PGNs

	Enzyme	Au NR + Enzyme
Laser	9.3 ± 1.1	13.4 ± 1.19
No Laser	9.2 ± 0.55	12.8 ± 1.96

Figure E2. (A) Specific activity (μmol min^{-1} mg^{-1}) of glucokinase Ca-alginate beads (enzyme + alginate) and the TE-PGN Ca-alginate beads (Au NR + enzyme + alginate) with laser irradiation (laser, 15 W) *vs.* no laser irradiation (respective bulk temperature controls). 5 beads were used per reaction run. (B) Specific activity (μmol min^{-1} mg^{-1}) of unencapsulated glucokinase only (enzyme) or the TE-PGNs (Au NR + enzyme) with laser irradiation (laser, 15 W) *vs.* no laser irradiation (respective bulk temperature controls). For both panels, standard deviations represent 3 replicates and bulk temperatures were 42 °C for all enzyme experiments and 44 °C for all TE-PGN experiments.

Appendix F

Supporting Information for Chapter 5

F1 Method for Detecting CO_2 After Seeded Growth Experiment.

Production of CO_2 was confirmed by preparing Sample 10 in a sealed glass vial and analyzing the vial head-space using an Agilent Technologies 6890 gas chromatograph (GC) equipped with a thermal conductivity detector and a packed column (ResTek PC 3533). Prior to CO introduction, the seed NPs and Au salt solution was purged with argon for 15 min so that no CO_2 was initially present. Injections (100 uL) from the vial head-space before and after CO introduction showed that CO_2 was formed following CO introduction and in tandem with seed NP growth. The experiment was repeated three times to ensure reproducibility.

F2 Small Angle X-ray Scattering Data Analysis.

Since the grown NPs appeared spherical in TEM images, the SAXS intensity, I(q), depends upon the form factor, F(q,D), for spherical particles and the Γ-distribution function, $P(D,D_0,\sigma)$ as seen in Equation F1.[1] The fraction, D_0^3/D^3, is included so that the distribution is represented in terms of a volume fraction. The form factor is the fourier transform of a sample's electron density fluctuations which vary with the particles' form.[1,2] As seen in Equation F2, the form factor depends upon Δp, the difference in electron density between the particles and surrounding media, D, particle diameter, and q, the scattering vector.

$$I(q)=\int_0^\infty |F(q,D)|^2 \times P(D, D_0,\sigma)\frac{D_0^3}{D^3}dD \qquad \text{(F1)}$$

$$F(q,D)=\Delta p\frac{4\pi}{q^3}\left(\sin\left[\frac{qD}{2}\right]-\frac{qD}{2}\cos\left[\frac{qD}{2}\right]\right) \qquad \text{(F2)}$$

q is related to the scattering angle, θ, and the incident X-ray wavelength, λ, as shown in Equation F3.

$$q = \frac{4\pi}{\lambda}\sin\theta \qquad \text{(F3)}$$

The distribution of particle sizes is expressed as the gamma (Γ)-distribution function, $P(D, D_0, \sigma)$, which as seen in Equation F4 depends upon the particle diameter, D, average particle diameter, D_0, and the normalized variance, σ.[1]

$$P(D, D_0, \sigma) = \frac{1}{\Gamma\left(\frac{1}{\sigma^2}\right)}\left(\frac{1}{\sigma^2 D_0}\right)^{1/\sigma^2} D^{-1+1/\sigma^2}\exp\left[-\frac{D}{D_0\sigma^2}\right] \qquad \text{(F4)}$$

F3 Tables.

Table F1. Particle diameters (nm) for controls with no seed NPs.

Sample	UV-Vis[a]	TEM Mean[b]	TEM Mode	SAXS Mean[b]	SAXS Mode
1	21.5 (0.5%)	–	–	12.1 ± 7.4	7.5
2	25.5 (7.4%)	–	–	13.8 ± 9.0	7.9
3	24.0 (5.0%)	–	–	15.4 ± 9.8	9.2
4	22.4 (4.1%)	–	–	16.2 ± 9.4	10.8
5	19.4 (5.0%)	23.9 ± 6.1	16.9	15.7 ± 7.4	12.2
6	18.0 (5.0%)	–	–	18.1 ± 10.2	12.7
7	16.3 (4.0%)	–	–	19.0 ± 10.6	13.2
8	15.7 (1.9%)	–	–	18.0 ± 8.7	13.8
9	15.8 (2.4%)	–	–	20.7 ± 12.0	13.9
10	16.1 (3.2%)	19.4 ± 5.6	23.7	19.9 ± 9.6	15.3

[a] Sizes calculated from absorbance spectra using Eqn. 5.2 in Chapter 5. RSDs (%) represent experimental error between three separate syntheses.
[b] Size distributions represent one standard deviation.

Table F2. Particle diameters for controls with no CO bubbling.

Sample	UV-Vis[a,b]	TEM Mean[c]	TEM Mode	SAXS Mean[c]	SAXS Mode
1	2.6 (4.0%)	–	–	3.2 ± 1.2	2.8
2	3.0 (7.0%)	–	–	3.2 ± 1.2	2.8
3	2.9 (6.0%)	–	–	3.2 ± 1.2	2.8
4	2.9 (4.0%)	–	–	3.2 ± 1.2	2.8
5	2.9 (10.0%)	4.5 ± 1.6	3.9	3.2 ± 1.2	2.8
6	3.1 (9.0%)	–	–	3.2 ± 1.2	2.8
7	3.4 (14.0%)	–	–	3.2 ± 1.2	2.8
8	3.3 (15.0%)	–	–	3.2 ± 1.2	2.8
9	3.3 (17.0%)	–	–	3.2 ± 1.2	2.8
10	3.3 (12.0%)	4.0 ± 1.2	3.3	3.2 ± 1.2	2.8

[a] Sizes calculated from absorbance spectra using Eqn. 5.2 in Chapter 5. RSDs (%) represent experimental error between three separate syntheses.
[b] Values outside the size range for Eqn 5.2 in Chapter 5.
[c] Size distributions represent one standard deviation.

Table F3. pH of sample sols before and after CO bubbling.[a]

Sample	Initial pH	Final pH
Seed particles	6.3	6.3
1	6.9	5.8
2	7.0	5.9
3	7.1	6.1
4	7.2	6.2
5	7.2	6.5
6	7.2	6.4
7	7.3	6.4
8	7.3	6.5
9	7.4	6.5
10	7.4	6.7

[a] RSD for all measurements is ±1.6%.

F4 Figures.

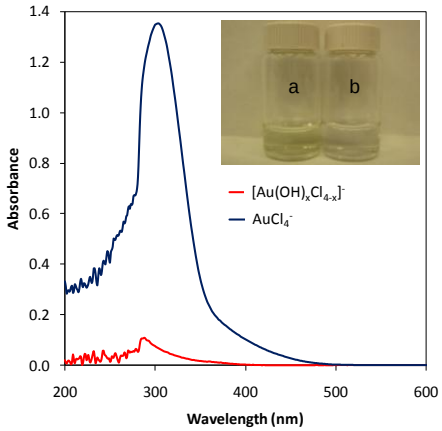

Figure F1. UV-Vis spectra of the 0.38 mM $HAuCl_4$ solution with no K_2CO_3 and the Au salt solution ~24 h after preparation. The inset shows a visual comparison of (a) the 0.38 mM $HAuCl_4$ solution with no K_2CO_3 and (b) the Au salt solution.

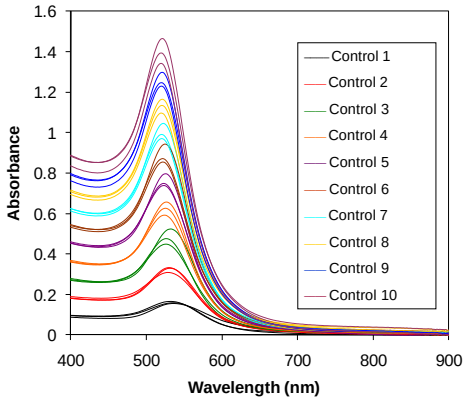

Figure F2. UV-Vis spectra of controls with Au salt solution bubbled with CO. No seed NPs are present.

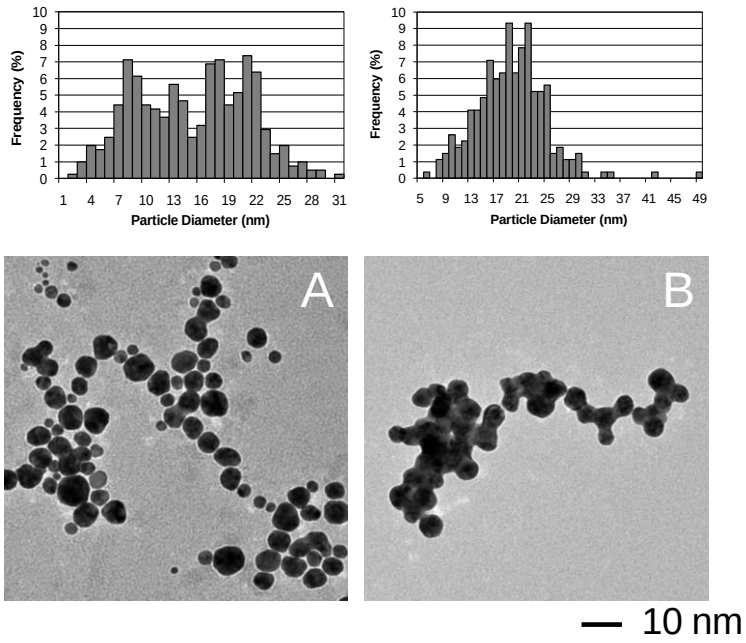

Figure F3. TEM images and size distributions of controls with Au salt solution bubbled with CO. No seed NPs are present. Au^{3+} concentrations are (A) ~190 µM (Control 5) and (B) ~370 µM (Control 10). These Au^{3+} concentrations were used in samples 5 and 10, respectively. TEM size distributions were determined based on ~300 particles.

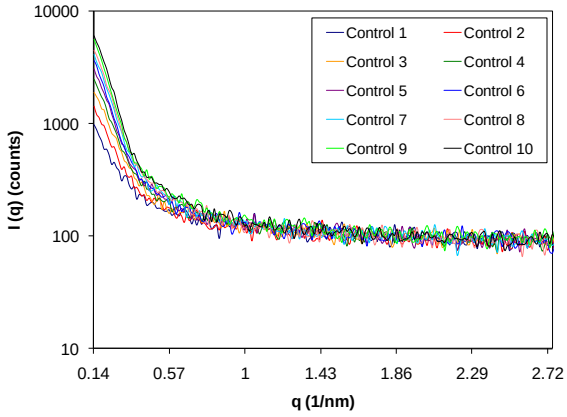

Figure F4. SAXS spectra of controls with Au salt solution bubbled with CO. No seed NPs were present. Only one spectra per control is shown.

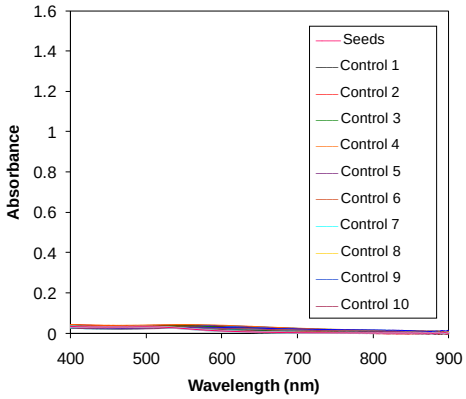

Figure F5. UV-Vis spectra of controls with Au salt solution and seed NPs. No CO was introduced.

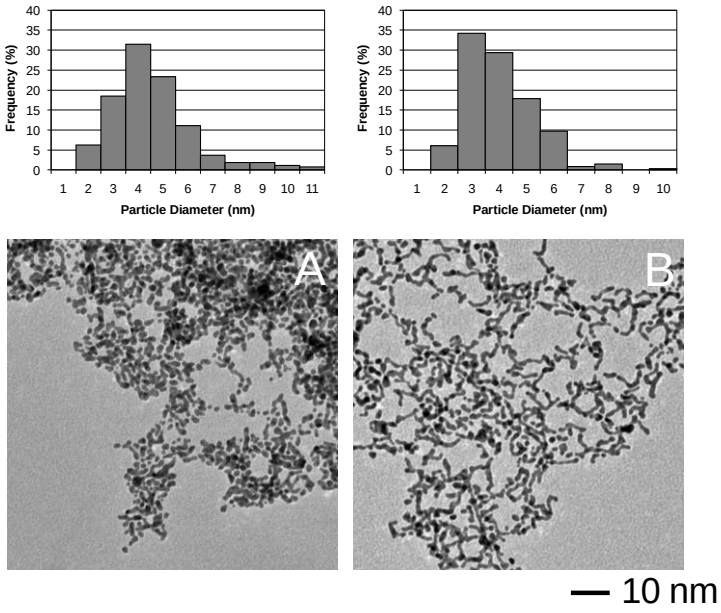

Figure F6. TEM images and size distributions of controls with seed NPs and Au^{3+} concentrations of (A) ~190 µM (Control 5) and (B) ~370 µM (Control 10). These Au^{3+} concentrations were used in samples 5 and 10, respectively. No CO was introduced. TEM size distributions were determined based on ~300 particles.

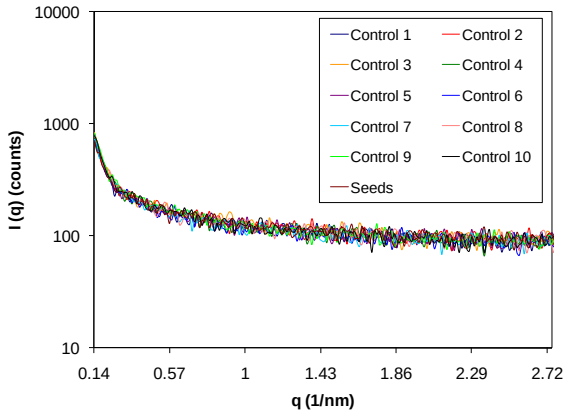

Figure F7. SAXS spectra of controls with seed NPs and Au salt solution. No CO was introduced. Only one spectra per control is shown.

F5 References.

(1) Sasaki, A. *The Rigaku Journal* **2005**, *22*, 31.

(2) Cao, G. Characterization and Properties of Nanomaterials. In *Nanostructures & Nanomaterials - Synthesis, Properties, and Applications*; Imperial College Press: Danvers, 2004; pp 329.